GRAVITATIONAL WAVE PROBES OF NEW PHYSICS

ECHOES FROM A SUPERCOOLED UNIVERSE

DISSERTATION ZUR ERLANGUNG DES DOKTORGRADES
DER NATURWISSENSCHAFTEN
VORGELEGT BEIM FACHBEREICH 13
DER JOHANN WOLFANG GOETHE-UNIVERSITÄT
IN FRANKFURT AM MAIN

VON

DANIEL MARCO SCHMITT
AUS ASCHAFFENBURG, DEUTSCHLAND

FRANKFURT AM MAIN (2025)
(D30)

Vom Fachbereich 13 der Johann Wolfgang Goethe-Universität als Dissertation angenommen.

Dekan:	Prof. Dr. Roger Erb
Gutachter:	Prof. Dr. Laura Sagunski
	Prof. Dr. Dietrich Bödeker
Datum der Disputation:	18. November 2025

The future is not what you've seen

It's not where you've been to at all.

Foals — Black Gold (2010)

ABSTRACT

Gravitational waves may have been produced during the earliest stages of the cosmic evolution, when the dominant energy component of the Universe was a hot plasma of charged particles. As a consequence of the weakness of gravity, such primordial gravitational waves free-stream through the cosmos, forming a stochastic gravitational wave background potentially detectable by future observatories. Since the Standard Model of particle physics does not predict a sizable abundance of cosmological gravitational waves, their detection would provide a clear indication of new physics beyond the Standard Model.

In this thesis, we explore the gravitational wave phenomenology of various Standard Model extensions. We begin by studying classically scale-invariant models, in which the mass of the Higgs field is generated dynamically. These models introduce a substantial period of supercooling into the cosmic thermal history. The exit from supercooling can proceed via various mechanisms, each potentially giving rise to a stochastic gravitational wave background. To this end, we investigate the modified dynamics of the quantum chromodynamics and electroweak phase transitions in a supercooled Universe.

In the second part of this work, we focus on the dynamics of axions coupled to Abelian gauge fields. These pseudoscalar fields were first introduced to solve the strong CP problem and are promising dark matter candidates. Oscillating axions or axion-like particles can trigger a tachyonic resonance in the equation of motion of a dark photon. This leads to an exponential production of gauge quanta, sourcing gravitational waves. We delay the onset of axion oscillations via trapped misalignment, which induces a period of supercooling that significantly enhances the associated gravitational wave background. Furthermore, this enables tachyonic production of Standard Model photons.

Finally, we study the impact of theoretical uncertainties on gravitational wave predictions from first-order phase transitions. We construct the thermal effective potential of the gauge-singlet extended Standard Model, which allows for a first-order electroweak phase transition, employing both conventional one-loop methods and state-of-the-art thermal effective field theory up to next-to-leading order. We perform parameter scans and compare the observable regions of parameter space between the different approaches. By reconstructing the underlying model parameters from a benchmark gravitational wave signal at the future Laser Interferometer Space Antenna, we show that theoretical uncertainties exceed experimental ones—even for signals just above the detection threshold.

PUBLICATIONS

This thesis is based on the following publications and pre-prints. For each of these works, the contributions of the author are highlighted.

[1] Laura Sagunski, Philipp Schicho, and Daniel Schmitt. "Supercool exit: Gravitational waves from QCD-triggered conformal symmetry breaking." In: *Phys. Rev. D* 107.12 (2023), p. 123512. DOI: 10.1103/PhysRevD.107.123512. arXiv: 2303.02450 [hep-ph]

All numerical results and figures were generated by the author. The details of the effective QCD models were worked out together with P. Schicho, while all co-authors contributed to the manuscript. This work forms the basis for chapter 6.

[2] Marek Lewicki, Marco Merchand, Laura Sagunski, Philipp Schicho, and Daniel Schmitt. "Impact of theoretical uncertainties on model parameter reconstruction from GW signals sourced by cosmological phase transitions." In: *Phys. Rev. D* 110.2 (2024), p. 023538. DOI: 10.1103/PhysRevD.110.023538. arXiv: 2403.03769 [hep-ph]

The author was responsible for the `Python` implementation of the dimensionally reduced effective potential. The final code has been published in collaboration with P. Schicho [3]. The parameter space scans were conducted by M. Merchand in collaboration with the author. The Fisher matrix analysis was performed by M. Lewicki. All co-authors contributed to the manuscript, while all figures in the final publication were created by M. Lewicki. This is indicated accordingly below. This work forms the majority of part iv.

[4] Daniel Schmitt and Laura Sagunski. "QCD-sourced tachyonic phase transition in a supercooled Universe." In: *JCAP* 02 (2025), p. 075. DOI: 10.1088/1475-7516/2025/02/075. arXiv: 2409.05851 [hep-ph]

The author has calculated all results and generated all figures. The manuscript was mostly written by the author. This work is described in chapter 7.

[5] Christopher Gerlach, Daniel Schmitt, and Pedro Schwaller. "Supercooled Audible Axions." In: (Apr. 2025). arXiv: 2504.05386 [hep-ph]

The numerical simulations were performed by the author, while the analytic estimates were obtained in collaboration. All co-authors contributed to the manuscript, while most of the figures were created by the author. Two figures were created by C. Gerlach, which is indicated accordingly below. This work forms the basis of part iii.

In addition, the following publications and pre-prints were completed during the course of the author's doctoral studies, however, they are beyond the scope of this thesis.

[6] Eric Madge, Wolfram Ratzinger, Daniel Schmitt, and Pedro Schwaller. "Audible axions with a booster: Stochastic gravitational waves from rotating ALPs." In: *SciPost Phys.* 12.5 (2022), p. 171. DOI: 10.21468/SciPostPhys.12.5.171. arXiv: 2111.12730 [hep-ph]

[7] Robin Fynn Diedrichs, Daniel Schmitt, and Laura Sagunski. "Binary systems in massive scalar-tensor theories: Next-to-leading order gravitational wave phase from effective field theory." In: *Phys. Rev. D* 110.10 (2024), p. 104073. DOI: 10.1103/PhysRevD.110.104073. arXiv: 2311.04274 [gr-qc]

[8] Maciej Kierkla, Nicklas Ramberg, Philipp Schicho, and Daniel Schmitt. "Theoretical uncertainties for primordial black holes from cosmological phase transitions." In: (June 2025). arXiv: 2506.15496 [hep-ph]

[9] Dietrich Bödeker, Jondalar Kuß, Laura Sagunski, and Daniel Schmitt. "Sterile neutrino dark matter and gravitational waves in a supercooled Universe." *to appear*.

SUMMARY

The first direct detection of gravitational waves from two merging black holes by the LIGO/Virgo collaboration [10] has not only provided yet another experimental confirmation of Einstein's theory of General Relativity [11, 12], but may also open a new window into the early Universe, shortly after the Big Bang. These ripples in the fabric of spacetime are produced in sizable amounts only by the most violent events in the cosmos and barely interact with matter—yet they may hold the key to answering some of the most pressing questions in fundamental physics.

Today's Universe is largely empty, dominated by a currently unknown form of vacuum energy—the cosmological constant—that drives the accelerated expansion of space. Extrapolating the cosmic history back to the first moments after the Big Bang, we arrive at a vastly hotter and denser state, where the energy density was dominated by a plasma of relativistic particles [13]. Despite its significance, little is known about this early epoch of the cosmic evolution. However, measurements of the cosmic microwave background [14], emitted approximately 380,000 years after the Big Bang, along with observations of the abundances of light elements, have shed some light on the state of the Universe up to MeV-scale temperatures [15].

Before the decoupling of the cosmic microwave background radiation, the Universe was opaque to electromagnetic radiation. This surface of last scattering hence sets a natural limit on the timescales accessible to conventional astronomical observations. To this end, gravitational waves may be crucial to extending our understanding of the primordial Universe. Interacting only weakly with its surroundings and thus decoupling at very high temperature close to the Planck scale [16, 17], gravitational waves propagate almost undisturbed through the hot thermal bath. Therefore, if the early Universe underwent a violent process associated with the emergence of large anisotropies, a primordial stochastic gravitational wave background would have been generated [18], potentially detectable by future gravitational wave observatories.

The dynamics of the primordial plasma is dictated by the Standard Model of particle physics, comprising all fundamental particles and their interactions. The Standard Model features various symmetry breaking mechanisms. Most notably, at a temperature of $T_{\mathrm{ew}} \sim \mathcal{O}(100\,\mathrm{GeV})$, electroweak symmetry breaking occurs. That is, the Higgs field acquires a vacuum expectation value, generating the masses of the weak gauge bosons, quarks, and

charged leptons. Around the QCD temperature $T_{\mathrm{QCD}} \sim \mathcal{O}(100\,\mathrm{MeV})$, the approximate chiral symmetry of the strong interactions is broken via the formation of quark condensates. This marks the transition of the early Universe from the quark phase to the hadronic phase, where the fundamental degrees of freedom are bound states, i.e., mesons and baryons. Intriguingly, both the electroweak and QCD transitions are crossovers in the Standard Model [19, 20], therefore not associated with a sizable gravitational wave background.

Despite having passed all experimental tests with remarkable precision, there is ample motivation that the Standard Model is not the ultimate theory. Apart from lacking a quantum theory of gravity, the Standard Model cannot explain, e.g., the masses of neutrinos [21] or the origin of dark matter [22]. Furthermore, the Standard Model does not provide a baryogenesis mechanism [23], responsible for generating the asymmetry of matter over antimatter in the Universe. This naturally raises the necessity of new physics beyond the Standard Model. Although laboratory experiments have set bounds on the properties of Standard Model extensions, new physics searches are limited by, for instance, feasible center-of-mass energies of Earth-based colliders. Given the large energies present in the primordial Universe, gravitational wave observations open a new window to high-energy physics. The detection of a cosmological gravitational wave background would therefore not only shine light on the cosmic evolution, but would also constitute evidence for physics beyond the Standard Model.

Recently, pulsar timing array collaborations have published strong evidence for the existence of a stochastic gravitational wave background in the nHz frequency band [24–33]. The favored sources are mergers of supermassive black hole binaries, which currently cannot be resolved independently. However, a primordial source has not been excluded to date [34], with possible sources including first-order phase transitions, cosmic strings, or scalar-induced gravitational waves. This underscores the remarkable potential of the still emerging field of gravitational wave cosmology. Furthermore, a multitude of future observatories are planned; recently, the space-based Laser Interferometer Space Antenna [35–37] was approved, starting its mission of detecting gravitational waves in the mHz regime in the 2030s. In the same time frame, the Earth-based Einstein Telescope [38–40], sensitive to the $\mathcal{O}(\mathrm{Hz} - \mathrm{kHz})$ region, aims to commence its operations. Given these exciting experimental developments, it is a timely and crucial endeavor to advance theoretical predictions of the primordial gravitational wave background.

In this thesis, we will delve into beyond the Standard Model physics and the potential of probing new physics via primordial gravitational waves. This work is divided in three parts, each exploring a different Standard Model extension, unified by their implications for gravitational wave phenomenology. We contribute both to the development of new

mechanisms that yield novel gravitational wave signatures and to the advancement of existing theoretical predictions, paving the way for robust gravitational wave templates that aid future data analyses.

First, we introduce the state of the art in modern high-energy physics in a concise yet pedagogical manner in part i. This includes the fields and interactions contained in the Standard Model of particle physics. Furthermore, we describe the cosmic evolution as predicted by the cosmological principle and the theory of General Relativity. We highlight open problems within the standard paradigm and discuss possible resolutions. The general features of a stochastic gravitational wave background are outlined, along with the necessary conditions for its generation. To illustrate the deep connection between particle physics and primordial gravitational waves, we examine in detail the dynamics of cosmological first-order phase transitions.

The first main part of this thesis, part ii, centers on modifications of the electroweak sector. Specifically, we study classically scale-invariant Standard Model extensions. These are characterized by a lack of mass terms at tree-level. Therefore, the negative Standard Model Higgs mass term $-\mu^2$, responsible for electroweak symmetry breaking, is replaced by a portal coupling to a new scalar field φ. This scalar is charged under an additional gauge symmetry, which is spontaneously broken via the Coleman–Weinberg mechanism, that is, by radiative corrections to the tree-level potential. As φ acquires a vacuum expectation value, the electroweak symmetry is broken dynamically; the negative Higgs mass emerges via the portal coupling to the new sector. To this end, we largely focus on the $\mathrm{U}(1)_{\text{B-L}}$ extension of the Standard Model [41], where the global "baryon – lepton number" symmetry is gauged. This theory contains three right-handed neutrinos, which, in addition to explaining the neutrino masses via the Seesaw mechanism [42], can constitute dark matter [43], and provide the necessary conditions for the generation of the baryon asymmetry via leptogenesis [44]. Hence, classically scale-invariant models exhibit rich phenomenology while relying on only a few input parameters, making them highly predictive.

Intriguingly, classically scale-invariant Standard Model extensions modify the thermal history of the primordial Universe. Scalar fields interacting with a thermal bath receive temperature-dependent mass corrections that restore gauge symmetries at high temperatures. Then, the thermal effective potential only possesses a minimum at the origin. As the Universe cools and a finite vacuum expectation forms, the scalar field transitions to the true vacuum state. In the absence of a negative tree-level mass term, however, a barrier is generated that separates the false from the true vacuum. The scalar field must overcome this barrier; that is, the theory undergoes a first-order phase transition. Intriguingly, the barrier persists at very small temperatures, delaying both the breaking of the

$\mathrm{U}(1)_{\mathrm{B\text{-}L}}$ and electroweak symmetry. If the phase transition is sufficiently supercooled, the false vacuum energy of the new scalar field eventually becomes comparable to the energy density of the thermal bath. Then, the Universe enters an intermediate period of thermal inflation which ends with the symmetry-breaking phase transition. First-order phase transitions proceed via the nucleation and percolation of true vacuum bubbles. The interactions of such bubbles with each other and with the thermal bath introduces large anisotropies, hence gravitational waves. Due to the substantial amount of supercooling, classically scale-invariant models generate particularly strong gravitational wave signals.

In chapter 6, we consider the possibility of a QCD-induced exit from supercooling. Classically scale-invariant models always feature a parameter space where electroweak symmetry breaking is delayed to the QCD scale. As a consequence, all Standard Model quarks remain massless during QCD chiral symmetry breaking. This allows for the possibility of a first-order quark–hadron transition [45]. The formation of quark condensates breaks classical scale invariance and induces a vacuum expectation value for the Higgs field [46]. This can trigger the conformal phase transition via the Higgs portal. While the latent heat is then dictated by the conformal sector, the timescale of the transition is determined by the nucleation rate of hadronic bubbles. To study the resulting gravitational wave background, we employ low-energy effective QCD models that predict a first-order phase transition in the chiral limit. We compute the phase transition dynamics in a supercooled Universe dominated by a classically scale-invariant sector. Intriguingly, we find that the transition timescale crucially depends on the background evolution, i.e., the Hubble parameter during thermal inflation. If the energy scale of new physics is large, the timescale of the QCD transition is extended. This implies a larger characteristic bubble size at collision, and therefore, an enhanced gravitational wave amplitude. Hence, we find excellent observational prospects at future observatories such as the Einstein Telescope. Furthermore, this mechanism provides a way to enhance gravitational wave backgrounds from more exotic strongly-coupled sectors, which are typically associated with small amplitudes due to their fast transition timescales.

Based on these results, we develop a novel gravitational wave production mechanism in classically scale-invariant models in chapter 7. Employing the $\mathrm{U}(1)_{\mathrm{B\text{-}L}}$ model, we show that if the gauge coupling in the new sector is small, $g_{B\text{-}L} \lesssim \mathcal{O}(10^{-2} - 10^{-1})$, one enters a regime of extreme supercooling where bubble percolation cannot drive the phase transition. Instead, the symmetry-breaking scalar field rolls towards the true minimum as the thermal barrier is canceled by QCD-induced effects. Then, φ crosses a region of the effective potential where its mass squared is negative. This signals a tachyonic instability, where long-wavelength fluctuations become unstable and grow exponentially; we call

this scenario a tachyonic phase transition. Such dynamics are known from tachyonic preheating models after cosmic inflation [47, 48]. The explosive amplification of fluctuations induces large-scale anisotropies in the energy–momentum tensor of the Universe, generating a stochastic gravitational wave background. Using previous results from lattice studies of tachyonic preheating, we estimate the peak frequency and amplitude of the resulting gravitational wave signal, and assess its observational prospects at future observatories. This predicts a unique signature and opens up previously unexplored parameter spaces within classically scale-invariant Standard model extensions.

In part iii, we study the dynamics of axions and axion-like particles in the early Universe. These pseudoscalar fields were initially introduced to solve the strong CP problem, associated with the absence of CP violation in QCD [49–52]. In addition, axion-like particles are promising dark matter candidates, as their coupling to Standard Model fields is naturally suppressed by a large energy scale f_ϕ. This energy scale is associated with the spontaneous breaking of the global $\mathrm{U}(1)_{\mathrm{PQ}}$ Peccei–Quinn symmetry, from which the axion emerges as a pseudo-Nambu–Goldstone boson. However, the suppressed coupling makes the detection of axions and axion-like particles extremely challenging. Therefore, it is crucial to develop mechanisms that allow for detection without relying on large couplings to the visible sector.

One such example is the audible axion mechanism [53], in which axion-like particles couple to a dark Abelian gauge field. Interestingly, the motion of the axion-like particle triggers a tachyonic instability in the equation of motion of the dark photon. This leads to a copious production of vector modes in a specific momentum band. Again, this induces anisotropies in the stress–energy tensor, sourcing stochastic gravitational waves. Due to the CP-violating nature of the axion-dark photon coupling, the resulting signal is chiral, providing a smoking-gun signature at future observatories.

The original audible axion mechanism exhibits two shortcomings. First, tachyonic dark photon production is only efficient for very large axion-dark photon couplings $\alpha \gtrsim 20$. Second, only large axion decay constants close to the Planck scale yield sizable signals. This severely limits the accessible parameter space. Inspired by part ii, we study the possibility of an axion-driven period of supercooling in the early Universe. This is achieved via additional, $\mathrm{U}(1)_{\mathrm{PQ}}$-breaking operators at high energy scales, trapping the axion initially and delaying the onset of its oscillations [54]. We derive bounds on this scenario and identify the cosmologically viable parameter space. We show that supercooled axions significantly enhance the resulting gravitational wave amplitude, opening up the parameter space probed via gravitational wave observations. In addition, this reduces the required coupling to $\alpha \sim 1$. Furthermore, we demonstrate that the supercooled audible axion sce-

nario allows for tachyonic production of Standard Model photons from the thermal bath. As a consequence, the mechanism is simplified, as it does not rely on the existence of a dark photon. To this end, we identify two distinct parameter regions at low and ultra-high frequencies that may feature sizable signals.

In the last main part, part iv, we examine the robustness of gravitational wave predictions from first-order phase transitions. In general, the computation of the phase transition dynamics is a delicate task, involving a multitude of physical scales and sources of uncertainty; we focus on the construction of the thermal effective potential. This is one of the most sensitive parts of the computation, as thermal quantum field theory suffers from slow convergence in the infrared [55]. To extend the regime in which the perturbative treatment is valid, thermal resummations of heavy plasma modes are required. Consequently, uncertainties in the effective potential propagate through the computation of the bubble dynamics and affect the final gravitational wave prediction. In some cases, incomplete resummation was shown to induce order-of-magnitude deviations in the resulting spectrum [56].

We extend the Standard Model by a real, gauge-singlet scalar field. If this new degree of freedom is sufficiently light, the electroweak phase transition is rendered first-order in certain parts of the parameter space. We study the robustness of this parameter space using different computational techniques, including both conventional, one-loop resummation and state-of-the-art thermal effective field theory up to two-loop order. We show that while one-loop results for single parameter points carry large uncertainties, the overall parameter space that features a strong first-order phase transition is more robust. Conversely, only the two-loop methods predict large parameter spaces that remain consistent under a variation of the renormalization group scale. Lastly, we reconstruct the underlying model parameters via Fisher matrix analyses using a benchmark signal at the future Laser Interferometer Space Antenna given the different approximations of the effective potential. Intriguingly, although the absolute deviation of the reconstructed parameters is small between the different approaches, the one-loop results are not compatible within their confidence levels; only the two-loop methods yield consistent parameter reconstructions. This implies that theoretical inconsistencies from incomplete resummation dominate over experimental uncertainties. This holds already for signals that barely exceed the detection threshold, highlighting the need for two-loop resummation and providing an important step forward in inferring the underlying microphysics from gravitational wave signals.

CONTENTS

Part I

PROLOGUE

1

INTRODUCTION

The 20th century witnessed the emergence of two revolutionary physical theories that reshaped our understanding of the Universe: General Relativity (GR) and the Standard Model (SM) of particle physics. The SM describes nature at its smallest scales, comprising the fundamental particles and their interactions. Its last missing piece—the *Higgs boson*, responsible for the generation of masses via *spontaneous symmetry breaking*—was detected in 2012 [57, 58], more than 40 years after it was first predicted [59–64]. Despite its remarkable experimental success, the existence of physics beyond the SM (BSM) is strongly motivated by, for instance, the lack of a quantum theory of gravity and the unexplained origin of neutrino masses [21].

Einstein's theory of GR is the mathematical framework that describes nature at its largest scales, capturing the interplay between the energy content of the Universe and the curvature of spacetime. Predicted in 1915, GR has been experimentally confirmed numerous times—most notably by the first direct detection of *gravitational waves* (GWs) [11, 12] from merging black holes by the LIGO/Virgo collaboration [10]. GWs are periodic perturbations of spacetime that propagate at the speed of light. As a consequence of the weakness of gravity, they are generated only by the most violent events in the cosmos. Intriguingly, in spite of the small coupling strength between GWs and matter, they may hold the key to the next fundamental breakthroughs in particle physics.

In addition to GWs from astrophysical systems such as black holes and neutron star binaries [65], GWs might have been produced in the earliest moments after the *Big Bang*. In this epoch, the Universe was significantly hotter and denser than today, with the dominant energy component being a plasma of charged particles. Remarkably, observations of the *cosmic microwave background* (CMB) [14] and measurements of element abundances allow us to reconstruct the cosmic history to the era of *Big Bang Nucleosynthesis* (BBN) [15]; this corresponds to the first formation of light elements at MeV-scale temperatures. These observations guided the development of the currently favored model of the evolution of the Universe: the Lambda Cold Dark Matter (ΛCDM) model. This model postulates the

existence of dark energy, driving the accelerated expansion of the Universe, and dark matter (DM), constituting a form of matter neither explained by GR nor by the SM. Furthermore, today's Universe shows an asymmetry of matter over antimatter. The cosmic history of the SM in the ΛCDM model, however, lacks a *baryogenesis* mechanism to generate this asymmetry.

In particular, generating the matter-antimatter asymmetry requires an out-of-equilibrium phenomenon in the early Universe [23], such as a *first-order phase transition* (FOPT). Analogously to the phase transition (PT) of water when brought to a boil, the primordial plasma might have changed its ground state through the nucleation of bubbles. If these bubbles carried a large fraction of the total energy density of the Universe and grew sufficiently large compared to the Hubble horizon, large anisotropies would have been generated. This inevitably leads to the emission of GWs, which propagate almost undisturbed to the present day. Such a signal would manifest as a cosmological *stochastic GW background* (SGWB)—a diffuse, persistent background of gravitational radiation rather than a transient signal.

The SM of particle physics features two symmetry-breaking mechanisms: *electroweak symmetry breaking* (EWSB) and *chiral symmetry breaking* (χSB) of quantum chromodynamics (QCD). While the former is responsible for giving fundamental particles their mass, the latter is associated with quarks confining to bound states, i.e., hadrons. Notably, both phenomena are realized as smooth crossovers [19, 20] which do not generate GWs. The detection of a primordial SGWB would therefore constitute evidence for BSM physics. This establishes a remarkable connection between the microphysics governing fundamental particles and the macrophysics of the Universe as a whole.

The emerging field of GW cosmology has already made an exciting step forward when various pulsar timing array (PTA) collaborations published strong evidence for a SGWB in the nHz frequency band [24–33]. While the favored explanation are unresolved supermassive black hole mergers, a primordial origin of the signal has not been excluded to date [34]. Furthermore, new observatories will start their mission in the foreseeable future. This includes, for instance, the space-based Laser Interferometer Space Antenna (LISA) [35–37] sensitive to the mHz band, and the Earth-based Einstein Telescope (ET) [38–40], detecting GWs at $\mathcal{O}(10\,\mathrm{Hz})$ frequencies. The broad frequency range covered by future experiments will enable testing new physics across energy scales spanning many orders of magnitude. Therefore, it is crucial to improve the precision of existing theoretical predictions and develop novel mechanisms that give rise to primordial GWs.

In this thesis, we will explore various BSM mechanisms that predict the existence of a SGWB. In the following chapters, we first give a concise introduction to the theoreti-

cal background, covering the foundations of modern high-energy physics and SGWBs. In part ii, we will investigate the cosmological implications of classically scale-invariant (CSI) SM extensions. These models are designed to dynamically generate EWSB. We will demonstrate that such theories significantly modify the thermal history of the Universe by a period of *supercooling*, therefore establish an intriguing connection between QCD and electroweak physics, and generate GW signals in the reach of future observatories. Part iii centers on axion-like particles (ALPs). These hypothetical, pseudoscalar particles represent promising DM candidates. Specifically, we will study the early Universe phenomenology of ALPs coupled to (dark) photons, which provide a mechanism for the production of DM along with a smoking-gun GW signature. Lastly, we will closely examine the robustness of GW predictions from FOPTs in part iv. By analyzing the dynamics of the electroweak PT (EWPT) under the influence of an additional gauge-singlet scalar field in increasing levels of computational diligence, we show that theoretical uncertainties dominate over experimental ones at the future LISA observatory. This highlights the necessity of employing robust theoretical frameworks and constitutes an important step forward regarding new physics searches via GWs. Finally, we summarize and conclude this thesis in part v.

1.1 NOTATION

Throughout this thesis, we employ natural units where $\hbar = c = 1$. Greek letters correspond to spacetime indices, $\mu \in \{0, 1, 2, 3\}$. Three-vectors are written as bold symbols ($\boldsymbol{x}$), with latin indices indicating the respective components (x_i). Einstein's sum convention, $\sum_\mu A_\mu B^\mu = A_\mu B^\mu$, and the Dirac slash notation, $\not{k} = k^\mu \gamma_\mu$, are used. The Minkowski metric reads $\eta_{\mu\nu} = \mathrm{diag}(1, -1, -1, -1)$. Partial derivatives with respect to a variable x are expressed as ∂_x. Spacetime derivative then read $\partial_\mu = \frac{\partial}{\partial x^\mu} = (\partial_t, \partial_i)$. We employ the reduced Planck mass $M_{\mathrm{Pl}} = (8\pi G)^{-\frac{1}{2}}$, where G is the gravitational constant.

2

CURRENT UNDERSTANDING OF THE UNIVERSE

The foundation of modern high energy physics consists of two theories: the SM of Particle Physics, which captures the microscopic interactions of fundamental particles, and the ΛCDM model, which describes the cosmological evolution on large scales. In the following, we first introduce the particle content of the SM and its symmetry breaking mechanisms. Thereafter, we outline the current paradigm of the cosmic evolution, focusing on the primordial Universe shortly after the Big Bang. Subsequently, we discuss various open puzzles, highlighting the close connection between particle physics and cosmology.

2.1 STANDARD MODEL OF PARTICLE PHYSICS

The SM of Particle Physics is a quantum field theory (QFT) which comprises all known elementary particles and their interactions. Developed in the 20th century [66–70], the SM was completed in 2012 [57, 58] with the discovery of the final predicted fundamental particle—the *Higgs boson*. Since then, the SM has passed all experimental tests with remarkable consistency. The agreement between theoretical predictions and experimental observations is unprecedented, making the SM the most precise scientific theory in history [71]. However, it is important to note that the SM cannot be the ultimate theory as it lacks, for instance, a quantum description of gravity and an explanation for neutrino masses [21].

PARTICLE CONTENT. The SM is based on *gauge symmetries* that dictate the interactions between quantum fields. The total gauge group is

$$\mathrm{SU}(3)_\mathrm{c} \times \mathrm{SU}(2)_\mathrm{L} \times \mathrm{U}(1)_\mathrm{Y}\,, \tag{2.1}$$

where $\mathrm{SU}(2)_\mathrm{L} \times \mathrm{U}(1)_\mathrm{Y}$ corresponds to the electroweak sector [67–69], while $\mathrm{SU}(3)_\mathrm{c}$ describes the strong interactions, i.e., QCD [72–76]. The matter fields in the SM come in three generations and are of fermionic nature. That is, spin–1/2 particles, where one distin-

Name	Field	$\mathrm{SU}(3)_\mathrm{c}$	$\mathrm{SU}(2)_\mathrm{L}$	$\mathrm{U}(1)_\mathrm{Y}$
Quarks	q_L^i	**3**	**2**	$+\frac{1}{6}$
	u_R^i	**3**	**1**	$+\frac{2}{3}$
	d_R^i	**3**	**1**	$-\frac{1}{3}$
Leptons	l_L^i	**1**	**2**	$-\frac{1}{2}$
	e_L^i	**1**	**1**	-1
Gluons	G	**8**	**1**	0
Electroweak gauge bosons	W	**1**	**3**	0
	B	**1**	**1**	0
Higgs	H	**1**	**2**	$\frac{1}{2}$

Table 2.1: Particle content of the SM. For each field, we indicate the corresponding charges under the respective gauge groups. The index $i \in \{1, 2, 3\}$ denotes the fermion generations, while the subscripts L and R indicate left- and right-handed chiralities.

guishes between *quarks* and *leptons*. Quarks are divided into up-type (up u, charm c, top t) and down-type (down d, strange s, bottom b) fields, which differ in their electromagnetic charge. Leptonic fields are the electron e, muon μ, tau-lepton τ, and the corresponding neutrinos $(\nu_e, \nu_\mu, \nu_\tau)$. The respective forces are mediated by spin–1 fields: the electroweak W and B gauge bosons, and the gluons of QCD. Furthermore, the SM contains the scalar, hence spin–0, Higgs field.

The dynamics are derived from the *Lagrangian density*, commonly referred to as the *Lagrangian*, which may be classified into three building blocks,

$$\mathcal{L}_\mathrm{SM} = \mathcal{L}_\mathrm{kin} + \mathcal{L}_\mathrm{Yuk} + \mathcal{L}_\mathrm{Higgs}\,. \tag{2.2}$$

Here, $\mathcal{L}_\mathrm{kin}$ corresponds the kinetic part, containing the dynamics of the fields and all gauge-mediated interactions. The Yukawa interactions between the matter fields and the Higgs boson are described by $\mathcal{L}_\mathrm{Yuk}$, while $\mathcal{L}_\mathrm{Higgs}$ comprises the Higgs potential.

An overview of the fundamental fields with their respective charges is given in table 2.1. The subscript L (R) denotes left-handed (right-handed) fields. Left-handed fermions are doublets under $\mathrm{SU}(2)_\mathrm{L}$, while the right-handed counterparts are singlets. That is, the weak interaction is maximally parity violating. Therefore, bare mass terms involving left- and right-handed fermions are forbidden as they would break gauge invariance. Quarks carry color charges, hence transform as triplets under $\mathrm{SU}(3)_\mathrm{c}$, while leptons are singlets. Furthermore, we see that gluons form an octet under $\mathrm{SU}(3)_\mathrm{c}$, i.e., they are self-interacting.

The same is true for the W boson, which transforms as a triplet under the weak gauge group. The Higgs field does not carry color charge, however, couples to the electroweak sector and is responsible for mass generation.

ELECTROWEAK SYMMETRY BREAKING. In the SM, the electroweak symmetry is spontaneously broken down to

$$\mathrm{SU}(2)_{\mathrm{L}} \times \mathrm{U}(1)_{\mathrm{Y}} \to \mathrm{U}(1)_{\mathrm{EM}} \tag{2.3}$$

via the *Higgs mechanism* [59–64]. Here, $\mathrm{U}(1)_{\mathrm{EM}}$ denotes the unbroken gauge group of quantum electrodynamics (QED) [77–81]. To see this, let us consider the Higgs potential in eq. (2.2)

$$V(H) = -\mu^2 H^\dagger H + \lambda (H^\dagger H)^2 \,, \tag{2.4}$$

where the mass term $\mu^2 > 0$, λ is the quartic self-interaction strength, and the Higgs doublet is given by

$$H = \begin{pmatrix} G^\pm \\ \frac{1}{\sqrt{2}}(v + h + iG^0) \end{pmatrix} . \tag{2.5}$$

The physical Higgs field is denoted by h, v corresponds to a classical background field, and $G^\pm/G^0$ are the Goldstone modes. By minimizing the Higgs potential along the real axis, we find that the negative mass term induces a finite vacuum expectation value (vev) [71]

$$v_0 = \sqrt{\frac{\mu^2}{\lambda}} \approx 246\,\mathrm{GeV} \,. \tag{2.6}$$

Expanding around this ground state of the theory yields mass terms for the electroweak gauge bosons via the covariant derivatives, spontaneously breaking the electroweak symmetry. This leads to the emergence of $W^\pm$ mass eigenstates, which are linear combinations of W_1 and W_2. The electrically neutral Z gauge boson forms as a superposition of W_3 and B_0. To this end, the Goldstone modes provide the longitudinal degrees of freedom. In addition, the massless photon remains as a second linear combination of W_3 and B_0, mediating electromagnetic interactions. The Higgs mechanism also generates fermion masses via the Yukawa couplings in eq. (2.2). However, note that this does not account for neutrino masses, as the SM lacks a right-handed neutrino component.

What is crucial for this work is that the SM does not exhibit a PT. That is, EWSB occurs via a *smooth crossover* at $T_c \approx 160\,\mathrm{GeV}$ [82] for the observed Higgs mass of $m_h \approx 125\,\mathrm{GeV}$ [19].

QCD CHIRAL SYMMETRY BREAKING. In QFTs, the couplings that parametrize the strength of a given interaction are not constant, but *run* with the energy scale μ; this behavior is captured by the β–functions. The β–function of a QCD-like, non-Abelian gauge theory with N_c colors and N_f flavors is given by [83]

$$\frac{\mathrm{d}g_s}{\mathrm{d}\ln\mu} = \beta(g_s) = -\frac{g_s^3}{(4\pi)^2}\left(\frac{11}{3}N_c - \frac{2}{3}N_f\right) \overset{\text{QCD}}{=} -7\frac{g_s^3}{(4\pi)^2}\,, \tag{2.7}$$

where g_s is the gauge coupling and we have specialized to QCD with $N_c = 3$ and $N_f = 6$ in the last step. The negative sign implies a decreasing coupling strength in the ultraviolet (UV), leading to the phenomenon of *asymptotic freedom* [76]. That is, quarks and gluons behave as free fields at sufficiently large energy scales, i.e., short distances. Conversely, g_s becomes large in the infrared (IR) below $\Lambda_{\text{QCD}} \sim \mathcal{O}(100\,\text{MeV})$, inducing *color confinement* at large distances [84, 85]. This implies the confinement of quarks into color-neutral bound states, called *hadrons*.

The QCD Lagrangian reads

$$\mathcal{L}_{\text{QCD}} = \sum_f \bar{q}_f \left(i\not{D} - m_f\right) q_f - \frac{1}{4}G^a_{\mu\nu}G_a^{\mu\nu}\,, \tag{2.8}$$

where $G_{\mu\nu}$ is the gluonic field strength tensor, a runs over the generators of $\mathrm{SU}(3)_\mathrm{c}$, $\not{D} = \gamma^\mu D_\mu$ with γ being the Dirac matrices, and f denotes the quark flavor. The quark mass m_f is set via the Yukawa couplings to the Higgs field. Since the masses of the light u, d, and s quarks are well below the confinement scale, the Lagrangian (2.8) possesses an approximate, global

$$\mathrm{SU}(3)_\mathrm{L} \times \mathrm{SU}(3)_\mathrm{R} \tag{2.9}$$

symmetry. This is known as the *chiral symmetry* of QCD, where the generators of $\mathrm{SU}(3)_\mathrm{L}$ and $\mathrm{SU}(3)_\mathrm{R}$ act on the left- and right-handed quark field components, respectively. Mass terms that couple left- and right-handed fields $\sim m_q\bar{q}_\mathrm{L}q_\mathrm{R}$ break this symmetry explicitly. In the hadronic phase spontaneous χSB occurs,

$$\mathrm{SU}(3)_\mathrm{L} \times \mathrm{SU}(3)_\mathrm{R} \to \mathrm{SU}(3)_\mathrm{V}\,, \tag{2.10}$$

through the formation of chiral condensates $\langle\bar{q}q\rangle = \langle\bar{q}_\mathrm{L}q_\mathrm{R} + \bar{q}_\mathrm{R}q_\mathrm{L}\rangle$. The remaining symmetry corresponds to $\mathrm{SU}(3)_\mathrm{V}$ vector transformations that treat left- and right-handed fields in the same way. As the chiral symmetry is not exact, the resulting pseudo-Nambu–Goldstone bosons are massive [86, 87]. These manifest as an octet of light pseudoscalar mesons: pions, kaons, and the η-meson.

Lattice studies indicate that the chiral transition is a crossover near $T_c \approx 155\,\text{MeV}$ for physical quark masses [20, 88]. Therefore, the SM does not feature any FOPTs.

2.2 COSMIC EVOLUTION

While the SM captures the microphysics of the Universe, its behavior on large scales is described by Einstein's theory of GR. The corresponding field equations read

$$M_{\mathrm{Pl}}^2 \left(R_{\mu\nu} - \frac{1}{2} R g_{\mu\nu} \right) = T_{\mu\nu} \,, \tag{2.11}$$

where $g_{\mu\nu}$ is the metric tensor. The gravitational constant is contained in the reduced Planck mass $M_{\mathrm{Pl}} = (8\pi G)^{-\frac{1}{2}} \simeq 2.435 \times 10^{18}\,\mathrm{GeV}$. Spacetime curvature is encoded on the left-hand side, where $R = g^{\mu\nu} R_{\mu\nu}$ is the Ricci scalar with $R_{\mu\nu} = \partial_\lambda \Gamma^\lambda_{\mu\nu} - \partial_\nu \Gamma^\lambda_{\mu\lambda} + \Gamma^\lambda_{\lambda\rho}\Gamma^\rho_{\mu\nu} - \Gamma^\rho_{\mu\lambda}\Gamma^\lambda_{\nu\rho}$ being the Ricci tensor. The Christoffel symbols $\Gamma^\lambda_{\mu\nu}$ describe the metric connection and are functions of $g_{\mu\nu}$ and its derivatives; hence, they are directly tied to the geometry of the Universe. The right-hand side of eq. (2.11) is the stress–energy tensor, which contains the energy and momentum of the cosmic fluids. This reveals the direct connection between spacetime curvature and the matter content of the Universe.

In the following, we will first introduce the metric that describes the Universe on its largest scales. By solving the Einstein equations, we then obtain the scaling laws for the different energy components in the Universe. Based on this theoretical background, we introduce the ΛCDM model, also called the Standard Model of Cosmology. Finally, we outline the thermal history of the primordial Universe. To this end, we largely follow refs. [89, 90].

FRIEDMANN-LEMAÎTRE-ROBERTSON-WALKER UNIVERSE. Observations of the CMB [14] strongly suggest that the Universe is *isotropic* on its largest scales. The cosmological principle states that Earth is not a special point in the cosmos. Under this assumption, we may conclude that the Universe is isotropic at every point, and hence *homogeneous*. This implies that the Universe does not have a preferred position or direction; accordingly, the spacetime metric must share these properties.

It is important to note that homogeneity and isotropy merely apply to the spatial part of the Universe, as the time component is dynamical. The most general metric that respects these symmetries was found in the 1920s, and is nowadays known as the *Friedmann–Lemaître–Robertson–Walker* (FLRW) metric,

$$\mathrm{d}s^2 = \mathrm{d}t^2 - a(t)^2 \left[\frac{\mathrm{d}r^2}{1-\kappa r^2} + r^2 \mathrm{d}\Omega^2 \right] = a(\tau)^2 \left[\mathrm{d}\tau^2 - \frac{\mathrm{d}r^2}{1-\kappa r^2} - r^2 \mathrm{d}\Omega^2 \right] , \tag{2.12}$$

where the angular part $\mathrm{d}\Omega^2 = r^2(\mathrm{d}\vartheta^2 + \sin^2\vartheta \mathrm{d}\varphi^2)$. The scale factor $a(t)$ parametrizes the expansion of the Universe and is taken to be dimensionless. Then, r has the dimension of length. To arrive at the second expression, we have introduced conformal time

$$\mathrm{d}\tau = \frac{\mathrm{d}t}{a}\,. \tag{2.13}$$

The parameter κ controls the overall geometry of the Universe, with $\kappa \in \{-1, 0, 1\}$ corresponding to negative, zero, and positive intrinsic curvature, respectively. Measurements indicate a flat Universe [14], therefore we set $\kappa = 0$ henceforth.

The matter content in a homogeneous and isotropic Universe, hence the source term of eq. (2.11) is described by a perfect fluid. That is, the energy–momentum tensor is parametrized merely in terms of energy density ρ and pressure p,

$$T_{\mu\nu} = \mathrm{diag}\,(\rho, -p, -p, -p)\,, \quad \text{with} \quad p = w\rho\,, \tag{2.14}$$

where the proportionality constant w determines the equation of state of the respective component.

To obtain the *Friedmann equations* that govern the expansion dynamics of the Universe, we insert eqs. (2.12) and (2.14) into the Einstein equations. This yields

$$H \equiv \frac{\dot{a}}{a} = \sqrt{\frac{\rho}{3M_{\mathrm{Pl}}^2}}\,, \tag{2.15}$$

$$\frac{\ddot{a}}{a} = -\frac{1}{6M_{\mathrm{Pl}}^2}(\rho + 3p)\,. \tag{2.16}$$

The first expression defines the Hubble parameter H, i.e., the expansion rate of the Universe, which is directly linked to the energy density of the Universe. The present value of $H_0 \approx 67\,\mathrm{km/Mpc/s}$ [14] as measured from the CMB is dubbed the Hubble constant.[1] Consequently, the total energy density today reads $\rho_{\mathrm{tot}} = 3H_0^2 M_{\mathrm{Pl}}^2$. The second equation determines the acceleration of the expansion rate. Fluids with $w > -1/3$ decelerate cosmic expansion. For $w < -1/3$, we find an accelerated expansion; such fluids are characterized as dark energy. Combining both Friedmann equations gives

$$\dot{\rho} + 3H(\rho + p) = 0\,, \tag{2.17}$$

which describes how matter responds to the expansion of space. Employing the relation between energy density and pressure (2.14), the solution of eq. (2.17) is

$$\rho \propto a^{-3(1+w)}\,. \tag{2.18}$$

1 Note that there is a discrepancy in the value of the Hubble constant determined using astrophysical standard candles, yielding $H_0 \approx 73\,\mathrm{km/Mpc/s}$ [91, 92]. This is known as the *Hubble tension*; see ref. [93] for possible solutions.

This expression determines how the energy density of a fluid dilutes with the cosmological expansion, hence provides crucial insights into the cosmic evolution.

We may now apply eq. (2.18) to three special cases that we will consider below:

$$\text{Matter :} \qquad w = 0 \quad \rightarrow \quad \rho_{\mathrm{m}} \propto a^{-3}\,, \tag{2.19}$$

$$\text{Radiation :} \qquad w = \frac{1}{3} \quad \rightarrow \quad \rho_{\mathrm{rad}} \propto a^{-4}\,, \tag{2.20}$$

$$\text{Cosmological constant :} \qquad w = -1 \quad \rightarrow \quad \rho_{\Lambda} \propto a^{0}\,. \tag{2.21}$$

Non-relativistic matter acts as pressureless dust, hence $w = 0$. The equation of state parameter for radiation, i.e., relativistic particles, comes from the fact that the trace of the stress–energy tensor has to vanish for massless fields. Fluids with constant energy density act as a cosmological constant Λ, hence $w = -1$. From eq. (2.15), we see that a Universe dominated by the cosmological constant expands exponentially fast, $a \propto \exp(Ht)$, where H is constant.

ΛCDM MODEL. The ΛCDM model is the current standard paradigm for the evolution of the Universe on large scales. It assumes a flat Universe dominated by dark energy, which is modeled as a cosmological constant ($w = -1$).[2] Furthermore, most of the matter content is attributed to DM, the nature of which is a long-standing puzzle (see sec. 2.3).[3] Ordinary baryonic matter and radiation (i.e., photons) make up a subdominant fraction of the total energy content. Introducing the relative energy density

$$\Omega_i = \frac{\rho_i}{\rho_{\mathrm{tot}}}\,, \quad \text{with} \quad \sum_i \Omega_i = 1\,, \tag{2.22}$$

the contributions of the respective fluids today read [14, 101]

$$\Omega_{\Lambda,0} \approx 0.69\,, \qquad \Omega_{\mathrm{m},0} \approx 0.31\,, \qquad \Omega_{\mathrm{rad},0} \approx 9 \times 10^{-5}\,. \tag{2.23}$$

The matter contribution is further divided into baryons and DM,

$$\Omega_{\mathrm{b},0} \approx 0.05\,, \qquad \Omega_{\mathrm{DM}} \approx 0.26\,. \tag{2.24}$$

By extrapolating today's energy content to the future using the Friedmann equations, we can predict its ultimate fate. The most likely outcome is a "big chill" scenario, in

2 While a cosmological constant remains the favored explanation for the accelerated expansion of the Universe, recent measurements of baryon acoustic oscillations [94–97] are consistent with a time-varying dark energy component. Extensive reviews of dark energy models are found in, e.g., refs. [98, 99].

3 Note that in the original model, DM is assumed to be cold and collisionless. However, this paradigm is currently challenged by astrophysical observations on small scales, with one possible solution being DM self-interactions [100].

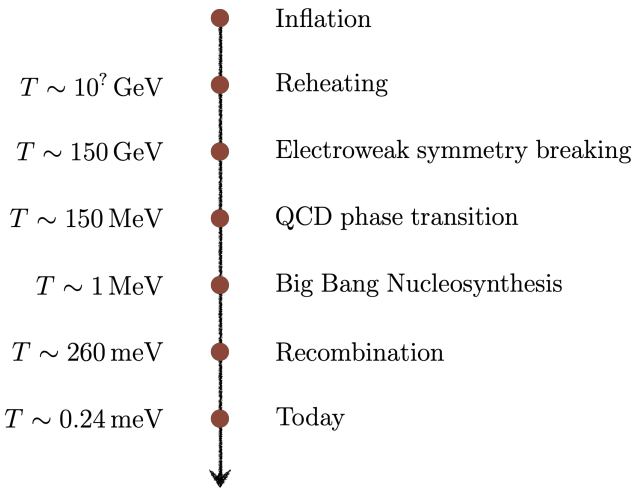

Figure 2.1: Overview of important events in the cosmic history.

which the cosmological constant continues to drive the accelerated expansion, galaxies keep receding from each other, and stars gradually burn out—resulting in a cold and dark Universe. Conversely, extrapolating the expansion history to the past provides a value for the current age of the Universe, $t_0 \approx 13.8\,\mathrm{Gyr}$. This also reveals that the Universe was significantly hotter and denser at very early times, dominated by a plasma of highly relativistic particles. As this thermal bath cooled, a series of critical events occurred, which we outline in the following.

THERMAL HISTORY. The thermal history of the early Universe as predicted by the ΛCDM model is sketched in fig. 2.1. The first conjectured event in the history of the Universe is *cosmic inflation* [102, 103]. During this epoch, the Universe was subject to an accelerated expansion driven by the vacuum energy of some new, typically very heavy, inflaton field. If such a field rolls sufficiently slowly along a flat direction in its potential, it effectively behaves as dark energy. The theory of inflation was developed to resolve the horizon, flatness, and magnetic monopole problems [104, 105], which otherwise require an extreme level of fine-tuning in the early Universe. To this end, inflation should have lasted for at least $N \approx 60$ e-folds, which corresponds to a growth of the scale factor by a factor of $e^{60} \sim 10^{26}$. Note that while the true nature of the inflaton field remains unknown, inflationary dynamics are constrained by CMB observations, restricting the maximum Hubble parameter during inflation to $H_{\mathrm{inf}} \lesssim 6 \times 10^{13}\,\mathrm{GeV}$ [101].

To enable the formation of light elements [15, 106], the Universe must have transitioned to radiation domination (RD) at some point in its evolution. This requires the end of cosmic inflation, which is achieved through a process known as *reheating* [107, 108], during which the inflaton field decays into SM particles that subsequently thermalize. The temperature at the end of reheating is unknown, however, constrained by $T_{\rm rh} \lesssim 10^{16}\,\text{GeV}$ [101]. From this moment on, the primordial Universe was dominated by a thermal bath of highly relativistic particles. The associated energy density is related to the temperature via [109]

$$\rho_{\rm rad}(T) = \frac{\pi^2}{30} g_{\star,\epsilon} T^4 \,, \tag{2.25}$$

where $g_\star$ denotes the effective relativistic degrees of freedom [110]. Hence, the Hubble parameter is (cf. eq. (2.15))

$$H \sim \frac{T^2}{M_{\rm Pl}} \,. \tag{2.26}$$

The entropy density of the primordial plasma is given by [89]

$$s = \frac{2\pi^2}{45} g_{\star,s} T^3 \,, \tag{2.27}$$

where $g_{\star,s}$ are the entropic degrees of freedom. Entropy conservation establishes a connection between the scale factor and temperature of the Universe

$$g_{\star,s}\, a^3 T^3 = \text{const.} \,, \tag{2.28}$$

hence T decreases linearly with the cosmic expansion.

As the temperature approaches $T \sim 150\,\text{GeV}$, EWSB occurs. That is, the Higgs field acquires a vev, generating a mass for the quarks, charged leptons, and weak gauge bosons. EWSB is realized as a crossover in the SM (cf. sec. 2.1). A particle species i with mass m_i becomes non-relativistic and Boltzmann suppressed once the temperature $T \lesssim m_i$, as thermal production ceases to be efficient. This gradually decreases the effective degrees of freedom in eqs. (2.25) and (2.28).

At $T \sim 150\,\text{MeV}$, the QCD quark–hadron transition takes place, where quarks confine into bound states. The breaking of the chiral symmetry proceeds as a crossover transition for physical quark masses; see sec. 2.1. This corresponds to the most significant drop in $g_\star$ during the cosmic evolution.

Around the MeV scale, neutrinos decoupled from the thermal bath. Furthermore, electrons and positrons annihilated, leaving behind a tiny net excess of electrons over positrons.[4] Then, the thermal bath consisted of nucleons, electrons and photons. This also marks the

4 The matter-antimatter asymmetry requires a baryogenesis mechanism [111]; see sec. 2.3.

onset of BBN [15, 106, 112], when the nuclei of light elements were formed. Astrophysical observations of element abundances align with theoretical predictions from BBN and therefore, remarkably, provide bounds on the state of the Universe approximately only minutes after the Big Bang. This represents one of the main successes of the ΛCDM model.

Because of the equation of state-dependent scaling law (cf. eq. (2.18)), the abundance of non-relativistic matter exceeds the one of radiation as the thermal bath approaches the eV scale; this is known as *matter-radiation equality*. Shortly after, during the *recombination* epoch, electrons and protons form neutral hydrogen. As a consequence, the photons decouple and start to free-stream. In other words, the Universe becomes translucent to electromagnetic radiation. The relic photons are observed today as the CMB, providing a snapshot of the Universe approximately 380 kyrs after the Big Bang [101, 113]. This marks the end of the primordial Universe. In this work, we will be concerned with the cosmic evolution prior to the BBN epoch. In particular, we will investigate the potential to probe this era via GWs induced by new physics, motivated by the puzzles outlined below.

2.3 OPEN PROBLEMS

Despite the remarkable success of the SM of particle physics and the ΛCDM model, there are limitations that necessitate new physics. In the following, our aim is to provide a concise summary of selected long-standing puzzles, which lays the foundation for the studies conducted in parts ii, iii, and iv.

NATURE OF DARK MATTER. Approximately 26 % of the energy content of the Universe is composed by DM [14], a yet unknown form of matter which interacts extremely weakly with the visible sector. Evidence for the existence of DM comes from many independent observations, including the velocity dispersion of the Coma cluster [114], galaxy rotation curves [115], colliding galaxy clusters [116–118], and the CMB [14]. Intriguingly, a certain abundance of DM is required in order for structures to form as observed today [119, 120].[5] Therefore, we may conclude that DM must have been produced in the primordial Universe; an extensive review of DM production mechanisms is found in ref. [22].

There exist a plethora of proposed DM candidates on a vast range of energy scales. This includes, e.g., wave-like DM (ultralight bosons, ALPs), particle DM (sterile neutrinos, weakly-interacting massive particles), and macroscopic objects (primordial black holes) [22]. Consequently, there are a multitude of current and future experiments that

5 Note that this rules out SM neutrinos as DM candidates, as they, being relativistic at the time, would have washed out small-scale structures.

search for DM through (in)direct detection [22]. Although these experiments were able to constrain certain DM properties, its true nature remains unknown. While a finite interaction strength between the dark and visible sectors is not guaranteed, DM does interact gravitationally. Therefore, GW observations from astrophysical or primordial origin may hold the key to understanding DM. To this end, we will study in part ii a particular SM extension that contains right-handed neutrinos as a DM candidate and induces GWs in the early Universe. In part iii, we investigate GW probes of ALPs.

BARYOGENESIS. The mere fact that we can observe today's Universe is evidence for an asymmetry between matter and antimatter. Assuming equal initial amounts of particles and antiparticles, their annihilation throughout the evolution of the early Universe should leave nothing but electromagnetic radiation.[6] This can be expressed by the baryon asymmetry of the Universe (BAU) η, inferred from CMB and BBN observations as [14]

$$\eta = \frac{n_{\mathrm{B}} - n_{\bar{\mathrm{B}}}}{s} \approx 8.7 \times 10^{-11} \,, \tag{2.29}$$

where s is the entropy density (2.27) and n_{B} ($n_{\bar{\mathrm{B}}}$) is the baryon (antibaryon) number density. The generation of the BAU, *baryogenesis*, requires three conditions [23]: (i) the violation of baryon number, (ii) charge-parity (CP) violation, and (iii) the departure from thermal equilibrium. The first condition is met by the SM through electroweak sphalerons [121]. Furthermore, a complex phase in the quark mass mixing matrix sources CP violation [122]. However, as discussed in sec. 2.2, both the electroweak and QCD PT are crossovers. Therefore, the SM does not provide sufficiently strong out-of-equilibrium conditions to establish the BAU. One possible mechanism is *electroweak baryogenesis* [123], which necessitates a first-order EWPT. Although we will not study baryogenesis explicitly, we will show how strong out-of-equilibrium conditions can be generated during EWSB in part ii . Furthermore, precise predictions of the BAU require theoretical control over the PT dynamics. This is the focus of part iv, where we investigate the theoretical uncertainties in FOPTs.

STRONG CP PROBLEM. The QCD Lagrangian generally allows for a topological term

$$\mathcal{L}_\theta = \theta \frac{g_s^2}{32\pi^2} G_{\mu\nu} \tilde{G}^{\mu\nu} \,, \tag{2.30}$$

where g_s is the strong gauge coupling and $G_{\mu\nu}$ denotes the gluonic field strength tensor. The dual field strength tensor is $\tilde{G}^{\mu\nu} = G_{\alpha\beta}\epsilon^{\mu\nu\alpha\beta}/2$. Intriguingly, this term is CP violating, with the magnitude of CP violation being controlled by the dimensionless constant θ.

6 Particles and antiparticles annihilate once the temperature drops below their mass.

This induces a neutron electric dipole moment, which is constrained by experiment such that $\theta \lesssim 10^{-10}$ [124]. In principle, θ also receives corrections from CP violation in the quark mass matrix. This cancellation between two independent contributions leading to the absence of CP violation in the strong interactions represents a fine-tuning problem, known as the *strong CP problem*.

The currently favored resolution amounts to the introduction of a global $\mathrm{U}(1)_{\mathrm{PQ}}$ symmetry [49, 50] that is spontaneously broken at the energy scale f_ϕ and anomalous under QCD. Then, the pseudoscalar *axion* ϕ emerges as Nambu-Goldstone boson [51, 52], coupling to the gluonic fields via

$$\mathcal{L}_\theta = -\frac{\phi}{f_\phi}\frac{g_s^2}{32\pi^2}G_{\mu\nu}\tilde{G}^{\mu\nu}\,. \tag{2.31}$$

During confinement, $G_{\mu\nu}\tilde{G}^{\mu\nu}$ receives a vev, which generates a potential for the axion. Since the minima of this potential are CP conserving [125], the axion can dynamically solve the strong CP problem as it is driven to the minimum during the cosmic evolution.

The axion potential reflects the periodic nature of the QCD vacuum, with the potential energy at the maxima given by $m_\phi^2 f_\phi^2 \sim \Lambda_{\mathrm{QCD}}^4$ [126], where Λ_{QCD} is the confinement scale. Therefore, if the $\mathrm{U}(1)_{\mathrm{PQ}}$ breaking scale is large, the axion is extremely light $m_\phi \sim \Lambda_{\mathrm{QCD}}^2/f_\phi$. Depending on the implementation to the SM, the axion has different coupling strengths to the SM fields [127, 128]. Most importantly, all couplings are suppressed by the axion decay constant f_ϕ^{-1}, hence the axion is invisible for large f_ϕ. This renders the pseudoscalar an excellent DM candidate [129–131], however, extremely difficult to probe experimentally. In part iii, we will be concerned with the dynamics of axion-like particles (ALPs)—a generalization of the QCD axion—in the primordial Universe. We will see that ALPs can, in the absence of large couplings to the SM, produce strong GW signals in the reach of future observatories.

3

STOCHASTIC GRAVITATIONAL WAVE BACKGROUNDS

The unresolved issues in the SM strongly suggest the presence of new physics. This naturally raises the question of how BSM physics can be probed by present and future experiments. While particle colliders are approaching the upper limit regarding feasible center-of-mass energies, the first direct detection of GWs from merging black holes [10, 132–134] has opened a window for new physics searches. Predicted by Einstein's theory of GR [11, 12], GWs are ripples in the fabric of spacetime, propagating at the speed of light and interacting only gravitationally with matter in the Universe. GWs can be divided into two classes, depending on whether their origin is astrophysical or cosmological. The latter may have been produced in the earliest moments after the Big Bang through particle physics processes that induced large anisotropies [18]. Subsequently, they propagated (almost) undisturbed until today, emerging as background noise rather than a transient signal from a single event. The detection of such a SGWB would not only provide insights into the state of the Universe right at the beginning of time, but also hold key information on BSM physics. While inflationary scenarios provide a source of GWs [103], let us note that we will focus on GWs generated in the radiation-dominated era of the cosmic evolution.

In the following, we first discuss general features of stochastic GWs, provide some intuition about the characteristic amplitudes, and demonstrate how the present frequency is directly linked to the temperature in the early Universe when the GWs were generated. Then, we discuss in more detail the dynamics of FOPTs, which are a prime example of the close relation between particle physics and the generation of primordial GWs.

3.1 GENERAL FEATURES

In contrast to GW signals from astrophysical binary systems, a SGWB does not allow for the discrimination of individual sources. Instead, it consists of many different waves at various frequencies, measured as background noise in a detector; a gravitational analogue to the CMB. A SGWB is described as a statistical ensemble, which is assumed to

be *homogeneous*, *isotropic*, *unpolarized*, and *Gaussian* [18, 135]. Here, homogeneity and isotropy directly follow from the properties of a FLRW Universe (cf. sec. 2.2). The assumption that GW backgrounds are unpolarized, however, only holds in the absence of a parity-violating source.[1] Then, both GW helicities are produced in the same way, leaving a zero net polarization. Gaussianity is expected since a SGWB originates from a multitude of uncorrelated regions in the early Universe. By the central limit theorem the result is a Gaussian distribution, formed as a superposition of all independent sources [135].

GENERATION. The generation of GWs is described in linearized GR. That is, a small perturbation $h_{\mu\nu}$ is introduced around a slowly varying background,

$$g_{\mu\nu}(x) = \bar{g}_{\mu\nu}(x) + h_{\mu\nu}(x)\,, \tag{3.1}$$

where $\bar{g}_{\mu\nu}$, in our case, corresponds to the FLRW metric. Then, one expands the Einstein equations (2.11) with a source term to linear order in h_{ij}, which, employing transverse-traceless (TT) gauge, yields [18]

$$\ddot{h}_{ij}(\boldsymbol{x},t) + 3H\dot{h}_{ij}(\boldsymbol{x},t) - \frac{1}{a^2}\boldsymbol{\nabla}^2 h_{ij}(\boldsymbol{x},t) = \frac{2}{M_{\rm Pl}^2}\Pi_{ij}^{\rm TT}(\boldsymbol{x},t)\,. \tag{3.2}$$

Here, the second term describes friction due to the expansion of space. The TT components of the energy momentum tensor of the GW source $\Pi_{ij}^{\rm TT}(\boldsymbol{x},t)$ correspond to the spatial, anisotropic part. The perturbation h_{ij} is a massless excitation and therefore has two polarization states, which are usually referred to as $\times$ and $+$. To obtain the GW spectrum for a certain scenario, one solves eq. (3.2)—analytically or numerically—for a given energy momentum tensor.

In most parts of this work, we will be interested in the spectral energy density of a given GW signal. This is defined via the metric perturbation as follows [18],

$$\Omega_{\rm GW}(f) \equiv \frac{1}{\rho_{\rm tot}}\frac{{\rm d}\rho_{\rm GW}(f)}{{\rm d}\log f}\,, \qquad \rho_{\rm GW} = T_{\rm GW}^{00} = \frac{M_{\rm Pl}^2}{4}\langle \dot{h}_{ij}\dot{h}^{ij}\rangle\,, \tag{3.3}$$

where $\rho_{\rm tot} = 3H^2M_{\rm Pl}^2$ is the total energy density of the Universe, $T_{\rm GW}^{\mu\nu}$ is the GW energy momentum tensor in TT gauge, and dots denote derivatives with respect to cosmic, or physical, time t. The brackets $\langle \dots \rangle$ denote averaging over a characteristic length scale ℓ, such that $\lambda \ll \ell \ll L_0$, where λ is the GW wavelength and L_0 is today's Hubble horizon.

A RULE OF THUMB. Instead of solving the linearized Einstein equations and extracting $\Omega_{\rm GW}$ for a specific example, we would like to give the reader an intuition about the properties required for a source to generate a sizable GW background.

1 In part iii, we will consider GWs from axions, representing a CP-violating source.

GWs from the early Universe are produced in a FLRW Universe, hence a curved spacetime. This introduces the notion of horizons; the expansion rate of the Universe determines the maximum length scale over which physical events can be in causal contact at a given time, $R_{\max} = H^{-1}$. Therefore, the characteristic wavelength λ of a primordial GW should be within the horizon $\lambda < H^{-1}$. Conversely, the characteristic timescale is required to be less than a Hubble time, $H < t^{-1} < \beta$. Connecting the inverse timescale β of the process to the characteristic physical momentum scale $k_{\rm GW}/a \sim \beta$, we have

$$\frac{k_{\rm GW}}{a} > H \propto \frac{T^2}{M_{\rm Pl}} \,. \tag{3.4}$$

Hence, for a causal, sub-horizon source the possible peak frequency is bounded from below by the Hubble parameter. The proportionality to the temperature T of the thermal bath holds in a radiation-dominated Universe (cf. eq. (2.25)).

Regarding an estimate for the GW amplitude, let us approximate eq. (3.2) for timescales smaller than a Hubble time, $\beta > H$, as [136]

$$\beta^2 h_{ij} \sim \frac{2}{M_{\rm Pl}^2} \Pi_{ij} \,. \tag{3.5}$$

This suggests that the time variation of the metric perturbation scales as

$$\dot{h}_{ij} \sim \frac{2}{M_{\rm Pl}^2} \Pi_{ij} \frac{1}{\beta} \,, \tag{3.6}$$

such that via eq. (3.3)

$$\rho_{\rm GW} \sim \frac{1}{M_{\rm Pl}^2} \left(\frac{\Pi_{ij}}{\beta} \right)^2 \,. \tag{3.7}$$

This yields [136–138]

$$\Omega_{\rm GW} \sim \left(\frac{\rho_{\rm source}}{\rho_{\rm tot}} \right)^2 \left(\frac{aH}{k_{\rm GW}} \right)^2 \,. \tag{3.8}$$

Here, we have identified the energy momentum tensor as the energy budget available for GW emission, $\Pi_{ij} \sim \rho_{\rm source}$. We observe that a source, which carries a larger fraction of the total energy density of the Universe, induces stronger GW signals. Furthermore, the GW abundance is enhanced if the timescale is not much shorter than a Hubble time $\beta \gtrsim H$. Then, the characteristic scale is close to the Hubble horizon $\lambda \lesssim R_{\max}$, sourcing larger spatial perturbations.

From this we learn that merely very violent events inducing substantial anisotropic stress on large scales generate sizable GWs. Potential sources include FOPTs, where the Universe transitions to a new vacuum state through the nucleation of macroscopic bubbles. This will be discussed in more detail in sec. 3.2, chapter 6, and part iv. As a second example,

resonant production of particles with wavelengths close to the Hubble horizon acts as a source of GWs. Those scenarios are typically relevant in the context of reheating after cosmic inflation [139–141]. In chapter 7 and part iii, we will explore how such dynamics may emerge in the radiation-dominated epoch of the Universe.

Apart from the specific examples discussed in this work, there exist a plethora of mechanisms that may source GWs in the early Universe, including cosmic defects [142, 143], scalar-induced curvature perturbations [144, 145], or production of tensor perturbations during inflation [102, 103], to name just a few. The crucial point is that none of these sources are predicted by the SM. Therefore, a detection would be a smoking-gun signature of new physics,[2] highlighting the promising prospects for fundamental discoveries via GWs.

REDSHIFTING TO TODAY. GWs produced in the early Universe free-stream from their production until today, hence are affected by the cosmic expansion history. To assess the present detection prospects, we have to redshift the GW frequency and amplitude today via

$$f_0 = \frac{k_\star}{a_0} = \frac{k_\star}{a_\star}\frac{T_0}{T_\star}\left(\frac{g_{s,0}}{g_{s,\star}}\right)^{\frac{1}{3}}, \tag{3.9}$$

$$h^2\Omega_{\mathrm{GW},0} = \Omega_{\mathrm{GW},\star}\left(\frac{g_{s,0}}{g_{s,\star}}\right)^{\frac{4}{3}}\left(\frac{T_0}{T_\star}\right)^4\left(\frac{H_\star}{H_{100}}\right)^2. \tag{3.10}$$

This expression holds for the standard cosmological evolution without, for instance, additional matter-dominated epochs in the early Universe. In addition, we have used that GWs propagate at the speed of light, hence redshift like radiation $\propto a^{-4}$. The subscripts 0 and $\star$ denote today and the time of production, g_s are the entropic degrees of freedom, and $T_0 = 2.73\,\mathrm{K}$ is the temperature associated with the CMB today [14, 146]. Furthermore, we have introduced $H_{100} = 100\,\mathrm{km/Mpc/s}$, such that $h \approx 0.67$ [14] is the dimensionless Hubble parameter today. By combining eqs. (3.4) and (3.9), we reveal the direct connection between today's frequency and the temperature of the primordial plasma,

$$f_0 \propto \frac{\beta}{H_\star}\frac{H_\star}{T_\star} \sim \frac{\beta}{H_\star}\frac{T_\star}{M_{\mathrm{Pl}}}, \tag{3.11}$$

2 Note that there is a SM-induced SGWB from gravitons decoupling from the thermal bath [16, 17]. This signal is predicted to lie at ultra-high frequencies, which remain challenging to probe experimentally.

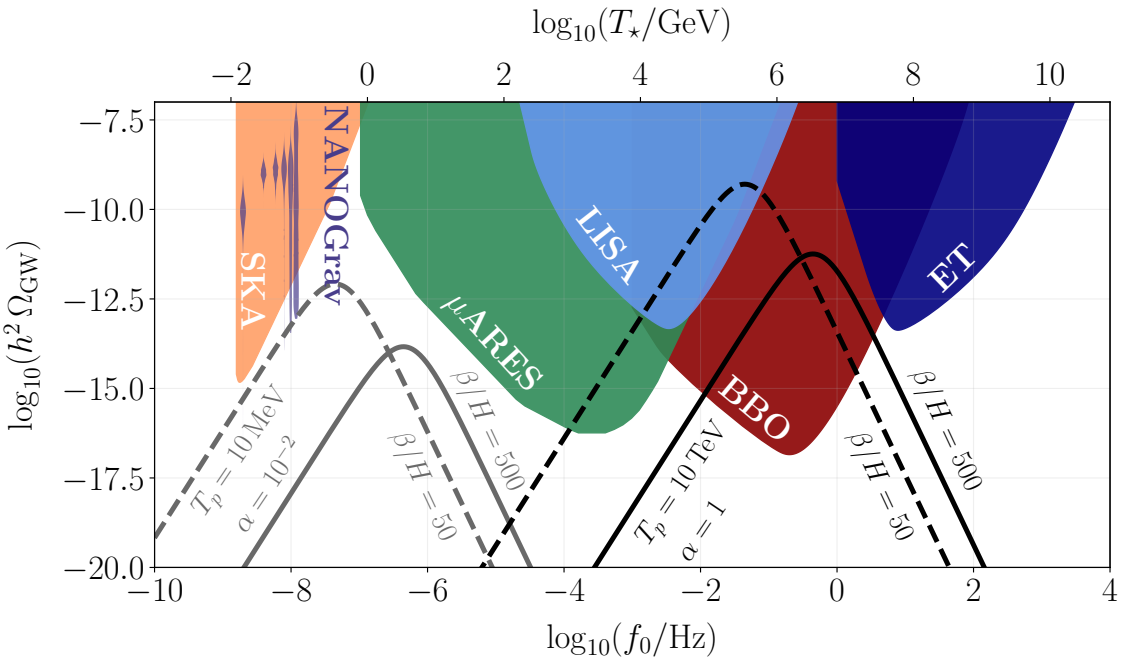

Figure 3.1: Projected GW landspace as a function of today's frequency f_0, which is related to the temperature of the thermal bath in the early Universe $T_\star$. In the mid- to long-term future, a multitude of GW experiments will probe gravitational radiation from the nHz to the kHz regime. The black and grey curves indicate some benchmark GW spectra (3.59) from FOPTs for varying transition strength α and percolation temperature T_p. Here, we employ characteristic values for the inverse timescale $\beta/H_\star = 50$ (dashed) and $\beta/H_\star = 500$ (see sec. 3.2). The purple violins correspond to the recent evidence for a nHz SGWB from the NANOGrav collaboration [29].

where typically $\beta/H_\star \sim \mathcal{O}(10 - 10^3)$. Therefore, detecting GWs in different frequency bands provides information about different epochs of the cosmic evolution. The redshift factors can further be rewritten as [147]

$$f_0 = 1.65 \times 10^{-7}\mathrm{Hz}\frac{k_\star}{aH_\star}\frac{T_\star}{\mathrm{GeV}}\left(\frac{g_\star}{100}\right)^{\frac{1}{6}}\,, \tag{3.12}$$

$$h^2\Omega_{\mathrm{GW},0} = 1.67 \times 10^{-5}\left(\frac{100}{g_\star}\right)^{\frac{1}{3}}\Omega_{\mathrm{GW},\star}\,, \tag{3.13}$$

where we have assumed $g_\star = g_{\star,s} = g_{\star,\epsilon}$.

FUTURE OBSERVATORIES. Future GW experiments can be divided in three classes: Earth-based interferometers such as ET [38–40], space-based observatories such as LISA [35–37] and the futuristic proposals Big Bang Observer (BBO) [148] and μARES [149], and

PTAs such as NANOGrav [29] and the Square Kilometre Array (SKA) [150].[3] In fig. 3.1 we display their projected power-law integrated (PLI) sensitivity curves; computational details on how to obtain the curves are found in, e.g., refs. [152, 153]. Depending on their size, each detector will be sensitive to a unique frequency range, collectively covering the nHz to kHz regime. As a consequence, observations of primordial GWs may provide information on BSM physics from the QCD scale at $T \sim 100\,\text{MeV}$, up to $T \sim 10^9\,\text{GeV}$.

As discussed earlier, several PTA collaborations have reported strong evidence for a SGWB in the nHz band [24–33]. We show the NANOGrav 15-year dataset by the purple violins [29]. While astrophysical supermassive black hole binaries remain the most plausible source, a signal of cosmological origin cannot be excluded to date [34].

In the course of this work, we will develop and study different mechanisms that generate GWs in various frequency windows. To provide a better understanding of the tight connection between QFT and GW emission, let us now turn our attention to a more in-depth discussion of a distinct source: cosmological FOPTs.

3.2 FIRST-ORDER PHASE TRANSITIONS

During a cosmological FOPT, a QFT transitions from a false to a true vacuum state as the Universe cools, spontaneously breaking an underlying symmetry and thereby encountering a discontinuity in the first derivative of its free energy. In other words, a symmetry-breaking field, such as the Higgs field in certain BSM theories, has to tunnel through a thermal barrier, which is accompanied by the nucleation and percolation of true vacuum bubbles. As these bubbles interact with each other and the thermal bath, large anisotropies, hence GWs, are generated. Therefore, FOPTs are a specific example how particle physics theories are intimately tied to the emission of stochastic GWs in the early Universe.

In the following, we aim to provide a short review of the formalism describing the dynamics of a FOPT. We first discuss some technical details on the computation of the thermal effective potential. Then, we switch focus from the microscopic to macroscopic scales, examining the emergence of bubbles and the associated GW spectra.

MATSUBARA FORMALISM. To begin our discussion of FOPTs, let us first introduce some aspects of the *Matsubara formalism* [154], also dubbed *imaginary time formalism*; a tool to describe the equilibrium thermodynamics of a QFT. A more comprehensive introduction to the imaginary time formalism is found in refs. [109, 155].

3 Let us also note the ongoing efforts to develop technologies for measuring GWs in the high-frequency band [151].

The central object in thermodynamics is the partition function,

$$Z(T) \equiv \mathrm{Tr}\left(e^{-\beta\mathcal{H}}\right) , \tag{3.14}$$

where $\beta = 1/T$ with T being the temperature; $\mathcal{H}$ is the Hamiltonian of the system. All thermodynamic observables, such as the free energy F or entropy S, can be derived from $Z(T)$. The expectation value of an operator A is defined as a thermally averaged sum,

$$\langle A\rangle_{\mathrm{T}} = \frac{1}{Z}\sum_n \langle n|A|n\rangle e^{-\beta\mathcal{H}} = \frac{1}{Z}\mathrm{Tr}\left(e^{-\beta\mathcal{H}}A\right) , \tag{3.15}$$

where $|n\rangle$ describe a complete set of orthonormal eigenstates of the Hamiltonian.

We can use eq. (3.15) to derive properties of the two-point correlation function of a quantum field $\phi(\boldsymbol{x},t)$ at finite temperature. Specifically, employing quantum mechanical time evolution, $\phi(\boldsymbol{x},t) = e^{i\mathcal{H}t}\phi(\boldsymbol{x},0)e^{-i\mathcal{H}t}$ and the cyclic permutation property of the trace, we have

$$\langle\phi(\boldsymbol{x},t)\phi(\boldsymbol{y},0)\rangle = \langle\phi(\boldsymbol{y},-i\beta)\phi(\boldsymbol{x},t)\rangle\,. \tag{3.16}$$

By performing a Wick rotation, i.e., introducing imaginary time $t \to \tau = it$, we obtain the Kubo-Martin-Schwinger relation [156, 157]

$$\phi(\boldsymbol{x},0) = \pm\phi(\boldsymbol{x},\beta)\,, \tag{3.17}$$

revealing the $\beta = 1/T$ periodicity of quantum fields in the imaginary time direction. The sign in eq. (3.17) depends on whether the field (anti-)commutes with itself, i.e., if the field is fermionic or bosonic. In the Matsubara formalism, the time direction is therefore compactified and directly connected to the temperature of the system. The resulting theory is static, that is, describes the equilibrium properties of the thermal bath.[4] As a consequence of the periodic nature of the imaginary time direction, the associated momenta can only take discrete values. Then, all momentum integrals are replaced with sum integrals over Euclidean momenta $k^0 = ik^0_{\mathrm{E}}$, i.e., $k^\mu_{\mathrm{E}} = (\omega_n, \boldsymbol{k}_{\mathrm{E}})$ [109, 159],

$$\int\frac{\mathrm{d}^4k_{\mathrm{E}}}{(2\pi)^4}f(k_{\mathrm{E}}) \to T\sum_{n=-\infty}^{\infty}\int\frac{\mathrm{d}^3k}{(2\pi)^4}f(\omega_n,\boldsymbol{k})\,. \tag{3.18}$$

Consequently, quantum fields are represented by

$$\phi(\boldsymbol{x}) = T\sum_{n=-\infty}^{\infty}\int\frac{\mathrm{d}^3k}{(2\pi)^3}\phi(\omega_n,\boldsymbol{k})e^{i(\omega_n\tau-\boldsymbol{k}\cdot\boldsymbol{x})}\,, \tag{3.19}$$

4 Out-of-equilibrium dynamics are typically studied in the real-time formalism, also dubbed *Schwinger-Keldysh* formalism [158].

where

$$\omega_n = \begin{cases} \pi T\, 2n & \text{for bosons}\,, \\ \pi T\, 2(n+1) & \text{for fermions}\,, \end{cases} \qquad n \in \mathbb{Z}\,, \tag{3.20}$$

are the Matsubara frequencies. In the following, we dub all non-zero Matsubara modes *hard modes*. Let us note that fermions do not exhibit a Matsubara zero mode, due to their anti-periodic boundary conditions (see eq. (3.17)), i.e., always exhibit a finite momentum in the (imaginary) time direction. This will shortly become important as the bosonic zero mode, which typically is the degree of freedom driving a PT, is sensitive to the IR dynamics.

THERMAL EFFECTIVE POTENTIAL. The Matsubara formalism provides a tool to compute the *thermal effective potential* $V_{\text{eff}}(\phi, T)$ of a QFT. To this end, consider a system consisting of a complex scalar field $\Phi = (\phi + iG)/\sqrt{2}$, charged under some gauge symmetry that contains a gauge boson A^μ and a fermion χ. The gauge coupling is denoted by g. We assume a Higgs-like tree-level potential

$$V_{\text{tree}}(\Phi) = -\mu^2\Phi^2 + \lambda\Phi^4\,, \tag{3.21}$$

where $\mu^2 > 0$ is the mass parameter and λ denotes the self-coupling, which we assume to be $\lambda \sim g^2$. We split the real component into a constant part $\bar{\phi}$ and a dynamical part φ, such that

$$\phi = \bar{\phi} + \varphi\,. \tag{3.22}$$

By minimizing the tree-level potential along the real axis, we find two non-trivial minima

$$v_\phi = \pm\sqrt{\frac{\mu^2}{\lambda}}\,, \tag{3.23}$$

which is called the vev, or true minimum. This is an analogue of the Higgs mechanism in the SM, where a negative tree-level mass term breaks the electroweak symmetry. The corresponding field-dependent mass of the physical scalar field is obtained by taking the second derivative with respect to the background field $\bar{\phi}$. The scalar tree-level mass in our example then reads

$$m_\phi^2(\bar{\phi}) = \frac{\partial^2 V_{\text{tree}}(\bar{\phi})}{\partial\bar{\phi}^2} = -\mu^2 + 3\lambda\bar{\phi}^2\,. \tag{3.24}$$

The goal of this section is to study this theory at finite temperature. We will see that at high temperature, gauge symmetries are generally restored. That is, at high temperatures the potential possesses only a minimum at the origin. This implies that at some point

in the cosmic evolution, the theory must have transitioned from the vacuum state at the origin to v_ϕ. To determine the relevant temperature scales and the symmetry breaking pattern, we construct the effective potential $V_{\text{eff}}(\bar{\phi}, T)$, which incorporates (thermal) loop corrections to eq. (3.21).

Let us first note that the effective potential of the scalar field is nothing but the free energy of the system [109]

$$F(T) = V_{\text{eff}}(\bar{\phi}, T)\,. \tag{3.25}$$

That is, we can investigate the phase structure of the theory by analyzing the evolution of the ground states of the effective potential. A FOPT is defined by a discontinutity in the first derivative of the free energy,

$$\frac{\mathrm{d}F(T)}{\mathrm{d}T} = \frac{\partial V_{\text{eff}}(\bar{\phi}, T)}{\partial T}\bigg|_{\bar{\phi}=\bar{\phi}_{\text{min}}}\,, \tag{3.26}$$

hence corresponds to a jump of the minimum of the effective potential at a critical temperature T_{c}. In other words, a FOPT occurs since the scalar field has to tunnel through a barrier to reach a new ground state (cf. fig. 3.2).

Diagrammatically, the effective potential is computed via [160]

$$V^{\ell}_{\text{eff}}(\bar{\phi}) = -\sum_{n=0}^{\infty} \frac{\phi^n}{n!}\Gamma^{(n)}_{\ell}(p=0)\,. \tag{3.27}$$

Here, $\Gamma^{(n)}_{\ell}(p=0)$ is the n-point effective vertex, where ℓ denotes the loop order, i.e., controls the expansion in $\hbar^{\ell}$. Here, all external momenta are set to zero, since we are interested in the evolution of the classical background field $\bar{\phi}$. Setting $\ell = 0$ simply gives the tree-level potential. The one-loop effective potential is computed by taking $\ell = 1$, i.e., summing all diagrams containing one loop insertion and n external scalar legs with zero

momentum. For our example, this amounts to the following diagrams, where dashed (solid, wiggly) lines denote scalar (fermion, gauge field) contributions:

$V^1_{\text{eff}}(\bar{\phi}) =$

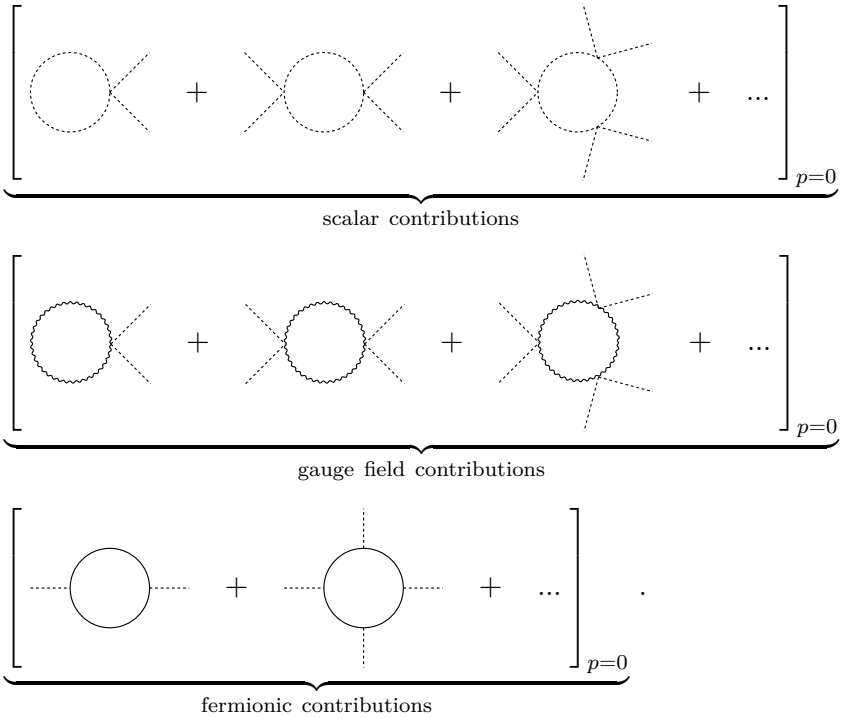

(3.28)

The functional shapes of these infinite series are known. Employing the Euclidean signature, the evaluation of eq. (3.28) yields [159]

$$V^1_{\text{eff}}(\bar{\phi}) = \sum_i \frac{\eta_i n_i}{2} \int \frac{\mathrm{d}^4 k_{\text{E}}}{(2\pi)^4} \ln\left(k_{\text{E}}^2 + m_i^2(\bar{\phi})\right) , \tag{3.29}$$

where the sum runs over all particle species i with degrees of freedom n_i and field-dependent mass $m_i(\bar{\phi})$. Furthermore, $\eta_i = +1(-1)$ for bosons (fermions). Since we work at finite temperature, we employ eq. (3.18) such that

$$\begin{aligned} V^1_{\text{eff}}(\bar{\phi}) &= \sum_i \frac{\eta_i n_i}{2} T \sum_{n=-\infty}^{\infty} \int \frac{\mathrm{d}^3 k}{(2\pi)^3} \ln\left(\omega_n^2 + k^2 + m_i^2(\bar{\phi})\right) \\ &= \sum_i \eta_i n_i \int \frac{\mathrm{d}^3 k}{(2\pi)^3} \left[\frac{k^2 + m_i^2(\bar{\phi})}{2} + T \ln\left(1 - \eta_i \exp\left(-\frac{k^2 + m_i^2(\bar{\phi})}{T}\right)\right)\right] \\ &= V_{\text{cw}}(\bar{\phi}) + V_{\text{T}}(\bar{\phi}, T) \,. \end{aligned} \tag{3.30}$$

In the last step, we have seperated the temperature-dependent and -independent contributions. The vacuum contribution is known as the Coleman–Weinberg term (CW) [161].

Employing dimensional regularization to treat the UV divergences, one obtains the final expression,

$$V_{\rm cw}(\bar{\phi}) = \sum_i \eta_i n_i \frac{m_i^4(\bar{\phi})}{64\pi^2}\left[\ln\left(\frac{m_i^2(\bar{\phi})}{\bar{\mu}^2}\right) - C_i\right], \tag{3.31}$$

where $C_i = \frac{3}{2}\left(\frac{5}{6}\right)$ for scalars and fermions (gauge bosons). Note that through the renormalization procedure, the renormalization group (RG) scale $\bar{\mu}$ enters the effective potential via dimensional transmutation. In principle $\bar{\mu}$ is an arbitrary integration constant that should not affect any physical results. Regarding $V_{\rm eff}$, the dependence on the RG scale cancels order-by-order. This translates to the usual loop expansion at zero temperature. At finite temperature, $V_{\rm eff}$ receives contributions from both one- and two-loop diagrams at $\mathcal{O}(g^4)$. Therefore, the dependence on $\bar{\mu}$ is only cancelled when including two-loop contributions; see, e.g., ref. [162].[5] While the RG scale is often chosen as a mass scale or vev of the theory, we will see that a more consistent choice is a T-dependent RG scale $\bar{\mu} \sim \pi T$ (cf. sec. 5.2 and part iv).

Thermal corrections then read

$$V_{\rm T}(\bar{\phi}, T) = \frac{T^4}{2\pi^2}\sum_i \eta_i n_i J_{\rm b/f}\left(\frac{m_i^2(\bar{\phi})}{T^2}\right), \quad \text{with} \tag{3.32}$$

$$J_{\rm b/f}(x^2) = \int_0^\infty {\rm d}y y^2 \ln\left[1 \mp \exp\left(-\sqrt{y^2+x^2}\right)\right], \tag{3.33}$$

with "b/f" for bosons/fermions. In the high-temperature limit where $z \to 0$, the thermal functions[6] $J_{\rm b/f}$ can be expanded to $\mathcal{O}(x^4)$ as [159]

$$J_{\rm b}(x^2) \approx -\frac{\pi^2}{45} + \frac{\pi^2}{12}x^2 - \frac{\pi}{6}x^3 - \frac{x^4}{32}\ln(x^2), \tag{3.34}$$

$$J_{\rm f}(x^2) \approx \frac{7\pi^4}{360} - \frac{\pi^2}{24}x^2 - \frac{x^4}{32}\ln(x^2). \tag{3.35}$$

We can now inspect the effect of the thermal contributions on the mass of the symmetry-breaking scalar field. To this end, we again take the second derivative of the effective potential around the origin with respect to the background field, which yields

$$m_\phi^2(\bar{\phi})\Big|_{\bar{\phi}\to 0} = \left.\frac{\partial^2 V_{\rm eff}(\bar{\phi})}{\partial \bar{\phi}^2}\right|_{\bar{\phi}\to 0} \sim -\mu^2 + \lambda T^2. \tag{3.36}$$

5 We will return to this issue in part iv, where we study the impact of RG scale dependence on GW predictions.

6 The thermal functions can introduce imaginary parts to the effective potential. While such imaginary parts can be treated in a strict EFT expansion [163, 164], one typically discards such contributions if $\mathrm{Im}\, V_{\rm eff} < \mathrm{Re}\, V_{\rm eff}$ at the minima [165].

Hence, the effective mass receives a positive thermal contribution. We note two important observations from the above expressions.

First, at high temperatures the term $\sim T^2\bar{\phi}^2$ dominates the effective potential. This implies that any non-trivial minimum at $\bar{\phi} \neq 0$ vanishes at sufficiently high temperatures where $T^2 \gg \mu^2$, leaving only a minimum at the origin. Conversely, as the T-dependent quadratic contributions become comparable to the tree-level mass term $\mu^2 \sim \lambda T^2$, the system becomes unstable, indicating the onset of a PT. Second, a cubic term naturally arises in the effective potential when integrating out UV scales, which plays a crucial role in the emergence of a thermal barrier.

DAISY RESUMMATION. To conclude our review of the computation of the effective potential, we turn our attention to a very important issue of perturbation theory at finite temperature: the breakdown of perturbativity in the IR, known as the *Linde problem* [55]. Besides the mass parameter μ^2, the temperature T enters as a second scale, such that the effective expansion parameter in finite-T field theory reads [109]

$$\epsilon \sim \frac{g^2 T}{\pi m_\phi}\,, \tag{3.37}$$

where m_ϕ receives contributions from the vacuum and thermal part of the effective potential. As the system becomes unstable, we have $\mu^2 \sim \lambda T^2$, such that $m_\phi^2 \to 0$ for the Matsubara zero mode and the perturbative expansion ceases to be valid.[7] In part iv we will introduce a systematic approach to extend the regime of perturbativity to higher loop orders: high-temperature dimensional reduction (DR) [166]. This effective field theory (EFT) method consistently integrates out hard Matsubara modes, generating a perturbative theory valid in the IR.

For now, we focus on the more conventional approach: Daisy resummation [167–169], applicable at one-loop order and used in part ii of this work. To this end, let us consider as an example the scalar self-interaction, in particular the contribution of a hard thermal loop with $\omega_n \neq 0$ to the propagator of the zero mode

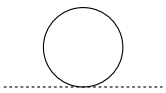

$$= \lambda T \sum_n \int \frac{\mathrm{d}k^3}{(2\pi)^3} \frac{1}{\omega_n^2 + k^2 + m_\phi^2} \overset{T \gg m_\phi}{\approx} \lambda T^2\,. \tag{3.38}$$

Integrating out the heavy scalar Matsubara non-zero modes induces a thermal mass $\Pi_\phi \sim \mathcal{O}(\lambda T^2)$. Likewise, hard loops involving gauge fields and fermions induce contributions to the thermal mass of the scalar zero mode. The same holds for the longitudinal zero

7 Fermions are IR-safe in the absence of a zero Matsubara mode, as $m \sim \pi T$ such that $\epsilon \sim (g/\pi)^2$.

mode of the gauge field, which receives a Debye mass $m_{\mathrm{D}} \sim \mathcal{O}(gT)$ by integrating out hard thermal loops [155]. Repeating this exercise with $N-1$ additional hard loops, we have [109]

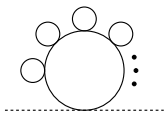

$$= \lambda T \sum_n \int \frac{\mathrm{d}k^3}{(2\pi)^3} \frac{1}{(\omega_n^2 + k^2)^{N-1}} + \left[\lambda T \sum_n \int \frac{\mathrm{d}k^3}{(2\pi)^3} \frac{1}{(\omega_n^2 + k^2)^{N-1}} \right]^{N-1}$$

$$\sim \left(\frac{\lambda T^2}{\mu^2} \right)^{N-\frac{3}{2}} \lambda^{\frac{3}{2}} T^2 \,. \tag{3.39}$$

As argued above, at the time of a PT $\mu^2 \sim \lambda T^2$ and the term in the parentheses in the last row becomes $\mathcal{O}(1)$. Then, all Daisy diagrams contribute at the order $\sim \lambda^{\frac{3}{2}} T^2$, independent of the number of attached loops. Therefore, the loop expansion does not hold, and diagrams involving any number of hard Matsubara loops cannot be ignored. The resummation of the infinite series of Daisy diagrams yields [109]

$\sum_N$ 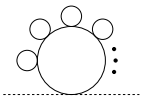

$$= -\sum_i \frac{T}{12\pi} (m_\phi^2(\bar{\phi}) + \Pi_\phi(T))^{\frac{3}{2}} \,, \tag{3.40}$$

hence a finite contribution at $\mathcal{O}(\lambda^{\frac{3}{2}})$ for $m_\phi^2 \to 0$. The corresponding correction to V_{eff} then reads [170]

$$V_{\mathrm{daisy}}(\phi, T) = -\sum_i \frac{T}{12\pi} \left((m_i^2(\bar{\phi}) + \Pi_\phi(T))^{\frac{3}{2}} - (m_i^2(\bar{\phi}))^{\frac{3}{2}} \right) \,, \tag{3.41}$$

where the second term is subtracted to avoid double counting of the cubic mass term. Here, the sum runs over all Matsubara zero modes, that is, scalars and longitudinally polarized gauge bosons. The thermal mass receives contributions from all hard modes coupled to the respective field. The same result can be achieved by taking

$$m_\phi^2 \to m_\phi^2 + \Pi_\phi \,, \tag{3.42}$$

in the one-loop corrections to V_{eff} [168]. With power counting $\lambda \sim g^2$, the replacement (3.42) yields a perturbative expansion parameter in the limit $m_\phi \to 0$, $\epsilon \sim g/\pi$. Hence, Daisy resummation extends the regime of perturbativity, but modifies the structure of the power expansion. To summarize, the full one-loop thermal effective potential of a given particle theory reads

$$V_{\mathrm{eff}}^{1-\mathrm{loop}}(\bar{\phi}, T) = V_{\mathrm{tree}}(\bar{\phi}) + V_{\mathrm{cw}}(\bar{\phi}) + V_{\mathrm{T}}(\bar{\phi}, T) + V_{\mathrm{daisy}}(\bar{\phi}, T) \,, \tag{3.43}$$

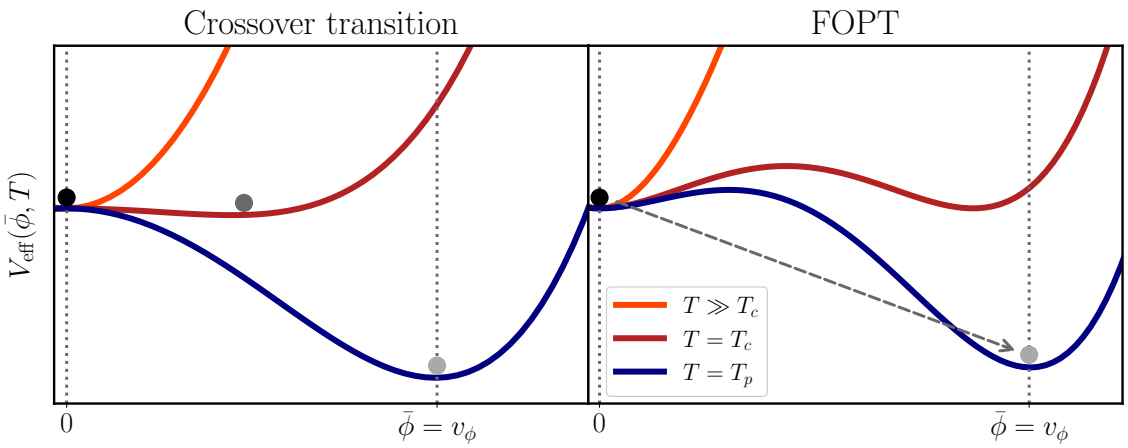

Figure 3.2: Two different symmetry breaking patterns as the Universe cools. The left panel corresponds to a crossover transition, during which the scalar field evolves smoothly with temperature. In the right panel, the true and false minimum are separated by a thermal barrier, which the scalar field has to overcome via thermal tunneling. The result is a FOPT, proceeding via nucleation of true vacuum bubbles.

where the loop contributions are given by eqs. (3.31), (3.32), and (3.41).

In fig. 3.2, we sketch two different symmetry breaking patterns. In both panels, we observe a symmetry restoration at high temperatures (orange). As the Universe cools, the vev starts to form, however, the shape of V_{eff} at this time is fundamentally different between the two cases. In the left panel, there is no thermal barrier that separates the true from the false vacuum; the background field evolves smoothly with temperature. This is equivalent to the SM case, where the EWPT is a crossover for the observed Higgs mass [19]. The right panel sketches the dynamics of a FOPT. Here the cubic term in the effective potential generates a thermal barrier, preventing the field to evolve to the true minimum. This corresponds to a discontinuity in the first derivative of the free energy at the critical temperature T_c, where both vacua become degenerate. A FOPT is predicted by a multitude of BSM theories. This includes scenarios where the electroweak or QCD dynamics is modified by new physics (see, e.g., [46, 171, 172], chapter 6 and part iv), or FOPTs in secluded dark sectors that interact only gravitationally with the SM [152, 173].

BUBBLE DYNAMICS. In a FOPT, the symmetry-breaking scalar field has to overcome a barrier via tunneling, leading to the formation of true vacuum bubbles. The relevant quan-

tity that describes the efficiency of thermal tunneling is the bubble nucleation rate [174–178]

$$\Gamma(T) = A_{\rm dyn} A_{\rm stat} \exp\left(-\frac{S_3(T)}{T}\right) , \tag{3.44}$$

where the prefactor is decomposed into a dynamical and a statistical contribution [179]. In this work we only include equilibrium dynamics [176, 177],[8] such that the prefactor is approximated by

$$A_{\rm stat} \approx T^3 \left(\frac{S_3(T)}{2\pi T}\right)^{\frac{3}{2}} , \qquad A_{\rm dyn} \approx T\,. \tag{3.45}$$

In the above expression $S_3/T \equiv \mathcal{S}_3$, where the leading order (LO) *bounce action* [175, 184]

$$S_3(T) = 4\pi \int {\rm d}r r^2 \left(\frac{1}{2}\left(\frac{{\rm d}\bar{\phi}}{{\rm d}r}\right)^2 + V_{\rm eff}(\bar{\phi}, T)\right) , \tag{3.46}$$

is the $O(3)$-symmetric action of the scalar field ϕ in Euclidean spacetime. This expression is evaluated for the critical bubble profile, i.e., a nucleating bubble with $\bar{\phi} \neq 0$ inside. The equation of motion associated with the action (3.46) is called *bounce equation* and reads

$$\frac{{\rm d}^2\bar{\phi}}{{\rm d}r^2} + \frac{2}{r}\frac{{\rm d}\bar{\phi}}{{\rm d}r} = \frac{{\rm d}V_{\rm eff}(\bar{\phi}, T)}{{\rm d}\bar{\phi}} , \tag{3.47}$$

with boundary conditions

$$\frac{{\rm d}\bar{\phi}(r=0,T)}{{\rm d}r} = 0\,, \qquad \lim_{r\to\infty} \bar{\phi} = 0\,. \tag{3.48}$$

This is typically solved numerically using over-/undershooting methods. To this end, we employ the `Python` package `CosmoTransitions` [185].

Next, let us introduce further relevant temperature scales that characterize FOPTs. The *nucleation temperature* $T_{\rm n}$ is defined at the time when, on average, one bubble has been nucleated per horizon patch. Specifically, we evaluate [176, 177]

$$N(T_n) = 1 = \int_{t_c}^{t_n} {\rm d}t \frac{\Gamma(t)}{H(t)^3} = \int_{T_c}^{T_n} \frac{{\rm d}T}{T}\frac{\Gamma(T)}{H(T)^4} , \tag{3.49}$$

where we have replaced cosmic time t by the temperature T in the last step.

To assess whether a FOPT has completed, one employs the *percolation temperature* $T_{\rm p}$ [186]. This is defined via the probability of a point in space to remain in the false vacuum $P = \exp(-I(T))$, where [187–189]

$$I(T_{\rm p}) = \frac{4\pi}{3}\int_{T_{\rm p}}^{T_{\rm c}} \frac{{\rm d}T'}{T'^4}\frac{\Gamma(T')}{H(T')}\left(\int_T^{T'} {\rm d}\tilde{T}\frac{v_{\rm w}}{H(\tilde{T})}\right)^3 = 0.34\,. \tag{3.50}$$

8 Note that this neglects the fluctuation determinant [180] which enters $A_{\rm stat}$. This can have a sizable impact in certain cases [56, 181–183].

Here, v_w is the bubble wall velocity, which we will briefly discuss below. The percolation temperature T_p hence marks the moment where all quantities relevant for GW emission are evaluated.

In the course of this work, we will be concerned with extremely supercooled FOPTs. In such scenarios, the Universe may undergo a short phase of thermal inflation when bubble percolation becomes efficient; that is, accelerated expansion takes place. Then, it is crucial to check whether the volume of space that is trapped in the false vacuum V_false is actually decreasing [13],

$$\frac{1}{V_\mathrm{false}}\frac{\mathrm{d}V_\mathrm{false}}{\mathrm{d}t} = H(T)\left(3 + T\frac{\mathrm{d}I(T)}{\mathrm{d}T}\right) < 0\,. \tag{3.51}$$

If this were not the case, the PT could never finish.

GRAVITATIONAL WAVE SOURCES. While nucleating bubbles are typically spherical, hence do not induce a quadrupole moment, the collision of bubbles and bubble-plasma interactions source anisotropic stress in the energy momentum tensor, hence GWs. Such GW signals are quantified by a few characteristic quantities, which we introduce in the following.

The *transition strength* α describes the latent heat released in the transition. This corresponds to [190–192]

$$\alpha(T) \equiv \frac{1}{\rho_\mathrm{rad}}\left(\Delta V_\mathrm{eff} - \frac{T}{4}\Delta\frac{\mathrm{d}V_\mathrm{eff}}{\mathrm{d}T}\right)\bigg|_{T=T_\mathrm{p}} \simeq \frac{\Delta V_\mathrm{eff}}{\rho_\mathrm{rad}(T_\mathrm{QCD})}\,, \tag{3.52}$$

where $\Delta V_\mathrm{eff} = V_\mathrm{eff}(0,T) - V_\mathrm{eff}(v_\phi,T)$ is the energetic difference between the true and false vacuum. The energy density in the radiation bath is denoted by ρ_rad (cf. eq. (2.25)). In strongly supercooled PTs, the transition strength is well approximated by the last term in eq. (3.52) [193].

The transition strength is connected to the velocity of the bubble walls v_w. A precision computation of v_w constitutes a highly challenging task [194–209], requiring out-of-equilibrium computations. We will only consider very strong transitions featuring $\alpha \gg 1$, often corresponding to *detonations*. Therefore, we will employ $v_\mathrm{w} = 1$ and relegate more precise analyses [209], taking into account possible small deviations, to the future.

The last quantity that enters the computation of the GW spectrum is the *inverse timescale* $\beta/H_\star$. Parametrizing the rate of the false vacuum decay as [13]

$$\Gamma(t) \sim \exp(-\beta t)\,, \tag{3.53}$$

one finds (cf. eq. (3.44))

$$\frac{\beta}{H_\star} = T\frac{\mathrm{d}\mathcal{S}_3}{\mathrm{d}T}\bigg|_{T=T_\mathrm{p}}\,, \tag{3.54}$$

where $\mathcal{S}_3 = S_3/T$. An alternative definition is obtained via the average bubble radius at collision [13, 210],

$$R_\star \equiv n_B^{-\frac{1}{3}} = \left[T_\mathrm{p}^3 \int_{T_\mathrm{p}}^{T_\mathrm{c}} \frac{\mathrm{d}T'}{T'^4} \frac{\Gamma(T')}{H(T')} e^{-I(T')} \right]^{-\frac{1}{3}} , \tag{3.55}$$

where n_B is the bubble number density. For moderately strong transitions the relation to the inverse timescale reads $R_\star = (8\pi)^{\frac{1}{3}}/\beta$ [210],[9] while a recent simulation [211] has shown that $R_\star \approx 5/\beta$ is more appropriate for strongly supercooled transitions.

The GW spectrum from FOPTs receives contributions from several distinct sources [191]. First, the collision of bubbles breaks their spherical symmetry, which sources anisotropies and, therefore, GWs. Second, during the expansion and collision of bubbles, some fraction of the latent heat is transferred to the thermal bath via bubble-plasma interactions. This leads to the formation of sound waves, which again induces a time-varying quadrupole moment and generates GWs. At some time, excitations of the plasma form turbulences, which act as a third source of GWs. In recent years, significant progress has been made on accurately computing the turbulence contribution [212–214]. Because of its remaining uncertainty, and since it is usually subdominant compared to the first two sources, we will solely consider bubble and sound wave contributions in the following.

The dominant source can be determined by considering the friction between the bubble wall and the plasma. This is discussed in chapter 6, where we use the bubble wall friction to derive an approximate upper bound on the scale of new physics in CSI SM extensions. In part iv, we consider PTs with moderate supercooling, which are usually dominated by sound wave contributions. For now, we therefore skip the discussion on how to determine the dominant source and focus on the GW spectra.

The computation of the GW spectra is highly involved, since strong FOPTs are non-perturbative processes involving a multitude of physical scales. To obtain a precise picture, expensive numerical simulations are required. Hence, the results of such simulations are typically fitted and parametrized in terms of α, β, v_w, and T_p, allowing for a direct connection between thermodynamic computations and the associated GW signal. While there is a large theoretical effort underway to increase our understanding of the different GW sources [192, 215–222], let us, in the following, focus merely on the templates employed in this work and discuss some of their characteristics.

In chapter 6, we will be concerned with FOPTs featuring $\alpha \gg 1$, which are difficult to simulate on a lattice because of the large hierarchy of scales. In a more simplified approach [211], it has been shown, however, that in such a case the GW spectrum from

9 Note that for weak transitions, the relation between β and $R_\star$ depends on the sound speed c_s via $\max\{v_\mathrm{w}, c_s\}$. We assume $v_\mathrm{w} > c_s$ and $v_\mathrm{w} \simeq 1$.

bubble collisions and sound waves are indistinguishable. This is because the fluid shells behave as ultra-relativistic shocks, mimicking the behavior of a bubble wall. Following ref. [211], we therefore employ

$$\Omega^{\rm sc}_{{\rm GW},\star}(f) = \left(\frac{H_\star}{\beta}\right)^2 \left(\frac{\alpha}{1+\alpha}\right)^2 S_{\rm fit}(f)\,, \tag{3.56}$$

with its spectral shape

$$S_{\rm fit}(f) = A(a+b)^c \left(\frac{f}{f_p}\right)^a \left[b + a\left(\frac{f}{f_p}\right)^{\frac{a+b}{c}}\right]^{-c}. \tag{3.57}$$

The fit parameters are $A = 0.0513$, $a = 2.41$, $b = 2.42$, and $c = 4.08$ [211], and the peak frequency reads

$$f_p \approx 0.12\,\beta\,. \tag{3.58}$$

For the sound wave spectrum in part iv, we will employ the results from lattice simulations [192, 215, 216]. We have

$$\Omega^{\rm sw}_{{\rm GW},\star}(f) = 2.47\times 10^{-2}\, R_\star H_\star \left(1 - \frac{1}{\sqrt{1+2\tau_{\rm sw}H_\star}}\right)\left(\frac{\alpha}{1+\alpha}\right)^2 S_{\rm sw}(f)\,, \tag{3.59}$$

with spectral shape

$$S_{\rm sw}(f) = \left(\frac{f}{f_{\rm sw}}\right)^3 \left[\frac{4}{7} + \frac{3}{7}\left(\frac{f}{f_{\rm sw}}\right)^2\right]^{-\frac{7}{2}}, \tag{3.60}$$

and peak frequency

$$f_{\rm sw} = 1.58\, R_\star^{-1}\,. \tag{3.61}$$

Sound waves typically propagate for a longer time, their GW spectrum is enhanced. This is captured in eq. (3.59) by the sound wave period normalized to the Hubble rate [186, 192, 223–225]

$$\tau_{\rm sw}H_\star = \frac{H_\star R_\star}{\bar{U}_f}\,, \qquad\qquad \bar{U}_f \approx \sqrt{\frac{3}{4}\frac{\alpha}{1+\alpha}}\,, \tag{3.62}$$

where $\bar{U}_f$ is the root-mean-square of the fluid velocity. To compare the GW signal to the sensitivity regions of future experiments, they are redshifted to today as outlined in sec. 3.1.

To conclude, let us discuss the main characteristics of the GW spectrum. First, we observe that the GW amplitude is enhanced by the transition strength α. That comes from the fact that a larger latent heat implies a larger energy budget available to be converted into GWs, hence a more violent PT. Second, the amplitude is suppressed by $(H_\star/\beta)^n$,

where $n = 2$ in the case of a strongly supercooled PT, and $n < 2$ in the case of a sound wave-induced signal. The general suppression by the inverse timescale can be understood from the fact that slower transitions allow for the bubbles to grow for a more extended period of time. This generates a larger characteristic bubble size $R_\star$ at percolation, hence larger spatial anisotropies (cf. eq. (3.8)). Since sound waves are active for a longer time than colliding bubbles, their suppression by the inverse timescale is alleviated by τ_{sw}.

To illustrate the impact of different thermodynamic parameters on the resulting GW signal, we show four different benchmark spectra from sound waves in fig. 3.1. Here, we set $(\alpha, T_{\mathrm{p}}) = (10^{-2}, 10\,\mathrm{MeV})$ (gray) and $(\alpha, T_{\mathrm{p}}) = (1, 10\,\mathrm{TeV})$, respectively. Clearly, increasing the percolation temperature shifts the GW peak to a higher frequency (cf. eq. (3.12)). A larger transition strength α enhances the amplitude. Furthermore, we vary the inverse timescale $\beta/H_\star \in \{50, 500\}$. A larger inverse timescale not only decreases the characteristic spatial scale, hence enhances the frequency, but also suppresses the GW amplitude (cf. eqs. (3.8), (3.12), and (3.59)).

With the above machinery, we are now ready to delve into the first main part of this work. In the following, we turn our attention to the interplay between EWSB and the QCD quark-hadron transition in a certain class of BSM theories, and explore various GW signatures potentially detectable at future observatories.

Part II

QCD-INDUCED ELECTROWEAK SYMMETRY BREAKING

4

PRELUDE

In the standard cosmic evolution, EWSB occurs at $T_{\text{ew}} \approx 160\,\text{GeV}$ [82], while the QCD quark–hadron transition takes place at $T_{\text{QCD}} \approx 155\,\text{MeV}$ [88]. For the measured Higgs mass $m_h \approx 125\,\text{GeV}$ and physical quark masses, both transitions are crossovers [19, 20]. In the absence of nucleating bubbles, one therefore does not expect relic GWs from the SM symmetry-breaking mechanisms. In the following, we will study how this picture changes in CSI SM extensions.

CSI models [41, 183, 226–250] exhibit one characteristic feature: the absence of mass terms in the tree-level potential. That is, the Higgs mass term in eq. (2.4) is replaced by a coupling to a new scalar field, $\mu^2 \to \lambda_p \Phi^2$, where λ_p denotes the portal coupling between the electroweak and dark sectors. The scalar field is charged under an additional gauge symmetry which is spontaneously broken, either by radiative corrections [41, 226–234] or non-perturbative dynamics [235–242]. As Φ acquires a vev, the portal term generates the SM vacuum, triggering EWSB. Besides the theoretically appealing explanation for the Higgs mass term [251], CSI models have gained popularity due to their interesting phenomenology, providing solutions to various open problems we have discussed in sec. 2.3. To this end, CSI theories allow for baryogenesis [252–261] and DM production mechanisms [262–275]. Moreover, the combined conformal-electroweak symmetry breaking is usually realized as a strongly supercooled FOPT in the early Universe, leaving behind a relic background of GWs potentially observable with future detectors [46, 183, 193, 243, 244, 246, 247, 276–280].

In this work, we will focus on weakly coupled BSM theories, in particular the CSI $\text{U}(1)_{\text{B-L}}$ model where the global B−L ("baryon−lepton number") symmetry is gauged. For small gauge couplings $g_{B\text{-}L} \lesssim \mathcal{O}(0.1)$ [46, 243, 244], it was shown that B−L PT has not yet occurred as the temperature of the thermal bath approaches the QCD scale. This significant delay of the EWPT induces an intermediate period of supercooling, where the false vacuum energy of the conformal sector sources an accelerated expansion. As the Universe is trapped at the origin of field space, all SM fields remain massless during χSB.

The formation of quark condensates induces a vev for the Higgs field via the Yukawa couplings, triggering EWSB[1] and the exit from supercooling. After reheating to a high temperature, the Universe then follows its standard evolution, satisfying all observational constraints.

In the following, we study different symmetry breaking patterns in the $\mathrm{U}(1)_{\text{B-L}}$ SM extension and analyze the resulting GW signals. First, we introduce the CSI $\mathrm{U}(1)_{\text{B-L}}$ model in chapter 5, including its field content, the thermal effective potential, and the modified cosmic thermal history. In chapter 6, we consider the possibility of a first-order electroweak-QCD phase transition (χPT). While for a long time the chiral phase transition (χPT) in the chiral, i.e., massless limit, was believed to be first-order [45, 288, 289], recent lattice results indicate a second-order transition [290]. In the absence of lattice studies investigating the combined electroweak-QCD transition, we explore the cosmological consequences of a possible FOPT. To this end, we construct different low-energy effective QCD models that predict a FOPT and compute the bubble dynamics in a thermally inflating Universe. The QCD transition then marks the escape from supercooling, i.e., naturally involves a large transition strength $\alpha \gg 1$. The characteristic timescale, however, strongly depends on the interplay between QCD and the scale of the conformal sector. We find that if the new physics energy scale is large compared to the electroweak scale, the GW spectrum from QCD-induced EWSB is significantly enhanced, implying great observational prospects at future observatories.

In chapter 7, we develop a novel GW production mechanism in the context of CSI models that does not rely on the order of the cosmic QCD transition. We show that for small gauge couplings $g_{B\text{-}L} \ll 0.1$, the period of supercooling continues past QCD χSB. We demonstrate that in a large part of the parameter space, bubble percolation becomes inefficient to drive the conformal PT compared to the expansion rate of the Universe. That is, the Universe remains trapped in the false vacuum until the breaking of scale symmetry via QCD cancels the thermal barrier in the potential of the CSI scalar field. The result is a *tachyonic phase transition*, where the scalar field rolls towards the true minimum. As it traverses a region in the effective potential where its squared mass is negative, long-wavelength fluctuations are exponentially produced. This preheats the supercooled Universe, while generating anisotropic stress, and therefore, GWs [6, 53, 140, 291–297]. Inspired by models of tachyonic preheating [47, 48, 139, 140, 291, 298–313], we estimate the GW amplitude. This mechanism opens up the possibility of probing a large region of parameter space at future GW experiments.

1 This goes back to an idea by Witten [281] and was further studied in, e.g., refs. [46, 256, 282–287].

5

CLASSICALLY CONFORMAL $U(1)_{B-L}$ EXTENDED STANDARD MODEL

We first introduce the particle content of the CSI $U(1)_{B-L}$ SM extension. Then, we construct one-loop, finite-temperature effective potential based on the foundations we set in the previous part, and outline how to fix the free model parameters to guarantee a successful generation of the electroweak scale. Lastly, we describe how a classical scale symmetry affects the thermal history of the early Universe.

5.1 FIELD CONTENT

In the CSI $U(1)_{B-L}$ model [41], the global B−L symmetry of the SM is promoted to a gauge symmetry, such that the total underlying gauge group is $SU(3)_c \times SU(2)_L \times U(1)_Y \times U(1)_{B-L}$. SM quarks and leptons then carry a B−L charge of $+1/3$ and -1, respectively. Besides the new Z' gauge boson associated with the $U(1)_{B-L}$ symmetry, we introduce an additional, complex scalar field $\Phi = (\varphi + iG)/\sqrt{2}$ with a B−L charge of $+2$. As a consequence of classical scale invariance, the tree-level scalar potential reads

$$V_{\text{tree}}(\Phi, H) = \lambda_h H^4 + \lambda_\varphi \Phi^4 - \lambda_p \Phi^2 H^2 \,, \tag{5.1}$$

where $H = (G_+, (h + iG_0)/\sqrt{2})$ is the SM Higgs doublet, while λ_h and λ_φ parametrize the strength of the scalar self-interactions. The SM Higgs mass term has been replaced by the portal coupling to the new scalar field, $\mu^2 \to \lambda_p \Phi^2$. We will eventually see that radiative corrections lead to the spontaneous breaking of the $U(1)_{B-L}$ symmetry, resulting in a mass for the vector boson

$$m_{Z'} = 2 g_{B-L} v_\varphi \,, \tag{5.2}$$

where g_{B-L} is the gauge coupling and v_φ denotes the scalar vev. Then, the electroweak scale is recovered by matching $\lambda_p \Phi^2$ to the Higgs mass parameter.

In addition to the scalar Φ and the Z' gauge boson, the model contains three right-handed neutrinos. That is due to gauge anomalies arising at the loop level, i.e., triangle

	$\mathrm{SU(3)_c}$	$\mathrm{SU(2)_L}$	$\mathrm{U(1)_Y}$	$\mathrm{U(1)_{B\text{-}L}}$
q_{L}^i	**3**	**2**	$+\frac{1}{6}$	$+\frac{1}{3}$
u_{R}^i	**3**	**1**	$+\frac{2}{3}$	$+\frac{1}{3}$
d_{R}^i	**3**	**1**	$-\frac{1}{3}$	$+\frac{1}{3}$
l_{L}^i	**1**	**2**	$-\frac{1}{2}$	-1
N_{R}^i	**1**	**1**	0	-1
e_{R}^i	**1**	**1**	-1	-1
H	**1**	**2**	$\frac{1}{2}$	0
Φ	**1**	**1**	0	$+2$

Table 5.1: Particle content of the CSI $\mathrm{U(1)_{B\text{-}L}}$ extended SM. Here, $i \in \{1,2,3\}$ denotes the number of generations, while the subscripts L/R indicate chirality. Apart from the SM fields and the $\mathrm{U(1)_{B\text{-}L}}$ gauge boson, the model contains a complex scalar Φ and three right-handed neutrinos. Table adapted from [41].

diagrams that break the B−L gauge symmetry, hence induce a current $J^\mu_{\mathrm{B\text{-}L}}$ with $\partial_\mu J^\mu_{\mathrm{B\text{-}L}} \propto Q^3_{\mathrm{B\text{-}L}}$. Summing over the B−L charges of all SM matter fields, one finds

$$\sum_{\text{fermions}} Q^3_{B\text{-}L} = 3\,. \tag{5.3}$$

That is, three generations of fermions N_{R}^i ($i \in \{1,2,3\}$) which carry B−L charge of -1 cancel the anomaly. In addition, the right-handed neutrinos account for the generation of neutrino masses via the Seesaw mechanism [42]. The relevant part of the Lagrangian reads

$$L_{\text{seesaw}} = -Y_{\mathrm{D}}^{ij}\bar{N}_{\mathrm{R}}^i H^\dagger l_{\mathrm{L}}^i - \frac{1}{2}Y_{\mathrm{N}}^i \Phi \bar{N}_{\mathrm{R}}^{ic} N_{\mathrm{R}}^i + \text{h.c.}\,. \tag{5.4}$$

Here, Y_D^{ij} and Y_N^i are the respective Yukawa couplings and "h.c." denotes the Hermitian conjugate. After spontaneous $\mathrm{U(1)_{B\text{-}L}}$ and electroweak symmetry breaking, this results in a Dirac neutrino mass term, while the second term generates Majorana mass terms for the right-handed neutrinos. Furthermore, the lightest right-handed neutrino represents a viable DM candidate, if the mixing angle with active neutrinos is sufficiently small [43, 314, 315]. A summary of the particle content is given in table 5.1.

5.2 EFFECTIVE POTENTIAL

Let us now construct the one-loop effective potential, following sec. 3.2. The effective potential will eventually be used to analyze the symmetry breaking pattern of the extended

SM in the early Universe, with a focus on various GW production mechanisms. Let us therefore first note that collider searches for the Z' boson [316, 317] exclude the parameter space of moderate gauge couplings and small Z' masses, such that $m_{Z'} \gtrsim \mathcal{O}(\text{TeV})$. Therefore, we generally have $v_\phi \gg v_h = 246\,\text{GeV}$ (cf. eq. (5.2)). In this case, it was shown that symmetry breaking occurs first along the B−L direction in field space [279]. Subsequently, the scalar evolves smoothly to the global electroweak minimum as in the SM. Hence the relevant step for potential GW generation is the first one, and it suffices to only consider the φ direction of the effective potential.

COLEMAN-WEINBERG CONTRIBUTIONS. We start by incoporating the zero-T, one-loop corrections to the tree-level potential (5.1). In sec. 3.2, we have computed the CW contribution, which in our case reads [161]

$$V_{\text{cw}}(\varphi, T) = \frac{3}{64\pi^2} m_{Z'}(\varphi)^4 \left[\log\left(\frac{m_{Z'}(\varphi)^2}{\mu(\varphi, T)^2} \right) - \frac{5}{6} \right] , \tag{5.5}$$

where $m_{Z'}(\varphi) = 2 g_{B\text{-}L} \varphi$. Note that already here, a temperature dependence arises via the renormalization scale $\mu(\varphi, T)$. We will discuss this choice below after having introduced the remaining contributions to V_{eff}. The logarithmic corrections in eq. (5.5) spontaneously break the $\text{U}(1)_{\text{B-L}}$ symmetry and classical scale invariance, generating a vev for the scalar field which induces the finite Z' mass (5.2) in the true vacuum.

Note that we only include the contribution from the Z' boson, i.e., we neglect the scalar self-interaction and the coupling to the right-handed neutrinos. Let us briefly justify this decision. To this end, we compute the derivative of the one-loop effective potential,

$$\frac{\partial}{\partial \varphi} \left(V_{\text{tree}}(\varphi) + V_{\text{cw}}(\varphi, T) \right) = \lambda_\varphi \varphi^3 + \frac{g_{B\text{-}L}^4}{\pi^2} \varphi^3 \left(3 \log\left(\frac{4 g_{B\text{-}L}^2 \varphi^2}{\mu(\varphi, T)^2} \right) - 1 \right) , \tag{5.6}$$

which we require to vanish around the true minimum $v_\varphi = m_{Z'}/(2 g_{B\text{-}L})$. Employing the Z' boson mass[1] as the relevant symmetry breaking scale, $\mu = m_{Z'}$, we find

$$\lambda_\varphi(\mu = m_{Z'}) = \frac{g_{B\text{-}L}^4}{\pi} . \tag{5.7}$$

This is a typical relation in Coleman Weinberg models. The crucial point is that $\lambda_\varphi \propto g_{B\text{-}L}^4$, hence the scalar contributions to the effective potential are suppressed relative to the vector contributions. In other words, the one-loop gauge boson corrections are formally of the same order $\sim g_{B\text{-}L}^4$ as the scalar tree-level term. This is expected, since the radiative corrections must become comparable to the LO terms to spontaneously break the symmetry.

1 We follow ref. [246] and identify the physical gauge boson mass with its tree-level value.

On the other hand, this tells us that it suffices to consider the Z' contribution at the loop level. To obtain the mass of the scalar field around the true minimum,[2] we evaluate

$$m_\varphi^2 = \frac{\partial^2}{\partial\varphi^2}\left(V_{\text{tree}}(\varphi) + V_{\text{cw}}(\varphi, T)\right)\Big|_{\varphi=v_\varphi} = \frac{6}{\pi^2} g_{B\text{-}L}^4 v_\varphi^2 = \frac{6}{4\pi^2} g_{B\text{-}L}^2 m_{\text{Z}'}^2 \,. \tag{5.8}$$

Hence, we note that the scalar mass is always suppressed with respect to $m_{\text{Z}'}$ for small values of $g_{B\text{-}L}$.

Let us now turn to right-handed neutrino contribution. To this end, we consider the contribution of the heaviest state N_3 with $m_{N_3}(\varphi) = Y_3\varphi/\sqrt{2}$,

$$V_{N_3} = -\frac{2}{64\pi^2} m_{N_3}(\varphi)^4 \left(\log\left(\frac{m_{N_3}^2}{\mu^2}\right) - \frac{3}{2}\right) . \tag{5.9}$$

Again, we compute the first derivative of the effective potential for $\mu = m_{\text{Z}'}(\varphi)$ taking into account V_{N_3}, which yields

$$\lambda_\varphi = \frac{g_{B\text{-}L}^4}{\pi^2} + \frac{Y_3^4}{32\pi^2}\left(\log\left(\frac{Y_3^2}{8g_{B\text{-}L}^2}\right) - 1\right) , \tag{5.10}$$

as the minimization condition. Plugging this expression back into V_{eff} and taking the second derivative with respect to φ, we obtain

$$m_\varphi^2 = \frac{\partial^2 V_{\text{eff}}}{\partial\varphi^2}\Big|_{\varphi=v_\varphi} = \frac{96 g_{B\text{-}L}^4 - Y_3^4}{16\pi^2} v_\varphi^2 \,. \tag{5.11}$$

For the potential to have a non-trivial minimum, we demand

$$g_{B\text{-}L}^4 \geq \frac{Y_3^4}{96} \,. \tag{5.12}$$

This can be translated into a bound on the largest right-handed neutrino mass,

$$m_{N_3} \leq \left(\frac{3}{2}\right)^{\frac{1}{4}} m_{\text{Z}'} \,. \tag{5.13}$$

If m_{N_3} exceeded this limit, the $\text{U}(1)_{\text{B-L}}$ symmetry would not be spontaneously broken, as the fermionic correction to V_{eff} enters with a negative sign, i.e., counteracts the Z' contribution. Then, also EWSB could not be realized and the model would not be consistent. Conversely, we note that the right-handed neutrinos only give a small contribution to the effective potential unless m_{N_3} is very close to $m_{\text{Z}'}$, since their respective contributions scale with the fourth power of the Yukawa coupling. Since the Yukawas are unknown and the parameter space where $m_{N_3} \approx m_{\text{Z}'}$ is extremely fine-tuned, we will henceforth assume that $Y_3 \ll g_{B\text{-}L}$, and neglect the impact of the right-handed neutrinos on the symmetry breaking dynamics.

2 Note that in principle, the scalar mass obtains corrections via mass mixing with the SM Higgs. Those contributions are, however, extremely suppressed due to the large hierarchy of the vevs, hence are neglected.

RECOVERING THE ELECTROWEAK SCALE. Having introduced the one-loop effective potential at zero temperature, let us now briefly describe how to fix the model parameters in order to reproduce EWSB. To this end, we follow the approach from ref. [246]. The model contains five variables [244]: three scalar couplings which enter eq. (5.1), the gauge coupling $g_{B\text{-}L}$, and the parameter $\tilde{g}$, associated to the kinetic mixing between the $\mathrm{U}(1)_Y$ and $\mathrm{U}(1)_{\mathrm{B\text{-}L}}$ gauge fields. Let us first note that $\tilde{g}$ only affects the running of the couplings via the renormalization group equations (RGE). Therefore, it has negligible impact on our results and we set $\tilde{g}(\mu = m_{\mathrm{Z}}) = 0$.[3] Regarding the remaining parameters, we will show that two are fixed by the requirement to generate the electroweak scale. Furthermore, we exchange the portal coupling for the Z' boson mass, such that our only input parameters are $g_{B\text{-}L}$ and $m_{\mathrm{Z}'}$ The procedure is as follows:

1. We choose a value for $g_{B\text{-}L}$ and $m_{\mathrm{Z}'}$ at the B−L symmetry breaking scale given by $\mu = m_{\mathrm{Z}'}$. As shown above, we minimize the effective potential and require that the true minimum sits at $v_\varphi = m_{\mathrm{Z}'}/(2g_{B\text{-}L})$. This yields eq. (5.7) which fixes λ_φ at $\mu = m_{\mathrm{Z}'}$.

2. Next, we employ the β-functions [234] to run $g_{B\text{-}L}$ and λ_φ down to the electroweak scale, $\mu = m_{\mathrm{Z}}$. Note that the portal coupling affects the running of the scalar self-coupling. Since its effect is numerically small, we neglect the λ_p-dependent term in this part of the computation. From the physical Z, $W^\pm$, top quark mass and the Fermi constant G_F [318, 319] we obtain the SM gauge couplings and Higgs vev at $\mu = m_{\mathrm{Z}}$. Further we neglect scalar mass mixing due to the extremely large hierarchy between v_φ and v_h, such that λ_h takes its SM value.

3. We minimize the effective potential again, now employing $\mu = m_{\mathrm{Z}}$, to numerically find a value for the vev at the electroweak scale $v_\varphi(\mu = m_{\mathrm{Z}})$. By minimizing the tree-level potential in the h direction,
$$\frac{\partial V_{\mathrm{tree}}}{\partial h} = \lambda_h h^3 - \frac{\lambda_p}{2} v_\varphi^2 h \,, \tag{5.14}$$
and demanding that $v_h = v_{h,\mathrm{SM}} = 246\,\mathrm{GeV}$, we find a condition for the portal coupling,
$$\lambda_p(\mu = m_{\mathrm{Z}}) = 2\lambda_h \left(\frac{v_{h,\mathrm{SM}}}{v_\varphi}\right)^2 = 2\left(\frac{\mu_{h,\mathrm{SM}}}{v_\varphi}\right)^2 . \tag{5.15}$$
Here, $\mu_{h,\mathrm{SM}}$ is the mass parameter that enters the Higgs potential in the SM. This ensures that EWSB takes place as in the SM. Furthermore, we see that since $v_\varphi \propto m_{\mathrm{Z}'} \gtrsim \mathcal{O}(\mathrm{TeV})$, the portal coupling is generally strongly suppressed for large $m_{\mathrm{Z}'}$.

3 An appropriate value of $\tilde{g}$ can stabilize the Higgs vacuum up to the Planck scale [243].

This completes the construction of the model in the vacuum, and we can move on to study the system at finite temperature.

FINITE-TEMPERATURE CONTRIBUTIONS. We have introduced the thermal corrections to the effective potential in sec. 3.2. Following the reasoning from the previous section, we only include the Z' contribution,

$$V_{\mathrm{T}}(\varphi, T) = \frac{3T^4}{2\pi^2} J_{\mathrm{B}}\left(\frac{m_{\mathrm{Z}'}(\varphi)^2}{T^2}\right) , \tag{5.16}$$

where the bosonic thermal integral is given by eq. (3.33). Further, we implement the Daisy contributions that extends the regime of perturbativity in the IR [168, 170],

$$V_{\mathrm{daisy}}(\varphi, T) = -\frac{T}{12\pi}\left[(m_{\mathrm{Z}'}(\varphi)^2 + \Pi_{\mathrm{Z}'}(T))^{\frac{3}{2}} - m_{\mathrm{Z}'}(\varphi)^{\frac{3}{2}}\right] . \tag{5.17}$$

Note that we have $n_{\mathrm{Z}'} = 1$ in eq. (5.17) as only the longitudinal degree of freedom with thermal mass [243, 244]

$$\Pi_{\mathrm{Z}'}(T) = 4g_{B\text{-}L}^2 T^2 , \tag{5.18}$$

is resummed. The transverse degrees of freedom do not receive a perturbative thermal mass [55]. Also, let us mention that we restrict ourselves to one-loop order. As discussed in sec. 3.2 and further demonstrated in part iv, the two-loop effective potential can be obtained via high-temperature DR [166] if the system exhibits a high-temperature scale hierarchy. Recently, this approach was used to study the CSI $\mathrm{SU}(2)_{\mathrm{X}}$ model at next-to-leading order (NLO) [183, 247]. We are, however, interested in the case where QCD χSB triggers the conformal PT (see below). Then, QCD-induced corrections enter the effective potential, which carry a natural uncertainty from non-perturbative dynamics during cosmic QCD transition. These uncertainties are expected to dominate, i.e., high-precision thermal resummation plays a secondary role, and we leave an NLO analysis of the CSI $\mathrm{U}(1)_{\mathrm{B\text{-}L}}$ model for future work.

Let us briefly investigate the effect of the thermal corrections. To this end, we employ the high-temperature expansion [109, 159] of the thermal bosonic integral (3.34), such that

$$V_{\mathrm{T}}(\varphi, T) = \frac{\pi^2 T^4}{30} + \frac{T^2 m_{\mathrm{Z}'}(\varphi)^2}{8} - \frac{T^4}{4\pi}\left(\frac{m_{\mathrm{Z}'}(\varphi)^2}{T^2}\right)^{\frac{3}{2}} + \dots . \tag{5.19}$$

Taking the second derivative of the effective potential with respect to φ around the origin yields

$$\left.\frac{\partial^2 (V_{\mathrm{tree}}(\varphi) + V_{\mathrm{cw}}(\varphi, T) + V_{\mathrm{T}}(\varphi, T) + V_{\mathrm{daisy}}(\varphi, T))}{\partial \varphi^2}\right|_{\varphi \to 0} = g_{B\text{-}L}^2 T^2 . \tag{5.20}$$

We see that the absence of quadratic terms in the tree-level potential leads to a positive mass around the origin. Intriguingly, this holds as $T \to 0$. In other words, since there is no negative mass term that counteracts the positive thermal mass, a thermal barrier emerges that remains down to very small temperatures. As the scalar field has to tunnel over the barrier to convert the Universe to the true vacuum state, CSI models typically feature strongly supercooled FOPTs, i.e., a large hierarchy between the critical temperature T_c and the percolation temperature T_p. This is exemplified in fig. 5.1, where we show the effective potential $V_\mathrm{eff} = V_\mathrm{tree} + V_\mathrm{cw} + V_\mathrm{T} + V_\mathrm{daisy}$ for $(g_{B\text{-}L}, m_{Z'}) = (0.1, 1\,\mathrm{TeV})$, varying the temperature. At $T = T_\mathrm{c}$, the true vacuum becomes degenerate with the origin. Decreasing the temperature, the thermal barrier shifts to smaller field values, however, persists due to the lack of a negative tree-level mass term.

QCD-INDUCED CONTRIBUTION. It has been shown that for small gauge couplings $g_{B\text{-}L} \lesssim \mathcal{O}(0.1)$, the Universe enters the regime of extreme supercooling [46, 243, 244]. Then, the bubble nucleation rate is sufficiently small such that percolation has not occurred as the temperature of the thermal bath approaches the QCD scale, $\Lambda_\mathrm{QCD} \sim \mathcal{O}(100\,\mathrm{MeV})$. Since the electroweak symmetry remains unbroken, both fields h and φ sit at the origin, such that the SM fields are massless during the QCD quark–hadron transition [45, 288–290]. The temperature associated with the breaking of the chiral symmetry, $\langle q\bar{q}\rangle \neq 0$, in the presence of six massless flavors is lower than for physical quark masses. Ref. [288], e.g., finds $T_\mathrm{QCD} \approx 85\,\mathrm{MeV}$.

The formation of quark condensates breaks the classical scale symmetry. To see this, let us consider the SM Higgs tree-level potential in the presence of quark condensates and $v_\varphi = 0$,

$$V_h = \frac{\lambda_h}{4} h^4 + \sum_i \frac{y_i}{\sqrt{2}} \langle q_i \bar{q}_i \rangle h \,. \tag{5.21}$$

Here, the sum over quark flavors is dominated by the top quark, as it exhibits the largest Yukawa coupling y_t. By minimizing eq. (5.21), we find that the Higgs takes a finite, QCD-scale vev [46, 282]

$$v_{h,\mathrm{QCD}} = \left[-\frac{y_t}{\sqrt{2}\lambda_h} \langle t\bar{t} \rangle \right]^{\frac{1}{3}} . \tag{5.22}$$

Hence the cosmic QCD transition triggers EWSB. A precise value of $v_{h,\mathrm{QCD}}$ can only be inferred from the lattice, since the formation of the $\langle t\bar{t}\rangle$ condensate is driven by strongly-coupled dynamics and the top quark Yukawa runs non-perturbatively large [283]. However,

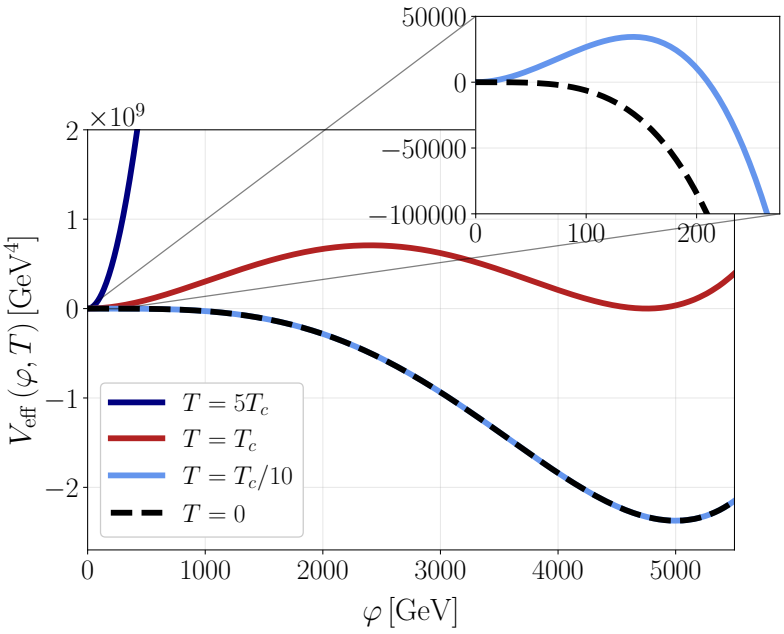

Figure 5.1: Exemplary effective potential for different temperatures, imposing $(g_{B\text{-}L}, m_{Z'}) = (0.1, 1\,\text{TeV})$. While at high temperatures (dark blue) the potential only possesses a minimum around the origin, the true vacuum becomes degenerate at $T_c \approx 313\,\text{GeV}$ (red). Further decreasing the temperature moves the barrier towards the origin (light blue). Nevertheless, the barrier remains intact, as seen in the inset figure where we compare to the zero-T potential (dashed black).

the numerical value is expected to be at the QCD scale. This can be estimated via, for instance, low-energy effective QCD models (see chapter 6). Therefore we employ

$$v_{h,\text{QCD}} = 100\,\text{MeV}\,, \tag{5.23}$$

throughout this work unless stated otherwise.

Coming back to the effective potential in the φ-direction in field space, we find that the QCD-induced breaking of the electroweak symmetry induces a negative mass term in the tree-level potential eq. (5.1) through the portal term,

$$V_{\text{QCD}} = -\frac{\lambda_p}{4} v_{h,\text{QCD}}^2 \varphi^2\,. \tag{5.24}$$

This term acts as a negative, temperature-independent mass,

$$\Delta m_{\text{QCD}}^2 = -\frac{\lambda_p}{2} v_{h,\text{QCD}}^2\,. \tag{5.25}$$

Repeating the exercise from eq. (5.20), we have

$$\left.\frac{\partial^2 V_{\text{eff}}(\varphi,T)}{\partial\varphi^2}\right|_{\varphi\to 0,T<T_{\text{QCD}}} = g_{B\text{-}L}^2 T^2 - \frac{\lambda_p}{2} v_{h,\text{QCD}}^2 \,. \tag{5.26}$$

The thermal barrier is counteracted by Δm^2_{QCD}, i.e., a temperature T_{roll} emerges where the barrier vanishes. Plugging in our model parameters, we find a tree-level estimate,

$$T_{\text{roll}} \simeq 2\sqrt{\lambda_h} v_{h,\text{SM}} \frac{v_{h,\text{QCD}}}{m_{Z'}} \approx 180 \frac{v_{h,\text{QCD}}}{m_{Z'}} \,\text{GeV} \,. \tag{5.27}$$

Conversely, for the barrier to vanish right at T_{QCD}, we have

$$m_{Z'} \lesssim 180 \frac{v_{h,\text{QCD}}}{T_{\text{QCD}}} \,\text{GeV} \,. \tag{5.28}$$

This interplay between QCD and the conformal sector leads to intriguing cosmological histories with interesting observational signatures, as outlined in sec. 5.3 and studied in chapters 6 and 7.

Finally, the full effective potential reads

$$V_{\text{eff}}(\varphi,T) = \begin{cases} V_{\text{tree}}(\varphi) + V_{\text{cw}}(\varphi,T) + V_{\text{T}}(\varphi,T) + V_{\text{daisy}}(\varphi,T) & \text{if } T > T_{\text{QCD}} \,, \\ V_{\text{tree}}(\varphi) + V_{\text{cw}}(\varphi,T) + V_{\text{T}}(\varphi,T) + V_{\text{daisy}}(\varphi,T) + V_{\text{QCD}}(\varphi) & \text{if } T \leq T_{\text{QCD}} \,, \end{cases} \tag{5.29}$$

where the relevant contributions are given in eqs. (5.1), (5.5), (5.16), (5.17), and (5.24). In fig. 5.2, we show the full effective potential (5.29) at $T = T_{\text{QCD}}$ for $(g_{B\text{-}L}, m_{Z'}) = (0.1, 1\,\text{TeV})$ (left) and $(g_{B\text{-}L}, m_{Z'}) = (0.1, 150\,\text{GeV})$ (right), respectively. We only display the field space around the thermal barrier, $\varphi \ll v_\varphi$. As expected from eq. (5.28) we observe the barrier, despite being diminished, to persist through the cosmic QCD transition for larger Z' masses. For smaller Z' masses, the barrier is directly canceled by the QCD-induced contribution.

RENORMALIZATION GROUP IMPROVEMENT. Before analyzing the cosmic history of the CSI SM, we need to specify the RG scale μ which enters the effective potential via dimensional transmutation. Note that in principle, the RG scale is not a physical quantity but merely an integration constant, therefore it should not affect any physical results. At zero temperature, the effective potential becomes independent of μ by RG improvement. In the case of our model this amounts to the replacements

$$\lambda_\varphi \to \lambda_\varphi(\mu) \,, \qquad g_{B\text{-}L} \to g_{B\text{-}L}(\mu) \,. \tag{5.30}$$

Then, the running of the coupling in the tree-level potential cancels the running of the logarithmic contributions in the CW term [320]. This is no longer true at finite temperature. Due to the additional, temperature-dependent contributions, the RG scale in fact cancels only at the two-loop order (see part iv). Since we restrict ourselves to the one-loop effective potential, a residual RG scale dependence of our results cannot be avoided. The μ-induced uncertainty in computations of FOPTs will be studied in part iv.

However, let us demonstrate that there exists a range of values that minimize the dependence on μ. In the high-T limit, we can express the temperature-dependent contributions according to eq. (3.34). Plugging this into the full potential (5.29), we find [320]

$$V_{\text{cw}} + V_{\text{T}} \supset -\frac{3}{64\pi^2} m_{\text{Z}'}(\varphi)^4 L_b(\mu)\,, \quad \text{with} \quad L_b(\mu) = 2\ln\left(\frac{\mu e^{\gamma_{\text{E}}}}{4\pi T}\right)\,. \tag{5.31}$$

The logarithmic mass dependence hence cancels between V_{cw} and V_{T}, solely leaving a dependence on μ and T. While the common approach in the literature is to fix μ by the largest mass scale or the scalar vev [244], eq. (5.31) clearly shows that the natural choice is a temperature-dependent RG scale. To this end, employed values are in the range $\frac{\pi}{2}T \leq \mu \leq 4\pi e^{-\gamma_{\text{E}}} T$, where the upper bound completely cancels the logarithm. Throughout the subsequent chapters, we will employ the hard Matsubara scale $\mu = \pi T$ unless stated otherwise.

While we could end the discussion at this point for models including a tree-level mass term, CSI theories require special attention [246, 247]. Due to the large amount of supercooling, we encounter a scale hierarchy

$$\pi T \ll m_\varphi(v_\varphi) \sim m_{\text{Z}'}(v_\varphi) \sim v_\varphi\,. \tag{5.32}$$

Then, the high-T limit is only valid in the regime of small field excursions where the field-dependent masses are small. Conversely, close to the true vacuum the respective masses are large, and the theory enters the low-T regime. In this case, the potential is dominated by the CW contribution and the relevant scale is set by the vacuum masses. Therefore, we follow refs. [246, 247] and evaluate all couplings that enter the effective potential at

$$\mu(\varphi, T) = \max\left\{m_{\text{Z}'}(\varphi), \pi T, \Lambda_{\text{QCD}}\right\}\,, \tag{5.33}$$

employing the β-functions from ref. [234]. Note that we have imposed a lower cutoff at $\Lambda_{\text{QCD}} = 100\,\text{MeV}$. Below the QCD scale the strong gauge coupling g_s becomes non-perturbative, causing a divergent RG flow of the top quark Yukawa y_t. Since y_t affects the RG evolution of the portal coupling λ_p, the numerical evaluation of the RGE becomes unstable. Therefore we freeze the running of the parameters below the QCD confinement

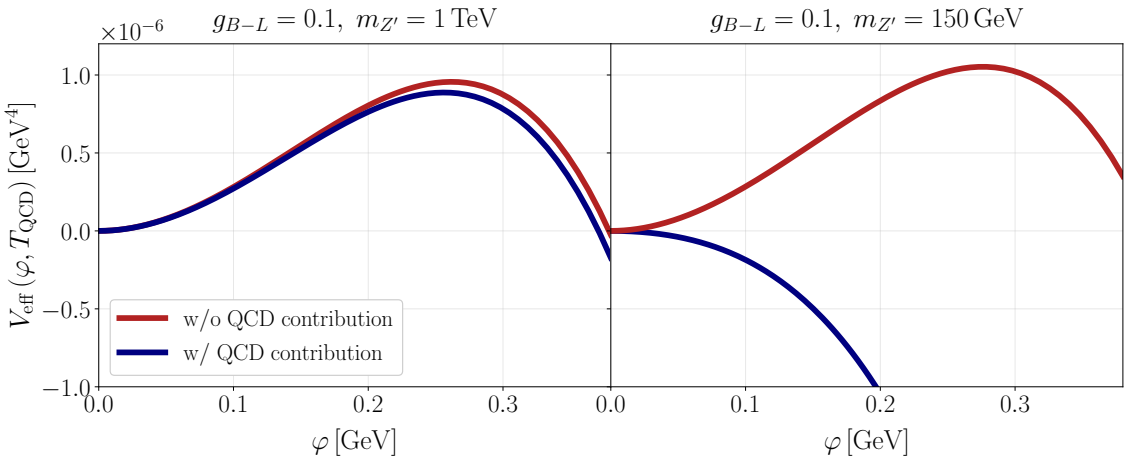

Figure 5.2: Full effective potential for small field values $\varphi \ll v_\varphi$, evaluated at the QCD scale $T = T_{\mathrm{QCD}}$ for $m_{Z'} = 1\,\mathrm{TeV}$ (left) and $m_{Z'} = 150\,\mathrm{GeV}$ (right). The blue line results from including the QCD-sourced mass term (5.24), while the red curve is obtained without Δm_{QCD}. For large Z' masses, the QCD contribution is not large enough to cancel the barrier. In the right panel, however, Δm_{QCD} dominates over the positive thermal mass and the field becomes free to roll towards the true minimum. Note that strictly speaking, the chosen model parameters in the right panel are exluded by experiment [316, 317], however, they are suitable for our demonstration of the impact of the QCD contribution.

scale. While this is a practical solution to the problem, a more rigorous treatment of the strongly coupled dynamics would involve, e.g., lattice techniques. This is beyond the scope of this work.

5.3 MODIFIED COSMIC THERMAL HISTORY

Let us now describe how CSI models affect the thermal history of the Universe and introduce the resulting symmetry breaking patterns. This provides an overview of the current literature and sets the foundation for the subsequent chapters, where we explore new directions.

THERMAL INFLATION. In sec. 3.2, we have introduced several temperature scales characterizing FOPTs. While those are sufficient to describe the dynamics in most models that include a tree-level mass term, CSI theories require a more careful treatment. Around eq. (5.20), we have shown that the effective mass around the origin of field space is always positive, i.e., a thermal barrier persists for all temperatures. Then, the symmetry-breaking

field may be trapped in the false vacuum for a long time, such that $T_\mathrm{p} \ll T_\mathrm{c}$ [243, 244]. Since the false vacuum energy density is constant while the background dilutes like radiation, we typically encounter a temperature where

$$\Delta V_\mathrm{eff}(T_i) = \frac{\pi^2}{30} g_\epsilon T_i^4 \,. \tag{5.34}$$

Here, g_ϵ denotes the relativistic degrees of freedom in the thermal bath, while $\Delta V_\mathrm{eff}(T_i) = V_\mathrm{eff}(0, T_i) - V_\mathrm{eff}(v_\varphi, T_i)$ is the difference in potential energy between the false and true vacuum. At T_i, the Universe enters a period of thermal inflation driven by the false vacuum energy of the conformal sector. Note that this epoch of vacuum domination is unrelated to the initial period of cosmic inflation [103].

Since the temperature hierarchy is typical large, $T_\mathrm{c} \gg T_i \gg T_\mathrm{p}$, the potential energy difference is well approximated by its zero-temperature value. In the case of the $\mathrm{U}(1)_\mathrm{B\text{-}L}$ extended SM, we have

$$\Delta V_\mathrm{eff}(T_i) \simeq \Delta V_\mathrm{eff}(T = 0) = \frac{3}{128\pi^2} m_{\mathrm{Z}'}^4 \,. \tag{5.35}$$

Then, the onset of thermal inflation is given by

$$T_i \simeq \left(\frac{90}{128\pi^4 g_\epsilon} \right)^{\frac{1}{4}} m_{\mathrm{Z}'} \,, \tag{5.36}$$

and the Hubble parameter becomes approximately constant,

$$H(T < T_i) \simeq \left(\frac{\Delta V_\mathrm{eff}(T = 0)}{3 M_\mathrm{Pl}^2} \right)^{\frac{1}{2}} = \frac{1}{\sqrt{128}\pi} \frac{m_{\mathrm{Z}'}^2}{M_\mathrm{Pl}} \,. \tag{5.37}$$

These approximate expressions are useful to obtain an intuition on the relation between the new physics scale $m_{\mathrm{Z}'}$ and the relevant cosmological parameters. However, for our quantitative studies in chapters 6 and 7, we always employ the full temperature dependence in the effective potential and determine T_i numerically.

EXIT FROM SUPERCOOLING. Depending on the duration of the supercooling period starting at T_i, different symmetry breaking patterns arise which we briefly describe in the following.

I. $T_\mathrm{p} > T_\mathrm{QCD}$: Bubble percolation is efficient before the thermal bath approaches the QCD scale. As shown in refs. [243, 244], this occurs for $g_{B\text{-}L} \gtrsim 0.2$. The result is a strong $\mathrm{U}(1)_\mathrm{B\text{-}L}$ FOPT, generating relic GWs in the reach of future observatories such as LISA or ET.

II. $T_\mathrm{p} \leq T_\mathrm{QCD}$: The $\mathrm{U}(1)_\mathrm{B\text{-}L}$ PT has not occurred yet as the temperature approaches T_QCD due to the inefficiency of bubble percolation in the inflating Universe. Then, the QCD-induced contribution (5.24) has to be taken into account and a negative tree-level mass term emerges. The cosmic history depends on whether the QCD-induced mass cancels the thermal barrier right at T_QCD. We distinguish two cases:

   (a) $T_\mathrm{p} = T_\mathrm{QCD}$: The QCD-induced mass Δm^2_QCD is large enough to cancel the thermal barrier, such that the $\mathrm{U}(1)_\mathrm{B\text{-}L}$ scalar rolls down the effective potential towards the true minimum [46]. This scenario is depicted in the right panel of fig. 5.2. The generation of a SGWB depends on the order of the cosmic QCD transition in the presence of massless quarks. If χSB proceeds via bubble nucleation, the thermal barrier merely disappears in regions of spacetime where the quark condensates have formed. Then, the false vacuum energy is released inside the hadronic bubbles, and the GW amplitude is determined by the timescale of the χPT.

   (b) $T_\mathrm{p} < T_\mathrm{QCD}$: The thermal barrier persists as the chiral symmetry is broken, as shown in the left panel of fig. 5.2. Then, the Universe keeps inflating at temperatures below the QCD scale, further suppressing the thermal mass of the scalar field and accelerating bubble nucleation. For moderate gauge couplings $g_{B\text{-}L} \sim 0.1$, the exit from supercooling is realized by a QCD-accelerated, first-order $\mathrm{U}(1)_\mathrm{B\text{-}L}$ PT [243, 244].

In the following chapters, we will study scenario II. While the QCD-induced exit from supercooling, i.e., scenario II (a), was proposed in ref. [46], the PT parameters were only estimated. Therefore, in chapter 6, we focus on the massless-quark electroweak-QCD PT in a supercooled Universe and calculate the resulting SGWB employing different low-energy effective models of QCD.

In chapter 7, we extend previous studies by considering the parameter space of small gauge couplings $g_{B\text{-}L} \ll 0.1$, i.e., scenario II (b). We show that as the gauge coupling decreases, supercooling becomes more significant, such that one eventually enters a regime where bubble percolation cannot drive the exit from superooling. Then, the barrier is cancelled at the temperature $T_\mathrm{roll} \ll T_\mathrm{QCD}$, and the symmetry-breaking field rolls towards the true minimum instead of undergoing a FOPT. As φ crosses a region in the effective potential where its mass is tachyonic, long-wavelength fluctuations are exponentially amplified, generating a unique GW background.

REHEATING THE UNIVERSE. To recover a consistent cosmological evolution we need to ensure an efficient reheating of the thermal bath after the exit from supercooling. This reheating process can proceed in two ways. If the FOPT is dominated by interactions between the bubble walls and the primordial plasma, the main source of GWs are sound waves. In this case, the false vacuum energy is efficiently transferred to the heat bath during bubble expansion, and we may assume reheating to be fast compared to the Hubble rate. If thermalization occurs in less than a Hubble time, the reheating temperature is well approximated by setting

$$\frac{\pi^2}{30} g_{\epsilon,\mathrm{rh}} T_{\mathrm{rh}}^4 = \Delta V_{\mathrm{eff}}(T_{\mathrm{p}}) \,, \tag{5.38}$$

where $\Delta V_{\mathrm{eff}}(T_{\mathrm{p}})$ is the potential energy difference at percolation, and $g_{\epsilon,\mathrm{rh}}$ denotes all relativistic degrees of freedom after the PT. Hence, in this case $T_{\mathrm{rh}} \approx T_i$ (cf. eq. (5.36)).

If, on the other hand, the PT is either driven by bubble collisions or not first-order, the false vacuum energy remains in the conformal sector after symmetry breaking. The $\mathrm{U}(1)_{\text{B-L}}$ scalar field oscillates about the true minimum, potentially causing a matter domination (MD) period which further dilutes the GW signal.[4] This depends on the decay rate of φ into SM particles. The simplest way to reheat Universe is by decays into the Higgs, provided $m_\varphi > 2m_h$. The associated decay rate reads [244, 322]

$$\Gamma_\varphi \approx \frac{\lambda_p^2 v_\varphi^2}{32\pi m_\varphi} \,. \tag{5.39}$$

Assuming rapid thermalization, reheating takes place when

$$\Gamma_\varphi = H_{\mathrm{rh}} = H_\star \left(\frac{a_\star}{a_{\mathrm{rh}}}\right)^{\frac{3}{2}} \,. \tag{5.40}$$

The reheating temperature then is

$$\frac{\pi^2}{30} g_{\star,\epsilon} T_{\mathrm{rh}}^4 = 3 M_{\mathrm{Pl}}^2 \mathrm{min}\left(H_\star^2, \Gamma_\varphi^2\right) \,, \tag{5.41}$$

i.e., reduces to eq. (5.38) if $\Gamma_\varphi > H_\star$. Employing our estimate (5.37), we have

$$\frac{\Gamma_\varphi}{H_\star} \approx 2 \times 10^{-3} g_{B\text{-}L} \left(\frac{10^6 \mathrm{GeV}}{m_{\mathrm{Z'}}}\right)^5 \,. \tag{5.42}$$

Hence, if the gauge coupling is sufficiently small, or conversely, $m_{\mathrm{Z'}}$ is sufficiently large, the reheating temperature reads

$$T_{\mathrm{rh}} \approx 1.4 \times 10^4 g_{\star,\epsilon}^{-\frac{1}{4}} g_{B\text{-}L}^{\frac{1}{2}} \left(\frac{10^6 \mathrm{GeV}}{m_{\mathrm{Z'}}}\right)^{\frac{3}{2}} \mathrm{GeV} \,. \tag{5.43}$$

4 In fact, the scalar field configuration after a FOPT is inhomogeneous, which may cause deviations from the matter-like behavior [321]. The impact on our results is expected to be small; therefore, we follow previous literature [244] and assume a matter-like scaling.

This immediately gives a bound on the model parameters by requiring that the Universe is radiation-dominated during BBN, i.e., $T_{\rm rh} > T_{\rm BBN} \sim \mathcal{O}(\text{MeV})$,

$$m_{\rm Z'} < 5.8 \times 10^{10} g_{\star,\epsilon}^{-\frac{1}{6}} g_{B\text{-}L}^{\frac{1}{3}} \text{GeV} \,. \tag{5.44}$$

Again, note that for our numerical results in the following chapters, we employ the full effective potential including the running of the model parameters to compute $T_{\rm rh}$. Also, let us mention that in principle, scalar mixing provides a way to efficiently reheat the Universe in a certain parameter space by direct decays into SM leptons [322]. However, the parameter space relevant to this work, $\varphi \to hh$ is the more efficient decay channel. In addition, decays into leptons and Higgs particles via right-handed neutrinos can quickly reheat the Universe [323]. This only occurs in a narrow region of the overall parameter space where the right-handed neutrino Yukawa couplings are tuned accordingly. Therefore we relegate a study of such reheating channels and the effect of sterile neutrinos on the GW signal to the future.

6

GRAVITATIONAL WAVES FROM QCD-TRIGGERED CONFORMAL SYMMETRY BREAKING

Motivated by the cosmic thermal history outlined above, we now study in detail the dynamics of the QCD χPT in a supercooled Universe. To this end, we are interested in scenario II (a) from sec. 5.3, where the cosmic QCD transition triggers the exit from supercooling by canceling the potential barrier in the CSI effective potential (cf. fig. 5.2). This involves a large energy budget, as the energy responsible for thermal inflation is released. The timescale of the transition, on the other hand, depends on the nucleation rate of hadronic bubbles, which in turn is affected by the Hubble rate during supercooling. While we have introduced such a symmetry breaking pattern in the case of the $\mathrm{U}(1)_{\mathrm{B\text{-}L}}$ extended SM, there is a multitude of models which may lead to similar dynamics [46, 256, 281–285]. Therefore, we remain agnostic about the particle content of the new sector. We leave the scale of new physics, i.e., the amount of supercooling, as a free parameter. The only assumption is a substantial period of thermal inflation induced by some conformal dynamics, delaying the EWPT to the QCD confinement scale, such that all SM fields remain massless. By computing the χPT dynamics, including the associated SGWB, merely as a function of T_i (5.34), our results can then easily be mapped to any SM extension.

During χSB, the chiral $\mathrm{SU}(N_\mathrm{f})_\mathrm{L} \times \mathrm{SU}(N_\mathrm{f})_\mathrm{R}$ symmetry of QCD is broken down to the vector subgroup $\mathrm{SU}(N_\mathrm{f})_\mathrm{V}$ by quark condensation, $\langle \bar{q}q \rangle \neq 0$. We note that the order of the χPT in the massless limit is a long-standing puzzle. While previous results [45, 289] imply a first-order χPT for $N_\mathrm{f} > 3$, a recent lattice study [290] indicates that the χPT remains second-order up to a large number of flavors. In contrast, analyses employing the functional renormalization group allow for the possibility of a first-order χPT [324]. Note that [290] considers pure QCD. The order of the transition may be affected by the large top quark Yukawa when including the Higgs field [283], which acquires a vev sourced by χSB in our scenario. To our knowledge, this combined massless six-flavor QCD + Higgs system has not been studied on the lattice to date, and the nature of such a transition remains unknown. For these reasons, we assume a first-order χPT in the following and

explore its phenomenological implications. In addition, our results provide crucial insights for further model building in strongly-coupled dark sectors.

To this end, we first construct three different low-energy effective theories of QCD which feature a first order χPT in secs. 6.1 and 6.2. In sec. 6.3, we compute the PT dynamics in a thermally inflating Universe, focusing on the transition timescale. Subsequently, we calculate the associated SGWB in sec. 6.4 as a function of the amount of supercooling. Intriguingly, we find a significant enhancement of the GW amplitude if the new physics scale is sufficiently large, implying excellent observational prospects.

6.1 NAMBU–JONA-LASINIO MODEL

Due to the strongly-coupled nature of QCD around the confinement scale, χSB cannot be studied by conventional perturbative methods. To this end, lattice QCD provides a non-perturbative way to simulate the dynamics from first principles [20, 290, 325]. Such simulations are, however, extremely expensive and hence unfeasible for parameter space scans in the context of early Universe cosmology. Instead, we employ low-energy effective theories of QCD [326]. Here, an effective Lagrangian is constructed which possesses the symmetries of the full theory. Subsequently, the model parameters are fitted to match physical observables such as the meson masses and decay constants. Although this approach captures certain phenomenological aspects of full QCD, it naturally introduces simplifications that limit predictive accuracy. We therefore use different effective descriptions to estimate the associated error band, including the quark-based Nambu–Jona-Lasinio (NJL) model [327] and two Polyakov loop [328] extended versions thereof, which include gluonic degrees of freedom.

Inspired by the theory of superconductivity, the NJL model was originally developed [327] as a mechanism for spontaneous symmetry breaking, i.e., to study the mass generation of elementary particles. Nowadays, the NJL model serves as a low-energy effective theory of QCD, with applications in strongly-coupled systems at finite temperature and density, such as early Universe phase transitions [329, 330] or neutron stars [331–334]. We refer the reader to refs. [335, 336] for reviews.

TREE-LEVEL POTENTIAL. The starting point for our analysis is the quark-based effective Lagrangian density [337, 338]

$$\mathcal{L}_{\text{NJL}} = \bar{q}(i\partial\!\!\!/ - \hat{m})q + \mathcal{L}_{4\text{F}} + \mathcal{L}_{6\text{F}}\,, \tag{6.1}$$

where q ($\bar{q}$) denote the SM (anti-) quark fields, and $\not{\partial} = \gamma^\mu \partial_\mu$ with γ^μ the Dirac matrices. The quark mass term, including up-, down-, and strange-quarks, reads

$$\hat{m} = \mathrm{diag}(m_u, m_d, m_s) = \mathrm{diag}(y_u, y_d, y_s)\frac{\langle h \rangle}{\sqrt{2}}\,, \tag{6.2}$$

where $\langle h \rangle$ is the expectation value of the Higgs field. This term will soon be set to zero as the electroweak symmetry remains unbroken in the supercooled Universe. Note that since the EWPT is delayed, all $N_\mathrm{f} = 6$ quark flavors remain massless, hence should be included in the model construction. Nevertheless, we restrict ourselves to $N_\mathrm{f} = N_\mathrm{c} = 3$, where N_c denotes the number of colors. This is based on our assumption that quark condensation occurs first in the light quark sector [283]. Moreover, all effective parameters can then be fixed by hadronic physics, since real QCD only features an (approximate) chiral symmetry for $q \in \{u, d, s\}$. Furthermore, we neglect the Higgs field in our study, which acquires a vev along χSB (cf. eq. (5.22)). If we were to compute the effective potential in the Higgs direction, we would integrate out all quark fields (cf. sec. 3.2). These quark fields, however, are the dynamical degrees of freedom undergoing χSB. It is currently unclear how this double counting issue is resolved, hence we postpone a more detailed study of the QCD + Higgs system to the future.

The effective Lagrangian (6.1) further contains a four-fermion interaction, $\mathcal{L}_{4\mathrm{F}}$, and a six-fermion determinant interaction, $\mathcal{L}_{6\mathrm{F}}$,

$$\mathcal{L}_{4\mathrm{F}} = G \sum_{a=0}^{N_\mathrm{f}^2-1} \left[\left(\bar{q}\, T^a q\right)^2 + \left(\bar{q}\, i\gamma_5 T^a q\right)^2 \right], \tag{6.3}$$

$$\mathcal{L}_{6\mathrm{F}} = G_\mathrm{D} \Big[\det\left(\bar{q}(1-\gamma_5)q\right) + \det\left(\bar{q}(1+\gamma_5)q\right) \Big], \tag{6.4}$$

where G and G_D are effective coupling parameters. The generators of the underlying flavor symmetry group $\mathrm{SU}(N_\mathrm{f})$ are denoted by T^a. $\mathcal{L}_{6\mathrm{F}}$ is the 't Hooft determinant [339–341]. This term is introduced since QCD exhibits a global, axial $\mathrm{U}(1)_\mathrm{A}$ symmetry at the classical level under which the Dirac spinors transform as

$$q \to e^{i\vartheta_5 \gamma_5} q\,, \tag{6.5}$$

with $\vartheta_5 \in \mathbb{R}$. In full QCD, this symmetry is anomalously broken [339], i.e., it does not hold at the quantum level. In the effective theory, this is mimicked by including the six-

point quark interaction, breaking $\mathrm{U}(1)_\mathrm{A}$ explicitly. In the massless limit, the remaining symmetry group is then $\mathrm{SU}(3)_\mathrm{L} \times \mathrm{SU}(3)_\mathrm{R} \times \mathrm{U}(1)_\mathrm{V}$, which transforms quarks field as

$$\begin{aligned} \mathrm{SU}(3)_\mathrm{L}: &\qquad q_\mathrm{L} \to U_\mathrm{L} q_\mathrm{L}\,, \\ \mathrm{SU}(3)_\mathrm{R}: &\qquad q_\mathrm{R} \to U_\mathrm{R} q_\mathrm{R}\,, \\ \mathrm{U}(1)_\mathrm{V}: &\qquad q \to e^{i\vartheta} q\,. \end{aligned} \tag{6.6}$$

Here, the subscripts L/R denote the left-/right-handed components respectively, $U_{\mathrm{L/R}}$ are unitary matrices with $\det(U_{\mathrm{L/R}}) = 1$, and $\vartheta \in \mathbb{R}$. Hence, the effective NJL Lagrangian features all symmetry properties required to be an appropriate low-energy effective theory of QCD. During χSB, the $\mathrm{SU}(3)_\mathrm{L} \times \mathrm{SU}(3)_\mathrm{R}$ subgroup is broken to $\mathrm{SU}(3)_\mathrm{V}$.

We continue the construction of the effective theory by introducting the self-consistent mean-field approximation (MFA) [342–344]. To this end, let us first reshape eq. (6.1) into a more compact form [237],

$$\begin{aligned} \mathcal{L}_\mathrm{NJL} &= \bar{q}\Big(i\partial\!\!\!/ - \hat{m}\Big) q + \mathcal{L}_\mathrm{4F} + \mathcal{L}_\mathrm{6F}\,, \\ \mathcal{L}_\mathrm{4F} &= 2G\,\mathrm{Tr}\left(\Psi^\dagger \Psi\right), \\ \mathcal{L}_\mathrm{6F} &= G_\mathrm{D}\Big(\det\Psi + \mathrm{h.c.}\Big)\,, \end{aligned} \tag{6.7}$$

where $\Psi_{ij} = \bar{q}_j(1-\gamma_5)q_i$ is the quark bilinear. In the MFA, eq. (6.7) is expressed by Ψ and its expectation value

$$-4G\langle\Psi\rangle = (\sigma + i\eta')\,\mathbb{1} + 2\,(a_a + i\pi_a)\,T^a\,, \tag{6.8}$$

where $\mathbb{1}$ is the unit matrix, and we have introduced mesonic auxiliary fields. These mesonic fields correspond to the different chiral condensates [329],

$$\sigma = -\frac{4G}{3}\langle\bar{q}q\rangle\,, \quad \eta' = -\frac{4iG}{3}\langle\bar{q}\gamma_5 q\rangle\,, \quad a_a = -4G\langle\bar{q}\,T^a q\rangle\,, \quad \pi_a = -4iG\langle\bar{q}\gamma_5 T^a q\rangle\,. \tag{6.9}$$

Here σ (η') is the (pseudo-)scalar singlet, while a_a (π_a) is the (pseudo-)scalar octet. Let us stress that during χSB, only σ can acquire a vev. This is because the $\mathrm{SU}(3)_\mathrm{V}$ isospin symmetry remains unbroken, hence mesons that mix different flavors, i.e., a_a and π_a cannot obtain a vev. Moreover, a pseudoscalar vev, $\eta' \neq 0$, is prohibited as the vacuum is parity-even.

The full NJL Lagrangian, expressed in the MFA, can be found in [329]. The tree-level potential reads

$$\begin{aligned} V_0^\mathrm{NJL}(\sigma,\eta',a_a,\pi_a) = &+ \frac{1}{8G}\left(3\sigma^2 + 3\eta'^2 + 2\pi_a\pi_a + 2a_a a_a\right) \\ &- \frac{G_\mathrm{D}}{16G^3}\left[\sigma(\sigma^2 + \pi_a\pi_a - 3\eta'^2 - a_a a_a) + 5a_a\pi_a\eta'\right]. \end{aligned} \tag{6.10}$$

Since only the σ-direction is relevant for studying χSB, we set $\eta' = \pi_a = a_a = 0$ and obtain

$$V_0^{\mathrm{NJL}}(\sigma) = \frac{3}{8G}\sigma^2 - \frac{G_{\mathrm{D}}}{16G^3}\sigma^3 \,. \tag{6.11}$$

RADIATIVE CORRECTIONS. In the next step, we add radiative corrections to the tree-level potential. This is done by integrating out the fermion fields, as outlined in sec. 3.2. The fermionic vacuum energy reads

$$V_1^{\mathrm{NJL}}(\sigma) = -2N_{\mathrm{c}} \sum_i \int \frac{\mathrm{d}^4 p}{(2\pi)^4} \ln\det\left(\not{p} - M_i\right) \,, \tag{6.12}$$

where the factor of two corresponds to the spin degrees of freedom, N_{c} is the number of colors, and the sum runs over the fermion flavors. M_i denote the constituent quark masses [345], which, in the chiral limit, read [329]

$$M_i \equiv M(\sigma) = \sigma - \frac{G_{\mathrm{D}}}{8G^2}\sigma^2 \,. \tag{6.13}$$

Eq. (6.12) is divergent, i.e., has to be regularized. As a consequence of the multifermion interactions in eq. (6.1), the NJL model is non-renormalizable. Therefore, a hard cutoff regularization is typically employed [346]. To this end, refs. [237, 239, 278, 329] impose a cutoff Λ on the four-dimensional (4D) momentum integral. Since we study the theory at finite temperature, it is, however, more natural to use a three-dimensional (3D) cutoff scheme, following refs. [330, 347, 348]. This amounts to replacing

$$\int \frac{\mathrm{d}^4 p}{(2\pi)^4} \to \int \frac{\mathrm{d}p_0}{2\pi} \int_{\boldsymbol{p}}^{\Lambda} \,, \tag{6.14}$$

with the d-dimensional measure $\int_{\boldsymbol{p}} \equiv \mu^{3-d} \int \frac{\mathrm{d}^d \boldsymbol{p}}{(2\pi)^d}$, $d = 3$. Then, thermal integrals containing a Matsubara sum may be treated with the same cutoff. Indeed, by comparing our results to the ones obtained with a 4D cutoff, we demonstrate in appendix 6.B that the 3D cutoff scheme is more reliable.

Evaluating eq. (6.12) yields [348]

$$V_{1,\mathrm{3D}}^{\mathrm{NJL}}(\sigma) = -2N_{\mathrm{c}}N_{\mathrm{f}} \int_{\boldsymbol{p}}^{\Lambda} E_p = -\frac{N_{\mathrm{c}}N_{\mathrm{f}}}{8\pi^2}\Lambda^4 \left[\left(2+\xi^2\right)\sqrt{1+\xi^2} + \frac{\xi^4}{2}\ln\frac{\sqrt{1+\xi^2}-1}{\sqrt{1+\xi^2}+1}\right] , \tag{6.15}$$

where $E_p = \sqrt{p^2 + M^2}$, $\xi = M/\Lambda$, and M is given by eq. (6.13). Hence, we note that the Λ enters the final expression of the one-loop contribution. Its choice hence crucially affects resulting predictions. Therefore, Λ is treated as a model parameter, such that, together with G and G_{D}, the NJL model contains three free parameters. By computing

meson masses and decay constants in the effective theory, the model parameters are fixed to reproduce the hadron spectrum of QCD. The parameters are found in ref. [345] and summarized in table 6.1.

THERMAL CORRECTIONS. Interactions with the thermal bath induce temperature-dependent corrections to the effective potential. Following the procedure from sec. 3.2, fermionic contributions read

$$V_{\mathrm{T}}^{\mathrm{NJL}}(\sigma, T) = g_q N_{\mathrm{c}} J_{\mathrm{f}} \left(\frac{M(\sigma)^2}{T^2} \right) . \tag{6.16}$$

The number of degrees of freedom is $g_q = N_{\mathrm{f}}$ (quarks) $\times$ 2 (antiquarks) $\times$ 2 (spin) $= 12$, and J_{f} corresponds to the fermionic thermal integral (3.33), which we treat with the same cutoff as eq. (6.15). Since fermions are IR-safe, we do not have to perform resummations, hence the construction of the effective potential in the NJL model is complete. In summary, we have

$$V_{\mathrm{eff}}^{\mathrm{NJL}}(\sigma, T) = V_0^{\mathrm{NJL}}(\sigma) + V_1^{\mathrm{NJL}}(\sigma) + V_{\mathrm{T}}^{\mathrm{NJL}}(\sigma, T) . \tag{6.17}$$

Fig. 6.1 shows the evolution of the effective potential as a function of the chiral condensate σ and the temperature T. At high temperatures, the chiral symmetry is restored, i.e., the global minimum is at the origin. As the temperature decreases, a second minimum forms, separated from the false vacuum by a thermal barrier, implying a FOPT. At the critical temperature $T_{\mathrm{c}} \approx 128\,\mathrm{MeV}$, both minima become degenerate, hence tunneling to the true vacuum becomes energetically favored.

6.2 POLYAKOV LOOP MODELING

While the NJL model provides an effective method to study the behavior of the quark condensate $\langle \bar{q} q \rangle$ at finite-T, it does not contain any gauge degrees of freedom. The goal of this section is to include the gluonic sector in an appropriate way, in order to obtain a more complete picture.

CENTER SYMMETRY AND POLYAKOV LOOP. Let us for the moment consider a pure Yang-Mills system, consisting of gluons coupled to infinitely heavy (i.e., non-dynamical)

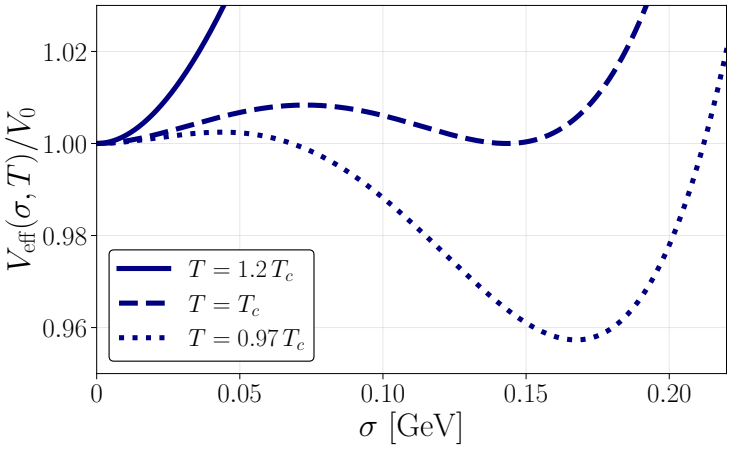

Figure 6.1: Exemplary effective potential obtained with the NJL model, as a function of the chiral condensate σ, and normalized to the false vacuum energy at the origin V_0. While for large temperatures the chiral symmetry is restored, we find a thermal barrier separating the hadronic phase (true minimum) from the quark phase (false minimum) at $T_\mathrm{c} = 128\,\mathrm{MeV}$. This implies a first-order χPT.

quarks. In the absence of chiral symmetry, the quantity that describes the critical behavior of this system, i.e., color confinement, is the fundamental traced Polyakov loop [328, 349],

$$\ell(\boldsymbol{x}) = \frac{1}{N_\mathrm{c}} \mathrm{Tr}_\mathrm{c}\, \boldsymbol{L}\,, \tag{6.18}$$

$$\boldsymbol{L}(\boldsymbol{x}) = \mathcal{P} \exp\left[i g_\mathrm{s} \int_0^\beta \mathrm{d}\tau A_4(\boldsymbol{x}, \tau)\right]. \tag{6.19}$$

Here, $\beta = 1/T$, $A_4 = iA_0$ is the temporal component of the gauge field in Euclidean time τ, g_s is the strong gauge coupling, Tr_c denotes the trace over color space, and $\mathcal{P}$ indicates path ordering along the time direction. At the mean-field level, A_4 is spatially homogeneous. See, e.g., ref. [326] for a detailed review of the Polyakov loop.

While being a gauge-invariant, hence physical quantity, the Polyakov loop is not invariant under *center transformations* [350, 351]. The center group Z_{N_c} comprises all elements z_k that commute with the elements of the associated gauge group $\mathrm{SU}(N_\mathrm{c})$,

$$z_k = e^{\frac{2\pi i k}{N_\mathrm{c}}}\,, \quad \text{with} \quad k = 0, 1, \ldots, N_\mathrm{c} - 1\,. \tag{6.20}$$

Hence, for $N_\mathrm{c} = 3$, the center group Z_3 contains three elements. Under gauge transformations $V(x) \in \mathrm{SU}(N_\mathrm{c})$, the gluonic fields transform as [352]

$$A_\mu(x) \to A'_\mu(x) = V(x) \left(A_\mu(x) - \frac{1}{i g_s} \partial_\mu \right) V^\dagger(x)\,. \tag{6.21}$$

Specializing to transformations of the form $V_k(x) = [z_k \mathbb{1}]^{\frac{\tau}{\beta}}$, we find (cf. eq. (6.21)) that the temporal gauge field component acquires a constant shift

$$A_4' = A_4 - \frac{2\pi k}{g_s N_c \beta} \,. \tag{6.22}$$

With eq. (6.18) it is now straightforward to see that the traced Polyakov loop transforms as

$$\ell \to \ell' = z_k \ell \,. \tag{6.23}$$

The gauge field is periodic under center transformations, $A_4'(x_4 = \beta) = A_4'(x_4 = 0)$, hence the gauge part of the action remains invariant. Quarks transform non-trivially under center transformations, which is why center symmetry is only exact in pure Yang-Mills theory.

The crucial property of the expectation value of the Polyakov loop is its connection to the free energy of a static (anti-)quark (pair) in a gluonic medium [353–355]

$$\langle \ell(\boldsymbol{x}) \rangle = e^{-\beta F_q} \,, \quad \langle \ell^\dagger(\boldsymbol{x}) \rangle = e^{-\beta F_{\bar{q}}} \,, \quad \langle \ell^\dagger(\boldsymbol{x}) \ell(\boldsymbol{y}) \rangle = e^{-\beta F_{\bar{q}q}(\boldsymbol{x}-\boldsymbol{y})} \,. \tag{6.24}$$

In a confined theory, such as pure Yang-Mills theory or QCD at low energy, the energy to create a single quark is infinitely large $F_q \to \infty$, i.e., $\langle \ell(\boldsymbol{x}) \rangle = 0$. Conversely, F_q is finite in the deconfined phase, such that the Polyakov loop expectation value can acquire a non-zero vev, $\langle \ell(\boldsymbol{x}) \rangle \neq 0$. This finite vev, however, breaks center symmetry (cf. eq. (6.23)). From these considerations it becomes clear that color confinement is intimately tied to the breaking/restoration of the Z_3 center symmetry, and that the expectation value of the traced Polyakov loop is the corresponding order parameter,

$$\begin{aligned} F_q \to \infty \quad &\to \quad \langle \ell(\boldsymbol{x}) \rangle = 0 \quad \to \quad \text{conserved center symmetry} \,, \\ F_q = \text{finite} \quad &\to \quad \langle \ell(\boldsymbol{x}) \rangle \neq 0 \quad \to \quad \text{broken center symmetry} \,. \end{aligned} \tag{6.25}$$

In the following, we will drop the brackets for brevity such that $\ell = \langle \ell(\boldsymbol{x}) \rangle$ and $\bar{\ell} = \langle \ell^\dagger(\boldsymbol{x}) \rangle$.

PNJL MODEL. Having identified the order parameter for the gluonic dynamics, we are ready to extend the NJL model by the Polyakov loop; this is known as the PNJL model. The corresponding Lagrangian density reads [356–358]

$$\mathcal{L}_{\text{PNJL}} = \mathcal{L}_{\text{NJL}} - V_{\text{glue}}(\ell, \bar{\ell}, T) \,, \tag{6.26}$$

where the partial derivative ∂_μ in $\mathcal{L}_{\text{NJL}}$ is replaced by the covariant one $D_\mu = \partial_\mu - iA_\mu$. The Polyakov loop potential V_{glue} [359, 360] cannot be computed from first principles.

Instead, it is parametrized and subsequently fitted to SU(3) lattice thermodynamics. While different parametrizations exist in the literature, we employ the logarithmic form [326, 361]

$$V_{\text{glue}}(\ell,\bar{\ell},T) = T^4\left[-\frac{1}{2}a(T)\ell\bar{\ell} + b(T)\ln\left(1-6\ell\bar{\ell}+4\left(\ell^3+\bar{\ell}^3\right)-3(\ell\bar{\ell})^2\right)\right]. \tag{6.27}$$

Here, the expectation value of the Polyakov loop is constrained to $\ell \in (0,1)$. Note that the choice of parametrization does not have a significant effect on our results. We have explicitly checked this by repeating the analysis with the polynomial parametrization found in refs. [326, 330, 358, 362]. The coefficients in eq. (6.27) read

$$a(T) = a_0 + a_1\left(\frac{T_{\text{glue}}}{T}\right) + a_2\left(\frac{T_{\text{glue}}}{T}\right)^2, \tag{6.28}$$

$$b(T) = b_3\left(\frac{T_{\text{glue}}}{T}\right)^3. \tag{6.29}$$

The confinement scale is indicated by $T_{\text{glue}} = 178$ MeV [363], i.e., the temperature of Z_3 center symmetry breaking [353] in the case of three massless flavors. The remaining parameters a_0, a_1, a_2, and b_3 are fitted against lattice data. The numerical values we employ are summarized in the lower panel of table 6.1.

Proceeding with the construction of the PNJL effective potential, we have

$$V_{\text{eff}}^{\text{PNJL}}(\sigma,T) = V_0^{\text{PNJL}}(\sigma) + V_1^{\text{PNJL}}(\sigma) + V_{\text{T}}^{\text{PNJL}}(\sigma,\ell,\bar{\ell},T) + V_{\text{glue}}(\ell,\bar{\ell},T), \tag{6.30}$$

where

$$V_0^{\text{PNJL}}(\sigma) = V_0^{\text{NJL}}(\sigma), \quad V_1^{\text{PNJL}}(\sigma) = V_1^{\text{NJL}}(\sigma), \tag{6.31}$$

remain unchanged compared to the NJL model (cf. eqs. (6.11) and (6.12)). Since the NLO medium interaction in eq. (6.16) is now affected by the presence of the Polyakov loop, we obtain a mixed term $V_{\text{T}}^{\text{PNJL}}(\sigma,\ell,\bar{\ell},T)$. To evaluate this term, we start be expressing the temporal gauge field via [326]

$$A_4 = \frac{2\pi}{g_s\beta}\text{diag}(q_0,q_1,q_2), \tag{6.32}$$

where we have employed Polyakov gauge and spatial homogeneity. Here q_0, q_1, q_2 have to satisfy $\sum_i q_i = 0$. Then, the Polyakov loop reads

$$\boldsymbol{L} = \text{diag}(z_0,z_1,z_2). \tag{6.33}$$

Λ [MeV]	$G\Lambda^2$	$G_{\mathrm{D}}\Lambda^5$
631.4	1.835	−9.29

a_0	a_1	a_2	b_3	T_{glue} [MeV]
3.51	−2.47	15.2	−1.75	178

Table 6.1: Upper panel: parameters used in the NJL model to reproduce the QCD meson spectrum [345]. Note that because of the different coupling conventions, we have rescaled G via $G = g_{\mathrm{S}}/2$, with g_{S} from [345]. Lower panel: parameters that enter the Polyakov loop potential [361].

By including the coupling to the gluons as an effective chemical potential in the grand canonical quark partition function, we obtain, at vanishing quark chemical potential μ [326],

$$\begin{aligned} V_{\mathrm{T}}^{\mathrm{PNJL}}(\sigma,\ell,\bar{\ell},T) &= -2N_{\mathrm{f}}T\int_{\boldsymbol{p}}\sum_{i=1}^{N_{\mathrm{c}}}\left[\ln\left(1+e^{-\beta E_p+2\pi i q_i}\right)+\ln\left(1+e^{-\beta E_p-2\pi i q_i}\right)\right] \\ &= -2N_{\mathrm{f}}T\int_{\boldsymbol{p}}\mathrm{Tr}_c\left[\ln\left(1+\boldsymbol{L}e^{-\beta E_p}\right)+\ln\left(1+\boldsymbol{L}^{\dagger}e^{-\beta E_p}\right)\right] \\ &= -2N_{\mathrm{f}}T\int_{\boldsymbol{p}}\Big[\ln\left(1+3\ell e^{-\beta E_p}+3\bar{\ell}e^{-2\beta E_p}+e^{-3\beta E_p}\right) \\ &\qquad +\ln\left(1+3\bar{\ell}e^{-\beta E_p}+3\ell e^{-2\beta E_p}+e^{-3\beta E_p}\right)\Big] \\ &= -g_q T\int_{\boldsymbol{p}}\left[\ln\left(1+3\ell e^{-\beta E_p}+3\ell e^{-2\beta E_p}+e^{-3\beta E_p}\right)\right]. \end{aligned} \tag{6.34}$$

Here $E_p = \sqrt{\boldsymbol{p}^2+M^2}$, where $M = M(\sigma)$ is given by eq. (6.13). In the first step, we have used eq. (6.19) and the property of the logarithm $\sum\ln(a_i) = \mathrm{Tr}\ln(\boldsymbol{A})$, where a_i are the eigenvalues of the matrix $\boldsymbol{A}$. In the second step, we have evaluated the color trace. Subsequently we have set $\ell = \bar{\ell}$ which holds at zero chemical potential [329, 364]. Eq. (6.34) can further be rewritten as [330]

$$V_{\mathrm{T}}^{\mathrm{PNJL}}(\sigma,\ell,\bar{\ell},T) = V_{\mathrm{T}}^{\mathrm{NJL}}(\sigma,T) - g_q T\int_{\boldsymbol{p}}\ln\left[1+(3\ell-1)e^{-E_p/T}+e^{-2E_p/T}\right]. \tag{6.35}$$

This concludes the construction of the effective potential in the PNJL model.

The left panel of fig. 6.2 displays the effective potential (6.30) around the critical temperature $T_{\mathrm{c}} \approx 159$ MeV. As for the pure NJL model, a barrier between the two vacua implies a first-order χPT.

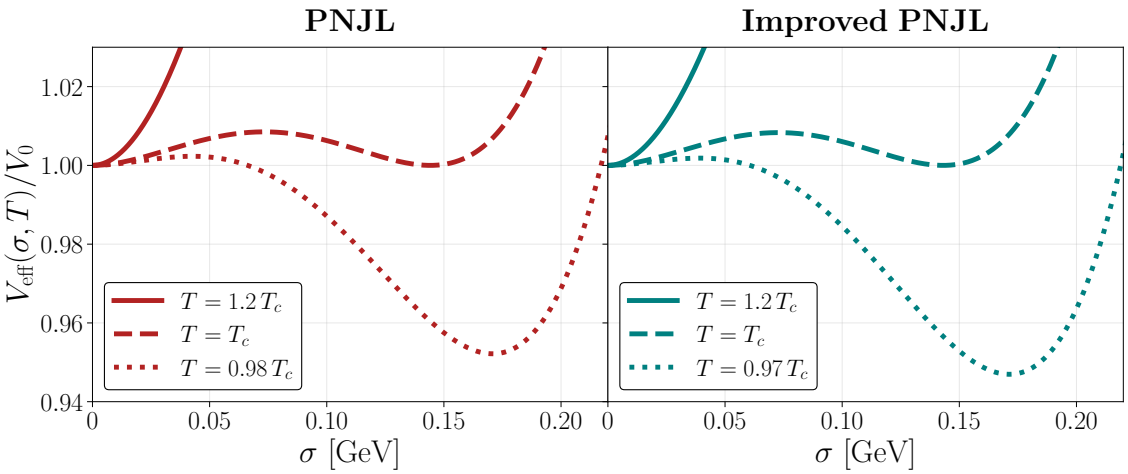

Figure 6.2: Effective potentials for the PNJL (left) and improved PNJL (right) models. Again, we normalize the potential energy to its value at the origin. As for the NJL model, we observe a thermal barrier separating the false and true vacua, indicating a FOPT. The respective critical temperatures read $T_c = 159\,\text{MeV}$ (left) and $T_c = 154\,\text{MeV}$ (right).

IMPROVED PNJL MODEL. The parameters in the Polyakov loop potential (6.27) in the PNJL model are fitted to pure Yang-Mills lattice data. Therefore the presence of quarks is not accounted for, which should, however, affect the thermodynamic properties of the gluon bath. Ref. [365] uses functional renormalization group techniques to show that an improved Polyakov loop potential, including quark backreaction, is obtained by a simple temperature rescaling. To this end, we first introduce the reduced temperatures

$$t_{\rm glue} = \frac{T - T_{\rm cr}^{\rm glue}}{T_{\rm cr}^{\rm glue}}\,, \quad t_{\rm YM} = \frac{T - T_{\rm cr}^{\rm YM}}{T_{\rm cr}^{\rm YM}}\,. \tag{6.36}$$

Here, $T_{\rm cr}^{\rm YM} = 270$ MeV [366] corresponds to the critical temperature in pure Yang-Mills. $T_{\rm cr}^{\rm glue}$ is the critical temperature of a QCD-like theory [363] with three massless flavors, which we have already employed in the Polyakov loop potential in eq. (6.27). With eq. (6.36), the $V_{\rm glue}$ is rewritten by replacing

$$\frac{T_{\rm glue}}{T} \to \frac{1}{1 + t_{\rm glue}}\,. \tag{6.37}$$

Further following ref. [365], one may construct an improved Polyakov loop potential by rescaling the given reduced glue temperature $t_{\rm glue}$

$$t_{\rm YM}(t_{\rm glue}) \approx 0.57\, t_{\rm glue}\,. \tag{6.38}$$

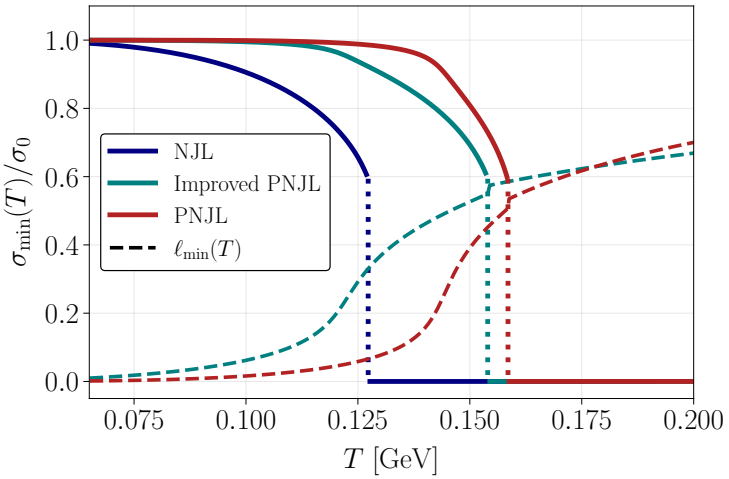

Figure 6.3: Evolution of the order parameters as a function of temperature. The solid lines indicate the dynamics of the chiral condensate σ, normalized to its value at the true minimum. For all effective QCD models, we observe a discontinuity in the evolution of the quark condensate (dotted lines), indicating a FOPT. The dashed lines denote the minima of the Polyakov loop potential $\ell_{\min}(T)$ in the PNJL models, which evolve smoothly with temperature.

Then,

$$\frac{V_{\text{glue}}(\ell, \bar{\ell}, t_{\text{glue}})}{T_{\text{glue}}^4} = \frac{V_{\text{YM}}(\ell, \bar{\ell}, t_{\text{YM}}(t_{\text{glue}}))}{T_{\text{YM}}^4} \,. \tag{6.39}$$

For completeness, the full effective potential in the improved PNJL approach reads

$$\begin{aligned} V_{\text{eff}}^{\text{PNJL}}(\sigma, T) = V_0^{\text{PNJL}}(\sigma) + V_1^{\text{PNJL}}(\sigma) \\ + V_{\text{T}}^{\text{PNJL}}(\sigma, \ell, \bar{\ell}, T) + \left(\frac{T_{\text{glue}}}{T_{\text{YM}}}\right)^4 V_{\text{glue}}(\ell, \bar{\ell}, t_{\text{YM}}(t_{\text{glue}})) \,. \end{aligned} \tag{6.40}$$

The potential is shown in the right panel of fig. 6.2. We again find a first-order χPT with $T_{\text{c}} \approx 154$ MeV.

6.3 SUPERCOOLED CHIRAL PHASE TRANSITION

We are now ready to study the QCD χPT in a supercooled Universe. To this end, let us first inspect the evolution of the respective order parameters, i.e., the chiral condensate $\sigma \sim \langle \bar{q}q \rangle$ and the Polyakov loop ℓ, as a function of temperature. This is shown in fig. 6.3, where different colors indicate different models. We first note that all three effective theories feature a discontinuity in the evolution of σ. Therefore, all models feature a FOPT, although the respective critical temperatures differ slightly. For the (improved)

PNJL model, we observe a smooth evolution of the Polyakov loop with temperature, approaching $\ell = 1$ in the deconfined phase $T > T_c$. Note that the slight discontinuity in the evolution of ℓ when σ develops a vev is caused by numerical artifacts of the minimization algorithm. Below the critical temperature, ℓ quickly relaxes to zero, indicating quark confinement.

HUBBLE PARAMETER. Since we assume the Universe undergoes a period of thermal inflation driven by the false vacuum energy of the CSI SM, the Hubble parameter at the QCD scale reads

$$H(T_{\mathrm{QCD}}) = \left(\frac{\rho_{\mathrm{vac}} + \rho_{\mathrm{rad}}(T_{\mathrm{QCD}})}{3M_{\mathrm{Pl}}^2}\right)^{\frac{1}{2}} \simeq \left(\frac{\pi^2}{90} g_{\star,\epsilon}(T_i) \frac{T_i^4}{M_{\mathrm{Pl}}^2}\right)^{\frac{1}{2}} \simeq H(T_i)\,. \tag{6.41}$$

Here, ρ_{vac} denotes the false vacuum energy, while ρ_{rad} is the contribution of the thermal bath to the total energy density. Let us stress again that we characterize the new physics merely by the temperature where thermal inflation starts, T_i (cf. eq. (5.34)). Below, we will derive a lower bound on this scale by demanding that the transition is strong enough to overcome the pressure exerted by the electroweak gauge bosons becoming massive. This restricts $T_i \gg T_{\mathrm{QCD}}$, hence the Hubble parameter becomes approximately constant. In our numerical analysis, however, we employ the full, temperature-dependent expression of the expansion rate. Without knowledge of the BSM field content, we assume $g_{\star,\epsilon}(T_i) = 106.75$, corresponding to the SM relativistic degrees of freedom, noting that the actual value is slightly larger. This has, however, negligible impact on our results. Let us stress once again that we assume scenario II (a) from sec. 5.3, where the cosmic QCD transition realizes the exit from supercooling.

SOLVING THE BOUNCE ACTION. To evaluate the decay rate of the false vacuum (cf. (3.44)), we start by computing the bounce action [182, 329]

$$S_3[\sigma] = 4\pi \int \mathrm{d}r\, r^2 \left[\frac{Z_\sigma^{-1}}{2}\left(\frac{\mathrm{d}\sigma}{\mathrm{d}r}\right)^2 + V_{\mathrm{eff}}(\sigma, T)\right], \tag{6.42}$$

related to the nucleation of hadronic bubbles which initiate the exit from supercooling. This expression is evaluated for the field configuration that solves the associated bounce equation of motion,

$$\frac{\mathrm{d}^2\sigma}{\mathrm{d}r^2} + \frac{2}{r}\frac{\mathrm{d}\sigma}{\mathrm{d}r} - \frac{1}{2}\frac{\mathrm{d}\log Z_\sigma}{\mathrm{d}\sigma}\left(\frac{\mathrm{d}\sigma}{\mathrm{d}r}\right)^2 = Z_\sigma \frac{\mathrm{d}V_{\mathrm{eff}}(\sigma, T)}{\mathrm{d}\sigma}\,. \tag{6.43}$$

Here, V_{eff} corresponds to the effective potential in the (improved) (P)NJL model which we constructed in the last section. In the case of the Polyakov loop extended models, we min-

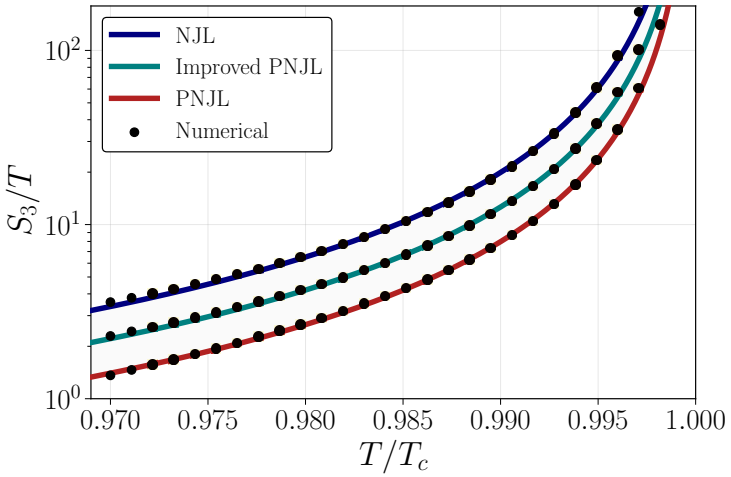

Figure 6.4: Three-dimensional bounce action divided by the temperature, S_3/T, as a function of temperature divided by the critical temperature, T/T_c. The black dots indicate the numerical solution of the bounce, while the colored curves correspond to the fits obtained with the parametrization (6.44). We observe that the bounce action decreases quickly below T_c for all low-energy theories. The Polyakov-loop extended models yield smaller values of S_3/T compared to the NJL model, implying a larger bubble nucleation rate.

imize the ℓ-direction of the potential for a given (σ, T). Then, $V_{\text{eff}}(\sigma, T) = V_{\text{eff}}(\sigma, \ell_{\text{min}}, T)$ only depends on the chiral condensate. Note that compared to (3.46), eq. (6.42) contains a wave function renormalization factor $Z_\sigma^{-1} = Z_\sigma^{-1}(\sigma, \ell, T)$. This quantity arises since the fundamental degrees of freedom in the NJL model are fermionic, hence the kinetic term for the bosonic condensate σ is generated at the loop level. The computation is analogous to ref. [330], and can be found in appendix 6.A for completeness. We then solve eq. (6.43) employing `CosmoTransitions` [185], modified appropriately to include the wave function renormalization.

Our results are shown in fig. 6.4. We display the value of the bounce action S_3/T as a function of T, normalized to the respective critical temperatures. The black dots correspond to the numerical solution. To facilitate further computations, we follow ref. [329] and parametrize the temperature dependence of the bounce action as

$$\frac{S_3(T)}{T} \simeq b \left(1 - \frac{T}{T_c}\right)^{-\gamma} . \tag{6.44}$$

We then fit the free parameters b and γ; see table 6.2 for the best-fit values. The parametrizations are indicated by the colored curves in fig. 6.4. For all models, we observe that the bounce action quickly decreases with temperature, which implies that the PT dynamics

	NJL	**PNJL**	**Improved PNJL**
b	0.0118	0.0054	0.0085
γ	1.614	1.583	1.585

Table 6.2: Best-fit value for the parametrization (6.44) of the bounce action, for the different low-energy models of QCD.

takes place close to T_c. This is expected, as strongly-coupled theories typically do not feature large amounts of supercooling [208, 329, 330, 367]. In addition we observe that S_3/T takes smaller values in the Polyakov loop extended models, indicating a larger bubble nucleation rate, i.e., a faster transition compared to the NJL model.

COMPLETING THE TRANSITION. Next, we compute the temperature scales which determine the onset and completion of the χPT, i.e., the nucleation (T_n) and percolation temperature (T_p). To this end, we follow the prescription outlined in sec. 3.2. The time when bubble nucleation becomes efficient is estimated by

$$\Gamma(T_n) = H(T_n)^4 \,, \tag{6.45}$$

where $\Gamma(T_n)$ is given by eq. (3.44). Percolation is assumed to terminate once the probability to find a space point in the false vacuum is $P = \exp(-I(T_p)) \approx 0.7$, where $I(T)$ is computed via eq. (3.50). Note that this calculation requires knowledge of the bubble wall velocity v_w. Since we study the scenario where the conformal PT is triggered by χSB, i.e., a large amount of vacuum energy is released, we employ $v_w = 1$. Lastly, we ensure that percolation is indeed efficient by checking that the space volume trapped in the false vacuum indeed decreases (cf. eq. (3.51)). This criterion will be useful when computing an upper bound on the scale of new physics.

Let us first discuss the evolution of $I(T)$, quantifying the exponential suppression of the false vacuum, displayed in fig. 6.5 as a function of T/T_c. Different panels (colors) correspond to different effective QCD models, while different linestyles imply a variation of T_i. Here the dash-dotted line is obtained by imposing no supercooling prior to the QCD scale. While this is not possible within our setup,[1] we include this scenario in order to compare our results to previous studies of dark confinement and chiral PTs [329, 330, 367]. The nucleation and percolation temperatures are marked by triangles and circles, respectively; the latter is defined by $I(T_p) = 0.34$ (gray line). For all three models, we observe that

1 For the quarks to remain massless, EWSB has to be delayed, e.g., a period of thermal inflation starting between the QCD end electroweak scale, at the latest, is unavoidable.

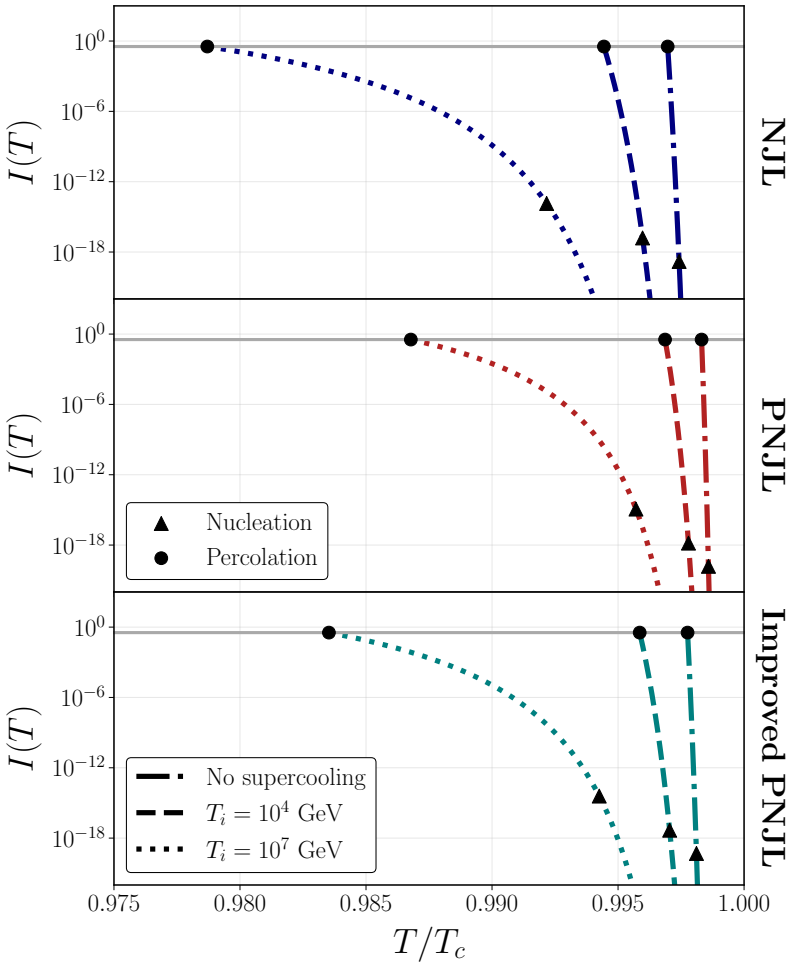

Figure 6.5: Suppression of the probability for a point to remain in the false vacuum (3.50) as a function of temperature relative to T_c. Different panels correspond to the various models of QCD, while different linestyles indicate a variation of the new physics scale T_i. Dots denote successful percolation, while the triangles mark the nucleation temperature. A finite period of thermal inflation decreases both T_n and T_p compared to the case of no supercooling-(dash-dotted), implying an enhancement of the transition timescale. As anticipated from the evolution of the bounce action (cf. fig. 6.4), the Polyakov-loop extended models predict the χPT to terminate faster compared to the NJL model.

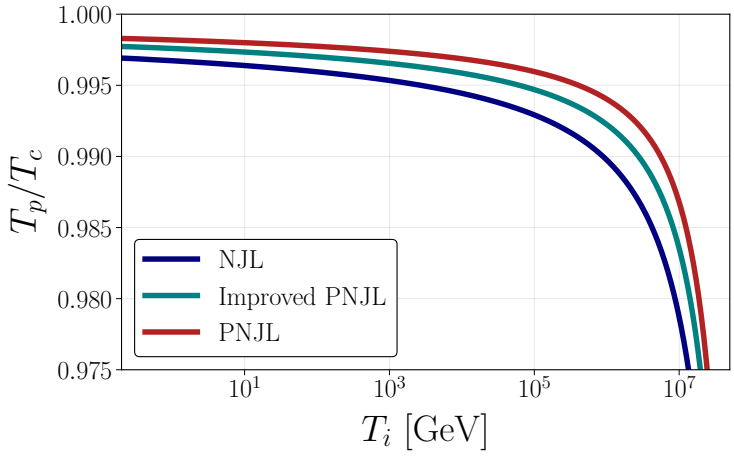

Figure 6.6: Evolution of the percolation temperature relative to the critical temperature as a function of the temperature where thermal inflation starts. Different colors indicate different low-energy models. While for small T_i percolation takes place close to T_c, the temperature ratio is significantly suppressed when increasing the length of supercooling prior to the QCD scale.

percolation occurs close to the critical temperature. Again, this indicates a fast transition, which is typical for strongly-coupled PTs. Intriguingly, once we switch on thermal inflation, as shown for $T_i \in \{10^4\,\text{GeV}, 10^7\,\text{GeV}\}$, both T_n and T_p are shifted to smaller values. This behavior is attributed to the expansion rate in the supercooled Universe. Since larger T_i indicates a larger Hubble parameter during χSB, a larger bubble nucleation rate, hence smaller S_3/T (cf. eq. (3.44)), is required for nucleation and eventually percolation to be efficient. From these considerations, it is straightforward to see why the completion of the χPT is delayed.

Fig. 6.6 shows the percolation temperature T_p normalized to the critical temperature T_c as a function of T_i, where different colors again indicate the respective QCD model. This temperature ratio provides information on the amount of supercooling involved in the χPT, in a Universe dominated by a CSI SM. While $T_\text{p}/T_\text{c} \lesssim 1$ for a late onset of thermal inflation, the percolation temperature is significantly decreased when shifting the new physics scale towards the UV. Comparing different models, we find that the NJL model features smaller T_p than the Polyakov loop extended versions, as we have already suspected in the discussion around fig. 6.4.

6.4 GRAVITATIONAL WAVE BACKGROUND

Next, we compute the characteristic PT parameters that enter the calculation of the GW spectrum; see sec. 3.2 for an overview. In addition to imposing (model-independent) constraints on the new physics scale T_i, this allows us to evaluate the observational prospects of QCD-sourced conformal symmetry breaking at future GW observatories.

TRANSITION STRENGTH AND BUBBLE WALL VELOCITY. We study the scenario in which the χPT triggers the exit from supercooling. Therefore, the false vacuum energy driving thermal inflation is released. The transition strength then reads

$$\alpha = \frac{\rho_{\text{vac}}}{\rho_{\text{rad}}(T_{\text{p}})} \approx \left(\frac{T_i}{T_{\text{p}}}\right)^4 \gg 1\,, \tag{6.46}$$

due to the temperature hierarchy $T_i \gg T_{\text{QCD}} \approx T_{\text{p}}$. As a consequence of the large transition strength in the entire parameter space, we assume $v_{\text{w}} = 1$ for the bubble wall velocity.

INVERSE TIMESCALE. While the transition strength is dictated by the new physics scale T_i, the transition timescale is determined by QCD. This comes from the fact that the false vacuum energy of the conformal sector can only be released in the patches of space where the chiral symmetry is broken. Hence, the overall timescale depends crucially on the nucleation rate of hadronic bubbles. To this end, we compute the characteristic length scale of the transition (3.55) [13, 210], which we translate to the inverse timescale via $\beta_\star = 5/R_\star$ [211].[2]

Our numerical results are shown in fig. 6.7. Here, the left panel displays the inverse transition timescale relative to the expansion rate of the Universe, $\beta_\star/H$, as a function of the temperature where thermal inflation starts T_i. For small T_i, i.e., a short period of supercooling, we find large transition timescales $\beta_\star/H = \mathcal{O}(10^5)$.[3] This is in agreement with previous studies of dark χPTs in strongly coupled hidden sectors [329, 330] and holographic studies of Yang-Mills confinement PTs [367, 368]. When increasing the scale of new physics, however, the inverse timescale decreases considerably. This comes from the fact that larger T_i corresponds to a larger Hubble parameter during χSB. Then, for bubble percolation to be efficient compared to the expansion rate of the Universe, lower temperatures, hence a larger overall transition timescale, are required. This can be seen

2 Note that the definition of $R_\star$ in ref. [1] contains a typographical error regarding the temperature scaling.
3 The exclusion region for small $T_i \lesssim 1\,\text{GeV}$ is based on the fact that the false vacuum energy is not sufficient to withstand the pressure exerted by the SM gauge bosons; see the discussion below.

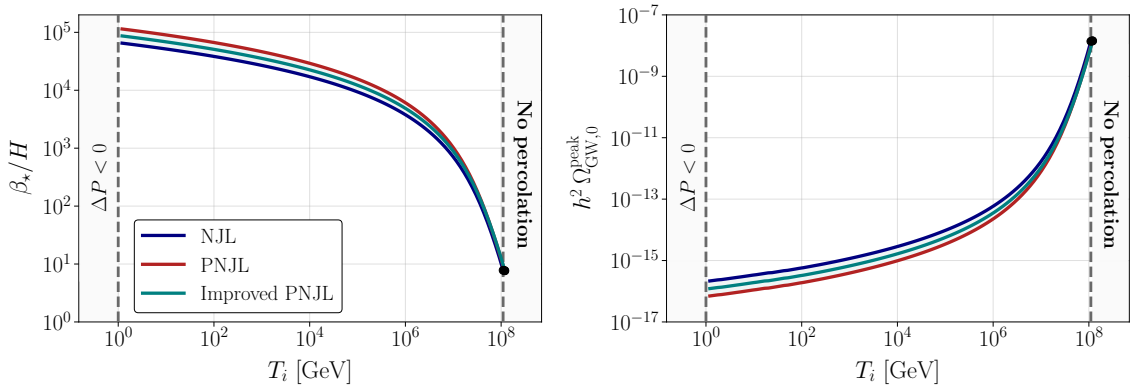

Figure 6.7: Left: Inverse transition timescale divided by the Hubble parameter as a function of the new physics scale. For a small amount of supercooling, the transition proceeds very fast. When increasing T_i, hence the duration of thermal inflation, the timescale is enhanced considerably, yielding $\beta_\star/H = \mathcal{O}(10)$ in the most extreme case. The left and right exclusion regions denote the cases where the true vacuum bubbles cannot withstand the pressure from the thermal bath (cf. eq. (6.53)), and where percolation is unsuccessful as a consequence of the large expansion rate of the Universe (cf. eq. (3.51)). Right: Associated GW amplitude, redshifted to today. While a small T_i predicts GW production to be strongly suppressed, the amplitude of the spectrum is enhanced by eight orders of magnitude for $T_i = \mathcal{O}(10^8\,\mathrm{GeV})$. This is a consequence of the enhanced transition timescale.

explicitly by considering the definition of the timescale via the bounce action (cf. eq. (3.54)). With the parametrization (6.44), we have

$$\frac{\beta_\star}{H} \simeq \gamma \left(\frac{T_\mathrm{c}}{T_\mathrm{p}} - 1 \right)^{-1} \frac{S_3(T)}{T} \,. \tag{6.47}$$

This reveals the direct impact of the decreased percolation temperature on the inverse transition timescale. Note, however, that $\beta_\star/H$ cannot be arbitrarily small. If the expansion rate becomes too large, for $T_i \gtrsim 10^8\,\mathrm{GeV}$, the condition for successful percolation (3.51) is not fulfilled anymore. Then, the Universe cannot be converted to the hadronic vacuum via bubble percolation.[4] Hence, we find a lower bound of $\beta_\star/H = \mathcal{O}(5-10)$, corresponding to $N_\mathrm{max} \simeq 20$ e-folds of thermal inflation. Let us also note that all effective QCD models show an excellent agreement for large T_i, while the low-T_i region reveals a $\mathcal{O}(1)$ deviation between the NJL and improved PNJL model.

4 In this parameter space, other mechanisms such as the growth of quantum fluctuations during thermal inflation [369] or tachyonic rolling of the BSM scalar field (see chapter 7) may eventually trigger the exit from supercooling.

GRAVITATIONAL WAVE SOURCES. Considerations of the friction exerted by the surrounding thermal bath on the bubble walls allows for a determination of the dominant GW source, i.e., the spectral shape [191, 192, 215, 216, 370, 371]. It was shown in ref. [211], however, that in the case of strongly supercooled transitions, the sound wave-induced GW contribution takes the same functional form as the spectrum from bubble collisions, implying $\Omega_{\rm GW} \propto (H/\beta_\star)^2$, independent of the dominant source. Nevertheless, we will in the following consider different sources of friction, since this will provide limits on the new physics scale T_i. In particular, we derive a model-independent lower bound for the transition to complete.

To this end, let us first introduce the pressure difference across the bubble wall,

$$\Delta P = \Delta V_{\rm eff} - P_{1\to 1} - P_{1\to N}\,. \tag{6.48}$$

Here, $\Delta V_{\rm eff}$ is the false vacuum energy, which is counteracted by various pressure contributions from the surrounding plasma. The LO term corresponds to all particles that become massive during the transition [372],

$$P_{1\to 1} \simeq \sum_i \frac{c_i k_i}{24} M_i^2 T_{\rm p}^2\,. \tag{6.49}$$

Here M_i is the physical mass of a species i, k_i denotes the massive degrees of freedom and $c_i = 1$ $(1/2)$ for bosons (fermions). The sum runs over all particles in the CSI SM, including the electroweak gauge bosons. The NLO term is generated by transition radiation at the bubble wall [373]

$$P_{1\to N} \simeq \gamma \sum_i g_i M_i T_{\rm p}^3\,, \tag{6.50}$$

where the sum runs over all gauge bosons i with coupling strength g_i. The strategy is to calculate a threshold on the Lorentz factor, $\gamma_{\rm eq}$, where the pressure contributions exactly cancel the false vacuum energy [223]. Then, a comparison with the actual Lorentz factor, $\gamma_\star$, determines whether the bubble walls reach a steady state with the radiation bath. Such a computation requires knowledge about the field content of the theory. Since we aim for a model-independent analysis by leaving T_i as an input parameter, we cannot reliably compute the Lorentz factor. Nevertheless, we can discuss certain relevant regimes, and derive a model-independent lower bound on T_i.

Let us first consider the scenario of extreme supercooling, $T_i \gg T_{\rm EW,SM} \gg T_{\rm QCD}$. Then, the false vacuum energy is dominated by new physics, and

$$\Delta V_{\rm eff} \sim M^4 \sim T_i^4 \gg T_{\rm p}^4\,. \tag{6.51}$$

The mass scale M then corresponds to the mass of the gauge boson of the CSI gauge group. This is a direct consequence of radiative symmetry breaking. Because of this large scale hierarchy, we can conclude that the friction terms are strongly suppressed with respect to the false vacuum energy. The result is a transition driven by bubble collisons. A confirmation of this estimate is found in ref. [244] for the $\mathrm{U}(1)_{\text{B-L}}$ extended SM, and in refs. [246, 247] for the $\mathrm{SU}(2)_X$ extension.

For $T_{\text{EW,SM}} > T_i > T_{\text{QCD}}$, on the other hand, there are no new mass scales above the electroweak scale. Therefore the dominant contribution to the bubble wall friction is exerted by the SM fields, in particular the top quark and the electroweak gauge bosons. We can therefore compute a lower bound on T_i by requiring that the vacuum energy overcomes the LO pressure,

$$\Delta V_{\text{eff}} = \frac{\pi^2}{30} g_{\star,\epsilon} T_i^4 = P_{1\to 1}\,. \tag{6.52}$$

With $M_i \in \{m_W, m_Z, m_t\}$, we obtain

$$T_{i,\text{min}} \approx 1 \text{ GeV}\,. \tag{6.53}$$

If thermal inflation was to start below $T_{i,\text{min}}$, the net pressure would be negative, preventing the true vacuum from expanding. The lower bound on T_i is indicated in fig. 6.7 by the $\Delta P < 0$ exclusion region.

REHEATING. Let us now briefly discuss the reheating process after bubble percolation. After supercooled PTs, a finite MD period, where the BSM scalar field oscillates around the true minimum, may dilute the GW spectrum (see sec. 3.2). In our model-independent setup, we cannot precisely compute the length of the MD phase due to a lack of knowledge of the coupling strengths. Therefore, we will assume for simplicity that reheating is instantaneous, such that the entire vacuum energy driving the transition is injected into the thermal bath. Then,

$$T_{\text{rh}} \approx T_i\,, \tag{6.54}$$

and the redshift factors take their standard form (cf. eqs. (3.12) and (3.13)). However, we keep in mind that once we map our results to a specific CSI SM extension, a finite MD period may weaken the GW background.

OBSERVATIONAL PROSPECTS Fig. 6.7 shows the GW peak amplitude computed via eq. (3.56) as a function of the new physics scale T_i. While $h^2\Omega_{\text{GW},0}^{\text{peak}} = \mathcal{O}(10^{-16})$ for the lower limit on T_i, we find an increase by eight orders of magnitude when imposing the maximum amount of supercooling. This is one of the main results of this study. A

supercooling period prior to the QCD PT induces a substantial amplification of the GW amplitude, as a consequence of the significantly increased transition timescale.

This behavior notably improves the observational prospects, as shown in fig. 6.8. Here, the three panels correspond to the different low-energy theories of QCD. We display three benchmark spectra, respectively, corresponding to different choices of T_i. The black curve shows the evolution of the GW peak as a function of T_i, with the black dot denoting the upper limit obtained by requiring successful percolation. In addition, we display the projected PLI sensitivity curves of the future GW observatories μARES [149], BBO [148], LISA [35–37], and ET [38, 39]. These are computed following ref. [152], and provide a simple way to predict whether a certain GW signal is detectable.

Let us first note that all QCD models yield consistent results. This is expected, since the largest deviation of the transition timescale is of $\mathcal{O}(1)$, leading to a relative deviation of the GW peak amplitude of $\mathcal{O}(5-10)$ for small $T_i \sim \mathcal{O}(\text{GeV})$. In this regime, the GW background from the supercooled χPT is barely visible; merely the NJL model predicts a slight overlap with the sensitivity region of μARES. This confirms the pessimistic observational prospects of strongly coupled PTs (e.g., [329, 330]). Increasing the length of the supercooling phase, we observe an increase of both the peak frequency and amplitude, reaching the sensitivity region of BBO. While the enhanced amplitude is ascribed to the increased transition timescale, the frequency shift can be understood from

$$f_\star \propto \frac{\beta_\star}{H(T_i)} H(T_i) \propto \frac{\beta_\star}{H(T_i)} T_i^2 \,. \tag{6.55}$$

Taking into account the redshift until today, we find

$$f_0 \propto \frac{\beta_\star}{H(T_i)} T_i \,. \tag{6.56}$$

Hence, the peak frequency is determined by the relation of the transition timescale and the temperature where thermal inflation starts. This is exactly the reason why f_0 eventually decreases again. For $T_i \gtrsim 5 \times 10^6\,\text{GeV}$, the decline of $\beta_\star/H$ is faster than the increase of T_i (cf. fig. 6.7), shifting the GW spectrum deep into the ET window. This is demonstrated by the third benchmark spectrum, where $T_i = 5 \times 10^7\,\text{GeV}$, which is slightly below the maximum value $T_i \simeq 10^8\,\text{GeV}$. Due to the sharp decline of the spectrum $\Omega_{\text{GW}} \propto f^3$ on superhorizon scales, we do not find any observational prospects for LISA.

6.5 CONCLUSION

Let us conclude the first part of this thesis by summarizing our main findings, certain shortcomings, and possible next steps.

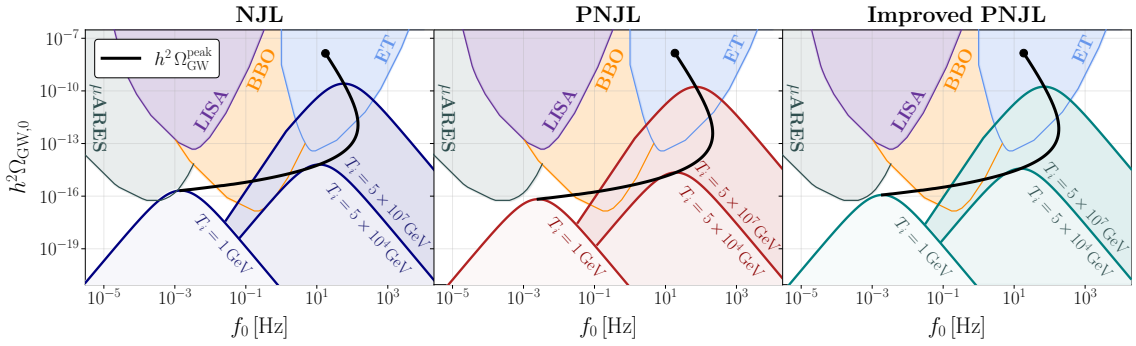

Figure 6.8: Projected GW spectra from the cosmic QCD PT triggering the exit from supercooling in CSI SM extensions. Different panels correspond to different low-energy models of QCD. We display three benchmark spectra, respectively, varying the scale of new physics T_i. The black curve shows the evolution of the GW peak, which ends at the black dot, where the percolation criterion (cf. eq. (3.51)) is violated. The increased transition timescale shifts the GW peak into the sensitivity regions of BBO and ET.

Based on the modified thermal history in CSI SM extensions, where EWSB can be triggered by χSB, we have employed three low-energy descriptions of QCD to analyze the cosmic QCD transition in a supercooled Universe. By parametrizing the new physics merely by the temperature where thermal inflation starts, our setup is independent of particle content of the extended SM. Therefore, our results can by mapped to any concrete theory, such as the CSI $\mathrm{U}(1)_{\text{B-L}}$ [46, 243, 244, 276] or $\mathrm{SU}(2)_X$ [183, 246, 247, 279] model, by identifying the parameter space where QCD initiates the exit from supercooling, and relating the characteristic mass scale to T_i.

The main quantity describing the strength of the transition is the inverse timescale $\beta_\star/H$, as slow transitions generate larger anisotropies, hence an enhanced SGWB. We have found that the thermal inflation period, induced by the delayed conformal-electroweak PT, strongly affects the observational prospects. For a small amount of supercooling, the GW amplitude is strongly suppressed, consistent with previous studies of massless QCD-like theories [329, 330] and confinement transitions in pure Yang-Mills systems [367]. Increasing the scale of new physics and thus the expansion rate of the Universe during the QCD transition requires larger bubble nucleation rates, necessarily suppressing the percolation temperature. Therefore, the overall transition timescale and thus the GW amplitude are enhanced, while the peak frequency shifts to the UV. As a consequence, we find the best detection prospects at the future observatories BBO and ET.

While our results are promising and the different QCD models show an excellent agreement between each other, we should note that our study naturally carries some uncertain-

ties. First, we assume χSB to take place initially in the light quark sector [283], hence we only incorporate three flavors instead of the full $\mathrm{SU}(6)_\mathrm{L} \times \mathrm{SU}(6)_\mathrm{R}$ chiral symmetry. Moreover, we neglect the effect of the Higgs field on the transition, which acquires a QCD-scale vev along χSB. This however introduces certain complications. When constructing the thermal effective potential for the Higgs field, the non-zero Matsubara modes, i.e., all SM quarks are integrated out (cf. sec. 3.2 and part iv). At the same time, quarks are the dynamical degrees of freedom during the breaking of the chiral symmetry. Hence it is not straightforward to construct an effective model incorporating both the electroweak and QCD sector, without encountering double counting of fermionic degrees of freedom. To obtain more precise results, a first-principle study of the outlined mechanism would be desirable. Recent lattice studies [290] indicate that QCD does not exhibit a FOPT, even for a large number of flavors and in the chiral limit. While the combined QCD + Higgs system may allow for a first-order transition, a lattice simulation of such a system in the massless limit is extremely challenging.

Lastly, let us mention the implications of our results on new physics searches. As already mentioned, our findings apply in large parameter spaces of CSI SM extensions [46, 242–244, 246, 247, 276, 279, 282]. Furthermore, we provide a mechanism to enhance the SGWB from strongly-coupled PTs, which typically predict extremely weak signals. Therefore, imposing similar dynamics in dark QCD-like [329, 330] or pure Yang Mills sectors [367] may open up new parameter regions testable by GWs. Additionally, our mechanism may have applications in grand unified theories (GUTs), such as Pati-Salam models [374], which feature symmetry breaking chains involving non-Abelian gauge groups.

APPENDIX OF CHAPTER 6

6.A WAVE FUNCTION RENORMALIZATION

For completeness, we outline the computation of the wave function renormalization (WFR) which enters the bounce action (6.42), for the NJL model. To this end, we largely follow ref. [330], which provides the corresponding calculation for Polyakov loop extended models.

In NJL-type, quark-based low energy effective theories of QCD, the chiral condensate σ is not a fundamental degree of freedom. Therefore, its kinetic term is generated at the loop level, necessitating the WFR Z_σ^{-1}. The strategy is to compute radiative corrections to the two-point function of σ up to one-loop order. To this end, we identify Feynman rules from the NJL Lagrangian in the MFA (6.7) and construct the relevant Feynman diagrams affecting the propagator,

$\Gamma_{\sigma\sigma}(q^0, \boldsymbol{q}, \sigma) \supset$ 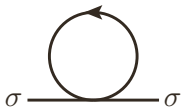 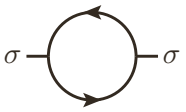 . (6.57)

Here, solid lines denote σ fields, while the fields running in the loop correspond to quarks. Then, the two-point function, including the mass term, reads

$$\Gamma_{\sigma\sigma}(q^0, \boldsymbol{q}, \sigma) = -\frac{3}{4G} + \frac{3G_{\mathrm{D}}}{8G^3}\sigma + \frac{G_{\mathrm{D}}}{4G^2} N_{\mathrm{f}} N_{\mathrm{c}} I_{\mathrm{V}}(\sigma) - \left(1 - \frac{G_{\mathrm{D}}\sigma}{4G^2}\right)^2 N_{\mathrm{f}} N_{\mathrm{c}} I_{\mathrm{S}}(q^0, \boldsymbol{q}, \sigma)\,, \quad (6.58)$$

up to one loop order. In the above expression, $N_{\mathrm{f}} = N_{\mathrm{c}} = 3$. $I_{\mathrm{V}}(\sigma)$ and $I_{\mathrm{S}}(q^0, \boldsymbol{q}, \sigma)$ are the one-loop integrals in eq. (6.57). Since we consider a thermal system, $q^0 = i\omega_n^{\mathrm{B}}$, with $\omega_n^{\mathrm{B}} = 2n\pi T$, $n \in \mathbb{Z}$, correspond to the bosonic Matsubara frequencies (cf. sec. 3.2). Proceeding with the computation, the WFR then reads

$$Z_\sigma^{-1} = -\frac{\mathrm{d}\Gamma_{\sigma\sigma}(q^0, \boldsymbol{q}, \sigma)}{\mathrm{d}\boldsymbol{q}^2}\bigg|_{q^0=0,\, \boldsymbol{q}=0}\,, \quad (6.59)$$

hence it is sufficient to merely consider the last term $\propto I_{\mathrm{S}}(q^0, \boldsymbol{q}, \sigma)$ in eq. (6.58). This is the only momentum-dependent contribution, given by

$$I_{\mathrm{S}}(i\omega_n^{\mathrm{B}}, \boldsymbol{q}, \sigma) = \frac{1}{N_{\mathrm{c}}} \mathrm{Tr}_{\mathrm{c}} \sum\!\!\!\!\!\!\int_{\{P\}}^{\Lambda} \frac{\mathrm{Tr}\,[(\not{p} + M)(\not{p} + \not{q} + M)]}{\left[p^2 - M^2\right]\left[(p+q)^2 - M^2\right]}\,. \quad (6.60)$$

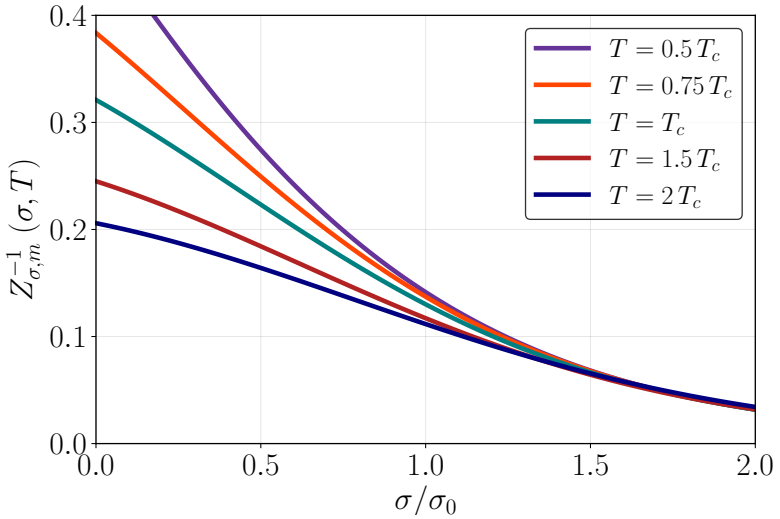

Figure 6.9: Modified WFR (6.66) as a function of the chiral condensate, plotted for different temperatures around T_c.

Here the curly brackets specify the fermionic nature of the sum-integral, $\oint\!\!\!\!\!\!\sum_{\{P\}} = T\sum_{\omega_n^{\mathrm{F}}}\int_{\boldsymbol{p}}$, where $P = (p^0, \boldsymbol{p})$, $p^0 = i\omega_n^{\mathrm{F}}$, and $\omega_n^{\mathrm{F}} = (2n+1)\pi T$ denote fermionic Matsubara frequencies. M is the effective quark mass (cf. eq. (6.13)) and Λ denotes the three-dimensional cutoff introduced to regularize the divergences in eq. (6.12). As further shown in ref. [330], one can decompose

$$Z_\sigma^{-1} = -\left(1 - \frac{G_{\mathrm{D}}\sigma}{4G^2}\right)^2 2N_{\mathrm{f}}N_{\mathrm{c}}\left[I(0) + 4M^2 I'(0)\right], \tag{6.61}$$

with

$$I(i\omega_n^{\mathrm{B}}, \boldsymbol{q}, \sigma) = \frac{1}{N_{\mathrm{c}}}\mathrm{Tr}_{\mathrm{c}}\oint\!\!\!\!\!\!\sum_{\{P\}}^{\Lambda}\frac{1}{\left[p^2 - M^2\right]\left[(p+q)^2 - M^2\right]}, \tag{6.62}$$

$$I(0) = I(i\omega_n^{\mathrm{B}} = 0, \mathbf{q} = 0, \sigma), \quad I'(0) = \left.\frac{\mathrm{d}I}{\mathrm{d}\mathbf{q}^2}\right|_{\omega_n = 0,\, \boldsymbol{q}=0}.$$

To evaluate the integral $I(i\omega_n^{\mathrm{B}}, \mathbf{q}, \sigma)$, the Matsubara sum is rewritten into a twofold sum with a Kronecker delta function $\delta(p_0) = T\int_0^\beta \mathrm{d}\tau \exp(ip_0\tau)$; see, e.g., refs. [167, 375, 376]. This gives

$$T\sum_{\omega_n^{\mathrm{F}}}\frac{e^{i(\omega_n^{\mathrm{F}} - i\mu)\tau}}{(\omega_n^{\mathrm{F}} - i\mu)^2 + E^2} = \frac{1}{2E}\left[f(E+\mu)e^{(\beta-\tau)E+\beta\mu} - f(E-\mu)e^{\tau E}\right]. \tag{6.63}$$

Λ [MeV]	$G\Lambda^2$	$G_{\mathrm{D}}\Lambda^5$
930	3.32	−63.06

	NJL	**PNJL**	**Improved PNJL**
b	0.223	0.008	0.028
γ	1.609	1.735	1.739
T_{c} [MeV]	71.71	121.77	101.10

Table 6.3: Upper panel: NJL parameters employed in the 4D cutoff scheme to reproduce the QCD hadron spectrum [239, 329]. Note that ref. [1] contains typographical errors in the upper panel of table III. Lower panel: best-fit parameters of the bounce action computed with the 4D cutoff scheme, obtained with the parametrization (6.44). In addition, we give the critical temperatures T_{c} for the respective low-energy models.

In the NJL model, we set the chemical potential to zero, $\mu = 0$, such that the Fermi-Dirac distribution reads

$$f(E) = \frac{1}{e^{\beta E} + 1}\,, \tag{6.64}$$

with $\beta = 1/T$. Note, however, that in the presence of gluonic degrees of freedom, eq. (6.64) obtains a ℓ-dependent contribution [330, 347], since the Polyakov loop acts as an effective chemical potential. The remaining piece is the τ-integral over the delta functions. This can be evaluated directly, yielding

$$I(0,\mathbf{q},\sigma) = \int_{\boldsymbol{p}}^{\Lambda} \frac{1}{2E_pE_{p+q}}\left[\frac{f(E_p)-f(E_{p+q})}{E_p-E_{p+q}} + \frac{1-f(E_p)-f(E_{p+q})}{E_p+E_{p+q}}\right]. \tag{6.65}$$

This expression is now inserted into eq. (6.61), which gives the WFR for the NJL model. Due to the breaking of Lorentz invariance in the 3D cutoff scheme, however, the final result is negative for a wide range of field values, as pointed out already in ref. [330] for the PNJL model. Therefore we follow the proposed solution from [330] and employ a modified WFR,

$$\begin{aligned} Z^{-1}_{\sigma,m}(\sigma,T) = \left(1-\frac{G_{\mathrm{D}}\sigma}{4G^2}\right)^2 \frac{N_{\mathrm{c}}N_{\mathrm{f}}}{4\pi^2}\Bigg(&\int_0^{\Lambda} \mathrm{d}p \frac{p^2}{E_p^3}\left[-2f(E_p) + 2E_p\frac{\mathrm{d}f(E_p)}{\mathrm{d}E_p} + 1\right] \\ &+M(\sigma)^2\int_0^{\Lambda}\mathrm{d}p\frac{p^2}{E_p^5}\left[6f(E_p) - 2E_p\frac{\mathrm{d}f(E_p)}{\mathrm{d}E_p} - 1\right]\Bigg)\,. \end{aligned} \tag{6.66}$$

Fig. 6.9 shows the modified WFR as a function of the chiral condensate and temperature. For the PNJL models, we employ the WFR from ref. [330].

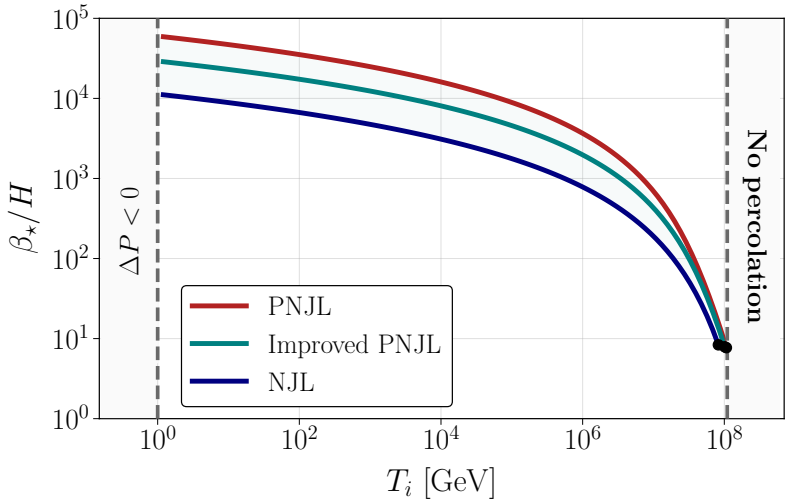

Figure 6.10: Inverse timescale $\beta_\star/H$ computed within the 4D cutoff scheme, as a function of the new physics scale, T_i. We observe the same qualitative behavior as for the 3D cutoff scheme. However, the results are much more dependent on the employed low-energy description of QCD.

6.B CUTOFF SCHEME DEPENDENCE

In the main part, we have employed the 3D cutoff scheme to regularize the divergence appearing in the one-loop contribution to the effective potential in the NJL model, eq. (6.12). Here, we repeat our analysis employing the 4D cutoff scheme used in, e.g., refs. [237, 329]. Within this scheme, the T-independent, NLO contribution to $V_{\text{eff}}^{\text{NJL}}$ is treated with a cutoff Λ on the four-dimensional momentum integral. This alters the structure of the one-loop potential, yielding

$$V_{1,4\text{D}}^{\text{NJL}}(\bar{\sigma}) = -\frac{N_c N_f}{(4\pi)^2}\Lambda^4\left[\ln\left(1+\xi^2\right) - \xi^4\ln\left(1+\xi^{-2}\right) + \xi^2\right], \tag{6.67}$$

where $\xi = M/\Lambda$, with M being the effective quark mass (6.13). While the thermal contributions to the effective potential are naturally three-dimensional, we do not impose a cutoff on the thermal momentum integrals, i.e., we take $\Lambda \to \infty$ when evaluating eq. (6.16). As the cutoff is treated as a model parameter in the low-energy description of QCD, new model parameters have to be introduced in the 4D scheme. These are found in, e.g., refs. [239, 329], and summarized in table 6.3.

We adopt the 4D WFR from ref. [329], which allows us to calculate the bounce action. Again, we fit the behavior of S_3/T to the parametrization (6.44). The results are listed in table 6.3. In addition, we indicate the critical temperatures for the different low-energy descriptions, which are generally slightly lower than the ones found within the 3D

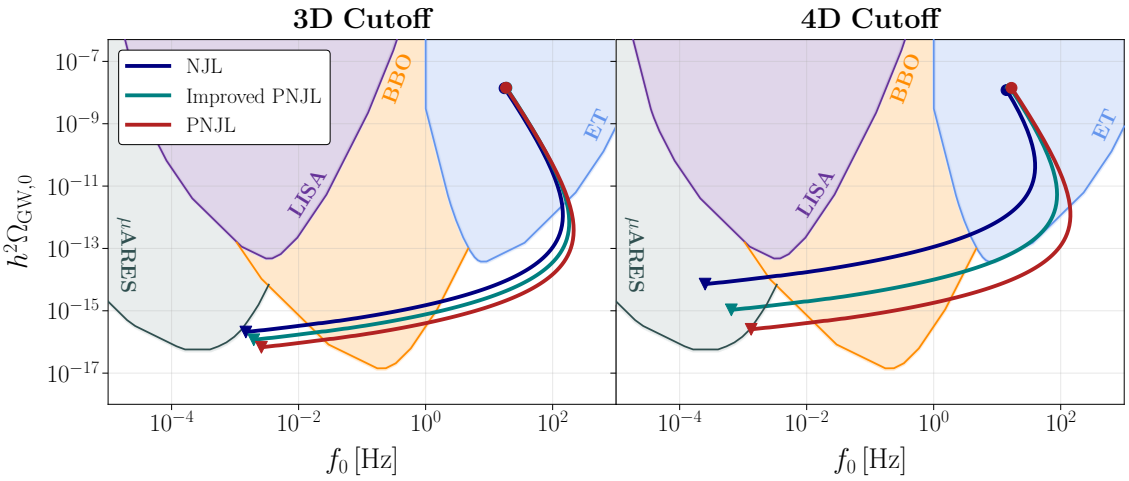

Figure 6.11: Evolution of the GW peak, as observed today, for the 3D (left) and 4D (right) cutoff schemes. The triangle and circle correspond to the minimum and maximum T_i for the transition to finish successfully. In the small-T_i region, both methods show a $\mathcal{O}(100)$ discrepancy regarding the peak amplitude, while showing a good agreement for large amounts of supercooling.

cutoff scheme (cf. fig. 6.3). We proceed by computing the percolation temperature, the inverse timescale of the transition, and eventually the resulting SGWB, as outlined in the main body. The inverse transition timescale, $\beta_\star/H$, is shown in fig. 6.10 as a function of the temperature where thermal inflation starts. We observe a similar qualitative behavior as for the the 3D cutoff scheme (cf. fig. 6.7). For small T_i, the χPT proceeds fast, $\beta_\star/H = \mathcal{O}(10^4 - 10^5)$, indicating a small GW amplitude. When increasing the amount of supercooling, the timescale is significantly enhanced. This is expected, since, as outlined in the main part, the enlargened timescale is purely a consequence of the modified background evolution, i.e., this qualitative trend should not change when changing the cutoff scheme. Nevertheless, let us stress two main differences to the 3D scheme. First, the 4D regularization predicts overall larger timescales, corresponding to a more prominent SGWB. Second, we observe a larger deviation between the different low-energy descriptions of QCD. While the maximum difference of the inverse timescale between the NJL and PNJL is of $\mathcal{O}(1)$ in the 3D cutoff scheme (cf. fig. 6.7), here we observe a $\mathcal{O}(10)$ uncertainty. In the large-T_i region, this model dependence becomes much milder, and the results agree well with the ones from the main body. Since this corresponds to the parameter space relevant for future observatories, we consider our results robust.

We can further investigate the cutoff scheme dependence by computing the GW spectrum. In fig. 6.11, we display the evolution of the GW peak as a function of T_i, redshifted

to today, together with the sensitivity regions of several future experiments. Here, the triangles denote the minimum T_i required for the transition to finish successfully, while the dots correspond to the maximum T_i for successful bubble percolation in an inflating Universe. As anticipated, the 4D cutoff scheme predicts overall stronger signals. This can be seen by a large overlap of the respective spectra with μARES in the small-T_i region. However, the enhanced model dependence is manifested in a $\mathcal{O}(10^2)$ deviation of the GW amplitude. Only in the strong-supercooling regime, both panels show consistent results. The 3D cutoff scheme, on the other hand, yields reliable results for all values of T_i. This may be expected, since high-temperature field theories are naturally three-dimensional. Therefore, installing a 3D cutoff is more consistent, since all momentum integrals are treated equally. Hence, we conclude that the 3D regularization scheme is overall more reliable for finite-temperature systems.

7

QCD-SOURCED TACHYONIC PHASE TRANSITION

In the last section, we have analyzed one possibility to exit the thermal inflation period in CSI SM extensions: a strong first-order QCD χPT triggering EWSB, sourcing the breaking of the classical scale symmetry. While this study was conducted independently of the specific BSM particle content, we now specify again to the $\mathrm{U(1)_{B\text{-}L}}$ extended SM. In particular, we consider the parameter range $g_{B\text{-}L} \lesssim 0.1$ and study scenario II (b) from sec. 5.3, that is, supercooling continues after the cosmic QCD transition. While previous studies have focused on a QCD-accelerated FOPT realizing the exit from supercooling [243, 244], we demonstrate that a FOPT occurs merely in a small part of the parameter space. Instead, we explore a novel symmetry breaking pattern that is independent of the order of the QCD transition, and has not been considered in the literature so far.

For large gauge boson masses and small gauge couplings, the negative QCD-induced contribution to the effective potential (cf. eq. (5.24)) grows relative to the positive thermal mass with decreasing temperature, until the potential barrier vanishes at $T_{\mathrm{roll}} \ll T_{\mathrm{QCD}}$ (cf. eq. (5.27)). Hence, the inclusion of $\Delta m^2_{\mathrm{QCD}}$ increases the false vacuum decay rate, accelerating bubble nucleation. For sufficiently small gauge couplings, however, this acceleration becomes too fast, such that bubble percolation does not take place until T_{roll}. Compared to the timescale associated with the expansion rate of the Universe, the barrier then appears to vanish instantaneously.

In this regime of extreme supercooling, the transition is not driven by bubble nucleation and the scalar field φ becomes free to roll down the potential towards the true minimum. This is, however, distinct from a conventional second-order PT, where the background field value closely follows the evolution of the true minimum and no large inhomogeneities are generated. In our case, the true minimum has already formed as the barrier vanishes. Hence, φ crosses a concave region in the effective potential where its mass is imaginary. This corresponds to a tachyonic instability, where long-wavelength modes become unstable and grow exponentially. Therefore, we will refer to our mechanism as *tachyonic phase transition*. Such dynamics are usually studied in the context of tachyonic preheating [47,

48, 139, 140, 291, 298–313] after cosmic inflation, where the growth of scalar fluctuations efficiently terminates the exponential expansion of the Universe. In our case, the characteristic momentum scale is determined by the QCD-induced mass which is $|\Delta m_{\rm QCD}| \gtrsim H$ in most of the parameter space. Exponential amplification of fluctuations that close to the Hubble horizon scale induce large anisotropies in the stress-energy tensor, leading to the production of GWs [6, 53, 140, 291–297]. This has crucial implications. First, since our mechanism takes place around the QCD scale, and the new physics mass scale is $m_{Z'} \sim \mathcal{O}(10^5 - 10^7)$ GeV, the resulting GW background is in the reach of future observatories. This feature is usually absent in cosmic preheating models due to the high energy scale of inflation. Second, as the GW spectrum is expected to differ from a FOPT-induced SGWB, our mechanism may provide a way to distinguish CSI models from other SM extensions.

In sec. 7.1 we first identify the parameter space where a tachyonic PT takes place, i.e., where bubble percolation becomes inefficient. In sec. 7.2, we study the amplification of scalar fluctuations employing numerical simulations of the linearized system. Finally, we estimate the resulting GW background based on previous lattice studies [140, 291] and discuss the associated observational prospects in sec. 7.3.

7.1 INEFFICIENCY OF BUBBLE PERCOLATION

We start by computing all quantities relevant for the PT dynamics, as introduced in sec. 3.2, employing the effective potential we constructed in sec. 5. To find the solution to the $\mathcal{O}(3)$ symmetric bounce equation (3.47), we again use `CosmoTransitions` [185]. For a given parameter combination $(g_{B\text{-}L}, m_{Z'})$, we scan the temperature range $T_{\rm roll} \leq T \leq T_{\rm QCD}$. As the temperature approaches $T_{\rm roll}$ and QCD effects start to accelerate the transition, we decrease the step size to accurately capture the dynamics. We then interpolate the bounce action and numerically integrate over the nucleation history to find the fraction of space trapped in the false vacuum at a given temperature $I(T)$ via eq. (3.50). Once $I(T_{\rm p}) = 0.34$, bubble percolation takes place.

Fig. 7.1 shows the results of three computations, imposing $m_{Z'} = 10^6$ GeV and $g_{B\text{-}L} \in \{0.23, 0.25, 0.27\}$ (blue, red, orange). The black dots indicate the percolation temperature. We first note that $\mathcal{S}_3 = S_3/T$ takes larger value with decreasing gauge coupling. This implies a larger suppression of the tunneling rate for small $g_{B\text{-}L}$. All curves show a shallow behavior for larger T, while steeply declining below $T \lesssim 10^{-2} T_{\rm QCD}$. This is caused by the negative QCD-induced mass (5.26) which counteracts the thermal barrier, hence accelerates tunneling. The moment when $\mathcal{S}_3$ crosses zero marks the cancellation of the

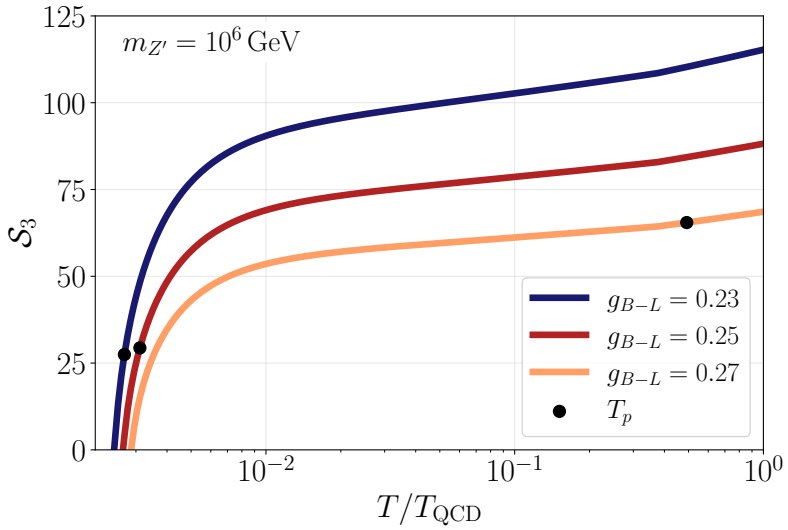

Figure 7.1: Evolution of the bounce action $\mathcal{S}_3 = S_3/T$ as a function of temperature, employing $g_{B\text{-}L} \in \{0.23, 0.25, 0.27\}$ (blue, red, orange) and $m_{Z'} = 10^6\,\mathrm{GeV}$. The black dots indicate successful percolation. For all benchmarks, the exit from supercooling is realized through a FOPT.

thermal barrier, indicating the onset rolling. In all benchmark points shown, percolation occurs before T_{roll}. While the transition completes close to T_{QCD} for $g_{B\text{-}L} = 0.27$, the QCD contribution is required to drive the transition for $g_{B\text{-}L} \in \{0.23, 0.25\}$.

Considering smaller gauge couplings, the situation changes, as shown in fig. 7.2 for $g_{B\text{-}L} \in \{10^{-3}, 5\times10^{-3}, 10^{-2}\}$. In this case, the tunneling rate is extremely suppressed, as $\mathcal{S}_3 \sim \mathcal{O}(10^6 - 10^9)$ for $T \sim T_{\mathrm{QCD}}$. Only when the temperature approaches T_{roll}, the bounce action drops rapidly before crossing zero as the barrier vanishes. This implies an extreme acceleration of the PT. During this decline we always find a moment when $\Gamma(T) \gtrsim H^4$, such that bubble nucleation is possible in principle. However, when integrating over the bubble nucleation history, we find $I(T_{\mathrm{roll}}) \ll 0.34$ for all three benchmarks. This indicates that time during which bubble nucleation is efficient does not suffice to convert a sizable fraction of the Universe to the false vacuum. Therefore, we conclude that in this case no FOPT takes place, but the field rolls towards the true minimum.[1]

This procedure is repeated for the entire parameter space. We then identify the region where a FOPT takes place, i.e., $I(T_{\mathrm{roll}}) \geq 0.34$. This is shown in fig. 7.4 by the upper left

1 Note that a similar setup has recently been studied on the lattice in [377]. The main result is that for reasonably small inverse timescales $\beta/H \sim \mathcal{O}(10^2 - 10^5)$, bubble percolation is efficient in driving the transition. In our case, $\beta/H \gtrsim \mathcal{O}(10^6)$ in the parameter space close to the no-percolation regime. Therefore, we expect the assumption of classical rolling to hold.

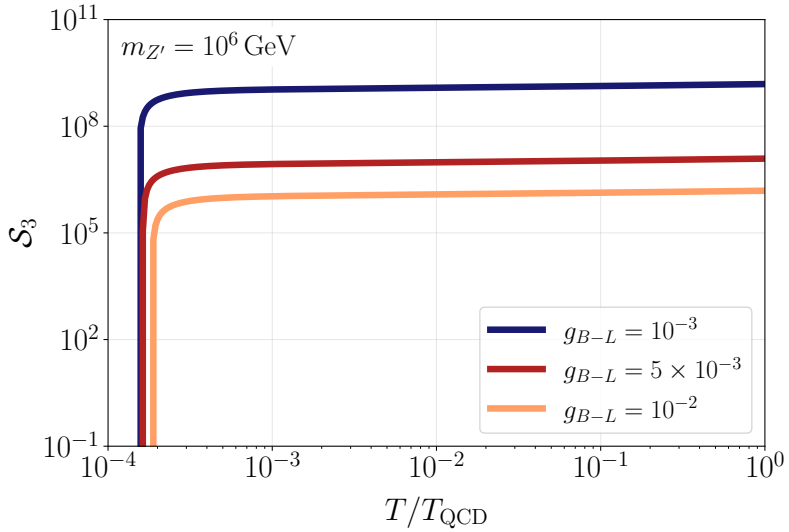

Figure 7.2: Bounce action $\mathcal{S}_3 = S_3/T$ as a function of temperature T. We employ $g_{B\text{-}L} \in \{10^{-3}, 5\times10^{-2}, 10^{-2}\}$ (blue, red, orange), i.e., smaller gauge couplings compared to fig. 7.1. For these benchmarks, bubble nucleation is extremely suppressed before the QCD-induced mass term accelerates tunneling. As a consequence, the Universe cannot be converted to the true vacuum before the barrier vanishes as $\mathcal{S}_3$ crosses zero. The result is a tachyonic PT driven by rolling of the scalar field.

exclusion region, while the blue-shaded region features a tachyonic PT. The duration of the thermal inflation period is characterized by the number of e-folds,

$$N = \log\left(\frac{T_i}{T_{\mathrm{roll}}}\right) , \tag{7.1}$$

where T_i is given by eq. (5.34). The maximum number of e-folds we encounter is $N \sim 25$. Hence, the scales probed by the CMB remain super-horizon and we do not run into conflict with observations [101].

7.2 SCALAR FIELD AMPLIFICATION

In this section, we analyze the behavior of the scalar field in the case where thermal tunneling is inefficient. Then, φ starts rolling towards the true minimum as the barrier vanishes at T_{roll}. While crossing the concave region of the effective potential, long-wavelength modes are exponentially amplified, preheating the supercooled Universe and producing GWs. As the scalar reaches the true minimum, decays into Higgs particles become efficient and the false vacuum energy is efficiently transferred back to the SM.

EQUATIONS OF MOTION. To study these dynamics, let us start from the scalar field action in curved spacetime,

$$S = \int \mathrm{d}^4x\sqrt{-g}\left(\frac{1}{2}\partial_\mu\varphi\partial^\mu\varphi - V_{\text{eff}}(\varphi,T)\right). \tag{7.2}$$

Here, $g = \det g_{\mu\nu}$ is the determinant of the FLRW metric, while $V_{\text{eff}}(\varphi,T)$ corresponds to the thermal effective potential (5.29). From the action, we compute the Euler-Lagrange equation of motion,

$$\ddot{\varphi} + \frac{1}{a^2}\boldsymbol{\nabla}^2\varphi + 3H\dot{\varphi} + \frac{\partial V_{\text{eff}}(\varphi,T)}{\partial\varphi} = 0\,, \tag{7.3}$$

where the Hubble parameter acts as a friction term. Given the absence of bubble dynamics, the scalar field remains homogeneous as the barrier vanishes at T_{roll}. Then, we can split the field into a homogeneous background $\varphi(t)$ and $\boldsymbol{x}$-dependent fluctuations $\delta\varphi(\boldsymbol{x},t)$,

$$\varphi(\boldsymbol{x},t) = \varphi(t) + \delta\varphi(\boldsymbol{x},t)\,. \tag{7.4}$$

We then move to Fourier space [378–380] and decompose the field via its mode functions $u_k(t)$,

$$\delta\varphi(\mathbf{x},t) = \int \frac{\mathrm{d}^3k}{(2\pi)^3}a_k u_k(t)\exp(ikt) + \text{h.c.}\,, \tag{7.5}$$

with the annihilation (a_k) and creation operators ($a_k^\dagger$) satisfying the commutation relation

$$[a_k, a_{k'}^\dagger] = (2\pi)^3\delta^{(3)}(k-k')\,. \tag{7.6}$$

The mode function $u_k(t)$ then describes the occupation number of a mode with momentum k as a function of time. As long as the fluctuations are small, we may linearize the system. To this end, we use the decomposition (7.4) together with eq. (7.5) and expand the equation of motion (7.3) to linear order in in the fluctuations. Explicitly, we have

$$\frac{\partial V_{\text{eff}}(\varphi,T)}{\partial\varphi} = \frac{\partial V_{\text{eff}}(\varphi,T)}{\partial\varphi} + \frac{\partial^2 V_{\text{eff}}(\varphi,T)}{\partial\varphi^2}\delta\varphi + \ldots\,, \tag{7.7}$$

where $\partial^2 V_{\text{eff}}(\varphi,T)/\partial\varphi^2 = m_\varphi^2$. This yields two coupled equations of motion,

$$\ddot{\varphi} + 3H\dot{\varphi} + \frac{\partial V_{\text{eff}}(\varphi,T)}{\partial\varphi} = 0\,, \tag{7.8}$$

$$\ddot{u}_k + 3H\dot{u}_k + \left(\frac{k^2}{a^2} + m_\varphi^2\right)u_k = 0\,. \tag{7.9}$$

The first equation describes the motion of the background field which is driven towards the true minimum, while being decelerated by Hubble friction. The second equation captures

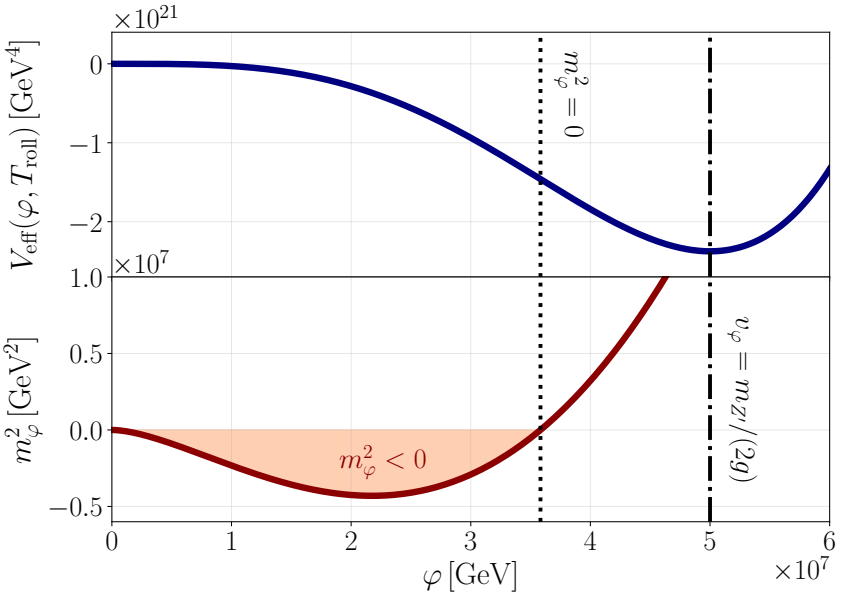

Figure 7.3: Effective potential (upper panel) and effective scalar mass squared (lower panel) at $T = T_{\text{roll}}$ for $g_{B\text{-}L} = 10^{-2}$ and $m_{Z'} = 10^6\,\text{GeV}$. The orange-shaded region indicates the imaginary mass-regime where long-wavelength modes are exponentially amplified. Approaching the true minimum, the effective mass turns positive again, and exponential growth terminates.

the time evolution of the mode functions. The momentum-dependent fluctuations behave like damped harmonic oscillators with a time-dependent frequency

$$\omega^2 = \frac{k^2}{a^2} + m_\varphi^2\,. \tag{7.10}$$

For positive masses $m_\varphi^2 > 0$, the solution shows an oscillating behavior, $u_k \propto \exp(-i\omega t)$. However, if the effective scalar mass is negative, modes in the range

$$0 \leq \frac{k}{a} \leq m_\varphi\,, \tag{7.11}$$

exhibit an imaginary oscillation frequency, $\omega^2 < 0$. Then, the solution to the equation of motion transitions from oscillating to exponentially growing, $u_k \propto \exp(|\omega| t)$. In fig. 7.3 we display the effective potential (upper panel) together with the scalar mass m_φ^2 (lower panel) at T_{roll} for $g_{B\text{-}L} = 10^{-2}$ and $m_{Z'} = 10^6\,\text{GeV}$. For small field values, the potential is concave, hence the effective mass is imaginary, as indicated by the orange-shaded region.

For $T > T_{\text{roll}}$, the field is trapped at the origin of field space. Then, the effective mass can be approximated by (cf. eq. (5.26))

$$m_{\varphi,0}^2 = \left.\frac{\partial^2 V_{\text{eff}}(\varphi, T_{\text{QCD}})}{\partial \varphi^2}\right|_{\varphi \to 0} \simeq \Delta m_{\text{QCD}}^2 + g_{B\text{-}L}^2 T^2\,, \tag{7.12}$$

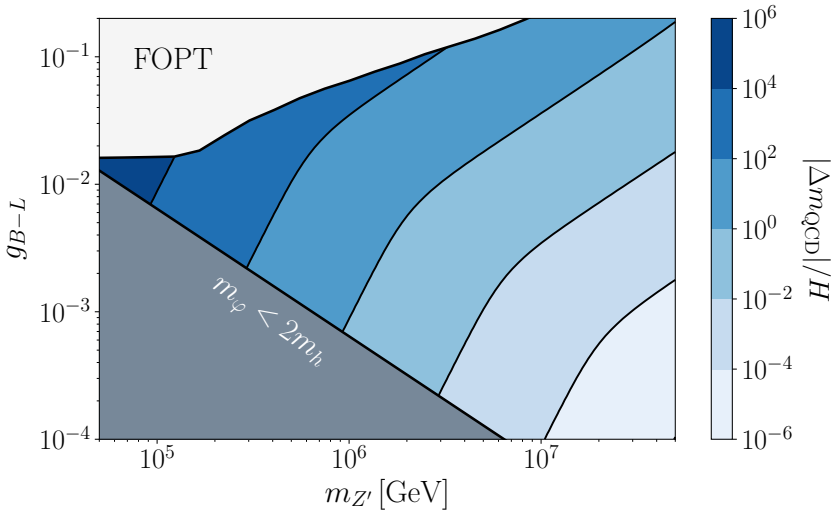

Figure 7.4: Ratio of the QCD-induced mass $|\Delta m_{\rm QCD}|$ and the Hubble parameter H for the parameter space we consider. The white-shaded region features a FOPT, hence is excluded in our study. In the gray-shaded region, reheating of the SM after the tachyonic production of scalar modes cannot proceed via decays to Higgs bosons. In a large fraction of the parameter region, $|\Delta m_{\rm QCD}| > H$, such that tachyonic growth is efficient.

where $\Delta m_{\rm QCD} = -\lambda_p v_{h,\rm QCD}^2/2$. With decreasing temperature, the thermal mass quickly becomes negligible, such that the QCD-induced mass dominates the growth rate, i.e., $|\omega| \simeq \Delta m_{\rm QCD}$ for $k/a \ll |\Delta m_{\rm QCD}|$. Fig. 7.4 shows the ratio $\Delta m_{\rm QCD}/H$ in the $m_{Z'} - g_{B\text{-}L}$ plane. The white-shaded region indicates the parameter space where a FOPT takes place, while we exclude the gray-shaded regime since the energy transfer back to the SM is hard to realize (cf. sec. 5.3). Regarding the tachyonic resonance, it is important to have $|\Delta m_{\rm QCD}| > H$, such that the unstable modes can grow efficiently compared to the expansion rate of the Universe. This is given for a large part of the parameter space. Increasing (decreasing) $m_{Z'}$ ($g_{B\text{-}L}$) flattens the effective potential, such that $\Delta m_{\rm QCD} \ll H$.

INITIAL CONDITIONS. Let us now specify our initial conditions for the homogeneous and inhomogeneous modes that we employ for our numerical study. While the scalar field is trapped around the origin, the Universe undergoes a substantial amount of supercooling. Hence, its expectation value is determined by the evolution of quantum fluctuations which grow during the thermal inflation period. Employing the Bunch-Davies solution [381], the field variance at $T_{\rm roll}$ in the presence of a thermal bath is expressed as [369, 377, 382, 383]

$$\langle\varphi^2\rangle = \langle\varphi^2\rangle_{\rm T} + \langle\varphi^2\rangle_{\rm V}\,. \tag{7.13}$$

Here, $\langle\varphi^2\rangle_{\mathrm{T}} \approx T_{\mathrm{roll}}^2/12$ and $\langle\varphi^2\rangle_{\mathrm{V}} \approx H^2 N/(4\pi^2)$, with N being the number of e-folds, denote the thermal and vacuum contributions. For the field to be driven to the true vacuum, it is important to check if classical rolling indeed dominates the dynamics. If the field value is sufficiently small, the dynamics continue to be dominated by quantum fluctuations, inducing random jumps around the potential maximum. To this end, we compare the rate of change by classical rolling in the slow-roll limit [384]

$$\Delta\varphi_{\mathrm{cl}} = \dot{\varphi}\Delta t = -\frac{V'_{\mathrm{eff}}(\varphi, T)}{3H^2}\,, \tag{7.14}$$

to the typical size of quantum fluctuations in de Sitter space,

$$\Delta\varphi_{\mathrm{quantum}} = \frac{H}{2\pi}\,. \tag{7.15}$$

Demanding $\Delta\varphi_{\mathrm{cl}} > \Delta\varphi_{\mathrm{quantum}}$, we find the field excursion which defines the classical regime,

$$V'_{\mathrm{eff}}(\varphi_{\mathrm{cl}}) = -\frac{3H^3}{2\pi}\,. \tag{7.16}$$

From these considerations, we first include all points in parameter space that satisfy $\sqrt{\langle\varphi^2\rangle} > \varphi_{\mathrm{cl}}$ at T_{roll}. Furthermore, it was shown that if $|m_\varphi| \gg H$, thermal inflation ends rather quickly due to efficiently growing modes destabilizing the false vacuum [369]. Conversely, if $|m_\varphi| \ll H$, we cannot ensure that thermal inflation terminates successfully. This may lead to a sizable number of e-folds after the thermal barrier has disappeared, potentially conflicting with CMB observations [101]. In extreme cases, quantum fluctuations dominate for all times, leading to eternal inflation [383]. Hence, for parameter points where $|m_\varphi| \ll H$, a more detailed study of the evolution during the de Sitter phase is required. This is beyond the scope of this work, hence we exclude this parameter space for now. For the remaining configurations, we choose

$$\varphi_i = \max\left\{\varphi_{\mathrm{cl}}, \sqrt{\langle\varphi^2\rangle}\right\}, \tag{7.17}$$

as the initial condition for the homogeneous mode. The second derivative of the effective potential is, however, dominated by the constant QCD-induced mass for small field values. Therefore, the growth rate is independent of the field excursion during a large part of the evolution. Then, our main results do not depend crucially on the initial condition.

Let us now turn our attention to the initial conditions of the scalar fluctuations. In cosmic preheating scenarios, the usual initial condition is given by the Bunch-Davies vacuum [381, 385],

$$u_{k,\mathrm{BD}}(\eta) = \frac{1}{\sqrt{2k}}\exp(ik\eta)\,, \tag{7.18}$$

expressed via comoving momenta and conformal time η. This is no longer appropriate in the presence of a thermal bath. Prior to $\mathrm{U}(1)_{\text{B-L}}$ symmetry breaking, the scalar modes represent massless particles. In the following, we assume that the scalar field is in thermal equilibrium with the SM.[2] Integrating over physical momenta, the total energy density of the scalar fluctuations then reads

$$\begin{aligned}\rho_{\delta\varphi}(T) &= \int \mathrm{d}k\, \frac{k^3}{2\pi^2} \left[\exp\left(\frac{k}{T}\right) - 1\right]^{-1} \\ &= \frac{\pi^2}{30} T^4 \,.\end{aligned} \tag{7.19}$$

Alternatively, we can express the energy density of a massless scalar field by

$$\rho_{\delta\varphi} = \frac{1}{2}\delta\dot{\varphi}^2 + \frac{1}{2a^2}(\boldsymbol{\nabla}\delta\varphi)^2 \,. \tag{7.20}$$

where the first (second) term denotes the kinetic (gradient) energy. Employing the Fourier decomposition (7.5), we can derive an expression for the mode functions in thermal equilibrium,

$$u_k(\eta) = \sqrt{2}\left(\exp\left(\frac{k}{T_{\text{roll}}}\right) - 1\right)^{-\frac{1}{2}} u_{k,\text{BD}}(\eta) \,. \tag{7.21}$$

That is, the scalar modes are modified by a Boltzmann factor.

Finally, let us briefly discuss the evolution of the SM Higgs field, which sits at $h = v_{h,\text{QCD}}$ after QCD χSB. For large field values $\varphi \lesssim v_\varphi$, the Higgs direction is destabilized, as the electroweak vacuum is generated (cf. chapter 5). This causes the field to roll towards the global minimum at $(\varphi, h) = (v_\varphi, v_h)$. During the initial stages of the evolution which we simulate below, $\varphi \ll v_\varphi$ and the Higgs direction in field space remains stable. Hence, h is not a dynamical degree of freedom during tachyonic growth, and we fix $h = v_{h,\text{QCD}}$.

NUMERICAL STUDY. In this section, we numerically study the initial phase of tachyonic amplification. To this end, we solve the linearized equations of motion (7.8) and (7.9) for $N_k = 1000$ scalar modes. Note that as the energy density of the scalar fluctuations grows large, the linear approximation breaks down. Therefore, we stop the simulation once

$$\rho_{\delta\varphi} = \Delta V_{\text{eff}} \,. \tag{7.22}$$

Here, ΔV_{eff} is the potential energy difference between the false and true vacua, i.e., the total initial energy density available to be converted into fluctuations. When eq. (7.22) is fulfilled,

2 Again, this assumption does not crucially influence our results, since the scalar fluctuations are amplified by many orders of magnitude. We have confirmed this numerically by repeating our analysis with Bunch-Davies initial conditions.

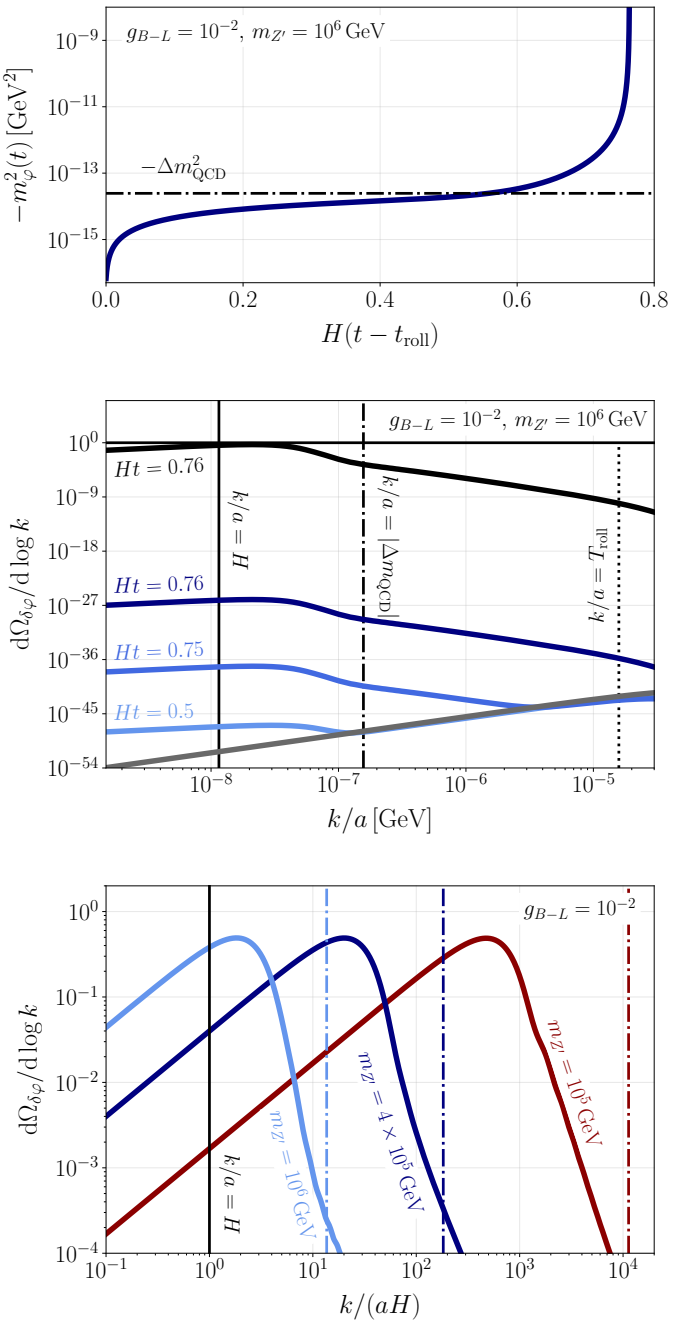

Figure 7.5: Upper panel: Effective mass parameter $-m_\varphi^2$ during the simulation. Center panel: Spectral fluctuation energy density at different times of the simulation. The grey curve denotes the initial thermal spectrum. Lower panel: Final energy spectrum of the amplified fluctuations for $g_{B\text{-}L} = 10^{-2}$ and $m_{Z'} \in \{10^5, 4 \times 10^5, 10^6\}$ GeV.

we expect fragmentation to set in, i.e., backreaction effects from the produced fluctuations onto the zero mode which becomes fully inhomogeneous. The non-linear regime can be studied using, e.g., lattice simulations [296, 386], which we relegate to future work. We aim to verify that the characteristic size of the fluctuations is indeed given by the QCD-induced mass. Since this scale is set during the initial stages of tachyonic growth where the linear approximation holds, we obtain a reliable estimate of the spectral peak. This is then used in sec. 7.3 to approximate the peak of the resulting GW signal.

The left-hand side of eq. (7.22) denotes the energy density of the fluctuations [48, 380]

$$\rho_{\delta\varphi} = \int \frac{\mathrm{d}^3k}{(2\pi)^3}\omega_k \left(n_k + \frac{1}{2}\right) , \tag{7.23}$$

where n_k is the occupation number of a harmonic oscillator,

$$n_k = \frac{\omega_k}{2}\left(\frac{|\dot{u}_k|^2}{\omega_k^2} + |u_k|^2\right) - \frac{1}{2} . \tag{7.24}$$

Strictly speaking, the above expression merely holds in the adiabatic limit, $\dot{\omega}_k/\omega_k^2 \ll 1$. This is clearly violated as the field-dependent mass, hence the growth rate, starts to grow rapidly at large field values. In addition, while the mass is tachyonic the concept particle number is ill-defined. This is a consequence of quantizing a theory on an unstable background. However, we stress again that the spectral peak forms during the initial stage where $\dot{\omega}_k/\omega_k^2 \ll 1$ is fulfilled. Hence, we expect a more sophisticated treatment of the system to not alter the location of the peak, but only the duration of tachyonic growth. Furthermore, to avoid negative energy densities, one usually defines [48]

$$\omega_k = \left|\frac{k}{a}\right| , \quad \text{or} \quad \omega_k = \sqrt{\left(\frac{k}{a}\right)^2 + |m_\varphi^2|} , \tag{7.25}$$

in the concave part of the effective potential. This choice has no impact on the characteristic size of the fluctuations, thus we employ $\omega_k = |k/a|$ in the following.

In fig. 7.5, we show the results of some benchmark simulations for different model parameters. The upper panel shows the evolution of the effective scalar mass $-m_\varphi^2$ as a function of time for $(g_{B\text{-}L}, m_{Z'}) = (10^{-2}, 10^6\,\mathrm{GeV})$. The dash-dotted line indicates $-\Delta m_{\mathrm{QCD}}^2$. Starting the simulation at T_{roll}, the effective mass is zero, since thermal and QCD-induced effects balance each other. As the temperature drops and the thermal mass decreases, the homogeneous mode starts to roll. Subsequently the mass slowly approaches Δm_{QCD}. At $H(t - t_{\mathrm{roll}}) \approx 0.6$, the scalar mass, i.e., the growth rate, starts to increase rapidly. This is because the field reaches the part of the effective potential that is dominated by radiative Z' corrections (cf. chapter 5), leading to an acceleration of the field towards the true minimum.

The center panel displays the associated spectral energy density of the scalar fluctuations, normalized to the total energy density. Here, the gray curve is the initial spectrum ($t_{\rm roll} = 0$) which peaks at $k/a = T_{\rm roll}$ (dotted line). Colored lines denote different times during the simulation, while vertical lines indicate the Hubble parameter (solid) and the QCD-induced mass term (dash-dotted). We observe that initially, only modes with $k/a < |\Delta m_{\rm QCD}|$ are amplified. This is expected, as the mass in the small-field regime is given by the QCD contribution. At later times, e.g., for $Ht \approx 0.75$, we find that the instability band extends further to the UV. Again, this matches our expectation, as the scalar mass at this time becomes significantly more negative (cf. upper panel), increasing both the width of the tachyonic band and the growth rate. The crucial point, however, is that the spectrum peaks around the scales that are amplified initially. This remains true up to the point where we stop the simulation (black), where the energy density in the fluctuations $\Omega_{\delta\varphi} \approx 1$. The entire evolution takes less than a Hubble time, and the linear approximation breaks down before the field starts to oscillate about the true minimum. We should stress that this efficient production of IR modes is a consequence of the conformal nature of the model and the resulting flat potential. Since the homogeneous mode spends a substantial time at small field excursions where $|m_\varphi| \sim |\Delta m_{\rm QCD}| \sim H$, long-wavelength modes close to the horizon dominate the final spectrum. If we considered a Higgs-like symmetry breaking with a negative tree-level mass term $|\mu| = \mathcal{O}(100\,\text{GeV}) \gg H$, the characteristic size of the associated fluctuations would be much smaller than the horizon.

To demonstrate that the above benchmark does not correspond to a special point in the parameter space, we show the final scalar spectra for $g_{B\text{-}L} = 10^{-2}$ and $m_{Z'} \in \{10^5, 4\times 10^5, 10^6\}\,\text{GeV}$ (red, dark blue, light blue) in the lower panel. The momenta are normalized to the Hubble parameter. The black vertical line again indicates the Hubble scale, while the colored vertical lines show the respective QCD-induced mass. In all cases, we observe that $|\Delta m_{\rm QCD}|$ determines the cutoff scale. The actual peak lies slightly below, since modes with $k/a \lesssim \Delta m_{\rm QCD}$ grow slower than modes with $k/a \ll \Delta m_{\rm QCD}$ (cf. eq. (7.10)). This effect is stronger for larger $m_{Z'}$, causing an $\mathcal{O}(1-10)$ deviation from $|\Delta m_{\rm QCD}|$. Nonetheless, the QCD-sourced mass provides a reasonable estimate of the characteristic scale, since we are merely interested in an order-of-magnitude estimate of the GW signal.

REHEATING THE SM. After the completion of the tachyonic PT, the scalar field is completely inhomogeneous and the $\text{U}(1)_{\text{B-L}}$ symmetry is broken. Hence, the produced scalar fluctuations emerge as particles with a well-defined mass given by eq. (5.8). In the absence of a lattice simulation which would allow us to determine the precise equation of state, we restrict ourselves to the treatment introduced in sec. 5.3. That is, we assume a

matter-like scaling for the scalar particles. This is a good approximation since their peak momentum $|\Delta m_{\rm QCD}| \ll m_\varphi$ in all of the parameter space, e.g., the fluctuations become non-relativistic. We then only consider the decay channel via the SM Higgs, assume that thermalization of the SM is quick and numerically determine the reheating temperature via eq. (5.41).

7.3 GRAVITATIONAL WAVE BACKGROUND

The exponential growth of scalar fluctuations in a specific momentum band corresponds to inhomogeneities on a preferred scale in position space. This leads to anisotropies in the stress-energy tensor and, therefore, a SGWB [6, 53, 140, 291–297]. The associated spectral energy density, normalized to the total energy density of the Universe, is given by eq. (3.3) and can be computed numerically by solving the linearized Einstein equations (3.2). This yields an expression that depends directly on the scalar mode functions; the full computation is found in [292]. However, it was shown on the lattice that for tachyonic preheating, the dominant part of GW production occurs during the non-linear evolution [140, 291]. As the system becomes non-linear, bubble-like structures form and collide, building up large field gradients responsible for GW emission. The characteristic bubble size is given by the spectral peak of the scalar fluctuations. Since our linear approach therefore cannot capture the full GW emission, we restrict ourselves to estimates.

ANALYTIC ESTIMATES. Refs. [140, 291] give a simple scaling relation for the GW peak extracted from the lattice (see also chapter 3),

$$\Omega_{\rm GW,\star} \approx \xi_{\rm eff} (R_\star H)^2 \,, \tag{7.26}$$

where the subscript "$\star$" denotes quantities evaluated at the time of production. Here, $\xi_{\rm eff}$ is a model-dependent efficiency factor. For chaotic inflation, $\xi_{\rm eff} \sim 0.15$ [140], while $\xi_{\rm eff} \sim 10^{-2}$ [211] for supercooled FOPTs. Since we cannot reliably compute $\xi_{\rm eff}$ for the tachyonic phase transition without employing the lattice, we simply take it as a free parameter which we vary to show its impact on our results. $R_\star = a_\star / k_\star$ is the physical size of the fluctuations, while $H_\star$ is the Hubble parameter. Larger $R_\star$ shift the fluctuations closer to the size of the horizon, inducing larger spatial perturbations, hence an enhanced GW amplitude.

In the following, we first express the estimate for the GW background in terms of our model parameters. To this end, we use the relations derived in chapter 5 and sec. 7.2. To obtain simple analytic expressions, we neglect the running of the model parameters

for now. For our final results, however, we use the full effective potential including RG improvement, and determine all relevant quantities numerically. In the last section, we have verified that the QCD-induced mass sets the peak of the scalar energy spectrum, i.e., the GW peak frequency is estimated by

$$\frac{1}{R_\star^2} = \frac{k_\star^2}{a_\star^2} \approx |\Delta m_{\rm QCD}|^2 \approx \frac{\lambda_p}{2} v_{h,\rm QCD}^2 \approx 4\mu_{h,\rm SM}^2 v_{h,\rm QCD}^2 \frac{g_{B\text{-}L}^2}{m_{\rm Z'}^2}\,, \tag{7.27}$$

at the time of production. Here we have employed eq. (5.15). Note that we have neglected the expansion of space between the onset of rolling and GW production. This is a good approximation since, in almost the entire parameter space, tachyonic growth terminates in less than a Hubble time. To arrive at today's GW peak frequency and amplitude we redshift [147],

$$f_0 = 1.65\times 10^{-7}{\rm Hz}\frac{k_\star}{aH_{\rm rh}}\frac{T_{\rm rh}}{\rm GeV}\left(\frac{g_{\star,\rm rh}}{100}\right)^{\frac{1}{6}}\frac{a_\star}{a_{\rm rh}}\,, \tag{7.28}$$

$$h^2\Omega_{0,\rm GW} = 1.67\times 10^{-5}\left(\frac{100}{g_{\star,\rm rh}}\right)^{\frac{1}{3}}\frac{a_\star}{a_{\rm rh}}\Omega_{\star,\rm GW}\,, \tag{7.29}$$

taking into account the MD period induced by the decay of the scalar field. In the above expression, we have set $g_{\star,s} = g_{\star,\epsilon}$ at the time of reheating. Eq. (5.40) gives the scale factor ratio, while eq. (5.41) is the reheating temperature. Using our analytic expression for the Hubble parameter (5.37), we have

$$f_0 \approx \begin{cases} 0.57\, g_{\star,\rm rh}^{-\frac{1}{12}}\left(\frac{g_{B\text{-}L}}{10^{-2}}\right)^{\frac{7}{6}}\left(\frac{v_{h,\rm QCD}}{\rm GeV}\right)\left(\frac{10^6\,{\rm GeV}}{m_{\rm Z'}}\right)^{\frac{17}{6}}{\rm Hz}\,, & \text{if } \Gamma_\varphi < H_\star\,, \\ 23.2\, g_{\star,\rm rh}^{-\frac{1}{12}}\left(\frac{g_{B\text{-}L}}{10^{-2}}\right)^{\frac{1}{2}}\left(\frac{v_{h,\rm QCD}}{\rm GeV}\right)\left(\frac{m_{\rm Z'}}{10^3\,{\rm GeV}}\right)^{\frac{1}{2}}{\rm Hz}\,, & \text{if } \Gamma_\varphi \geq H_\star\,, \end{cases} \tag{7.30}$$

$$h^2\Omega_{0,\rm GW} \approx \begin{cases} 5.5\times 10^{-13}\,\xi_{\rm eff}\left(\frac{100}{g_{\star,\rm rh}}\right)^{\frac{1}{3}}\left(\frac{10^{-2}}{g_{B\text{-}L}}\right)^{\frac{4}{3}}\left(\frac{\rm GeV}{v_{h,\rm QCD}}\right)^2\left(\frac{m_{\rm Z'}}{10^6{\rm GeV}}\right)^{\frac{8}{3}}\,, & \text{if } \Gamma_\varphi < H_\star\,, \\ 7.0\times 10^{-10}\,\xi_{\rm eff}\left(\frac{100}{g_{\star,\rm rh}}\right)^{\frac{1}{3}}\left(\frac{10^{-2}}{g_{B\text{-}L}}\right)^{2}\left(\frac{\rm GeV}{v_{h,\rm QCD}}\right)^2\left(\frac{m_{\rm Z'}}{10^6{\rm GeV}}\right)^{6}\,, & \text{if } \Gamma_\varphi \geq H_\star\,. \end{cases} \tag{7.31}$$

From this expression we note that both a larger gauge coupling $g_{B\text{-}L}$ and QCD-induced Higgs vev $v_{h,\rm QCD}$ shift the GW peak to larger frequencies and suppress the amplitude. This is due to the fact that $\Delta m_{\rm QCD}^2 \propto (g_{B\text{-}L} v_{h,\rm QCD})^2$. A large Z' mass, on the other hand, flattens the potential, hence enhances the amplitude as the characteristic scale moves closer to the horizon. Regarding the peak frequency, the scaling with $m_{\rm Z'}$ depends on whether

reheating is instantaneous. If this is the case, $m_{Z'}$ enhances the peak frequency. This corresponds to the usual scenario, where a large scale is connected to a larger temperature T_i (cf. eq. (5.36)), hence a larger peak frequency. If decays into the Higgs are prohibited initially, the Universe undergoes a MD phase. Due to the extreme suppression of $\Gamma_\varphi/H \propto m_{Z'}^{-5}$, the additional redshift factor $a_\star/a_{\rm rh}$ can become large. Then, the frequency today is suppressed by the new physics scale.

OBSERVATIONAL PROSPECTS. To assess the observational prospects of the tachyonic PT in the CSI $U(1)_{B\text{-}L}$ model, we compute our estimate of the GW peak numerically, including the running of all model parameters (cf. eq. (5.33)). That is, we evaluate the QCD-induced mass at the high-T scale $\mu = \pi T_{\rm roll}$ as tachyonic growth takes places in the small-field regime. The decay rate is computed at the SM scale, $\mu = m_Z$. We compute the PLI sensitivity curves $h^2\Omega_{\rm PLI}(f)$ of several future GW observatories following ref. [152]. Then, parameter points for which $h^2\Omega_{0,\rm GW}(f_0) \geq h^2\Omega_{\rm PLI}(f_0)$ are considered detectable. A more rigorous analysis would include the computation of signal-to-noise ratios (SNRs), which, however, necessitates the spectral shape of the signal. Such an analysis is relegated to the future. Nevertheless, our simplified approach gives us a good overview of the general detection prospects.

Fig. 7.6 shows our final results. Here, the colored curves indicated the sensitivity regions of ET [38] (light blue), BBO [148] (blue), DECIGO [387–389] (red), and LISA [35, 37] (orange). We employ different values of the efficiency factor $\xi_{\rm eff} \in \{10^{-1}, 10^{-3}, 10^{-5}\}$. The upper left white-shaded region again shows the parameter space where thermal tunneling is efficient before the onset of rolling, i.e., a FOPT takes place. The lower right white-shaded region requires a careful analysis of the evolution of quantum fluctuations during thermal inflation, hence is excluded in this work. In the lower left gray-shaded regime, reheating of the SM via decays to the Higgs is prohibited.

In general, we find excellent observational prospects as a consequence of the large fluctuation scale close to the Hubble horizon. Hence, for moderately large efficiency factors $\xi_{\rm eff}$ BBO and DECIGO are sensitive in a major fraction of the parameter space. Particularly strong signals where $|\Delta m_{\rm QCD}| \sim H$ are in the range of LISA. It is interesting to note that usually, space-based observatories such as LISA are sensitive to smaller energy scales compared to experiments on Earth, such as ET. In fig. 7.6, this order is clearly reversed due to the long MD period for large $m_{Z'}$. Furthermore, we do not find strong signals at high frequencies, since small $m_{Z'}$ implies $|\Delta m_{\rm QCD}| \gg H_{\rm rh}$. Thus, ET only covers a small fraction of the parameter space if $\xi_{\rm eff}$ is sufficiently large.

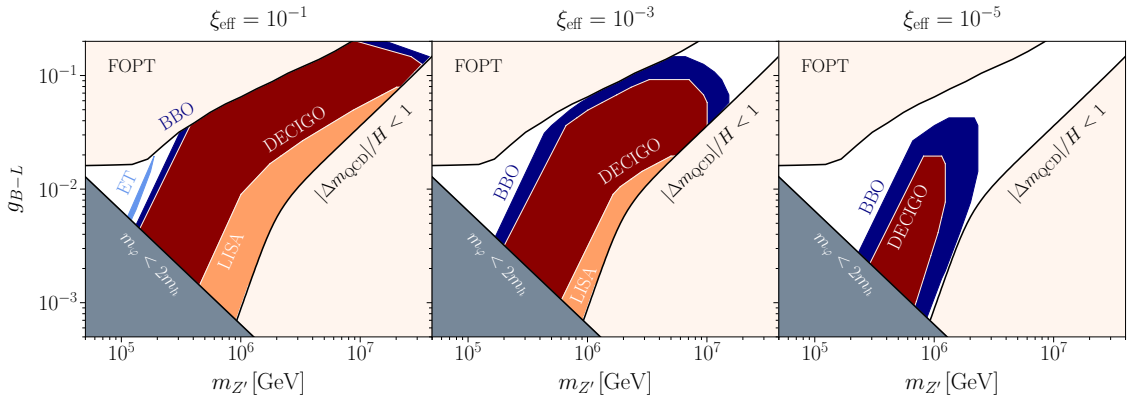

Figure 7.6: Observational prospects of the QCD-induced tachyonic PT in a supercooled Universe, computed via our analytic estimate of the GW peak. We employ three different values of the efficiency factor $\xi_{\text{eff}} \in \{10^{-1}, 10^{-3}, 10^{-5}\}$. In the upper left region, a FOPT driven by thermal tunneling takes place. The lower right region is excluded for now since the classical rolling limit may not hold as thermal inflation ends. Since we focus on reheating via decays to the SM Higgs, we further exclude the lower left region where the decay is kinematically forbidden. We find very promising observational prospects if ξ_{eff} is sufficiently large. BBO and DECIGO span almost the entire parameter space, while LISA is sensitive to strong signals, where $|\Delta m_{\text{QCD}}| \sim H$. ET will only probe a small part of the parameter space.

7.4 CONCLUSION

We have studied a novel symmetry breaking pattern in CSI SM extensions: a tachyonic PT. While most previous works have analyzed the exit from supercooling via a FOPT, we have shown that in a large parameter space of the CSI $\text{U}(1)_{\text{B-L}}$ model, tunneling becomes inefficient. Instead, the symmetry-breaking field starts rolling towards the true minimum as the cosmic QCD transition breaks scale invariance. While the field crosses a region in the effective potential where its mass squared is negative, tachyonic preheating sets in. That is, unstable modes are amplified from the thermal bath, quickly dominating the energy density of the Universe. Once these modes emerge as scalar particles after $\text{U}(1)_{\text{B-L}}$ symmetry breaking, the Universe reheats via decays into the SM Higgs. During this process, stochastic GWs are emitted. The resulting amplitude depends on the scale of the fluctuations compared to the Hubble horizon. Employing results from previous lattice simulations [140, 291], we have estimated the location of the GW peak. Intriguingly, we find excellent observational prospects at future observatories across the entire available parameter space.

Let us note that our results do not only apply to the $\mathrm{U}(1)_{\mathrm{B\text{-}L}}$ model, but may be extended to other CSI theories, such as the $\mathrm{SU}(2)_X$ extended SM [183, 246, 247]. While the QCD-induced exit from supercooling has not been studied in detail in this model, a parameter space should exist where bubble percolation ceases to drive the transition. Interestingly, this opens up a large parameter space that will be tested by forthcoming GW experiments. Moreover, we expect the spectral shape of the outlined mechanism to differ from a FOPT-induced GW signal. Since preheating-like GW spectra typically lie at ultra-high frequencies because of the large scale of cosmic inflation, the QCD-induced tachyonic PT may source a smoking-gun signature at lower frequencies. To assess the ability of future experiments to distinguish between the different symmetry-breaking mechanism, a more precise knowledge of the spectral shape, i.e., a lattice simulation [296, 386], is required.

Another exciting aspect we have neglected in our study is the generation of scalar-induced GWs during the phase of thermal inflation, i.e., before the onset of tachyonic preheating. Due to the large number of e-folds and the negative mass around the origin, large super-horizon perturbations are generated. Once such perturbations re-enter the Hubble horizon after reheating, sizable scalar-induced GWs may be emitted [369], possibly accompanied by the formation of PBHs [383]. This would not only imply a doubly-peaked GW spectrum across several detectors, but also a novel DM candidate.

Furthermore, we have solely focused on the $\varphi \to hh$ reheating channel. For a certain range of Yukawa couplings, however, scalar decays via right-handed neutrinos into the SM Higgs plus leptons are expected to become efficient [323]. First, this may allow for a faster reheating process, shortening the MD period and thus enhancing the GW amplitude. Second, since the right-handed neutrino decay violates CP, the out-of-equilibrium conditions after tachyonic preheating may successfully generate the BAU via leptogenesis [44]. All these intriguing questions are left for future work.

Part III

SUPERCOOLED AUDIBLE AXIONS

8

PRELUDE

In the previous part, we have seen that conformal SM extensions induce a substantial period of supercooling and source a sizable SGWB in the early Universe. In the following, we develop a similar mechanism in the context of axion-like particles (ALPs). The axion was introduced in sec. 2.3 as a hypothetical particle to solve the strong CP problem [49–52]. The ALP is its generalized counterpart. It is a pseudoscalar field, however, does not necessarily generate CP conservation in the strong interactions. Instead, ALPs are natural DM candidates [129–131] due to their suppressed couplings to the SM. Furthermore, they may explain the initial exponential expansion of the Universe via natural inflation [390–396] and are motivated from string theory [397–399].

The viable ALP parameter space is characterized by two quantities: the mass m_ϕ and decay constant f_ϕ, which are independent quantities, in contrast to the case of the QCD axion. Possible values for m_ϕ and f_ϕ span orders of magnitude [400]. As all couplings of the ALP are suppressed by the decay constant, the ALP becomes invisible to laboratory experiments for large f_ϕ [129]. Therefore, it is crucial to investigate mechanisms which can provide observational signatures of ALPs, however, do not rely on a large coupling to SM fields.

One example for such dynamics is the *audible axion* mechanism [53], which is an extension of the *misalignment mechanism* that takes place in the radiation-dominated era of the early Universe. Here, the ALP is initially misaligned from a minimum in its potential, about which it starts to oscillate when the Hubble parameter drops below its mass, $H_{\text{osc}} \sim m_\phi$ [128]. If the ALP is coupled to a dark Abelian gauge field ("dark photon"), its motion generates a tachyonic instability in the vector equation of motion. This is similar to the tachyonic instability due to an imaginary mass that we encountered in chapter 7. Analogously, exponentially growing dark photon modes source anisotropic stress, and hence stochastic GWs. For further studies investigating GWs from ALPs, see [6, 107, 108, 140, 380, 401–429].

To estimate the amplitude of the resulting SGWB in the original audible axion model, we note that the relative energy density at the start of ALP oscillations is $\Omega_{\phi,\mathrm{osc}} \sim (f_\phi / M_{\mathrm{Pl}})^2$. Employing our rule of thumb (3.8), one then finds

$$\Omega_{\mathrm{GW}} \sim \left(\frac{f_\phi}{M_{\mathrm{Pl}}}\right)^4 , \tag{8.1}$$

in the minimal model [53, 295]. Furthermore, a large value of the axion-dark photon coupling $\alpha \gtrsim 20$ is required to enable efficient tachyonic growth. This limits GW probes to merely a small part of the overall parameter space. In the following, we show how further model building can increase the observational prospects of ALPs.

Specifically, we extend the audible axion mechanism by *trapped misalignment* [54, 430–435]. That is, the axion is initially trapped in a false minimum due to additional $U(1)_{\mathrm{PQ}}$ violating operators in the potential. Then, ALP oscillations are delayed to $H_{\mathrm{osc}} \ll m_\phi$, instead of $H_{\mathrm{osc}} \sim m_\phi$ in the original setup. Therefore, we call this scenario the *supercooled audible axion*. This modification will lead to three main results:

- Due to the decreased Hubble parameter compared to the original scenario, tachyonic growth becomes much more rapid relative to the expansion rate of the Universe. This enables GW production for small $\alpha \sim 1$.
- The relative energy density of the ALP at the onset of oscillations is enhanced, such that the scaling of the GW amplitude changes to $\Omega_{\mathrm{GW}} \sim (f_\phi / M_{\mathrm{Pl}})^2$. This opens up the testable parameter space towards smaller decay constants.
- Tachyonic production of SM photons becomes possible, i.e., the mechanism does not rely on the existence of a dark gauge boson.

In chapter 9, we first introduce the concept of axion-like particles, the misalignment mechanism, and discuss how a coupling to a (dark) photon is generated. Then, we review the minimal audible axion mechanism and explain how the axion can source a period of supercooling in chapter 10. In the subsequent chapter 11, we apply the modified setup to ALP-dark photon systems, before investigating GWs from SM photons in 12.

9

AXION-LIKE PARTICLES

The QCD axion ϕ was proposed as a solution to the strong CP problem [51]. This is achieved by a coupling of the form $(\phi/f_\phi)G_{\mu\nu}\tilde{G}^{\mu\nu}$, where $G_{\mu\nu}$ and $\tilde{G}^{\mu\nu}$ denote the gluonic field strength tensor and its dual. As QCD undergoes confinement, $G_{\mu\nu}\tilde{G}^{\mu\nu}$ receives a vev and generates an axion potential of the form

$$V_{\mathrm{QCD}}(\phi) = \chi(T)\left(1 - \cos\left(\frac{\phi}{f_\phi}\right)\right) . \tag{9.1}$$

The functional shape reflects the periodicity of the QCD vacuum [436, 437]. For the QCD axion, the QCD topological susceptibility fixes the relation between the axion mass and decay constant, $\chi(T=0) = m_\phi^2 f_\phi^2$ [126], hence determines the height of the maxima. This quantity is connected to the pion decay constant and mass $\chi(T=0) \sim m_\pi^2 f_\pi^2$, relating m_ϕ and f_ϕ. In the case of ALPs, m_ϕ and f_ϕ are independent, since they are not associated with the QCD axial anomaly. These generalized pseudoscalar fields are the focus of this part of this work. As we present our results in the $m_\phi - f_\phi^{-1}$ plane, the QCD axion represents a special case, forming a line in the two-dimensional parameter space.

Inspired by the QCD axion, we employ the usual, T-independent approximation for the ALP potential [53]

$$V(\phi) = m_\phi^2 f_\phi^2\left(1 - \cos\left(\frac{\phi}{f_\phi}\right)\right) , \tag{9.2}$$

explicitly breaking the $U(1)_{\mathrm{PQ}}$ symmetry. We further assume that the spontaneous breaking of $U(1)_{\mathrm{PQ}}$, which generates the ALP as a Nambu-Goldstone boson, occurs during inflation; this is known as the *pre-inflationary* scenario [128]. Then, inhomogeneities are diluted away, and initial misalignment angle θ is homogeneous across the Universe. The Euler-Lagrange equation of motion in a FLRW Universe reads

$$\ddot{\phi} + 3H\dot{\phi} + \frac{\partial V(\phi)}{\partial \phi} = 0 , \tag{9.3}$$

where dots denote derivatives with respect to cosmic time. Due to Hubble friction, the ALP initially sits frozen at $\phi_i = \theta f_\phi$ until the Hubble parameter becomes of the order of the ALP

mass, $H_{\rm osc} \sim m_\phi$. From naturalness arguments [438], we typically have $\theta \sim \mathcal{O}(1)$ [129]. Subsequently, the ALP oscillates about the minimum, scaling as matter, $\rho_\phi \propto a^{-3}$, making it a viable DM candidate [128].

Probing ALPs experimentally is challenging due to their f_ϕ^{-1} suppressed couplings. To this end, ALP searches typically rely on the ALP-photon coupling

$$\mathcal{L}_{\phi\gamma\gamma} = -\frac{\phi}{f_\phi}\frac{g^2}{32\pi^2}F_{\mu\nu}\tilde{F}^{\mu\nu}\,, \tag{9.4}$$

where $F_{\mu\nu}$ is the electromagnetic field strength tensor with its dual $\tilde{F}^{\mu\nu}$; g is the corresponding gauge coupling. Such a coupling can, for example, be generated via a heavy quark q, which is charged under $U(1)_{\rm PQ}$ and $\mathrm{U}(1)_{\rm Y}$. The axion implementation into the SM via heavy quarks is known as the Kim-Shifman-Vainshtein-Zakharov axion [439, 440]. After $U(1)_{\rm PQ}$ symmetry breaking, the quarks obtain a mass $m_q \sim \mathcal{O}(f_\phi)$, and can be integrated out. This generates a coupling of the form (9.4) in the low-energy effective theory. Current constraints on the ALP parameter space inferred from the coupling to photons are found in [400].

Likewise, the ALP may couple to a dark photon X, i.e., an Abelian gauge field from an additional $U(1)_{\rm D}$ symmetry,

$$\mathcal{L}_{\phi XX} = -\frac{\phi}{f_\phi}\frac{g_{\rm D}^2}{32\pi^2}X_{\mu\nu}\tilde{X}^{\mu\nu}\,, \tag{9.5}$$

if the heavy quarks carry a $U(1)_{\rm D}$ charge. In the following chapters, we remain agnostic about the UV completion that generates the respective couplings, and study the phenomenology of the operators (9.4) and (9.5).

10

AUDIBLE AXIONS

We first introduce the original audible axion mechanism, where ALPs generate GW signals via a coupling to a dark photon field. Then, we describe our modification by a delayed onset of oscillations. Note that in the following, we will use ALP and axion interchangeably, i.e., the pseudoscalar is not required to solve the strong CP problem.

10.1 STANDARD MECHANISM

In the audible axion mechanism, a pseudoscalar ALP ϕ is coupled to a massless dark $U(1)_{\mathrm{D}}$ gauge field X [53], which has no couplings to the SM, hence is not thermalized. The action reads

$$\mathcal{S} = \int \mathrm{d}^4x\sqrt{-g}\left[\frac{1}{2}\partial_\mu\phi\partial^\mu\phi - V(\phi) - \frac{1}{4}X_{\mu\nu}X^{\mu\nu} - \frac{\alpha}{4f_\phi}\phi X_{\mu\nu}\tilde{X}^{\mu\nu}\right], \tag{10.1}$$

where α is the axion-dark photon coupling, f_ϕ is the ALP decay constant, g is the determinant of the FLRW metric, and $V(\phi)$ is the ALP potential (9.2). The dark electromagnetic field strength tensor is denoted by $X_{\mu\nu}$, while its dual is $\tilde{X}^{\mu\nu} = \epsilon^{\mu\nu\alpha\beta}X_{\alpha\beta}$, with $\epsilon^{\mu\nu\alpha\beta}$ being the Levi-Civita tensor. The line element is given by

$$ds^2 = a(\tau)^2(d\tau^2 - \delta_{ij}dx^i dx^j)\,, \tag{10.2}$$

where $a(\tau)$ is the scale factor, and τ denotes conformal time. Computing the Euler-Lagrange equation of motion for ϕ, we obtain

$$\phi'' + 2aH\phi' + a^2\frac{\partial V}{\partial\phi} = \frac{\alpha}{f_\phi}a^2\boldsymbol{E}\cdot\boldsymbol{B}\,, \tag{10.3}$$

where primes denote derivative with respect to conformal time. The Hubble parameter $H = a'/a^2$ enters as a friction term, and the right-hand side corresponds to the backreaction from the dark electromagnetic fields $\boldsymbol{E}$ and $\boldsymbol{B}$. In the misalignment mechanism, the ALP initially sits displaced from its minimum by $\phi_i = \theta f_\phi$ with the misalignment angle

$\theta \sim 1$. Oscillations around the minimum start as the Hubble parameter approaches the axion mass

$$H_{\rm osc,aa} \approx m_\phi \,. \tag{10.4}$$

This is related to the temperature of the thermal bath

$$T_{\rm osc,aa} \equiv \left(\frac{90}{\pi^2 g_\epsilon^{\rm osc,aa}}\right)^{\frac{1}{4}} \sqrt{m_\phi M_{\rm Pl}}\,, \tag{10.5}$$

where $M_{\rm Pl}$ is the Planck mass and $g_\epsilon^{\rm osc,aa}$ denotes the relativistic degrees of freedom. Hence, the initial relative energy density stored in the axion field reads

$$\Omega_{\phi,\rm osc}^{\rm aa} = \frac{V(\phi_i)}{3H_{\rm osc,aa}^2 M_{\rm Pl}^2} \approx \frac{1}{6}\left(\frac{\theta f_\phi}{M_{\rm Pl}}\right)^2 , \tag{10.6}$$

where $\rho_{\phi,\rm osc}^{\rm aa} = V(\phi_i) \approx \theta^2 m_\phi^2 f_\phi^2/2$. The last expression holds for small misalignment angles.

The Euler-Lagrange equation of motion for the dark photon is [401–404]

$$\left(\frac{\partial^2}{\partial\tau^2} - \boldsymbol{\nabla}^2 - \alpha\frac{\phi'}{f_\phi}\boldsymbol{\nabla}\times\right)\boldsymbol{X} = 0\,. \tag{10.7}$$

To investigate the gauge field dynamics in the presence of the axion, one quantizes the field as

$$\begin{aligned}\hat{X}^i(\boldsymbol{x},\tau) &= \int \frac{\mathrm{d}^3k}{(2\pi)^3}\hat{X}^i(\boldsymbol{k},\tau)\exp\left(i\boldsymbol{k}\boldsymbol{x}\right)\\ &= \sum_{\lambda=\pm}\int \frac{\mathrm{d}^3k}{(2\pi)^3} v_\lambda(k,\tau)\epsilon_\lambda^i(\boldsymbol{k})\hat{a}_\lambda(\boldsymbol{k})\exp\left(i\boldsymbol{k}\boldsymbol{x}\right) + \text{h.c.}\,,\end{aligned} \tag{10.8}$$

where the creation and annihilation operators satisfy $[\hat{a}_\lambda(\boldsymbol{k}), \hat{a}^\dagger_{\lambda'}(\boldsymbol{k}')] = (2\pi)^3\delta_{\lambda\lambda'}\delta(\boldsymbol{k}-\boldsymbol{k}')$ and the sum runs over the two photon helicities. The circular polarization vectors follow $\boldsymbol{k}\cdot\epsilon^\pm = 0$, $\boldsymbol{k}\times\epsilon^\pm = \mp ik\epsilon^\pm$, $\epsilon^\pm\cdot\epsilon^\pm = 0$, and $\epsilon^\pm\cdot\epsilon^\mp = 1$. A mode function $v_\lambda(k,\tau)$ then captures the time evolution of a dark photon mode with three-momentum $k = |\boldsymbol{k}|$. The decomposition (10.8) allows us to rewrite eq. (10.7) in Fourier space via the mode functions,

$$v_\pm''(k,\tau) + \left(k^2 \mp k\frac{\alpha}{f}\phi'\right)v_\pm(k,\tau) = 0\,, \tag{10.9}$$

where the momenta k are expressed in comoving coordinates. This is nothing but the equation of motion of a harmonic oscillator in an expanding spacetime. We see that the presence of the axion modifies the dispersion relation of the dark photon,

$$\omega_\pm^2 = k^2 \mp k\frac{\alpha}{f}\phi'\,. \tag{10.10}$$

As the axion starts to oscillate, hence picks up a non-vanishing velocity $\phi' \neq 0$, we find a range of comoving momenta

$$0 < k < \alpha \frac{|\phi'|}{f_\phi} \,, \tag{10.11}$$

that have an imaginary effective oscillation frequency, $\omega^2 < 0$, for one dark photon helicity at a time. In the instability band (10.11) the solution to eq. (10.9) changes from an oscillating behavior to an exponentially growing one,

$$v(k,\tau) \propto \exp(|\omega|\tau) \,. \tag{10.12}$$

Therefore, the presence of the axion induces a tachyonic instability in the dark photon equation of motion, sourcing the exponential production of dark photon modes in a distinct momentum band. This is similar to the tachyonic resonance that we have encountered in chapter 7, where an imaginary effective mass led to the exponential production of scalar field fluctuations.

The production of dark photons generates anisotropies in the energy-momentum tensor of the Universe, acting as a source of GWs [6, 53, 295, 417]. Intriguingly, as the population of dark photons is dominated by the helicity is amplified first, the resulting SGWB is highly chiral, providing a smoking-gun signature at future observatories.[1] The energy density available for GW emission is $\propto (f_\phi/M_{\rm Pl})^2$ (cf. eq. (10.6)). Therefore, the GW peak amplitude scales as [53]

$$\tilde{\Omega}_{\rm GW,0} \sim (\Omega^{\rm aa}_{\phi,\rm osc})^2 \left(\frac{a_\star H_\star}{k_{\rm peak}}\right)^2 \sim \left(\frac{f_\phi}{M_{\rm Pl}}\right)^4 \,, \tag{10.13}$$

hence is strongly suppressed for small decay constants. Furthermore, to open the tachyonic band for a sufficient amount of time to have efficient dark photon production, a large coupling $\alpha \gtrsim 20$ is required [53, 417].[2]

10.2 SUPERCOOLED AUDIBLE AXIONS

Let us now introduce the supercooled audible axion. To this end, we first provide a specific mechanism which leads to a delayed onset of axion oscillations: trapped misalignment [54, 430–435]. This modification of the minimal misalignment mechanism is motivated, for example, by the fact that quantum gravity generally does not respect global symmetries [443]. That is, the global $\mathrm{U}(1)_{\rm PQ}$ may not be exact in the UV, such that the axion

1 Note that the chirality is partially washed out by backreaction effects for certain values of the axion-photon coupling [417].

2 Such a large coupling can be generated by introducing multiple axion fields in the UV [441, 442].

potential receives additional explicit $\mathrm{U}(1)_{\mathrm{PQ}}$ breaking operators. One explicit example is a temperature-dependent axion potential of the form [54]

$$V(\phi, T) = m_\phi^2 f_\phi^2 \left(1 - \cos\frac{\phi}{f_\phi}\right) + \Lambda^{4-q}\, T^q \left(1 - \cos\left(n\frac{\phi}{f_\phi} + \delta\right)\right) , \tag{10.14}$$

where Λ is the scale of the explicit $\mathrm{U}(1)_{\mathrm{PQ}}$ symmetry breaking effects and q controls the T-dependence. The displacement of the new contribution from the original ALP potential is determined by δ, while the integer n gives the number of false minima. It is then straightforward to check that the ALP can initially, at $H \sim m_\phi$, be trapped by a barrier between one of the false vacua and the true vacuum. The pseudoscalar becomes free to roll once at the temperature T_{osc}, defined by the conditions

$$\frac{\partial V(\phi, T)}{\partial \phi} = 0\,, \qquad \frac{\partial^2 V(\phi, T)}{\partial \phi^2} = 0\,. \tag{10.15}$$

The ratio between the oscillation temperature in the original audible axion mechanism and the one in the case of axion trapping can then be expressed by the supercooling ratio

$$r_{\mathrm{sc}} \equiv \frac{T_{\mathrm{osc}}}{T_{\mathrm{osc,aa}}}\,. \tag{10.16}$$

Via eq. (10.5), we can estimate the oscillation temperature as

$$T_{\mathrm{osc}} \approx r_{\mathrm{sc}} \sqrt{m_\phi M_{\mathrm{Pl}}}\,. \tag{10.17}$$

Inserting this expression into eqs. (10.15) and solving for r_{sc}, we find the corresponding new physics scale to achieve a certain supercooling ratio

$$\Lambda \sim \left(r_{sc}^{-q} m_\phi^{2-q/2} M_{\mathrm{Pl}}^{-q/2} f_\phi^2\right)^{\frac{1}{4-q}}\,. \tag{10.18}$$

This quantity is shown in fig. 10.1 as a function of r_{sc} for varying f_ϕ and q, and fixed m_ϕ, n, and δ. We see that we can easily generate large temperature ratios r_{sc} by varying the scale Λ. Therefore, we take the supercooling ratio as a free parameter in the following and express all quantities through r_{sc}. Then, our results can easily be mapped to other mechanisms that delay the onset of axion oscillations.

For a given r_{sc}, the axion energy density relative to the total energy density of the Universe reads

$$\Omega_{\phi,\mathrm{osc}} = r_{\mathrm{sc}}^{-4}\, \Omega_{\phi,\mathrm{osc}}^{\mathrm{aa}}\, \frac{g_\epsilon^{\mathrm{osc,aa}}}{g_\epsilon^{\mathrm{osc}}}\,, \tag{10.19}$$

i.e., is enhanced compared to the original setup (cf. eq. (10.6)). Here we have used the T^4 scaling of the radiation energy density, while $\rho_{\phi,\mathrm{osc}} \approx \theta^2 m_\phi^2 f_\phi^2/2$ is unchanged. For

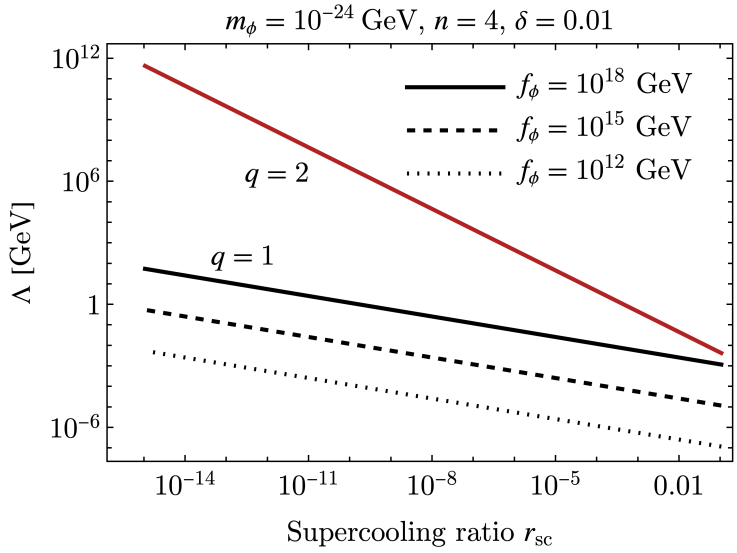

Figure 10.1: UV scale Λ, which enters the trapping potential, as a function of the supercooling ratio $r_{\rm sc}$, for fixed m_ϕ, n, δ, and three values of f_ϕ. By adjusting Λ, we can achieve a delay of axion oscillations down to very small temperatures $T_{\rm osc} \ll T_{\rm osc,aa}$. Figure created by C. Gerlach.

sufficiently small $r_{\rm sc}$, the axion energy density $\rho_{\phi,\rm osc}$ starts to exceed the radiation energy density. By solving $\rho_{\phi,\rm osc} = \rho_{\rm rad}(T_i)$, we find

$$r_{{\rm sc},i} = \left(\frac{g_\epsilon^{\rm osc,aa}}{g_\epsilon^{\rm osc}}\right)^{\frac{1}{4}} \left(\frac{\theta f_\phi}{\sqrt{6} M_{\rm Pl}}\right)^{\frac{1}{2}} \approx \left(\frac{f_\phi}{M_{\rm Pl}}\right)^{\frac{1}{2}} . \tag{10.20}$$

If $T_{\rm osc} < T_i$, or equivalently, $r_{\rm sc} < r_{{\rm sc},i}$, the ALP dominates the energy density of the Universe, $\Omega_{\phi,\rm osc} \to 1$. In this case, the Universe undergoes a period of axion-induced thermal inflation, which ends with the onset of oscillations. This is analogous to the dynamics that typically occurs in strongly supercooled FOPTs (see part ii), where a scalar field drives an exponential expansion before the PT occurs.

The Hubble parameter at $T_{\rm osc}$ reads

$$H_{\rm osc} = \max\left\{ m_\phi r_{\rm sc}^2 \left(\frac{g_\epsilon^{\rm osc}}{g_\epsilon^{\rm osc,aa}}\right)^{\frac{1}{2}}, \frac{\theta m_\phi f_\phi}{\sqrt{6} M_{\rm Pl}} \right\} . \tag{10.21}$$

Here, the first expression applies if the Universe remains radiation-dominated. Then, the Hubble parameter is simply decreased $\propto r_{\rm sc}^2$ compared to original setup (cf. eq. (10.4)). If the ALP dominates the expansion rate, however, we obtain the second term in eq. (10.21) via the Friedmann equation (2.15). In the following, we first revisit the ALP-dark photon system in this modified setup. Subsequently, we show that delayed axion oscillations allow for replacing the dark gauge field with the SM photon.

11

SUPERCOOLED AXION-DARK PHOTON SYSTEMS

We start with our analysis of trapped ALPs that couple to a dark photon, which we assume to be secluded from the SM. To this end, we first clarify the involved temperature scales and the resulting cosmic history. In addition, we give some analytic estimates of the key quantities.

The ALP starts to oscillate at $T_{\rm osc}$ defined by eq. (10.16), triggering the exponential production of dark photon quanta via the tachyonic instability. The instability band is given by eq. (10.11). Thus, the fastest growing dark photon mode is the one with

$$\tilde{k}_{\rm osc} = \frac{\alpha}{2f_\phi}|\phi'| = \tilde{\omega}_{\rm osc}\,, \tag{11.1}$$

hence the growth rate coincides with the momentum of the mode. To provide some intuitive understanding, the evolution of ϕ can be approximated in physical time by [53] $\phi(t) = \phi_i(a_{\rm osc}/a)^{\frac{3}{2}}\cos(m_\phi t)$, as the axion mass m_ϕ dictates the oscillation frequency. Solving for the envelope of $|\phi'|$ at the onset of oscillations [53],

$$|\phi'|_{a=a_{\rm osc}} = \left|\frac{{\rm d}\phi}{{\rm d}t}\frac{{\rm d}t}{{\rm d}\tau}\right|_{a=a_{\rm osc}} = \theta f_\phi m_\phi a_{\rm osc}\,, \tag{11.2}$$

we have

$$\tilde{k}_{\rm osc} = \frac{\alpha}{2}\theta m_\phi a_{\rm osc}\,. \tag{11.3}$$

The spectral peak of the amplified dark photon modes is hence mainly determined by the ALP mass.

The energy density of the dark photon reads

$$\rho_X = \frac{1}{a^4}\sum_{\lambda=\pm}\int\frac{{\rm d}^3k}{(2\pi)^3}\left(|v_\lambda'(k,\tau)|^2 + k^2|v_\lambda(k,\tau)|^2\right)\,. \tag{11.4}$$

Since this expression depends on the square of the mode functions, we conclude that the energy density grows with $\rho \propto \exp(2|\omega|\tau)$. We define the temperature $T_\star$ as the time when the ALP has transferred most of its energy to the dark gauge field such that

$\rho_X(\tau_\star) \sim \rho_\phi(\tau_\star)$, which also sets the relevant scale for GW emission. The timescale of dark photon growth can thus be estimated by setting

$$\rho_X(\tau_\star) \approx \rho_X(\tau_{\rm osc}) \exp(2\langle\tilde{\omega}_{\rm osc}\rangle\tau_\star)\,, \tag{11.5}$$

where $\langle\tilde{\omega}_{\rm osc}\rangle$ is the peak growth rate, averaged over one oscillation period. The evaluation of this expression, which is relegated to appendix 14.A, yields

$$\frac{a_\star}{a_{\rm osc}} \approx 1 + \frac{\pi}{\alpha\theta} r_{\rm sc}^2 \ln\left(\frac{128\pi^2}{\alpha^4\theta^2}\frac{f_\phi^2}{m_\phi^2}\right)\,, \tag{11.6}$$

in terms of our model parameters. From this we directly see that a large amount of supercooling, $r_{\rm sc} \ll 1$, significantly suppresses the time required for the amplification of dark vector modes.

To have efficient tachyonic growth, the dark photon growth timescale should be smaller than the oscillation time.[1] This comes from the fact that the unstable dark photon helicity switches when ϕ' changes sign. As the conformal oscillation frequency is am_ϕ, we demand $(2\omega)^2 = -(am_\phi)^2$, where ω is given by the dominant helicity in eq. (10.10). The solution yields

$$\frac{a_{\rm close}}{a_{\rm osc}} = (\alpha\theta)^{\frac{2}{3}}\,. \tag{11.7}$$

This is the approximate scale factor ratio at the time where the tachyonic resonance ceases to be efficient. The comparison of eqs. (11.6) and (11.7) then gives us the minimal value of α by setting

$$a_\star < a_{\rm close}\,. \tag{11.8}$$

Since $a_\star$ is suppressed by $r_{\rm sc}^2$ it becomes clear why a delay of axion oscillations allows for much smaller α. For $\theta \sim 1$, we find $\alpha \sim 1$ to be sufficient in most of the parameter space (see appendix 14.A for details).

The produced dark photons henceforth free-stream as dark radiation and contribute to the effective number of relativistic degrees of freedom $N_{\rm eff}$. The ALP, on the other hand, scales as matter after photon production becomes inefficient. If its decay rate to dark photons is small, such that its lifetime is larger than the age of the Universe, it contributes to the DM density. If the decay rate is sufficiently large, the axion depletes its remaining energy density via perturbative decays into gauge field quanta, inducing an additional contribution to $N_{\rm eff}$.

1 Note that this is a conservative criterion as we discuss in sec. 11.2.

11.1 COSMOLOGICAL CONSTRAINTS

Before delving into the numerical study of the axion-dark photon dynamics, we first derive the constraints on the model to ensure a consistent cosmic history. To this end, we employ the analytic relations we have established above.

AMOUNT OF SUPERCOOLING. Regarding the maximum amount of supercooling that we may impose, let us note that eq. (10.20) defines a strict upper bound on $T_{\rm osc}$. If $r_{\rm sc} < r_{{\rm sc},i}$, the ALP is the dominant energy component of the Universe at the time of production. Due to the absence of couplings to the SM, the Universe would remain dominated either by ALPs or dark photons after the tachyonic resonance, which is inconsistent with observations.

A stricter limit is, however, given by the dark photon contribution to the relativistic degrees of freedom at recombination,

$$\begin{aligned}\Delta N_{\rm eff} &= \frac{8}{7}\left(\frac{11}{4}\right)^{\frac{4}{3}} \frac{\rho_X}{\rho_\gamma}\bigg|_{T=T_{\rm rec}} \\ &= \frac{8}{7}\left(\frac{11}{4}\right)^{\frac{4}{3}} \frac{g_\epsilon^\star}{g_\gamma}\left(\frac{g_s^0}{g_s^\star}\right)^{\frac{4}{3}} \Omega_{\phi,\star} < 0.3\,.\end{aligned} \tag{11.9}$$

Here, the limit results from the 2018 Planck dataset [14] and ρ_γ denotes the energy density of the SM photon with $g_\gamma = 2$. Additionally, we have expressed the energy densities at recombination by their values at dark photon production $T_\star$. Furthermore, we have used the fact that a significant fraction of the ALP energy density is converted to dark photons and set $\rho_{X,\star} = \rho_{\phi,\star}$, representing a conservative upper limit.

From the onset of oscillations, the ALP energy density is enhanced compared to the background due to its matter-like scaling,

$$\Omega_{\phi,\star} = \Omega_{\phi,{\rm osc}} \frac{a_\star}{a_{\rm osc}}\,, \tag{11.10}$$

where $a_\star/a_{\rm osc}$ is given by eq. (11.6). Via eq. (10.19), we can then translate the bound on $N_{\rm eff}$ into a minimal supercooling ratio,

$$r_{\rm sc}^{\rm min} \simeq 1.25 \left(\frac{g_s^0}{g_s^\star}\right)^{\frac{1}{3}} \left(\frac{g_\epsilon^\star g_\epsilon^{\rm osc,aa}}{g_\gamma g_\epsilon^{\rm osc}}\right)^{\frac{1}{4}} \left(\frac{a_\star}{a_{\rm osc}}\right)^{\frac{1}{4}} \left(\frac{\theta f_\phi}{M_{\rm Pl}}\right)^{\frac{1}{2}}\,, \tag{11.11}$$

for which the model is consistent. We set $r_{\rm sc} = r_{\rm sc}^{\rm min}$ in the following, as we aim to study the upper limit on the GW amplitude from axion-photon systems.

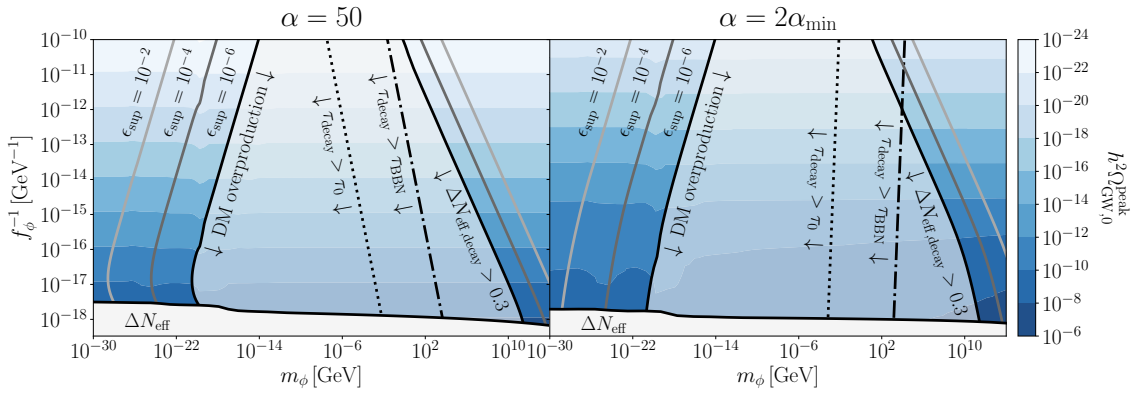

Figure 11.1: Overview of the available parameter space for supercooled ALP-dark photon systems, employing $\alpha = 50$ (left) and $\alpha = 2\alpha_{\min}$ (right). The white-shaded region is excluded due to a violation of the N_{eff} constraint, even without supercooling. The dotted and dash-dotted lines indicate where the axion is stable until today and BBN, respectively. Constraints from DM overproduction and N_{eff} violation from late axion decays are displayed by the solid lines for $\epsilon_{\sup} \in \{10^{-6}, 10^{4}, 10^{-2}\}$. The color coding reflects our estimate of the GW peak amplitude today (11.28).

DARK MATTER AND AXION DECAYS. For a given amount of supercooling, we still need to ensure that the model neither overproduces DM nor dark radiation from axions decaying into dark photons. Since these are two distinct scenarios, we split the parameter space into heavy axions that decay before BBN and cosmologically stable axions that constitute DM. To this end, we compare the ALP decay rate to the Hubble parameter at BBN,

$$\Gamma_{\phi\to XX} = \frac{\alpha^2 m_\phi^3}{64\pi f_\phi^2} > H_{\text{BBN}} = \left(\frac{\pi^2}{90} g_\epsilon^{\text{BBN}} \frac{T_{\text{BBN}}^4}{M_{\text{Pl}}^2}\right)^{\frac{1}{2}} , \tag{11.12}$$

where $T_{\text{BBN}} \sim$ MeV.

The axion energy density after dark photon production is parametrized by

$$\Omega_\phi^{\text{after}} = \epsilon_{\sup} \Omega_{\phi,\star} , \tag{11.13}$$

where $\epsilon_{\sup}$ denotes the suppression of the abundance through the tachyonic resonance. This quantity can only be accurately determined by a lattice simulation (see sec. 11.2 and ref. [417]). Since this is beyond the scope of this work, we simply treat $\epsilon_{\sup}$ as a free parameter and compute its upper bound.

Regarding the light ALP parameter space, we redshift the relic abundance until today and compare the result to the observed DM abundance via eqs. (2.19) and (2.28),

$$h^2\Omega_{\phi,0} = \epsilon_{\sup} \Omega_{\phi,\star} \left(\frac{H_\star}{H_{100}}\right)^2 \left(\frac{T_0}{T_\star}\right)^3 \frac{g_s^0}{g_s^\star} \leq 0.12 , \tag{11.14}$$

Relegating the details to appendix 14.B, we find

$$\epsilon_{\rm sup}^{\rm DM} \lesssim 2.89 \times 10^{-9} \left(\frac{g_\epsilon^\star}{g_\epsilon^{\rm osc}} \frac{a_\star}{a_{\rm osc}}\right)^{\frac{3}{4}} \left(\frac{\rm eV}{m_\phi}\right)^{\frac{1}{2}} \left(\frac{10^{10}\,{\rm GeV}}{\theta f_\phi}\right)^{\frac{1}{2}} . \tag{11.15}$$

This defines the required suppression of the ALP abundance through the resonance to not overproduce DM. That is, large masses and decay constants necessitate a very efficient energy transfer through the tachyonic resonance.

In the heavy axion parameter space, the contribution to $N_{\rm eff}$ via late decays to dark photons reads

$$\Delta N_{\rm eff}^{\rm decay} = \frac{8}{7}\left(\frac{11}{4}\right)^{\frac{4}{3}} \frac{g_\epsilon^\star}{g_\gamma} \left(\frac{g_s^0}{g_s^\star}\right)^{\frac{4}{3}} \epsilon_{\rm sup} \Omega_{\phi,\star} \frac{a_{\rm decay}}{a_\star} . \tag{11.16}$$

Here we include the suppression of the axion abundance through the resonance $\epsilon_{\rm sup}$, as well as its subsequent enhancement $\propto a_{\rm decay}/a_\star$ from the time of production until the onset of perturbative decays. The detailed derivation is again left for appendix 14.B. Our final result, i.e., the upper limit on $\epsilon_{\rm sup}$ for the heavy axion regime, is

$$\epsilon_{\rm sup}^{\rm decay} \lesssim 6.64 \times 10^{-8} \left(g_\epsilon^\star\right)^{-\frac{1}{4}} \left(g_s^\star\right)^{\frac{1}{3}} \left(\frac{a_\star}{a_{\rm osc}}\right)^{\frac{3}{4}} \frac{\alpha}{\theta^{\frac{1}{2}}} \frac{m_\phi}{\rm GeV} \left(\frac{10^{10}\,{\rm GeV}}{f_\phi}\right)^{\frac{3}{2}} . \tag{11.17}$$

In fig. 11.1, we show an overview of the available parameter space in the $m_\phi - f_\phi^{-1}$ plane, imposing $\theta = 1$. Here we set $\alpha = 50\,(2\alpha_{\rm min})$ in the left (right) panel, with $\alpha_{\rm min} \sim 1$ in a substantial fraction of the parameter space (cf. appendix 14.A). The white-shaded region at the bottom is excluded due to a violation of the $N_{\rm eff}$ constraint in the limit of no supercooling. The dotted (dash-dotted) line indicates the parameter space where the axion is stable until today (BBN). Constraints by DM overproduction are shown by the solid lines in the small-m_ϕ regime for $\epsilon_{\rm sup} \in \{10^{-6}, 10^{-4}, 10^{-2}\}$. Let us note that previous lattice results indicate $\epsilon_{\rm sup} \approx 10^{-2}$ for $\alpha \gtrsim 20$, which, in the original setup, corresponds to the lower threshold on the ALP-dark photon coupling for the tachyonic resonance to be effective. In our case, dark photon production occurs for $\alpha \gtrsim 1$. The smaller value of α could then affect the efficiency of the dark photon backreaction, allowing for a suppressed $\epsilon_{\rm sup}$. While relegating a lattice study of the small-coupling regime to the future, we indicate the effect of small $\epsilon_{\rm sup}$ on the parameter space.

The limits in the large-m_ϕ range stem from the contribution to $N_{\rm eff}$ from late axion decays. In addition, the color coding shows the projected GW amplitudes (see below). We see that the cosmological limits translate in two distinct regions in the ALP parameter space. A small suppression of the axion abundance, hence large $\epsilon_{\rm sup}$, severely constrains the viable model parameters.

11.2 NUMERICAL SIMULATIONS

So far, we have introduced the setup and derived cosmological constraints on the model parameters. In the following, we solve the axion-dark photon dynamics numerically, which is the basis for our GW computation in the next section. In addition, the numerical study provides a verification of our analytic growth time (11.6) and band closure (11.7) estimates.

For our numerical simulation of the axion-dark photon system, we follow the approach from refs. [6, 53, 423]. That is, we first replace the backreaction term in the axion equation of motion (10.3) by

$$\boldsymbol{E}\cdot\boldsymbol{B} \quad \to \quad \langle 0|\boldsymbol{E}\cdot\boldsymbol{B}|0\rangle = \frac{1}{a^4}\sum_{\lambda=\pm}\lambda\int\frac{\mathrm{d}^3k}{(2\pi)^3}\mathrm{Re}\left(v_\lambda(k,\tau), v_\lambda'(k,\tau)\right) . \tag{11.18}$$

This effectively treats the right-hand side of eq. (10.3) as a mean-field, thus only approximates the dark photon backreaction on the axion dynamics. We will soon comment on the shortcomings of this approach. The axion is trapped and misaligned, i.e., its initial conditions read

$$\phi_i = \theta f_\phi\,, \qquad\qquad \phi_i' = 0\,. \tag{11.19}$$

Regarding the dark photon mode functions, we choose Bunch-Davies initial conditions [381]

$$v_\lambda(k,\tau\ll\tau_{\rm osc}) = \frac{1}{\sqrt{2k}}\exp(-ik\tau)\,, \qquad v_\lambda'(k,\tau\ll\tau_{\rm osc}) = -i\sqrt{\frac{k}{2}}\exp(-ik\tau)\,. \tag{11.20}$$

This is a reasonable assumption in the absence of couplings to the SM. Our results, however, do note crucially depend on the choice of initial conditions.

Equipped with our initial conditions, we are now ready to solve the coupled axion-dark photon equations of motion numerically. To this end, we evolve eqs. (10.3) and (10.7) for $N_k = \mathcal{O}(10^4)$ dark photon modes from $T_{\rm osc}$ to some later time when the axion has transferred most of its energy to the gauge field. The results for $m_\phi = 10^{-11}\,\mathrm{GeV}$, $f_\phi = 10^{17}\,\mathrm{GeV}$, $\theta = 1.2$, and $\alpha \in \{20, 30, 40, 55\}$ are shown in fig. 11.2. These model parameters correspond to benchmark 2 from ref. [53], hence provide a cross check of our numerics and illustrate the effect of supercooling. The upper panel represents the original setup without supercooling, such that $H_{\rm osc} \approx m_\phi$. In the lower panel, we impose the maximum amount of supercooling as dictated by eq. (11.11), hence $H_{\rm osc} < m_\phi$. The dark blue (dark red) lines indicate the comoving energy density of the ALP (dark photon) as a function of the scale factor $a/a_{\rm osc}$. All quantities are redshifted to today and normalized to the present

DM abundance.[2] The black dashed line is our growth time estimate (11.6), while the red dotted line displays the estimated time of band closure (11.7).

First, let us note that after the onset axion oscillations, efficient dark photon production starts until we reach $\rho_X \sim \rho_\phi$. Then, backreaction from the dark photon becomes important, and the energy density of the ALP starts to decrease, i.e., we observe a deviation from the matter-like scaling. This moment is very well captured by our growth time estimate. In addition, we observe that tachyonic growth quickly becomes inefficient as $a_\star > a_{\rm close}$, as seen in the two rightmost upper panels. While dark photon production is barely possible for $\alpha = 30$ where $a_\star \sim a_{\rm close}$, it quickly shuts off for $\alpha = 20$. This situation changes when axion oscillations are delayed. As the dynamics take place at a lower temperature, hence a smaller Hubble parameter $H_{\rm osc} \propto r_{\rm sc}^2$, the dark photon modes can grow more efficiently compared to the expansion rate of the Universe. This is reflected in the overall timescales of $a_\star/a_{\rm osc} \sim \mathcal{O}(1)$, while $a_\star/a_{\rm osc} \sim \mathcal{O}(10)$ without supercooling. As a consequence, much smaller values of α are allowed, as is clearly verified by the numerical results.[3] In addition, the relic dark photons fulfill the upper bound from the $N_{\rm eff}$ constraint, as indicated by the black dash-dotted line. This confirms our analytic computation of the maximum amount of supercooling (11.11).

To conclude, let us note that while our linearized simulation gives us reliable insights into the initial stages of tachyonic growth where GWs are predominantly produced, it does not capture the late stages accurately. Specifically, already in the case of no supercooling, the simulation indicates a suppression of the axion abundance by $\epsilon_{\rm sup} \sim \mathcal{O}(10^{-10})$ through the tachyonic resonance and the subsequent phase of parametric resonance [53]. It was shown on the lattice [417] that this is an overestimation. Higher-order backreaction effects, which are not included in the linearized approach, decrease the efficiency of energy transfer to the dark photon, restricting $\epsilon_{\rm sup} \sim \mathcal{O}(10^{-2})$. It is, however, unclear how this is modified in our setup of supercooled oscillations and the resulting small axion-dark photon couplings. This is the reason why we do not extract $\epsilon_{\rm sup}$ from the numerical solution of the equations of motion, but rather treat it as a free parameter and relegate a lattice study to the future.

2 Note that the different redshift behavior of the dark photon and axion induces in the large separation between the abundances today. At the time of production, we have indeed $\rho_\phi(\tau_\star) = \rho_X(\tau_\star)$.

3 Note that in the case of supercooling, we do not plot the full evolution and only focus on the initial stage of tachyonic growth to highlight the differences in the growth time.

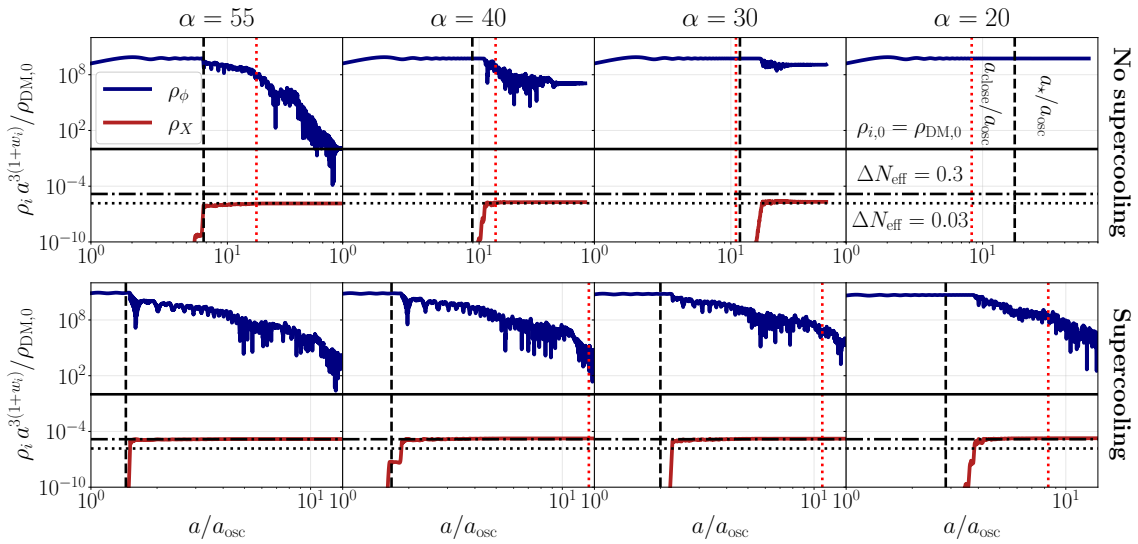

Figure 11.2: Benchmark simulations of the supercooled ALP-dark photon system, employing $N_k = \mathcal{O}(10^4)$ dark photon modes, $m_\phi = 10^{-11}\,\text{GeV}$, $f_\phi = 10^{17}\,\text{GeV}$, and $\theta = 1.2$. The upper panel corresponds to the original setup without supercooling, while we impose delayed oscillations in the lower panel. Furthermore, we vary α across the columns. The dark blue (dark red) line is the comoving ALP (dark photon) energy density as a function of the scale factor $a/a_{\rm osc}$, where we incorporate the redshift factor until today and normalize to the present DM energy density. The black solid (dash-dotted) line corresponds to the constraint from DM overproduction ($N_{\rm eff}$). Our analytic estimates of the growth time and band close show a great agreement with the numerical results, as displayed by the black dashed and red dotted lines.

11.3 GRAVITATIONAL WAVE SIGNAL

Let us now study the GW signal from supercooled axion-dark photon systems. First, we numerically compute the spectrum from our simulations, which we then parametrize and fit; this allows for an investigation of the entire parameter space without running simulations for every parameter combination. Subsequently, we map the GW prospects at future observatories to the $m_\phi - f_\phi^{-1}$ plane, demonstrating that trapped axions significantly extend the testable parameter space.

NUMERICAL RESULTS AND FITS. From the time evolution of the simulated mode functions, one can directly compute the resulting GW spectrum. To this end, one solves the linearized Einstein equations, which, in a radiation-dominated Universe, read

$$\left(\frac{\partial^2}{\partial\tau^2} + k^2\right) a(\tau) h_{ij}(\boldsymbol{k},\tau) = \frac{2a(\tau)}{M_{\rm Pl}^2}\Pi_{ij}(\boldsymbol{k},\tau)\,. \tag{11.21}$$

Here, h_{ij} is a perturbation around flat spacetime, and

$$\Pi_{ij}(\boldsymbol{k},\tau) = \frac{\Lambda_{ij}^{ab}}{a(\tau)^2}\int\frac{\mathrm{d}^3q}{(2\pi)^3}\left(E_a(\boldsymbol{q},\tau)E_b(\boldsymbol{k}-\boldsymbol{q},\tau) + B_a(\boldsymbol{q},\tau)B_b(\boldsymbol{k}-\boldsymbol{q},\tau)\right)\,, \tag{11.22}$$

is the anisotropic stress-energy of the dark photon, with Λ_{ij}^{ab} being the TT projector. This reveals the direct connection between GWs and the dark electromagnetic fields. From the solution of eq. (11.21), one can compute the GW energy density

$$\rho_{\rm GW} = \frac{M_{\rm Pl}^2}{4}\langle\dot{h}_{ij}h^{ij}\rangle\,, \tag{11.23}$$

via the dark photon mode functions and their derivatives. As this result has not been obtained here for the first time, we refrain from including the explicit computation and refer the reader to ref. [53].

In order to predict the GW spectrum for a large number of model parameters, we employ the parametrization from refs. [6, 295],[4]

$$\Omega_{\rm GW,0}(f) = \mathcal{A}_s\tilde{\Omega}_{\rm GW,0}\frac{\left(\tilde{f}/f_s\right)^p}{1+\left(\tilde{f}/f_s\right)^p\exp\left[\gamma\left(\tilde{f}/f_s-1\right)\right]}\,, \tag{11.24}$$

where $\tilde{f} = f/\tilde{f}_0$. In the above expression, $\mathcal{A}_s$, f_s, γ, and p are free parameters that are fitted to our numerical benchmark simulations. $\tilde{\Omega}_{\rm GW,0}$ and $\tilde{f}_0$ denote the peak amplitude

4 Note that ref. [420] employs a different parametrization, motivated by lattice simulations [417], is proposed, which indicates a polynomial decline in the UV.

$\mathcal{A}_s$	f_s	γ	p
268.57	0.46	8.34	1.75

Table 11.1: Best-fit parameters for the GW parametrization (11.24).

and frequency today. These parameters can be estimated at the time of production as [6, 53, 138, 294, 295]

$$\tilde{\Omega}_{\mathrm{GW},\star} = c_{\mathrm{eff}}^2\, \Omega_{\phi,\star}^2 \left(\frac{H_\star a_\star}{2\tilde{k}_\star}\right)^2 , \tag{11.25}$$

$$\tilde{f}_{\mathrm{GW},\star} = 2\frac{\tilde{k}_\star}{a_\star} = \alpha\theta m_\phi \left(\frac{a_{\mathrm{osc}}}{a_\star}\right)^{\frac{3}{2}} , \tag{11.26}$$

where c_{eff} is an efficiency factor that we absorb into $\mathcal{A}_s$. The first equation is a familiar expression, as it was used in, e.g., sec. 7.3 and refs. [140, 291] to estimate the GW spectrum from tachyonic preheating. Also, note that the factor two comes from the fact that the GW peak frequency is formed by the addition of two photon momenta [53]. For the last expression, we have evaluated eq. (11.1) at the time of production using our growth time estimate (11.6). We now employ eqs. (10.21), (11.1), and (11.10) to express the peak amplitude in terms of our model parameters. This yields[5]

$$\tilde{\Omega}_{\mathrm{GW},\star} \simeq 0.99 \frac{(g_s^\star)^{\frac{4}{3}}}{g_\epsilon^\star} \left(\frac{f_\phi}{M_{\mathrm{Pl}}}\right)^2 \frac{1}{\alpha^2} . \tag{11.27}$$

From this expression, we directly note two differences compared to the original setup.

First, the scaling of the amplitude changes from $(f_\phi/M_{\mathrm{Pl}})^4$ to $(f_\phi/M_{\mathrm{Pl}})^2$, that is, the signal is enhanced for small decay constants. This is a result of the enhancement of the relative axion energy density $\Omega_{\phi,\star} \propto r_{\mathrm{sc}}^{-4}$. At the same time, however, the Hubble parameter at production decreases $H_\star \propto r_{\mathrm{sc}}^2$. Therefore, the relevant fluctuation scale moves deeper into the horizon, weakening the signal. This leaves an overall $r_{\mathrm{sc}}^{-4} \sim (M_{\mathrm{Pl}}/f_\phi)^2$ enhancement of the GW spectrum.

Second, the amplitude apparently becomes independent of the misalignment angle θ. Since we fix the onset of oscillations by the requirement that the N_{eff} constraint is respected, we implicitly fix the relative axion energy density at the start of the simulation. A smaller θ then solely leads to a longer period of trapping. Note, however, that smaller misalignment angles require a larger coupling α for tachyonic growth to be efficient (cf. eqs. (11.6) and (11.7)). This again reduces the amplitude. For more details, see appendices 14.A and 14.C.

5 Note that this expression already includes the best-fit value for the amplitude, $\mathcal{A}_s = 268.57$.

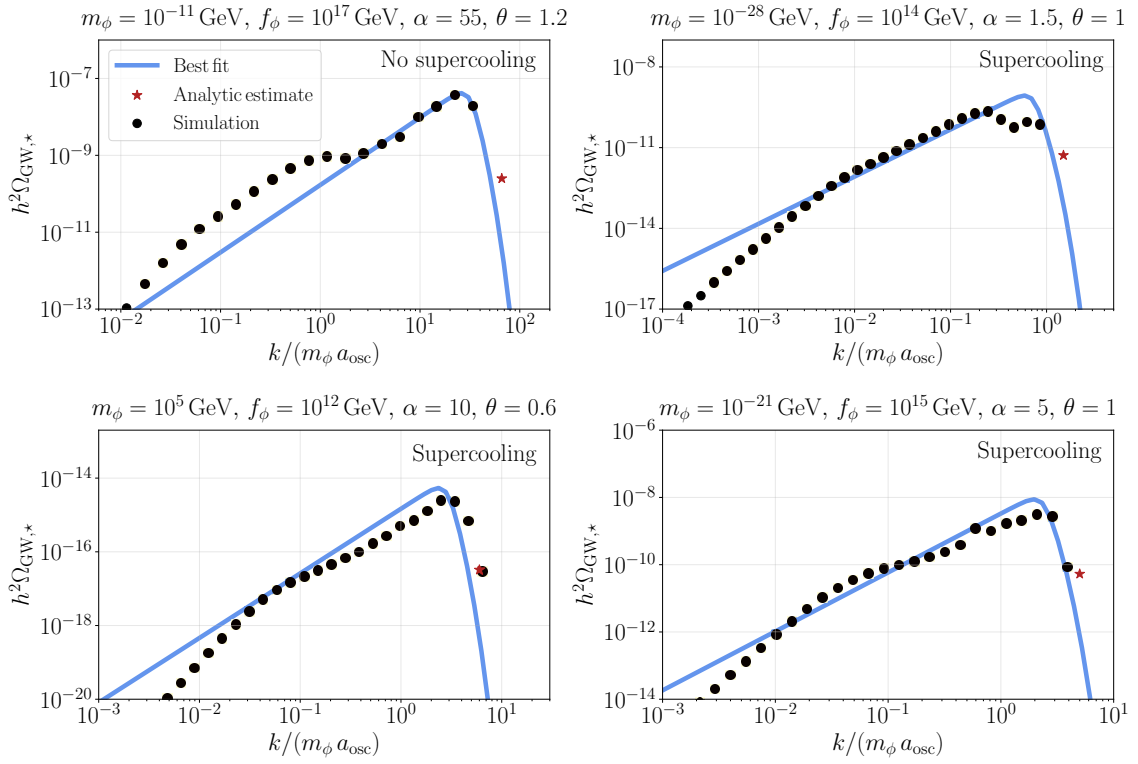

Figure 11.3: GW signal at the time of production for different model parameters, normalizing the momenta to the axion mass. The black dots are our numerical results, while the red star corresponds to our analytic estimate of the peak. The blue lines show the GW parametrization (11.24) with the best-fit parameters from table 11.1, which show a very good agreement with the numerical computation.

With eqs. (11.26) and (11.27), we are now ready to fit the GW spectrum to the numerical results. To this end, we repeat the simulations from the last section for varying model parameters. Then, we numerically compute the GW spectrum by the approach outlined in the beginning of this section and the appendix of ref. [53]. The result is shown by the black dots in fig. 11.3, where we normalize the physical GW momenta to the axion mass. Our analytic estimates of the peak frequency and amplitude are indicated by the red stars. We then select the spectrum obtained in the original setup without supercooling in the upper left panel as our benchmark and fit the parameterization of the signal (11.24) to the peak. The corresponding best-fit values are found in table 11.1. As demonstrated by the blue lines in the remaining panels, the fit gives excellent agreement with the numerical results—also in the supercooled scenario—despite varying the model parameters over a wide range. This confirms that we have incorporated the correct scaling of all the parameters in our analytic peak estimates.

OBSERVABLE PARAMETER SPACE. To assess the detection prospects of our model, we first need to redshift the spectrum to today. Since no modification of the cosmic history is allowed in the case of the dark photon (see sec. 11.1), we recover the standard redshift factors in a radiation-dominated Universe, eqs. (3.12) and (3.13). The peak frequency and amplitude today can be expressed by our model parameters by inserting eqs. (11.26) and (11.27),

$$h^2\tilde{\Omega}_{\mathrm{GW},0} = 7.69\times10^{-5}\left(\frac{f_\phi}{M_{\mathrm{Pl}}}\right)^2\frac{1}{\alpha^2}\,, \tag{11.28}$$

$$\tilde{f}_0 = 28.53\,\mathrm{Hz}\left(\frac{a_{\mathrm{osc}}}{a_\star}\right)^{\frac{3}{4}}\alpha\theta^{\frac{1}{2}}\left(\frac{m_\phi}{\mathrm{eV}}\right)^{\frac{1}{2}}\left(\frac{10^{10}\,\mathrm{GeV}}{f_\phi}\right)^{\frac{1}{2}}\,. \tag{11.29}$$

We have set $g_\epsilon^\star = g_{\epsilon,\mathrm{aa}}^{\mathrm{osc}} = g_s^\star$ for simplicity. Note that for our numerical results, we take into account the exact dependence on the effective degrees of freedom. In addition to the enhancement of the peak amplitude, we observe that the frequency receives a dependence on $f_\phi^{-\frac{1}{2}}$, a feature that was absent in the original setup [53]. This is because a lower decay constant induces a longer period of supercooling, i.e., a smaller value of the Hubble parameter at the time of production. As a consequence, the modes redshift for a shorter amount of time until today, and the frequency is enhanced for small f_ϕ. However, the peak frequency is still mainly controlled by the ALP mass m_ϕ, which we vary over several orders of magnitude in the following.

Eqs. (11.28) and (11.29) are now used together with our parametrization of the signal (11.24) to compute SNRs at SKA [150], μARES [149], LISA [35–37], BBO [148], and

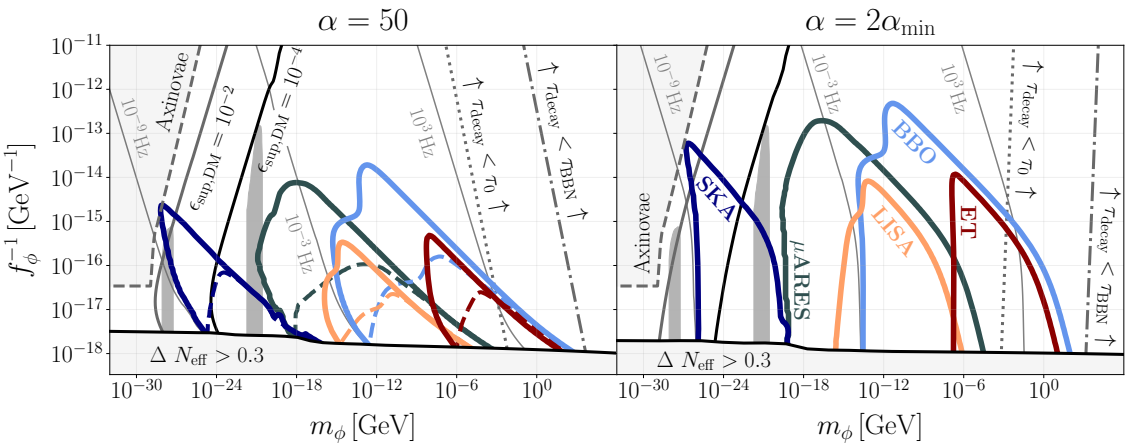

Figure 11.4: Observational prospects for supercooled audible axions coupled to dark photons. The colored curves correspond to the sensitivity regions of SKA [150], μARES [149], LISA [35–37], BBO [148], and ET [39] for $\alpha = 50$ (left) and $\alpha = 2\alpha_{\min}$ (right). The dashed curves are computed in the original setup, while the solid curves employ the maximum amount of supercooling. The detection prospects are significantly enhanced in the case of delayed oscillations. The solid gray and black lines indicate constraints from DM overproduction, while the thin gray lines denote the regions of constant peak frequency. The axion lifetime is displayed by the dotted and dash-dotted gray lines. Furthermore, we show the exclusion regions from black hole superradiance [400, 444–449] (dark gray). The axinovae bound [450] (light gray, dashed) presumes large overdensities that trigger the formation and subsequent collapse of axion stars. Whether sufficiently large overdensities are generated via the backreaction from the dark photon modes onto the ALP in our case remains an open question that requires lattice studies. Nevertheless, we include this bound for completeness.

ET [39]. To this end, we follow ref. [152]; see the appendix therein for the respective formulae and detection thresholds.[6] The SNRs are then translated into sensitivity regions in the axion parameter space, i.e., the $m_\phi - f_\phi^{-1}$ plane. This is shown in fig. 11.4 for $\alpha = 50$ (left) and $\alpha = 2\alpha_{\rm min}$ (right). The dashed lines in the left panel correspond to the original setup without supercooling, i.e., $r_{\rm sc} = 1$, while the solid curves are obtained with $r_{\rm sc} = r_{\rm sc}^{\rm min}$. We find that delayed axion oscillations substantially boost the detection prospects across the entire frequency range. This is due to the milder f_ϕ^2 dependence of the peak amplitude. As a concrete example, while BBO is sensitive to decay constants of $f_\phi \sim \mathcal{O}(10^{16}\,\text{GeV})$ for $\alpha = 50$, delayed axion oscillations extend this window by two orders of magnitude down to $f_\phi \sim \mathcal{O}(10^{14}\,\text{GeV})$. As the frequency scales $\propto f_\phi^{-\frac{1}{2}}$, the sensitivity regions are tilted.

In the right panel, we impose twice the minimal axion-dark photon coupling, with $\alpha_{\rm min} \sim \mathcal{O}(1)$; see appendix 14.A. Clearly, this further enhances the amplitude, since the wavelengths of the relevant modes are shifted closer to the horizon, alleviating the suppression $\tilde{\Omega}_{\text{GW},\star} \propto (H_\star a_\star/\tilde{k}_\star)^2$. In this case, the testable parameter space extends to $f_\phi \sim \mathcal{O}(10^{12}\,\text{GeV})$ for futuristic observatories such as BBO. We find LISA to be sensitive to decay constants $f_\phi \sim 10^{14}\,\text{GeV}$, which is three orders of magnitude below the detection threshold $f_\phi \sim 10^{17}\,\text{GeV}$ in the original setup. Therefore, the right panel represents the approximate upper limit on GW detection prospects from axion-dark photon systems; without additional modifications such as kinetic misalignment [6, 424, 426]. Note that in this case the tilt of the sensitivity regions decreases since smaller decay constants allow for smaller couplings (cf. appendix 14.A and eq. (11.29)).

Let us conclude this section by mentioning that the presented mechanism still suffers from an overproduction of DM in most of the parameter space. Previous lattice studies [417] indicate $\epsilon_{\rm sup} \sim 10^{-2}$, which would only leave a small part of the overall parameter space that will be tested at SKA, as indicated by the gray solid line. We relegate a lattice study and hence an accurate determination of $\epsilon_{\rm sup}$ in our modified setup to the future. The reduced coupling may, however, suppress the dark photon backreaction and enable a larger suppression of the axion abundance, opening up the consistent parameter region towards larger masses. Let us also note that a variation of the minimal scenario, such as a time-varying axion mass [451–456], alleviates these problems.

6 The projected sensitivity of μARES is found in [149], where a detection treshold of SNR = 10 was imposed.

12

AUDIBLE AXIONS AND THE STANDARD MODEL PHOTON

In this chapter, we will answer a simple yet central question: Does the audible axion mechanism work in the absence of a dark photon? In other words, can GWs probe ALPs via their coupling to the SM photon? This would eliminate the requirement of additional new physics, since such an interaction is generic for most implementations of the axion into the SM.

The replacement of the dark gauge field with the SM, however, induces two main obstacles:

- The SM photon is coupled to the thermal bath. Therefore, its initial state is not described by the Bunch-Davies vacuum, but by a thermal equilibrium distribution. The dispersion relation is modified by finite-temperature effects [155] and, as a consequence, the growth rate of tachyonic modes is suppressed [422] by the Debye mass $m_{\mathrm{D}} \sim eT$, where e is the electromagnetic charge.

- The emergence of strong electromagnetic fields inevitably leads to the spontaneous generation of electron-positron pairs; this is known as the Schwinger effect [457]. The fermions are accelerated along the field lines, drawing energy from the photon field, and hence impeding efficient photon and GW production through the tachyonic resonance [395, 458, 459].

In the following, we will demonstrate how delayed axion oscillations enable tachyonic production of the SM photon. We identify two distinct parameter regions for very light and very heavy axions, respectively, where the Schwinger effect is suppressed and the production of sizable GWs from axion-SM photon systems is feasible.

12.1 TACHYONIC GROWTH AT FINITE TEMPERATURE

In this section, we first introduce the photon dispersion relation at finite temperature. Subsequently, we compute the amount of supercooling required to allow for efficient tachyonic photon production.

PHOTON DISPERSION RELATION. The central object of our study will be the finite-T dispersion relation of the SM photon which, in a QED plasma, reads [155, 460, 461]

$$\omega^2 - k^2 \mp k\frac{\alpha}{f}\phi' = \frac{a^2 m_{\rm D}^2}{2}\left[\frac{\omega}{2k}\ln\left(\frac{\omega+k}{\omega-k}\right) - \frac{\omega^3}{2k^3}\ln\left(\frac{\omega+k}{\omega-k}\right) + \frac{\omega^2}{k^2}\right] . \tag{12.1}$$

Here $m_{\rm D} = eT/\sqrt{3}$ denotes the Debye mass of the photon, with $e \simeq 0.3$ being the electromagnetic charge at the eV scale.[1] As in the last section, we consistently use comoving momenta in the above expression. To simplify eq. (12.1), we expand in small comoving oscillation frequencies, $\omega \ll k$, which yields

$$\omega^2 - k^2 \mp k\frac{\alpha}{f}\phi' \approx -i\omega\frac{a^2 m_{\rm D}^2 \pi}{4k} + \frac{a^2 m_{\rm D}^2 \omega^2}{k^2} . \tag{12.2}$$

To identify the tachyonic modes, we neglect the negative solution and take ω to be imaginary, i.e., $\omega \to i\omega$. In addition, we only consider the absolute value of these imaginary modes $|\omega|$, which corresponds to the growth rate of the tachyonic modes. Furthermore, let us, for now, neglect the quadratic terms in the above expression, which is valid for $\omega/a \ll k/a \ll T$ [422]. This gives

$$\omega \approx \frac{4k}{a^2 m_{\rm D}^2 \pi}\left(k^2 - k\frac{\alpha}{f_\phi}|\phi'|\right) . \tag{12.3}$$

We determine the width of the tachyonic band by setting $\omega = 0$,

$$0 < k < \frac{\alpha}{f_\phi}|\phi'| = k_{\rm close} . \tag{12.4}$$

Intriguingly, this is equivalent to the zero-temperature result (10.11). By demanding $\partial\omega/\partial k = 0$, we find the mode which experiences the fastest growth,

$$\tilde{k}_{\rm T,osc} \approx \frac{2}{3}\frac{\alpha}{f_\phi}|\phi'| = \frac{4}{3}\tilde{k}_{\rm osc} , \tag{12.5}$$

1 Note that we neglect the running of the gauge coupling in this study. First of all, we will see that in most of the parameter space a large amount of supercooling is required. Hence, the temperature at photon production will be extremely low, such that choosing the IR value for e is justified. Second, uncertainties from the running gauge coupling are subdominant compared to other aspects, such as Schwinger pair production of fermions; see below.

where the subscript indicates the presence of the thermal bath and $\tilde{k}_{\rm osc}$ is given by eq. (11.1). The associated growth rate reads

$$\tilde{\omega}_{\rm T,osc} = |\omega(\tilde{k}_{\rm T,osc})| \approx \frac{16}{27\pi}\frac{\left(\frac{\alpha|\phi'|}{f_\phi}\right)^3}{a^2 m_{\rm D}^2} \approx \frac{16}{9\pi}\frac{(\alpha\theta m_\phi)^3}{(eT)^2} a_{\rm osc} \sim \tilde{k}_{\rm osc}\left(\frac{m_\phi}{T}\right)^2 , \tag{12.6}$$

where we have expressed $|\phi'|$ in terms of the model parameters via eq. (11.2).

Let us take a moment to note some interesting observations. In the presence of an ALP, the SM photon always exhibits a range of modes which are unstable toward exponential growth. This is different from the conjectured behavior in ref. [295] where the Debye mass of the photon was assumed to remove imaginary momenta. While the width of this tachyonic band is the same as in the dark photon case, its peak momentum is slightly shifted to the UV. Most importantly, however, the effective growth rate is strongly suppressed at high temperatures $T \gg \tilde{k}_{\rm osc}/a_{\rm osc} \sim m_\phi$ due to the dependence of the dispersion relation on the Debye mass. This is the crucial difference to the zero-T computation, where $\tilde{\omega}_{\rm osc} = \tilde{k}_{\rm osc}$, while $\tilde{\omega}_{\rm T,osc} \ll \tilde{k}_{\rm T,osc}$ at high temperatures. From this it becomes clear how trapped misalignment can provide a solution to this issue. If oscillations are delayed, $T_{\rm osc}$ is decreased and the suppression of $\tilde{\omega}_{\rm T,osc}$ is alleviated, enhancing the efficiency of the tachyonic resonance. Let us stress again that eq. (12.6) is only valid as long as $\omega/a \ll k/a \ll T$. For small temperatures, the tachyonic growth rate approaches its zero-T value, which can be seen from eq. (12.2). This is exemplified in fig. 12.1, where we show the instability band at zero and finite temperature, with and without supercooling.

AMOUNT OF SUPERCOOLING. Let us now compute the amount of supercooling required for the photon modes to grow efficiently. For a first estimate, we follow our analysis of the dark photon case and require the peak growth rate to exceed $\tilde{\omega}_{\rm T,osc} > a_{\rm osc} m_\phi/2$. With eq. (12.6), this yields

$$T_{\rm osc}^2 = r_{\rm sc}^2 T_{\rm osc,aa}^2 \lesssim \frac{32}{9\pi}\frac{(\alpha\theta)^3}{e^2} m_\phi^2 . \tag{12.7}$$

Since $T_{\rm osc,aa} \sim \sqrt{m_\phi M_{\rm Pl}}$, we have $r_{\rm sc} \sim (m_\phi/M_{\rm Pl})^{\frac{1}{2}}$, i.e., smaller masses require more supercooling. Note that the ALP starts to dominate the energy density of the Universe if $r_{\rm sc} < r_{{\rm sc},i} \sim (f_\phi/M_{\rm Pl})^{\frac{1}{2}}$ (cf. eq. (10.20)). In terms of the model parameters, this condition translates to

$$m_\phi \lesssim 1.09\ (g_\epsilon^{\rm osc})^{-\frac{1}{2}}\left(\frac{e}{\alpha^{\frac{3}{2}}\theta}\right)^2 f_\phi . \tag{12.8}$$

That is, unless the axion mass is extremely large, the ALP is required to drive a period of thermal inflation before the onset of oscillations in order to source efficient tachyonic

growth of the SM photon. In the absence of dark radiation, an intermediate axion-driven phase of inflation does not pose a problem, as long as the Universe can efficiently reheat via the exponential production of photons through the tachyonic resonance or perturbative axion decays (see sec. 12.3). The number of e-folds then reads

$$N = \ln\left(\frac{T_i}{T_{\rm osc}}\right) \approx \ln\left((g_\epsilon^{{\rm osc},i})^{-\frac{1}{4}} \frac{e}{\alpha^{\frac{3}{2}}\theta}\left(\frac{f_\phi}{m_\phi}\right)^{\frac{1}{2}}\right) , \tag{12.9}$$

where T_i is computed by setting $\rho_{\phi,{\rm osc}} = V(\phi_i) = \rho_{\rm rad}(T_i)$. We find $N_{\rm max} \approx 40$, i.e., the scales relevant for the CMB remain outside of the Hubble horizon and are thus unaffected by the axion-photon dynamics [101].

The criterion (12.7) defines the exact moment when tachyonic growth of the peak mode becomes efficient. As the axion velocity scales as $\dot\phi \propto a^{-\frac{3}{2}}$, while the temperature decreases as $T \propto a^{-1}$, the physical peak growth rate (12.6) quickly drops below $m_\phi/2$ after the onset of oscillations. To this end, we install a more conservative criterion to ensure that most of the tachyonic band can efficiently grow. That is, we use the second-order dispersion relation (12.2), compute the growth rate at $k = 0.985\, k_{\rm close}$, and demand

$$|\omega(0.985\, k_{\rm close})| = \frac{m_\phi}{2} . \tag{12.10}$$

Here, the value 0.985 is chosen since then the peak growth rate exceeds $m_\phi/2$ by one order of magnitude. With this criterion, we compute $r_{\rm sc}$, and thus $T_{\rm osc}$, numerically. However, note that the difference between criteria (12.7) and (12.10) has negligible impact on our results.

EMISSION TIMESCALE. To estimate the time of GW emission, we again follow the procedure outlined in appendix 14.A. The computation largely proceeds in the same way as for the dark photon case. The crucial difference is that, as demonstrated in the last section, the SM photon case allows for an axion-driven period of thermal inflation before the onset of oscillations. Then, the Universe can either be radiation- or matter-dominated at the time of GW emission. Furthermore, the photon initial conditions are not given by the Bunch-Davies vacuum, but by a thermal equilibrium distribution. Accounting for these details, we find (see appendix 14.A for details)

$$\frac{a_\star}{a_{\rm osc}} = \begin{cases} 1 + \dfrac{a_{\rm osc} m_\phi}{\langle\tilde\omega_{\rm T}\rangle} r_{\rm sc}^2 \ln\left(\dfrac{\theta^2 m_\phi^2 f_\phi^2}{2\rho_\gamma(\tau_{\rm osc})}\right) , & {\rm RD} , \\ \left[1 + \dfrac{a_{\rm osc}\theta m_\phi f_\phi}{2\sqrt{6} M_{\rm Pl}\langle\tilde\omega_{\rm T}\rangle} \ln\left(\dfrac{\theta^2 m_\phi^2 f_\phi^2}{2\rho_\gamma(\tau_{\rm osc})}\right)\right]^2 , & {\rm MD} , \end{cases} \tag{12.11}$$

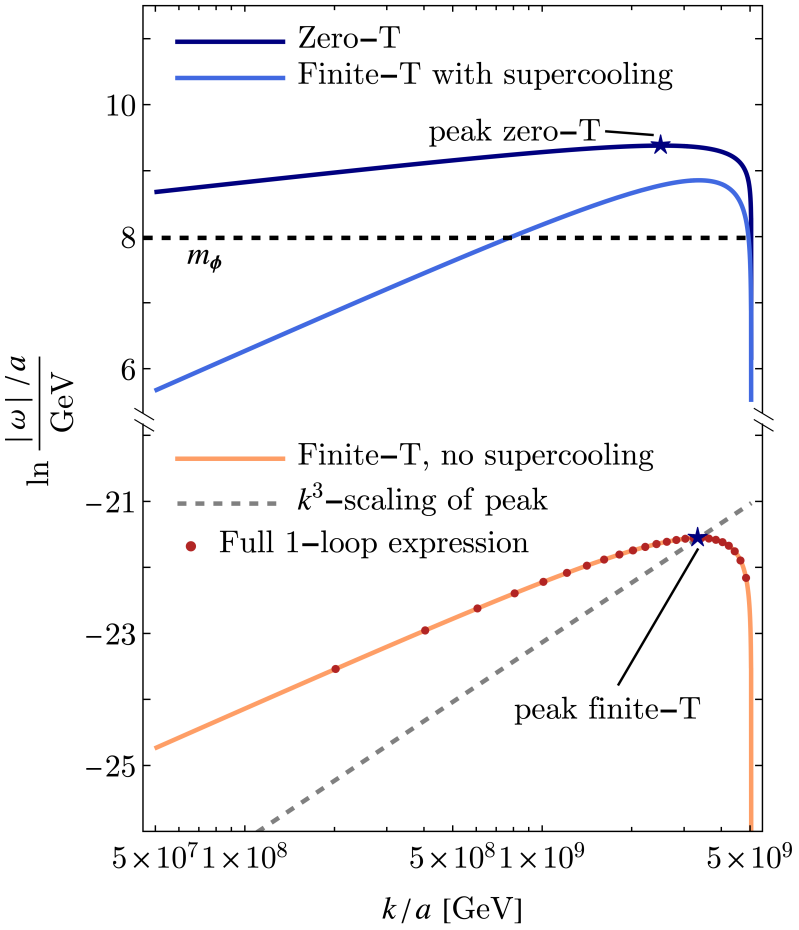

Figure 12.1: Physical growth rate $|\omega|/a$ of the tachyonic modes as a function of the physical momentum k/a. Here the dark blue (orange) curve corresponds to the original (SM photon) setup without supercooling, while the light blue curve shows the SM photon growth rates for a finite amount of supercooling. In the supercooled case, the SM photon band approaches the zero-T case, enabling efficient tachyonic growth as $|\omega| \sim m_\phi$. Figure created by C. Gerlach.

where $\langle\tilde{\omega}_{\mathrm{T}}\rangle = 4/(3\pi)\tilde{\omega}_{\mathrm{T}}$ is the average finite-T peak growth rate. As a consequence of the large amount of supercooling, we typically have $\langle\tilde{\omega}_{\mathrm{T}}\rangle \gg H_{\mathrm{osc}}$, such that the exponential growth of photon modes terminates within less than one Hubble time.

To determine the minimal α, we again demand $a_{\mathrm{close}} > a_\star$. Here the time of tachyonic band closure is estimated by the same criterion (11.7) as in the dark photon case. This is a good approximation since both the zero-T and finite-T instability band share the cutoff momentum k_{close}. In addition, in most of the parameter space we need to impose a large supercooling ratio r_{sc}, such that the finite-T dispersion relation approaches its zero-T counterpart (cf. eq. (12.2)). As in the dark photon case, we find $\alpha_{\mathrm{min}} \sim 1$ in most of the parameter space. Hence, resonant SM photon production still requires an enhanced axion-photon coupling relative to $\alpha_{\mathrm{em}} \sim 1/137$.

12.2 SCHWINGER PAIR PRODUCTION

We are now ready to tackle the second issue we have introduced in the beginning of this chapter: Schwinger pair production of light SM fermions [395, 457–459, 462–464]. That is, electron-positron pairs are created from a strong background electric field and subsequently accelerated along the field lines. This process extracts energy from the photon field, reducing the energy available for GW emission. Therefore, we need to identify the parameter space where the Schwinger effect is suppressed.

To this end, we first introduce the efficiency factor

$$\xi = \frac{\tilde{\omega}_{\mathrm{T,osc}}}{a_{\mathrm{osc}} H_{\mathrm{osc}}}\,, \tag{12.12}$$

where $\tilde{\omega}_{\mathrm{T,osc}}$ is given by eq. (12.6) and H_{osc} is the Hubble parameter at the onset of oscillations (10.21). Due to the large amount of supercooling in most of the parameter space (see above), we typically encounter a hierarchy $\tilde{\omega}_{\mathrm{T,osc}} > m_\phi \gg H_{\mathrm{osc}}$, such that $\xi \gg 1$.

Since an accurate numerical study of the axion-SM photon system including fermionic degrees of freedom is technically extremely involved and beyond the scope of this work, we follow ref. [395] and derive upper bounds on the maximum energy density that can be transferred to the photon without decaying into electron-positron pairs. To this end, we employ an energy balance equation,

$$\dot{\rho}_\gamma = -4H\rho_\gamma + 2\xi HEB - eQEJ_{\mathrm{ind}}\,. \tag{12.13}$$

The photon energy density is given by $\rho_\gamma = \frac{1}{2}(E^2 + B^2)$, where $E = |\boldsymbol{E}|$ and $B = |\boldsymbol{B}|$. The first term on the right-hand side then describes the dilution of the energy density due

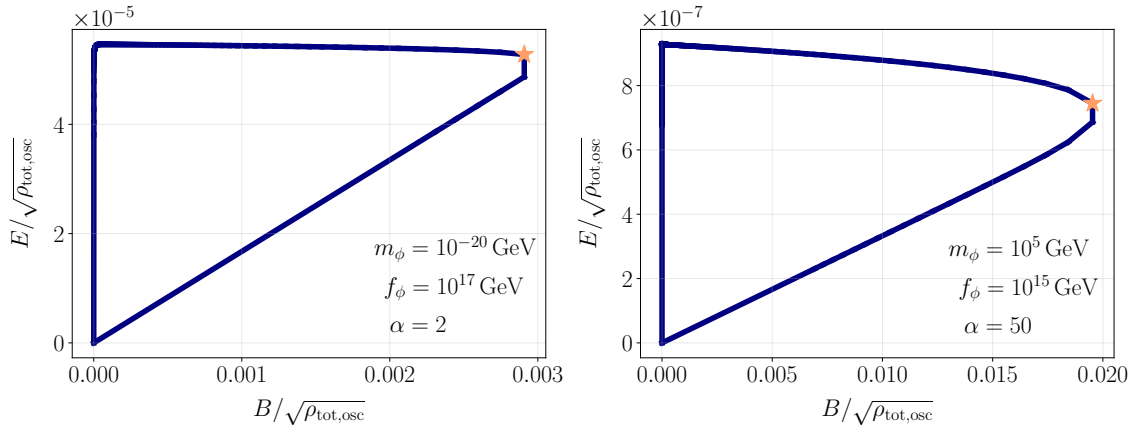

Figure 12.2: Closed contours in the $B - E$ plane that solve eq. (12.17) for two different sets of benchmark parameters $\{m_\phi, f_\phi, \alpha\}$ and $\theta = 1$. The blue lines indicate all possible solutions, while the orange star corresponds to the maximum photon energy density that we use for our estimates of the upper limit on the GW amplitude.

to Hubble friction, the second term corresponds to photon production from the tachyonic instability, and the third term described the decays into fermion pairs, with Q being the charge factor. The induced fermion current from a strong background electromagnetic field reads [395]

$$eQJ_{\rm ind} = \frac{(e|Q|)^3}{6\pi^2}\frac{EB}{H}\coth\left(\frac{\pi B}{E}\right)\exp\left(-\frac{\pi m_e^2}{e|Q|E}\right), \tag{12.14}$$

where we have only taken into account the electron with $m_e \approx 511\,\text{keV}$ [319] as the lightest, hence dominant degree of freedom. From the above expression, we directly note that the Schwinger effect is exponentially suppressed by the electron mass. This defines the Schwinger limit,

$$E_s = \frac{\pi m_e^2}{e|Q|}, \tag{12.15}$$

which yields a temperature $T \lesssim 2.2\,\text{MeV}/(g_\epsilon)^{\frac{1}{4}}$ below which the production of fermions is inefficient. However, this bound is weaker than the ones we determine numerically (see below).

We will vary the axion mass over many orders of magnitude. As we have seen in the previous section, larger masses require less supercooling, such that the temperature may remain comparable to the scale of tachyonic growth. In this case, we expect the thermal screening of the fermions to impede their acceleration along the electric field lines. In other words, the friction from the thermal bath will affect the energy transfer of the gauge field to the fermions. While an accurate analysis of the Schwinger effect in the presence of a

thermal plasma requires a re-derivation of eq. (12.14), starting from the full fermionic finite-T dispersion relation, we approximate the situation by replacing $m_e^2 \to m_e^2 + m_{e,\mathrm{th}}^2$ with $m_{e,\mathrm{th}}^2 = (eT)^2/8$ being the thermal mass of the electron. This will provide some insights into potentially interesting parameter spaces at very high temperatures. A more precise computation is relegated to the future. To summarize, we then have

$$m_e = \begin{cases} 511\,\mathrm{keV} + \dfrac{eT_{\mathrm{osc}}}{\sqrt{8}} & \text{if} \quad T_{\mathrm{osc}} < T_{\mathrm{ew}}\,, \\ \dfrac{eT_{\mathrm{osc}}}{\sqrt{8}} & \text{if} \quad T_{\mathrm{osc}} > T_{\mathrm{ew}}\,, \end{cases} \tag{12.16}$$

depending on whether the EWPT has already occurred, with $T_{\mathrm{ew}} \approx 160\,\mathrm{GeV}$ [82].

Assuming that the ALP, photon, and fermions quickly reach dynamical equilibrium, one can set $\dot{\rho}_\gamma = 0$ in eq. (12.13), which gives [395]

$$E^2 + B^2 - \xi EB + \frac{eQ}{2}\frac{E}{H} J_{\mathrm{ind}} = 0\,. \tag{12.17}$$

This is justified in our case since tachyonic growth, if efficient, happens in much less than one Hubble time due to the large efficiency factors $\xi \gg 1$. Further following [395], we note that for $J_{\mathrm{ind}} \neq 0$, solutions to eq. (12.17) form a closed contour in the $B - E$ plane. The strategy hence is as follows. For a given set of model parameters $\{m_\phi, f_\phi, \alpha, \theta\}$, we first compute T_{osc} numerically as outlined in the previous section. This fixes the finite-T growth rate $\tilde{\omega}_{\mathrm{T,osc}}$ and the Hubble parameter H_{osc}, thus the efficiency parameter ξ. Then, we numerically compute the solutions of eq. (12.17), and maximize the photon energy density

$$\Omega_{\gamma,\mathrm{max}} = \frac{1}{\rho_{\mathrm{tot}}}\frac{1}{2}\left(E^2 + B^2\right)_{\mathrm{max}}\,, \tag{12.18}$$

over the contour. This is shown in fig. 12.2 for different model parameters. The blue curve are the solutions to the constraint equation, while the orange stars indicate the upper bound on the energy density of the photon, which is employed below to estimate the maximum GW amplitude.

Fig. 12.3 shows the the upper limit on the relative photon energy density $\Omega_{\gamma,\mathrm{max}}$ in the presence of Schwinger pair production. Here, we set $\alpha = 2\alpha_{\mathrm{min}}$, $\theta = 1$, and $f_\phi \in \{10^{10}, 10^{12}, 10^{14}, 10^{16}\}\,\mathrm{GeV}$. The axion mass m_ϕ is varied over several orders of magnitude and translated to the would-be reheating temperature after tachyonic production,

$$T_{\mathrm{rh}} = \left(\frac{90}{\pi^2 g_{\epsilon,\mathrm{rh}}}\right)^{\frac{1}{4}} \sqrt{H_{\mathrm{osc}} M_{\mathrm{Pl}}} \propto m_\phi^{\frac{1}{2}}\,, \tag{12.19}$$

where H_{osc} is the Hubble parameter at the onset of oscillations (10.21). First, let us note that $T_{\mathrm{rh}} > T_{\mathrm{BBN}} \sim \mathrm{MeV}$ provides the first lower bound on the model parameters (light

gray-shaded region). In the small-m_ϕ regime, a period of thermal inflation always occurs, implying that the Universe would be vacuum-dominated during BBN if $T_{\rm rh} < T_{\rm BBN}$. Second, we observe that Schwinger pair production becomes negligible for $T_{\rm rh} \gtrsim T_{\rm BBN}$, such that $\Omega_{\gamma,\rm max} = 1$. Since the energy density $\sqrt{\rho_{\rm tot}} \sim T^2 \sim m_e^2 \sim E^2$, the exponential suppression of the Schwinger effect by the vacuum electron mass enables efficient photon production. Increasing the axion mass, hence $T_{\rm rh}$, we find that Schwinger pair production becomes increasingly efficient due to the large hierarchy $T \gg m_e$, prohibiting an efficient energy transfer to the photon. For sufficiently large $T_{\rm rh}$, however, the thermal mass of the electron becomes relevant, again blocking fermion production. Considering even larger reheating temperatures, the relative contribution of the photon to the total energy density declines again. That is because of the little amount of supercooling that is required to open the tachyonic band in this regime. As a consequence, $r_{\rm sc}$ becomes larger and $\Omega_{\phi,\rm osc}$, hence $\Omega_{\gamma,\rm max}$, decreases (cf. eq. (10.19)). To summarize, we identify two relevant regimes at very small and very large axion masses which allow for the emission of sizable GWs.

Lastly, let us stress the impact of f_ϕ on the efficiency of Schwinger pair production. The Hubble parameter at the onset of oscillation (10.21) scales as $H_{\rm osc} \propto f_\phi$. Hence, small f_ϕ lead to large efficiency parameters $\xi \gg 1$, such that photon growth completes in much less than one Hubble time. Therefore, energy transfer from the axion to the photon is increasingly efficient for small decay constants, opening up the parameter range in terms of m_ϕ where fermion production is negligible. Conversely, the large-f_ϕ region is severely constrained by the Schwinger mechanism.

12.3 COSMOLOGICAL CONSTRAINTS

As for the dark photon scenario, let us briefly discuss cosmological constraints on the model. In the case of the SM, constraints from $N_{\rm eff}$ are irrelevant as no dark radiation is involved.[2] Instead, it is necessary to achieve a consistent cosmological history by: i) avoiding DM overproduction, and ii) ensuring efficient reheating such that the Universe is radiation-dominated during BBN. This depends on the decay rate of the ALP (11.12) and the efficiency of Schwinger pair production.

Let us start by discussing light, i.e., cosmologically stable ALPs. First, we remind ourselves that in this mass regime we always encounter a period of axion-driven thermal inflation before the onset of oscillations (cf. eq. (12.8)), where the Universe transitions to MD. Therefore, it is crucial that the Schwinger effect is sufficiently suppressed such that

2 GWs act as dark radiation, however, the amplitudes we encounter are well below the upper bound from $N_{\rm eff}$.

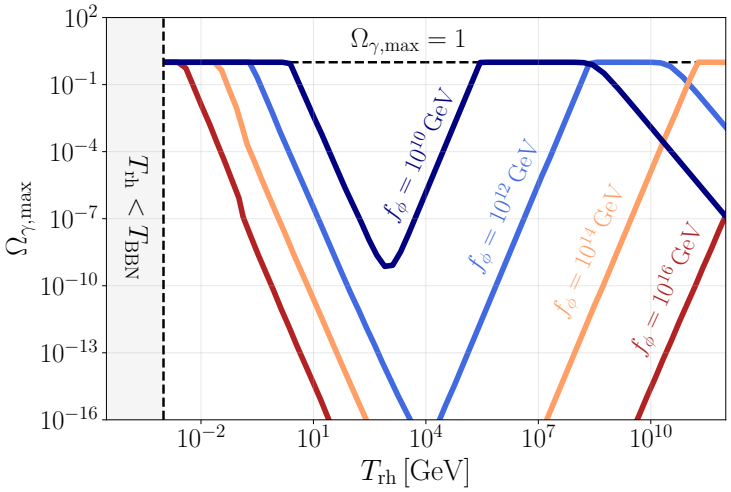

Figure 12.3: Maximum energy density of the SM photon field after the tachyonic resonance in the presence of Schwinger production of fermion pairs. Here, the reheating temperature encodes the relation to the ALP mass m_ϕ. The left region is excluded due to inconsistencies with BBN. We identify two interesting parameter regions where the Schwinger effect is suppressed: For light (heavy) axion masses, the vacuum (thermal) electron mass prohibits pair production, allowing for $\Omega_{\gamma,\max} = 1$.

$\Omega_{\gamma,\max} = 1$. Otherwise, MD would continue throughout BBN in the absence of efficient decay channels to the SM. Hence, the parameter space where $\Gamma_{\phi\to\gamma\gamma} < H_{\rm BBN}$ and $\Omega_{\gamma,\max} < 1$ is excluded.

In the regime where $\Gamma_{\phi\to\gamma\gamma} < H_0$ and $\Omega_{\gamma,\max} = 1$, the the only relevant constraint is given by the present DM abundance. To this end, we again parametrize the suppression of the ALP abundance through the tachyonic resonance via eq. (11.13). We redshift the axion energy density to today and compare to $\Omega_{\rm DM,0}$ (see appendix 14.B for details) . This gives the required suppression,

$$\epsilon_{\rm sup}^{\rm SM,DM} \lesssim 1.66\times 10^{-10}\, g_s^{\rm rh}(g_{\epsilon,\rm rh})^{-\frac{3}{4}} \left(\frac{a_\star}{a_{\rm osc}}\right)^{\frac{3}{4}} \left(\frac{\rm eV}{m_\phi}\right)^{\frac{1}{2}} \left(\frac{10^{10}\,\rm GeV}{\theta f_\phi}\right)^{\frac{1}{2}} . \tag{12.20}$$

As in the dark photon case, large decay constants and masses necessitate small $\epsilon_{\rm sup}$, i.e., a strong suppression through the resonance.

Let us now focus on the parameter space where $\Gamma_{\phi\to\gamma\gamma} > H_{\rm BBN}$. In this mass range, the model is always cosmologically consistent, independent of the efficiency of the Schwinger effect. Even if the production of fermions completely blocks the energy transfer to the photon, the ALP can always decay perturbatively into photons before BBN. However, the combination of the axion mass, the efficiency of Schwinger pair production, and the sup-

pression of the ALP abundance $\epsilon_{\rm sup}$ can lead to various thermal histories. This only affects the GW signal via modified redshift factors, which have to be determined numerically. To this end, we refer to appendix 14.B for details.

12.4 GRAVITATIONAL WAVE SIGNAL

We now have all the ingredients to compute the GW signal in the cosmologically viable regions of the parameter space. To this end, we rely on our numerical simulations from sec. 11.2 to obtain semi-analytic estimates of the GW peak frequency and amplitude. For a given set of model parameters, we first calculate the maximum energy density available for GW emission under the influence of Schwinger pair production,

$$\Omega_\gamma^{\rm after} = \chi_{\rm sp}\Omega_{\phi,\star}\,, \tag{12.21}$$

where $\chi_{\rm sp} \in (0,1)$ is determined as outlined in sec. 12.2. Then, we employ eq. (11.25) and (11.26), including our best-fit parameters $\mathcal{A}_s$ and f_s (see table 11.1), to estimate the position of the peak at the time of production,

$$\tilde{\Omega}_{\rm GW,\star} = \mathcal{A}_s\,\chi_{\rm sp}^2\Omega_{\phi,\star}^2\left(\frac{H_\star a_\star}{2\tilde{k}_\star}\right)^2\,, \tag{12.22}$$

$$\tilde{f}_{\rm GW,\star} = 2f_s\frac{\tilde{k}_\star}{a_\star} = f_s\alpha\theta m_\phi\left(\frac{a_{\rm osc}}{a_\star}\right)^{\frac{3}{2}}\,. \tag{12.23}$$

Here, the expression for the finite-T peak momentum is given by eq. (12.5) and the Hubble parameter at $T_{\rm osc}$ is computed via eq. (10.21). Both quantities are evolved to the time of production through eq. (12.11). We plug in the model parameters, redshift to today (see appendix 14.B), and distinguish whether we have RD or MD at the time of production. This yields

$$\tilde{f}_0 = 8.69\times10^{-8}\,{\rm Hz}\left(\frac{100}{g_{\epsilon,{\rm rh}}}\right)^{\frac{1}{12}}\alpha\theta\,\frac{m_\phi}{\rm eV}\left(\frac{a_{\rm osc}}{a_\star}\right)^{\frac{3}{2}}\left(\frac{\rm GeV}{H_{\rm rh}}\right)^{\frac{1}{2}}\min\left\{1,\frac{a_\star}{a_{\rm rh}}\right\}\,, \tag{12.24}$$

$$h^2\tilde{\Omega}_{\rm GW,0}^{\rm MD} = 4.20\times10^{-4}\left(\frac{100}{g_\epsilon^\star}\right)^{\frac{1}{3}}\chi_{\rm sp}^2\left(\frac{f_\phi}{\alpha M_{\rm Pl}}\right)^2\min\left\{1,\frac{a_{\rm md}}{a_{\rm rh}}\right\}\,, \tag{12.25}$$

$$h^2\tilde{\Omega}_{\rm GW,0}^{\rm RD} = 7.01\times10^{-5}\left(\frac{100}{g_\epsilon^\star}\right)^{\frac{1}{3}}\chi_{\rm sp}^2\left(\frac{\theta}{\alpha}\right)^2\left(\frac{f_\phi}{r_{\rm sc}M_{\rm Pl}}\right)^4\left(\frac{a_\star}{a_{\rm osc}}\right)\min\left\{1,\frac{a_{\rm md}}{a_{\rm rh}}\right\}\,. \tag{12.26}$$

Here the scale factor ratio $a_\star/a_{\rm rh}$ is associated with a finite duration of the reheating period, i.e., if the axion does not deplete its entire energy density during or right after the

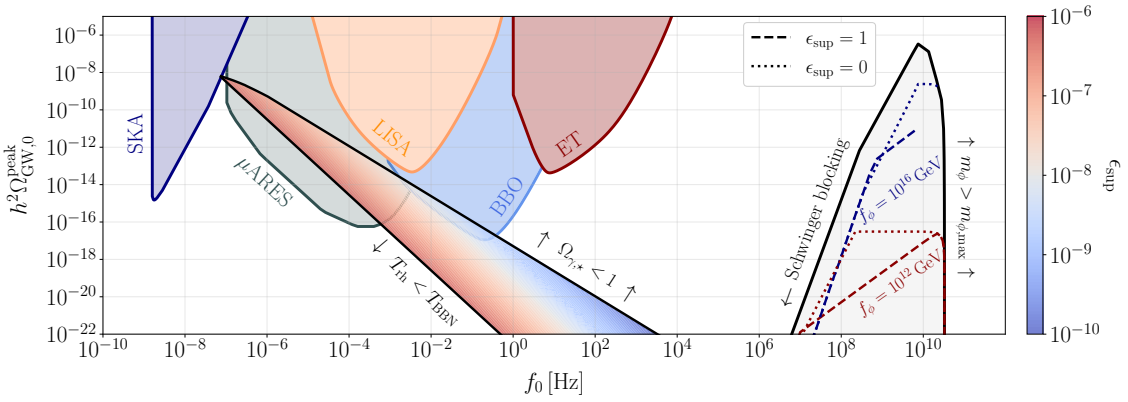

Figure 12.4: Projected locations of the spectral GW peak from axion-SM photon systems in a supercooled Universe. In addition, we indicate the PLI sensitivity curves of the future observatories SKA, μARES, LISA, BBO, and ET. Two relevant parameter regions are identified, where the vacuum and thermal electron mass, respectively, block Schwinger pair production. In the low-f_0 region, corresponding to light axions, the best detection propects are found at μARES and BBO, while the required suppression of the axion abundance to constitute DM is $\epsilon_{\rm sup} = \mathcal{O}(10^{-6} - 10^{-10})$. The high-$f_0$ (heavy-axion) regime extends up to $f_0 \sim 10^{10}\,$Hz and $h^2\tilde{\Omega}_{\rm GW,0} \sim \mathcal{O}(10^{-6})$, evading cosmological constraints since the ALP decays before BBN.

tachyonic resonance. This affects the redshift factor of the frequency. As the amplitude redshift factor only receives a modification if the background evolution differs from radiation, $a_\star/a_{\rm rh}$ reduces to $a_{\rm md}/a_{\rm rh}$ in eqs. (12.25) and (12.26). The Hubble parameter after reheating, $H_{\rm rh}$, is either equal to $H_\star$ or $\Gamma_{\phi\to\gamma\gamma}$; this depends on the cosmic history (see appendix 14.B). Perhaps not surprisingly, we again find a $(f_\phi/M_{\rm Pl})^2$ scaling of the peak amplitude. Therefore, GWs are enhanced compared to the original setup without supercooling. In addition, we typically have $\Omega_{\phi,\star} \simeq 1$ (eq. (12.25)). Hence, axion-SM photon systems generally predict stronger signals compared to the dark photon case, provided the MD period is sufficiently short and $\chi_{\rm sp} \simeq 1$.

The main results for $\theta = 1$ and $\alpha = 2\alpha_{\rm min}$ are shown in fig. 12.4, where we vary m_ϕ and f_ϕ across the viable parameter space and plot the projected peaks, representing the (approximate) upper limit on GW signals from axion-SM photon systems. We clearly see how the two relevant regions at small and large m_ϕ that we identified in sec. 12.2 translate to the $f_0 - h^2\tilde{\Omega}_{\rm GW,0}$ plane. The low-f_0 region, where the lower limit is given by the condition $T_{\rm rh} > T_{\rm BBN}$, is associated with cosmologically stable axions. Therefore, we plot the required suppression of the abundance through the tachyonic resonance $\epsilon_{\rm sup}$. As predicted by eq. (12.20), smaller masses and decay constants allow for larger $\epsilon_{\rm sup} \lesssim 10^{-6}$, hence alleviate the DM constraint. Note, however, that a lattice simulation of the axion-SM

photon system remains to be done to accurately determine the possible value of $\epsilon_{\rm sup}$. To the right, the small-m_ϕ parameter space is bounded by efficient Schwinger production $\Omega_{\gamma,\star} < 1$, such that the Universe would be axion-dominated during BBN. This mainly affects large decay constants, i.e., the low-frequency parameter space allows for $f_\phi \lesssim 5 \times 10^{16}\,\text{GeV}$. The best detection prospects are found at μARES and BBO. Note that although $T_{\rm rh} \gtrsim T_{\rm BBN}$ and $H_{\rm BBN} \sim \mathcal{O}\,(10^{-10}\,\text{Hz})$, the peak frequencies are shifted to the μHz regime. That is due to the fact that in the supercooled Universe, the unstable modes are deep in the horizon such that $\tilde{k}_\star/(a_{\rm rh}H_{\rm rh}) \gg 1$. This also suppresses the GW amplitude.

The large-m_ϕ region is bounded by $m_{\phi,\max} = 6 \times 10^{13}\,\text{GeV} = H_{\rm inf}^{\max} \geq H_{\rm osc,aa}$, which we impose such that the original mechanism complies with Planck measurements [101]. Let us remind ourselves that in this regime, ALPs decay before BBN, hence the cosmological consistency is ensured and constraints on $\epsilon_{\rm sup}$ do not apply. Instead, the efficiency of the tachyonic instability only affects the redshift factors of the GW spectrum (see appendix 14.B). Therefore, we scan over a large range of values in the $m_\phi - f_\phi$ plane, imposing the most extreme values $\epsilon_{\rm sup} \in \{0, 1\}$. The gray-shaded region displays the envelope of this parameter scan. In addition, we plot the GW peak for two benchmark values $f_\phi \in \{10^{12}, 10^{16}\}\,\text{GeV}$ (dark red, dark blue), varying m_ϕ. Here, we observe that while Schwinger pair production is efficient and the relic axion abundance is fixed, the dotted ($\epsilon_{\rm sup} = 0$) and dashed ($\epsilon_{\rm sup} = 1$) curves agree. As the acceleration of fermion-antifermion pairs is impeded at high temperatures by the thermal electron mass, a more efficient suppression of the axion abundance, $\epsilon_{\rm sup} = 0$, leads to stronger signals due to the shortened MD period. In that case, we find frequencies up to $\tilde{f}_0 = \mathcal{O}(10^{10}\,\text{GeV})$ and amplitudes up to $h^2\tilde{\Omega}_{\rm GW,0} = \mathcal{O}(10^{-6})$. This ultra-high frequency regime provides a promising avenue for new physics searches [151] in the absence of astrophysical foregrounds.

13

CONCLUSION

In the second part of this work, we have studied the early Universe phenomenology of ALPs coupled to dark and SM photons, respectively. Specifically, we have extended the audible axion mechanism by a period of supercooling, which arises if the pseudoscalar is trapped in a local minimum induced by explicit $\mathrm{U}(1)_{\mathrm{PQ}}$-breaking operators. We have seen that this extension can alleviate various shortcomings of the original setup; the minimal mechanism requires large decay constants $f_\phi \gtrsim 10^{16}\,\mathrm{GeV}$ and axion-dark photon couplings $\alpha \gtrsim 20$ to generate GWs in the reach of future observatories.

In chapter 11, we have shown that in the case of axion-dark photon systems, a delay of ALP oscillations alleviates the suppression of the GW amplitude for small decay constants. As a consequence, $f_\phi \sim 10^{12}\,\mathrm{GeV}$ is sufficient to produce observable signals. In addition, the relative efficiency of tachyonic growth compared to the expansion rate of the Universe is enhanced. Then, dark photon production becomes possible for $\alpha \gtrsim 1$, extending the parameter space that is testable via future GW observations.

In chapter 12, we have shown that supercooled axion oscillations enable tachyonic production of SM gauge fields. To this end, we have studied the phenomenology of the axion-SM photon coupling, taking into account the effect of the thermal bath on the photon dispersion relation. A delayed onset of axion oscillations, i.e., supercooling the plasma, suppresses the Debye mass of the photon and enables efficient tachyonic growth. The viable parameter space is then further constrained by the production of light fermion pairs via the Schwinger effect. Interestingly, this leaves two distinct parameter regimes that are cosmologically consistent. We find GW signals observable by μARES and BBO for $f_\phi \lesssim 5 \times 10^{16}\,\mathrm{GeV}$ and small ALP masses. Heavy ALPs that decay before BBN can source sizable GWs at ultra-high frequencies, $f_0 \sim \mathcal{O}(10^8 - 10^{10})\,\mathrm{Hz}$. This frequency regime, however, remains challenging to access through experiment.

Let us now mention some aspects that warrant further investigation. First, both the dark photon and SM photon cases suffer from an overproduction of ALP DM in a large part of the parameter space. To this end, we have introduced the parameter ϵ_{sup} quantifying the

suppression of the ALP abundance through the tachyonic resonance. We have treated $\epsilon_{\rm sup}$ as a free parameter and computed the value required to have a consistent cosmological history. In the future, the suppression of the ALP abundance should be studied on the lattice. Previous works [417] find $\epsilon_{\rm sup} \approx 10^{-2}$ employing $\alpha \approx 20$. In our case, we can significantly decrease the axion-photon coupling while retaining the efficiency of tachyonic particle production. It will be interesting to see how this affects the backreaction of the produced gauge modes onto the ALP. However, a small $\epsilon_{\rm sup}$ can also be achieved by further model building, such as a time-varying ALP mass.

Second, we have estimated the effect of the thermal bath on Schwinger pair production of light fermions in sec. (12.2) via the fermionic thermal mass. Although this provides a reasonable estimate of the high-frequency regime that enables tachyonic SM photon production, an accurate description of the finite-temperature Schwinger effect remains to be developed. This will allow for a precise determination of the parameter space that features sizable GWs.

Lastly, the tachyonic production of SM photons allows for observables complementary to GWs. Specifically, helical magnetic fields sourced by the ALP motion may constitute intergalactic magnetic fields [465–470]. This provides an intriguing connection between the production of ALP DM, future GW experiments, and current astrophysical observations.

14

APPENDIX

In the appendix of part iii, we provide more details on the computations outlined in the main text. This comprises our calculation of the (dark) photon growth time, the resulting minimal value of the axion-photon coupling α, and the derivation of the cosmological constraints. Furthermore, we vary the initial ALP misalignment angle θ and study its impact on our main results.

14.A GROWTH TIME ESTIMATE AND MINIMAL α

In this section, we compute the growth time of the unstable (dark) vector modes, which allows us to set bounds on α in order to have efficient photon production. To estimate the growth time, let us note that the energy density of the gauge field evolves as

$$\rho_{X,\gamma}(\tau) \approx \rho_{X,\gamma}(\tau_{\rm osc}) \exp(2\tilde{\omega}\tau)\,, \tag{14.1}$$

Here, the factor two enters since the energy density is proportional to the square of the mode functions (see eq. (11.4)). We will shorty specify the characteristic growth rate $\tilde{\omega}$. First, we need to account for the fact that tachyonic growth of the dominant photon helicity only occurs while the ALP moves in its initial direction. That is, the relevant helicity is only amplified half of the time, and the elapsed conformal time reads

$$\frac{\delta\tau}{\tau_{\rm osc}} = \frac{\tau_\star - \tau_{\rm osc}}{\tau_{\rm osc}} = \frac{a_{\rm osc}H_{\rm osc}}{\tilde{\omega}} \ln\left(\frac{\rho_{X,\gamma}(\tau_\star)}{\rho_{X,\gamma}(\tau_{\rm osc})}\right)\,, \tag{14.2}$$

where $\tau_\star$ denotes the moment when $\rho_X(\tau_\star) = \rho_\phi(\tau_\star)$. Furthermore, the fastest growing mode is amplified, on average, by the mean of the peak growth rate over one oscillation cycle, $\langle\tilde{\omega}\rangle$, i.e., we replace $\tilde{\omega} \to \langle\tilde{\omega}\rangle$ in the above expression. Also, note that eq. (14.2) neglects the redshift of all quantities between the onset of oscillations and GW emission. Tachyonic amplification ceases to be efficient when the (dark) photon energy density becomes comparable to the axion energy density. Hence we set

$$\rho_{X,\gamma}(\tau_\star) = \frac{\theta^2}{2} m_\phi^2 f_\phi^2\,, \tag{14.3}$$

to obtain a conservative estimate of the growth time. To summarize, the conformal time from ALP oscillations to GW emission reads

$$\frac{\delta\tau}{\tau_{\rm osc}} = \frac{\tau_\star - \tau_{\rm osc}}{\tau_{\rm osc}} = \frac{a_{\rm osc}H_{\rm osc}}{\langle\tilde{\omega}\rangle}\ln\left(\frac{\theta^2 m_\phi^2 f_\phi^2}{2\rho_{X,\gamma}(\tau_{\rm osc})}\right). \tag{14.4}$$

For a given background evolution, this can be translated to a scale factor ration by solving

$$H = \frac{a'}{a^2}. \tag{14.5}$$

This is done for the dark and SM photon case, respectively, in the following.

DARK PHOTON CASE. As already stated in the main text, we assume the dark photon case to be completely decoupled from the SM. Therefore, the Bunch-Davies vacuum $v_\lambda(k, \tau \ll \tau_{\rm osc}) = \exp(-ik\tau)/\sqrt{2k}$ is a natural choice as initial condition [381]. By integrating over the mode functions, we find the total initial energy density in the instability band

$$\rho_X(\tau_{\rm osc}) \approx \frac{1}{16\pi^2}\left(\frac{\tilde{k}}{a_{\rm osc}}\right)^4, \tag{14.6}$$

where $\tilde{k} = \tilde{\omega} = \alpha\theta m_\phi a_{\rm osc}/2$ is the comoving peak momentum of the dark photon energy spectrum. Furthermore, we compute the average growth rate of the most tachyonic mode as

$$\langle\tilde{\omega}\rangle = \tilde{\omega}\langle|\sin(m_\phi t)|\rangle = \frac{2}{\pi}\tilde{\omega}, \tag{14.7}$$

where we have used that the oscillation frequency is given by m_ϕ. Since a MD period is forbidden in the case of the dark photon, we only need to solve eq. (14.5) for a radiation-dominated Universe. We have $a \propto \tau$, hence

$$\frac{a_\star}{a_{\rm osc}} = 1 + \frac{\pi}{\alpha\theta}r_{\rm sc}^2\ln\left(\frac{128\pi^2}{\alpha^4\theta^2}\frac{f_\phi^2}{m_\phi^2}\right). \tag{14.8}$$

From this, we clearly see that a finite period of supercooling, $r_{\rm sc} < 1$, directly decreases the dark photon growth time, rendering tachyonic growth more efficient relative to the expansion rate of the Universe.

Regarding the closure of the tachyonic band, we require

$$\omega^2 = -\left(\frac{am_\phi}{2}\right)^2, \tag{14.9}$$

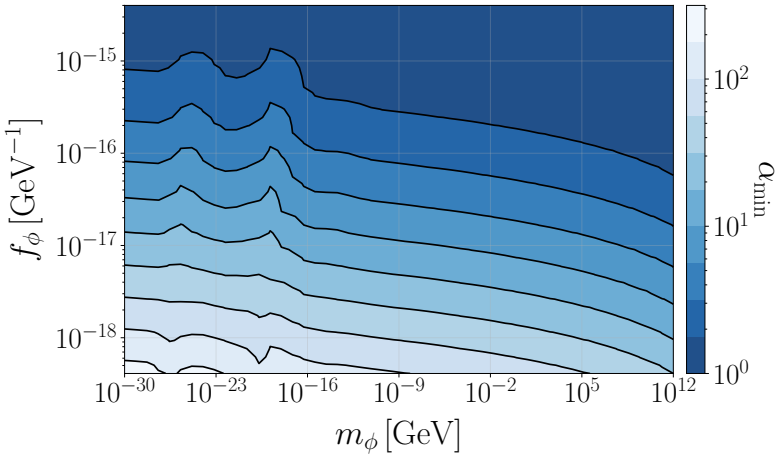

Figure 14.1: Minimum value of the axion-dark photon coupling α in the $m_\phi - f_\phi$ plane. Smaller values of the decay constant $f_\phi \lesssim 10^{16}\,\mathrm{GeV}$ allow for $\alpha_{\mathrm{min}} \sim 1$ to have efficient dark photon production, while the original setup required $\alpha \gtrsim 20$ [53]. Note that the odd behavior of the contour lines below $m_\phi \sim 10^{-16}\,\mathrm{GeV}$ is caused by the rapid change of the relativistic degrees of freedom during the QCD epoch, which enters the maximum amount of supercooling $r_{\mathrm{sc}}^{\mathrm{min}}$ (see eq. (11.11)).

where ω is given by eq. (10.10). That amounts to all modes which are tachyonic and have physical growth times less than $m_\phi/2$. Then, the growth rate of the energy density is larger than the oscillation frequency.[1] Employing the estimate (11.2), we find

$$\frac{a_{\mathrm{close}}}{a_{\mathrm{osc}}} = (\alpha\theta)^{\frac{2}{3}}\,. \tag{14.10}$$

This describes the scale factor at the moment where dark photon production ceases to be efficient. We then demand $a_\star < a_{\mathrm{close}}$ to find the minimal value of $\alpha = \alpha_{\mathrm{min}}$ for a set of model parameters $\{m_\phi, f_\phi, \theta\}$. The results are shown in fig. 14.1 for $\theta = 1$. We find that for $f_\phi \lesssim 10^{16}\,\mathrm{GeV}$, $\alpha \sim 1$ is sufficient to have tachyonic dark photon amplification due to the increased growth rate $\tilde{\omega}/H_{\mathrm{osc}} \propto r_{\mathrm{sc}}^{-2}$, while large decay constants require $\alpha \sim \mathcal{O}(10-100)$. As a consequence, the resulting GW spectrum is enhanced (cf. eq. (11.28)). To estimate the maximum GW amplitude, however, we choose a more conservative value $\alpha = 2\alpha_{\mathrm{min}}$ (see, e.g., fig. 11.4) since for $\alpha = \alpha_{\mathrm{min}}$, we have $a_\star = a_{\mathrm{close}}$ and the tachyonic instability stops being efficient right after the onset of oscillations. Let us mention that the possibility of lowering α in the case of trapped misalignment has already been found in ref. [435].

1 Note that this corresponds to a conservative criterion, which is confirmed by our numerical simulations. In principle, tachyonic growth may remain efficient for $|\omega| \lesssim am_\phi/2$, if the unstable modes spend more than one oscillation time in the tachyonic band.

SM PHOTON CASE. We will now repeat the calculation of the growth time for the SM photon case. Here, Bunch-Davies initial conditions do not apply, since the photon is thermalized. Hence, its initial state is described by a Bose-Einstein distribution, and the total energy density reads

$$\rho_\gamma(\tau_{\rm osc}) = \frac{g_\gamma}{2\pi^2 a_{\rm osc}^4}\int_0^{k_{\rm close}} dk k^3 \left(\exp\left(\frac{k}{a_{\rm osc}T}\right)-1\right)^{-1}\,, \tag{14.11}$$

where we integrate over the tachyonic band with $k_{\rm close} = \alpha\theta m_\phi a_{\rm osc}$ (see. sec. 12.1), and $g_\gamma = 2$. For a set of model parameters, we evaluate this expression numerically. As the peak growth rate at finite temperature scales as $\omega_{\rm T} \propto \tilde{k}^3 \propto |\phi'|^3 \propto \sin^3(m_\phi t)$, and $\langle \sin^3(m_\phi t)\rangle = 4/(3\pi)$, we have

$$\langle \tilde{\omega}_{\rm T}\rangle = \frac{4}{3\pi}\tilde{\omega}_{\rm T}\,. \tag{14.12}$$

Here $\tilde{\omega}_{\rm T}$ is given by eq. (12.6). As an axion-driven period of thermal inflation is allowed before the onset of oscillations, the Universe is either radiation- or matter-dominated at the onset of tachyonic growth. Distinguishing those cases, we have

$$\frac{a_\star}{a_{\rm osc}} = \begin{cases} 1+\dfrac{a_{\rm osc}m_\phi}{\langle\tilde{\omega}_{\rm T}\rangle} r_{\rm sc}^2 \ln\left(\dfrac{\theta^2 m_\phi^2 f_\phi^2}{2\rho_\gamma(\tau_{\rm osc})}\right)\,, & \text{RD}\,, \\ \left[1+\dfrac{a_{\rm osc}\theta m_\phi f_\phi}{2\sqrt{6}M_{\rm Pl}\langle\tilde{\omega}_{\rm T}\rangle}\ln\left(\dfrac{\theta^2 m_\phi^2 f_\phi^2}{2\rho_\gamma(\tau_{\rm osc})}\right)\right]^2\,, & \text{MD}\,, \end{cases} \tag{14.13}$$

where the first (second) expression applies for light (very heavy) ALPs (cf. sec. 12.1). Compared to the dark photon case, we typically have much more supercooling for the SM photon, hence the growth times are much smaller such that $a_\star/a_{\rm osc} \sim 1$ in most of the parameter space. To approximate the moment of band closure, we assume relation (14.10). This holds since i) the SM photon instability band hase the same cutoff momentum as in the dark photon case, and ii) a large amount of supercooling is required, such that the difference between the finite-T and zero-T dispersion relations is negligible in most of the parameter space. Then, $\alpha_{\rm min} \sim 1$ in a large part of the parameter space.

14.B DETAILS ON THE COSMOLOGICAL CONSTRAINTS

In the following, we derive the cosmological constraints on the audible axion model in the case of delayed oscillations. To this end, we again treat the dark photon and SM photon case separately.

DARK PHOTON CASE. Let us first consider the parameter space where the ALP is cosmologically stable, that is, its decay rate into dark photons (11.12) is below the

present expansion rate of the Universe H_0. Here, the ALP contributes to the present DM abundance, hence we need to ensure that

$$h^2\Omega_{\phi,0} = \epsilon_{\rm sup}\Omega_{\phi,\star}\left(\frac{H_\star}{H_{100}}\right)^2\left(\frac{T_0}{T_\star}\right)^3\frac{g_s^0}{g_s^\star} \leq 0.12\,, \tag{14.14}$$

where $H_{100} = 100\,\mathrm{km(Mpc\,s)^{-1}}$ and $T_0 = 2.73\,\mathrm{K}$ is the present temperature of the CMB. Via eqs. (10.21), (11.6), (11.10), and (11.11), we obtain

$$h^2\Omega_{\phi,0} \simeq 4.95\times10^{-5}\epsilon_{\rm sup}\left(\frac{\theta f_\phi}{10^{10}\,\mathrm{GeV}}\right)^2\left(\frac{m_\phi}{\mathrm{eV}}\right)^{\frac{1}{2}} r_{\rm sc}^{-3}(g_\epsilon^{\rm osc,aa})^{\frac{3}{4}}(g_s^\star)^{-1}\,, \tag{14.15}$$

in terms of our model parameters. This is translated on the required suppression of the axion abundance through the tachyonic resonance,

$$\epsilon_{\rm sup}^{\rm DM} \lesssim 2.89\times10^{-9}\left(\frac{g_\epsilon^\star}{g_\epsilon^{\rm osc}}\frac{a_\star}{a_{\rm osc}}\right)^{\frac{3}{4}}\left(\frac{\mathrm{eV}}{m_\phi}\right)^{\frac{1}{2}}\left(\frac{10^{10}\,\mathrm{GeV}}{\theta f_\phi}\right)^{\frac{1}{2}}\,. \tag{14.16}$$

Hence, larger masses and decay constants require a larger suppression of the abundance, i.e., smaller $\epsilon_{\rm sup}$. This bound is shown in the light-m_ϕ region of, e.g., figs 11.1 and 11.4.

Moving on to the heavy ALP parameter region, we note that DM constraints are evaded since the pseudoscalar decays before BBN. The decay products are dark photons which behave as dark radiation, hence they contribute to the effective relativistic degrees of freedom (cf. eq. (11.16)) via

$$\Delta N_{\rm eff}^{\rm decay} = \frac{8}{7}\left(\frac{11}{4}\right)^{\frac{4}{3}}\frac{g_\epsilon^\star}{g_\gamma}\left(\frac{g_s^0}{g_s^\star}\right)^{\frac{4}{3}}\epsilon_{\rm sup}\Omega_{\phi,\star}\frac{a_{\rm decay}}{a_\star}\,, \tag{14.17}$$

Here, the scale factor ratio which parametrizes the duration of the period between GW production and axion decay reads

$$\frac{a_\star}{a_{\rm decay}} = \min\left\{1, \left(\frac{\Gamma_{\phi\to XX}}{H_\star}\right)^{\frac{1}{2}}\right\}\,, \tag{14.18}$$

under the assumption that the ALPs decay right at $\Gamma_{\phi\to XX} = H$. We find

$$\frac{\Gamma_{\phi\to XX}}{H_\star} \simeq 4.42\times10^{-15}\frac{(g_s^\star)^{\frac{2}{3}}}{(g_\epsilon^\star)^{\frac{1}{2}}}\left(\frac{a_\star}{a_{\rm osc}}\right)^{\frac{3}{2}}\frac{\alpha^2}{\theta}\left(\frac{m_\phi}{\mathrm{GeV}}\right)^2\left(\frac{10^{10}\,\mathrm{GeV}}{f_\phi}\right)^3\,, \tag{14.19}$$

which means that only extremely heavy ALPs fulfill $\Gamma_{\phi\to XX} = H_\star$, i.e., decay right after GW emission. Since we do not consider such large masses in the dark photon case, we

specify to the second scenario on the right-hand side of eq. (14.18). Then the contribution to $N_{\rm eff}$ amounts to

$$\Delta N_{\rm eff}^{\rm decay} \simeq 4.52 \times 10^6 \epsilon_{\rm sup} (g_\epsilon^\star)^{\frac{1}{4}} (g_s^\star)^{-\frac{1}{3}} \left(\frac{a_{\rm osc}}{a_\star}\right)^{\frac{3}{4}} \frac{\theta^{\frac{1}{2}}}{\alpha} \frac{\rm GeV}{m_\phi} \left(\frac{f_\phi}{10^{10}\,\rm GeV}\right)^{\frac{3}{2}} . \tag{14.20}$$

Imposing $\Delta N_{\rm eff}^{\rm decay} < 0.3$ [14], we have

$$\epsilon_{\rm sup}^{\rm decay} \lesssim 6.64 \times 10^{-8} (g_\epsilon^\star)^{-\frac{1}{4}} (g_s^\star)^{\frac{1}{3}} \left(\frac{a_\star}{a_{\rm osc}}\right)^{\frac{3}{4}} \frac{\alpha}{\theta^{\frac{1}{2}}} \frac{m_\phi}{\rm GeV} \left(\frac{10^{10}\,\rm GeV}{f_\phi}\right)^{\frac{3}{2}} . \tag{14.21}$$

Contrary to the DM bound (14.16), larger masses now allow for larger values of $\epsilon_{\rm sup}$. This is because heavy ALPs decay earlier. We show the limit on the efficiency of the tachyonic instabilty in the large-m_ϕ region of fig. 11.1.

SM PHOTON CASE. In the case of the SM photon, all $N_{\rm eff}$ constraints computed above are evaded since no dark radiation—aside from GWs—is produced. Therefore, the only hard constraint is imposed by the relic DM abundance in the small-m_ϕ parameter space. Heavy ALPs that decay before BBN necessarily lead to a consistent cosmological evolution. However, depending on the efficiency of Schwinger pair production, the axion suppression during the tachyonic resonance, and the axion decay rate, a MD period may emerge. This modification of the cosmic history affects the relic GW abundance and the location of its spectral peak.

For light axions where $\Gamma_{\phi\to\gamma\gamma} < H_{\rm BBN}$, we have found in the main text that an axion-driven period of thermal inflation is unavoidable for efficient tachyonic growth (cf. eq. (12.8)). Then, it is crucial that the Schwinger effect is suppressed, such that $\Omega_{\gamma,\rm max} = 1$. If this was not the case, the ALP would continue to carry a substantial fraction of the total energy density of the Universe after GW emission. As perturbative decays are forbidden, we would encounter a MD period during BBN. This is inconsistent with observations, hence we exclude the parameter space where $\Gamma_{\phi\to\gamma\gamma} < H_{\rm BBN}$ and $\Omega_{\gamma,\rm max} < 1$.

If fermion production is inefficient, the axion abundance can efficiently be suppressed by the production of photons, such that the Universe transitions to RD after GW emission. If the SM photons thermalize quickly after production, the associated reheating temperature is

$$T_{\rm rh} = \left(\frac{90}{\pi^2 g_{\epsilon,\rm rh}}\right)^{\frac{1}{4}} \sqrt{H_{\rm rh} M_{\rm Pl}} , \tag{14.22}$$

where

$$H_{\rm rh} = H_{\rm osc} \left(\frac{a_{\rm osc}}{a_\star}\right)^{\frac{3}{2}} = \left(\frac{\rho_{\phi,\rm osc}}{3M_{\rm Pl}^2}\right)^{\frac{1}{2}} \left(\frac{a_{\rm osc}}{a_\star}\right)^{\frac{3}{2}} . \tag{14.23}$$

In terms of the model parameters, this translates to

$$T_{\rm rh} \simeq 3.51\,{\rm GeV}(g_{\epsilon,{\rm rh}})^{-\frac{1}{4}} \left(\frac{a_{\rm osc}}{a_\star}\right)^{\frac{3}{4}} \theta^{\frac{1}{2}} \left(\frac{m_\phi}{\rm eV}\right)^{\frac{1}{2}} \left(\frac{f_\phi}{10^{10}\,{\rm GeV}}\right)^{\frac{1}{2}} , \tag{14.24}$$

where $a_{\rm osc}/a_\star$ is the growth time estimate (14.13). Here, both m_ϕ and f_ϕ lower the reheating temperature as $\rho_{\phi,{\rm osc}} \sim m_\phi^2 f_\phi^2$. The requirement that $T_{\rm rh} > T_{\rm BBN}$ gives the first constraint, which is, shown in figs. 12.3 and 11.4. By redshifting the relic axion abundance to today, we find

$$h^2\Omega_{\phi,0} = 7.24\times 10^8 \epsilon_{\rm sup} (g_s^{\rm rh})^{-1} (g_{\epsilon,{\rm rh}})^{\frac{3}{4}} \left(\frac{a_{\rm osc}}{a_\star}\right)^{\frac{3}{4}} \theta^{\frac{1}{2}} \left(\frac{m_\phi}{\rm eV}\right)^{\frac{1}{2}} \left(\frac{f_\phi}{10^{10}\,{\rm GeV}}\right)^{\frac{1}{2}} , \tag{14.25}$$

which translates to the required suppression of the abundance for the axion to constitute all of DM

$$\epsilon_{\rm sup}^{\rm SM,DM} \lesssim 1.66\times 10^{-10} g_s^{\rm rh} (g_{\epsilon,{\rm rh}})^{-\frac{3}{4}} \left(\frac{a_\star}{a_{\rm osc}}\right)^{\frac{3}{4}} \left(\frac{\rm eV}{m_\phi}\right)^{\frac{1}{2}} \left(\frac{10^{10}\,{\rm GeV}}{\theta f_\phi}\right)^{\frac{1}{2}} . \tag{14.26}$$

This is essentially the same condition as for the dark photon scenario (14.16) with a $\mathcal{O}(1)$ suppressed prefactor. That comes from the fact that the ALP carries a larger fraction of the total energy density as the coupling to the SM photon necessitates more supercooling. This requires a more efficient energy transfer. If the above bound is fulfilled, the GW frequency and amplitude are redshifted in the standard way defined by eqs. (3.12) and (3.13).

Finally, let us compute the length of the MD period and its associated redshift factors for heavy axions, i.e., $\Gamma_{\phi\to\gamma\gamma} > H_{\rm BBN}$. The Hubble parameter at GW emission reads

$$H_\star = \left[\frac{1}{3M_{\rm Pl}^2}\left(\rho_{\phi,\star} + \rho_{{\rm rad},\star}\right)\right]^{\frac{1}{2}} , \tag{14.27}$$

where

$$\begin{aligned} \rho_{\phi,\star} &= \rho_{\phi,{\rm osc}} \left(\frac{a_{\rm osc}}{a_\star}\right)^3 , \\ \rho_{{\rm rad},\star} &= \rho_{\rm rad}(T_{\rm osc}) \left(\frac{a_{\rm osc}}{a_\star}\right)^4 . \end{aligned} \tag{14.28}$$

Here we have accounted for the fact that the ALP may carry only a subdominant part of the total energy density for large masses (see eq. (12.8)). $T_{\rm osc}$ is obtained as described in sec. 12.1, i.e., by requiring that a sufficient number of photon modes can grow efficiently. If $\Gamma_{\phi\to\gamma\gamma} > H_\star$, ALPs start to decay right after the onset of oscillations and a MD period is avoided. For $\Gamma_{\phi\to\gamma\gamma} < H_\star$, the Universe may experience an ALP-driven period of MD; this depends on the efficiency of the Schwinger effect. If the production of fermions blocks

the tachyonic resonance, we have $\Omega_\gamma^{\rm after} \ll 1$, and the axion abundance is fixed. In the case where the Schwinger effect can be neglected, we have $\Omega_\gamma^{\rm after} = 1$ and the axion abundance is affected by the efficiency of the tachyonic instability, parametrized by $\epsilon_{\rm sup}$. Then,

$$\rho_\phi^{\rm after} = \begin{cases} \rho_{\phi,\star} - \rho_\gamma^{\rm after}\,, & \rho_\gamma^{\rm after} < \rho_{\phi,\star}\,, \\ \epsilon_{\rm sup}\,\rho_{\phi,\star}\,, & \rho_\gamma^{\rm after} = \rho_{\phi,\star}\,. \end{cases} \tag{14.29}$$

This defines the radiation energy density after photon production

$$\rho_{\rm rad}^{\rm after} = 3H_\star^2 M_{\rm Pl}^2 - \rho_\phi^{\rm after}\,. \tag{14.30}$$

As the resonance ceases to be efficient, the ALPs scale as matter, i.e., are enhanced $\propto a$ compared to the radiation energy density. Therefore, MD starts once

$$\frac{a_\star}{a_{\rm md}} = \min\left\{1, \frac{\rho_\phi^{\rm after}}{\rho_{\rm rad}^{\rm after}}\right\}, \tag{14.31}$$

and ends when the Hubble parameter is of order of the ALP decay rate

$$H_{\rm rh} = \Gamma_{\phi\to\gamma\gamma}\,, \tag{14.32}$$

where

$$H_{\rm rh} = \left[\frac{1}{3M_{\rm Pl}^2}\left(\rho_\phi^{\rm after}\left(\frac{a_\star}{a_{\rm rh}}\right)^3 + \rho_{\rm rad}^{\rm after}\left(\frac{a_\star}{a_{\rm rh}}\right)^4\right)\right]^{\frac{1}{2}}. \tag{14.33}$$

A MD period hence is avoided if $a_{\rm md} \geq a_{\rm rh}$. In this case, the GW redshift factors again reduce to their standard form (cf. eqs. (3.12) and (3.13)). An intermediate MD period emerges if $a_{\rm md} < a_{\rm rh}$. The length of this epoch is then obtained by solving

$$H_{\rm decay} = \left[\frac{1}{3M_{\rm Pl}^2}\left(\rho_\phi^{\rm md}\left(\frac{a_{\rm md}}{a_{\rm rh}}\right)^3 + \rho_{\rm rad}^{\rm md}\left(\frac{a_{\rm md}}{a_{\rm rh}}\right)^4\right)\right]^{\frac{1}{2}} = \Gamma_{\phi\to\gamma\gamma}\,, \tag{14.34}$$

for $a_{\rm md}/a_{\rm rh}$. In the above expression, the energy densities at the onset of MD fulfill

$$\rho_\phi^{\rm md} = \rho_\phi^{\rm after}\left(\frac{a_\star}{a_{\rm md}}\right)^3 = \rho_{\rm rad}^{\rm after}\left(\frac{a_\star}{a_{\rm md}}\right)^4 = \rho_{\rm rad}^{\rm md}\,, \tag{14.35}$$

where $a_\star/a_{\rm md}$ if defined by eq. (14.31). By computing the modification of the cosmic history numerically, that is, solving for the redshift factors, we obtain the appropriate scaling of the GW peak amplitude and frequency:

$$h^2\tilde{\Omega}_{\rm GW,0} = 1.67\times10^{-5}\left(\frac{100}{g_\epsilon^{\rm rh}}\right)^{\frac{1}{3}}\tilde{\Omega}_{\rm GW,\star}\frac{a_{\rm md}}{a_{\rm rh}}\,, \tag{14.36}$$

$$\tilde{f}_0 = 1.65\times10^{-7}\,{\rm Hz}\,\frac{2\tilde{k}_\star}{a_\star H_{\rm rh}}\frac{T_{\rm rh}}{\rm GeV}\left(\frac{g_{\epsilon,{\rm rh}}}{100}\right)^{\frac{1}{6}}\frac{a_\star}{a_{\rm rh}}\,. \tag{14.37}$$

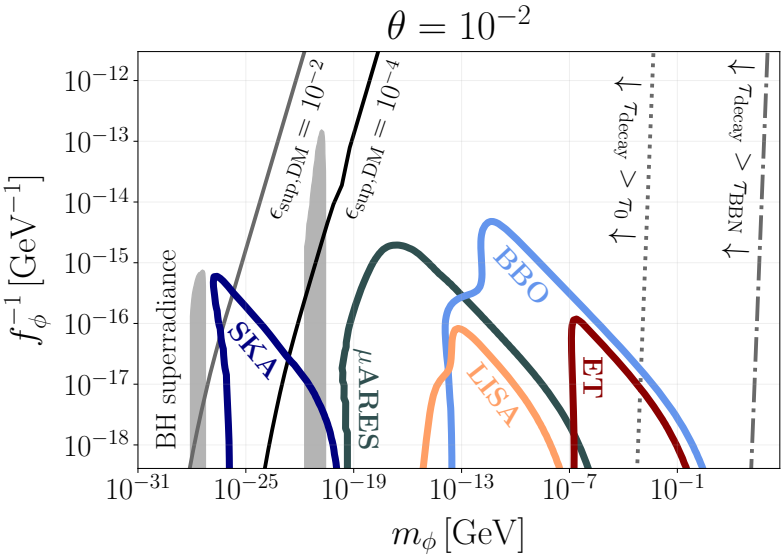

Figure 14.2: Testable parameter space in the $m_\phi - f_\phi^{-1}$ plane for supercooled axion-dark photon systems, employing $\alpha = 2\alpha_{\mathrm{min}}$ and $\theta = 10^{-2}$. The colored curves indicate the detection prospects of several future experiments, while the gray and black solid lines show the bound from the present DM abundance. While the parameter space where the axion can constitute DM opens up, the GW amplitude is decreased for small values of the misalignment angle.

Note that GWs scale as radiation, i.e., the peak amplitude is only affected by an additional MD period. The peak frequency, on the other hand, obtains its standard redshift from T_{rh}, however, is affected by both intermediate RD and MD periods. This is why $a_\star/a_{\mathrm{rh}}$ enters in eq. (14.37).

14.C VARYING THE MISALIGNMENT ANGLE θ

In the last section of part iii, we repeat our analysis from chapter 11 for a different value of the misalignment angle $\theta = 10^{-2}$ and $\alpha = 2\alpha_{\mathrm{min}}$. The resulting sensitivity curves of several future observatories are shown in fig. 14.2. We observe that the parameter space where the axion can constitute the entirety of DM for moderate values of ϵ_{sup} opens up. That is a consequence of eq. (14.15), where we have found that the relic abundance is enhanced by θ^2. A smaller misalignment angle, however, necessitates a larger coupling α for efficient GW production (cf. eq. (11.7)). Increasing α shifts the characteristic momenta to the UV, i.e., deeper inside the Hubble horizon. This in turn suppresses the GW amplitude (see eq. (11.28)). Therefore, the size of the parameter space where the axion can both constitute DM and produce sizable GW signals is effectively independent of θ.

Part IV

IMPACT OF THEORETICAL UNCERTAINTIES ON GRAVITATIONAL WAVE PREDICTIONS FROM FIRST-ORDER PHASE TRANSITIONS

15

PRELUDE

In the previous parts, we have studied in detail the GW phenomenology of several SM extensions. In the last main part of this work, we turn our attention to a more formal aspect of such GW computations, focusing on FOPTs. Analyses of FOPTs involve several computational steps: the construction of the effective potential, the calculation of the bubble nucleation rate, and hydrodynamical simulations of the colliding bubbles in a thermal bath. Each of these steps is a potential source for theoretical uncertainties accumulating in the final GW spectrum.

In the following, we focus on the calculation of the finite-temperature effective potential and its impact on GW predictions. This is a particularly delicate part of the computational pipeline due to the breakdown of perturbativity at high temperature [55]. In principle, non-perturbative calculations are therefore necessary [162, 471–474], however, often unfeasible for large parameter scans. To this end, we have introduced one-loop Daisy resummation in sec. 3.2, where propagators are supplemented by thermal masses, extending the validity of perturbative treatments. While most of the PT literature relies on one-loop resummation (e.g. [165, 228, 475–482]) it is well known that this approach carries large uncertainties, dominantly sourced by the RG-scale dependence of the effective potential [56], inducing up to $\mathcal{O}(10^4)$ uncertainties of the predicted GW amplitude; see fig. 15.1. This is cured by implementing a more systematic approach to thermal resummation: high-temperature DR [166, 483, 484]. For PTs involving a thermal scale hierarchy [164], non-zero Matsubara modes are integrated out, resulting in a three-dimensional (3D) EFT for the scalar zero mode driving the transition. Maintaining a consistent power counting, higher-order contributions are systematically incorporated, which significantly alleviates the RG scale dependence [171, 320]. Let us also note that dimensionally reduced effective potentials show a remarkable agreement with non-perturbative lattice analyses [164, 485].

As previous studies have focused mainly on the thermodynamic properties of a given model [56, 171, 320, 486, 487], we will go further and study the impact of thermal resummation on the overall parameter space and the GW inverse problem [191, 487–492]. This

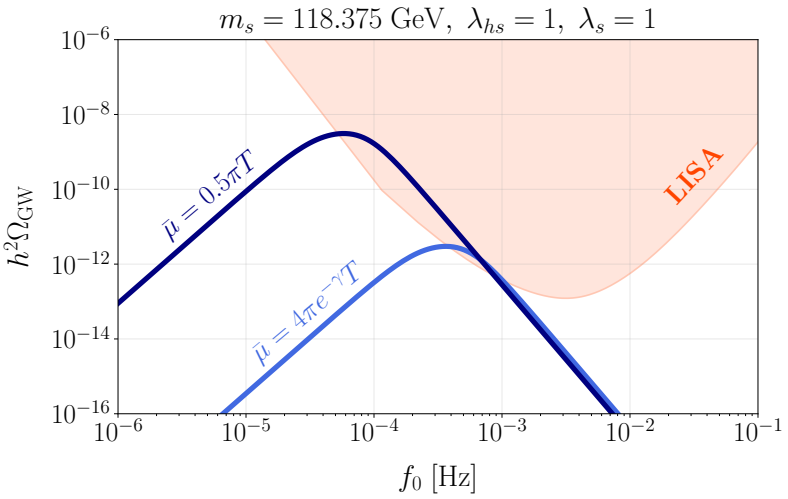

Figure 15.1: Benchmark GW prediction from the EWPT in the xSM, computed with the EFT approach employing one-loop matching (see sec. 17.3). A variation of the RG scale $\bar{\mu}$ shifts the GW amplitude by almost four orders of magnitude.

concerns the determination of the microscopic parameters of a QFT from a given GW signal. In light of the upcoming LISA observatory [35], sensitive to the electroweak scale, it is crucial to study the effect of theoretical uncertainties on the reconstruction of model parameters.

Since a first-order EWPT requires new dynamical degrees of freedom in the IR [224, 493], we extend the SM by a light, real, gauge-singlet scalar field (xSM) [171, 320, 478, 493–497]. We construct the 3D EFT of the xSM at increasing levels of diligence using the Mathematica software `DRAlgo` [179]. By performing large-scale scans we then investigate how the large uncertainty of single parameter points, shown in fig. 15.1, affects the overall observable parameter space.[1] Finally, we compare our predictions to the projected sensitivity region of LISA. For a benchmark signal, we reconstruct the model parameters via a Fisher matrix analysis [500], employing different approximations of the effective potential. Intriguingly, we find that incomplete thermal resummation induces errors on the reconstructed parameters of $\mathcal{O}(1\%)$, which, despite being numerically small, dominate over experimental uncertainties, even for barely detectable signals.

In sec. 16, we first outline the formalism of DR, before introducing the xSM at zero and finite temperature in sec. 17. Then, we study the associated theoretical errors on both the thermodynamics and GW signals in sec. 18.

1 Note that after the publication of [2], further scans of the xSM have been conducted [498, 499].

16

THERMAL EFFECTIVE FIELD THEORY

In the following, we aim to discuss the concept of dimensionally reduced thermal EFT. Given a full theory, an EFT is generally constructed by

1. identifying light and heavy degrees of freedom,
2. constructing an effective IR Lagrangian that respects all underlying symmetries, and
3. matching the effective parameters to the full theory.

The result is an effective theory in the IR, valid up to some cutoff scale where heavy physics becomes important. To this end, we first outline the scale hierarchy emerging at finite temperature, before exemplarily constructing the 3D EFT in a simple scalar field theory. We demonstrate the equivalence to Daisy resummation (cf. sec. 3.2) at one-loop order and show how to extend the EFT to higher loop orders.

16.1 THERMAL SCALE HIERARCHY

To identify the light and heavy degrees of freedom at finite temperature, let us discuss the finite-temperature scale hierarchy. Let us assume a scalar field with mass m, charged under some gauge symmetry with corresponding coupling g. The corresponding effective expansion parameter then reads [109]

$$\epsilon_b \sim \frac{g^2 T}{\pi m} \,. \tag{16.1}$$

As already discussed in sec. 3.2, non-zero Matsubara modes have $\omega \sim \pi T$, hence are IR safe. They defined the highest energy scale; the *hard scale*. For hard modes, the expansion parameter reduces to $\epsilon_b \sim (g/\pi)^2$, which is perturbative.

Conversely, eq. (16.1) immediately defines scale where finite-temperature QFT becomes inherently non-perturbative. For masses below the *ultrasoft scale* $m \sim g^2 T/\pi$, associated with the thermal mass of color-magnetic fields [55], we have $\epsilon_b \sim \mathcal{O}(1)$ and perturbation

theory breaks down. This is known as the *Linde problem*. Hence, PTs occurring at the ultrasoft scale can only be studied by non-perturbative techniques such as lattice simulations. This is the case for the EWPT in the SM [19].

Fortunately, strong FOPTs typically occur at a scale between hard and ultrasoft. This comes from the fact that the dynamics of the zero-mode is screened by UV fluctuations. That is, hard modes induce thermal masses for the Matsubara zero-mode. Such thermal masses, that we have already encountered in secs. 3.2 and 5.2, live at the *soft scale* $\sim gT$, defined by the thermal Debye masses of longitudinal gauge field modes [155, 501]. The procedure of integrating out heavy fields with masses $m \sim \pi T$ is known as DR [166, 502]. Regarding the expansion parameter (16.1), we find $\epsilon_b \sim g/\pi$, i.e., perturbation theory is applicable at the soft scale.

As already noted in sec. 3.2, at the time of a PT we encounter partial cancellations between the vacuum and thermal masses of the scalar field [164],

$$\mu_3^2 \approx \mu^2 + cg^2T^2 \ll g^2T^2 \,. \tag{16.2}$$

Here, the subscript "3" indicates masses at finite temperature, and the second term is the thermal mass with c being a $\mathcal{O}(1)$ prefactor. Those cancellations may render the scalar field lighter than soft, but heavier than ultrasoft. As a consequence soft fields, e.g., longitudinal gauge bosons, can be integrated out.[1] This induces a $\mathcal{O}(g^3T^2/\pi)$ contribution, such that the scalar zero-mode lives at the *supersoft scale* $\sim g^{\frac{3}{2}}T/\sqrt{\pi}$ [164]. The associated expansion parameter reads $\epsilon_b \sim (g/\pi)^{\frac{1}{2}}$. The supersoft EFT has been introduced in ref. [182], and is mainly relevant for radiative symmetry breaking PTs [164].

To summarize, the relevant energy scales[2] are given by

$$\underbrace{\pi T}_{=\text{hard scale}} \gg \underbrace{\left(\frac{g}{\pi}\right)\pi T}_{=\text{soft scale}} \gg \underbrace{\left(\frac{g}{\pi}\right)^{\frac{3}{2}}\pi T}_{=\text{supersoft scale}} \gg \underbrace{\left(\frac{g}{\pi}\right)^{2}\pi T}_{=\text{ultrasoft scale}} \,. \tag{16.3}$$

While the ultrasoft scale is non-perturbative, the remaining scales admit a perturbative expansion. In the next step, we discuss the technical details on how to employ said scale hierarchy to construct an EFT for a transitioning soft scalar field.

1 The supersoft theory is constructed in the broken phase, where also spatial gauge boson modes are integrated out due to their large field-dependent masses [164].

2 Note that there are further scales that emerge at finite temperature, such as the semi-soft scale $\sim \sqrt{\pi g}T$, which are however not relevant in our context.

16.2 DIMENSIONAL REDUCTION

Since the scale of UV temperature fluctuations is much smaller than the size of a nucleating macroscopic bubble, cosmological FOPTs are inherently driven by IR dynamics. To this end, hard modes can be integrated out, resulting in an effective, static, bosonic 3D theory at the soft scale, capturing the long-distance physics. Originally developed in the 1990s [166, 502], DR has gained popularity in light of future GW observatories potentially sensitive to a FOPT. The main advantage of DR compared to the more conventional 4D one-loop approach (cf. secs. 3.2 and 5.2), where hard modes are resummed, is the possibility of consistently including higher loop orders. This allows for a precision computation of the effective potential, alleviating theoretical uncertainties such as gauge and RG scale dependence [56]. For recent studies of FOPTs using DR, see, e.g., refs. [163, 164, 171, 179, 181–183, 247, 320, 473, 474, 485, 486, 493, 497–499, 503–510]. Let us also highlight the Mathematica package `DRAlgo` [511], which provides matching relations and the effective potential up to two-loop order for generic BSM theories. While we will employ `DRAlgo` for our analysis of the xSM in chapter 18, we aim to give the reader an informative introduction in this section.

To this end, let us focus on a simple benchmark model: $\lambda\Phi^4$-theory in the Z_2-symmetric limit [167, 502, 512]. In Euclidean signature, the Lagrangian reads

$$\mathcal{L} = \underbrace{\frac{1}{2}(\partial_\tau \Phi)^2 + \frac{1}{2}(\boldsymbol{\nabla}\Phi)^2}_{=\mathcal{L}_{\text{free}}} + \underbrace{\frac{m^2}{2}\Phi^2 + \frac{\lambda}{4!}\Phi^4}_{=\mathcal{L}_{\text{int}}}, \tag{16.4}$$

where τ is imaginary time (cf. sec. 3.2) and the scalar self-interaction parametrized by λ. Furthermore, we treat the mass term $\sim m$ as a small perturbation, hence include it in the interaction Lagrangian. This is justified in the high-T limit where the characteristic scale of the free Lagrangian $\pi T \gg m$ [512]. In the absence of gauge fields, we only encounter two scales in the theory: soft and hard degrees of freedom, corresponding to the scalar Matsubara zero and non-zero modes, respectively. Integrating out the hard modes, the static dimensionally reduced 3D effective theory takes the form

$$\mathcal{L}_3 = \underbrace{\frac{1}{2}(\boldsymbol{\nabla}\bar{\phi})^2}_{=\mathcal{L}_{3,\text{free}}} + \underbrace{\frac{m_3^2}{2}\bar{\phi}^2 + \frac{\lambda_3}{4!}\bar{\phi}^4}_{=\mathcal{L}_{3,\text{int}}}, \tag{16.5}$$

where we have introduced the subscript "3" to indicate effective parameters. Note that the 3D field $\bar{\phi} = \Phi/\sqrt{T}$ carries mass dimension $1/2$; λ_3 has mass dimension 1. In principle, eq. (16.5) contains higher-dimensional operators, which we neglect for this demonstration.

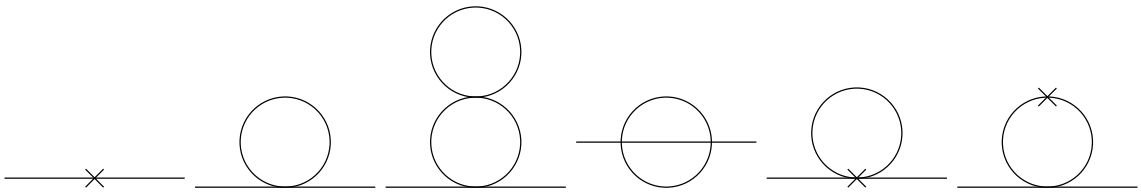

Figure 16.1: Diagrams contributing to the two-point correlation function of the scalar field up to two-loop order.

The goal in this section is to determine the EFT parameters m_3 and λ_3 by matching the respective correlation functions between the full and effective theory. The correlators are denoted by $\Gamma^{(k)}$, where all one-particle irreducible diagrams with k external legs contribute.

Let us first focus on the two-point correlation function; the corresponding diagrams are shown in fig. 16.1. Here the crosses denote insertions of counterterms δm and $\delta\lambda$ that are required to cancel the UV divergences. In the full theory, the two-point correlation function up to two-loop order is [512]

$$\begin{aligned}\Gamma^{(2)}(-\boldsymbol{p},\boldsymbol{p}) = p^2 + m^2 + \delta m^2 + \frac{\lambda}{2}\sum\!\!\!\!\!\!\int_Q \frac{1}{Q^2} - \frac{\lambda^2}{4}\sum\!\!\!\!\!\!\int_{QR} \frac{1}{Q^4R^2} - \frac{\lambda^2}{6}\sum\!\!\!\!\!\!\int_{QR} \frac{1}{Q^2R^2(Q+R)^2} \\ + \frac{\delta\lambda}{2}\sum\!\!\!\!\!\!\int_Q \frac{1}{Q^2} - \frac{\lambda}{2}(m^2+\delta m^2)\sum\!\!\!\!\!\!\int_Q \frac{1}{Q^4}\,,\end{aligned} \tag{16.6}$$

where we have abbreviated Matsubara sum integrals by

$$\sum\!\!\!\!\!\!\int_P \equiv T\sum_{n=-\infty}^{\infty}\int_P . \tag{16.7}$$

UV divergencies are regulated using the modified minimal subtraction ($\overline{\text{MS}}$) scheme. The counterterms and the integrals are known [512], yielding

$$\begin{aligned}\Gamma^{(2)}(-\boldsymbol{p},\boldsymbol{p}) = p^2 + m^2 + \frac{\lambda T^2}{24} + \frac{1}{(4\pi)^2}\bigg[\frac{\lambda^2T^2}{12}\left(\frac{1}{2\epsilon} + \frac{1}{4}L_b(\Lambda) - \gamma + 12\log(A)\right) \\ - \frac{1}{2}\lambda m^2 L_b(\Lambda)\bigg]\,,\end{aligned} \tag{16.8}$$

where

$$L_b(\Lambda) \equiv 2\log\left(\frac{e^\gamma\Lambda}{4\pi T}\right)\,, \tag{16.9}$$

and A is the Glaisher–Kinkelin constant. The EFT matching scale is denoted by Λ.

The effective theory only contains the Matsubara zero mode with $\omega_n = 0$, i.e., the loop integrals in fig. 16.1 do not include a mass scale. Such integrals vanish in dimensional regularization, therefore [512]

$$\Gamma_3^{(2)}(-\boldsymbol{p},\boldsymbol{p}) = p^2 + m_3^2 + \delta m_3^2\,. \tag{16.10}$$

Figure 16.2: Diagrams that contribute to the four-point correlation function up to $\mathcal{O}(\lambda^2)$.

Here the counterterm δm_3^2 is chosen to cancel the $1/\epsilon$ divergence of $\Gamma^{(2)}(-\boldsymbol{p},\boldsymbol{p})$. The same procedure is done for the four-point correlation function, which yields thermal corrections to the scalar self-coupling. The relevant one-loop diagrams, contributing at $\mathcal{O}(\lambda^2)$, are shown in fig. 16.2. The computation yields [512]

$$\Gamma^{(4)}(\boldsymbol{p},\boldsymbol{q},\boldsymbol{r},-\boldsymbol{p}-\boldsymbol{q}-\boldsymbol{r}) = \lambda - \frac{1}{(4\pi)^2}\frac{3}{2}\lambda^2 L_b(\Lambda)\,, \tag{16.11}$$

$$\Gamma^{(3)}(\boldsymbol{p},\boldsymbol{q},\boldsymbol{r},-\boldsymbol{p}-\boldsymbol{q}-\boldsymbol{r}) = \lambda_3 + \delta\lambda_3\,. \tag{16.12}$$

By matching the 3D and 4D computations, we obtain the EFT parameters at $\mathcal{O}(\lambda^2)$,

$$m_3^2 = \bar{m}^2 + \frac{\bar{\lambda}T^2}{24} + \frac{\lambda_3^2}{6(4\pi)^2}\left[\log\left(\frac{\Lambda}{3T}\right) - c\right]\,, \tag{16.13}$$

$$\lambda_3 = T\bar{\lambda}\,, \tag{16.14}$$

where the constant $c \equiv \log\left(3e^{\gamma/2}A^6/(4\pi)\right)$. In addition, the barred quantities correspond to $\bar{\kappa} \equiv \kappa - (1/2)\beta_\kappa L_b(\bar{\mu})$ with $\kappa \in \{m^2,\lambda\}$, where the β-functions are found in ref. [512]. Here the 4D couplings are run to an arbitrary RG scale $\bar{\mu}$, while the 3D couplings are defined at the matching scale Λ.

Let us now highlight some important observations. First, at $\mathcal{O}(\lambda)$, the scalar mass is merely supplemented by the thermal mass $\lambda T^2/24$. That is, integrating out non-zero Matsubara modes and matching the full and effective theory is, at LO, equivalent to the resummation of Daisy diagrams we have seen in sec. 3.2. The EFT approach however allows for matching the correlation functions at higher orders, automatically incorporating the resummations required to extend the perturbative regime. At $\mathcal{O}(\lambda^2)$, this induces additional thermal mass corrections, as well as corrections to the quartic coupling constant. Second, the barred quantities in eqs. (16.13) and (16.14) are RG-invariant. The only remaining RG scale dependence is carried by the $\log(\Lambda/(3T))$ term in the effective mass [512],

$$\frac{\mathrm{d}m_3^2(\Lambda)}{\mathrm{d}\log(\Lambda)} = \frac{\lambda_3^2}{6(4\pi)^2}\,. \tag{16.15}$$

This corresponds to the β-function of the 3D theory. Therefore one may replace $\Lambda \to \bar{\mu}_3$, where $\bar{\mu}_3$ is the RG scale that will enter at two-loop order in the effective theory.

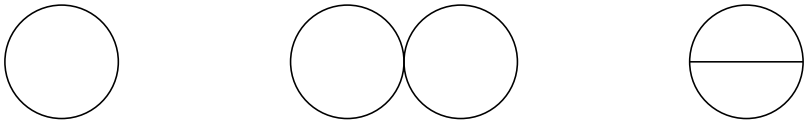

Figure 16.3: Digrams that contribute to the computation of the effective potential in $\lambda\Phi^4$-theory up to two-loop order. Note that the sunset diagram only emerges for finite background field values, where a cubic term is generated through the breaking of the Z_2 symmetry.

The construction of V_{eff} is equivalent to the procedure outlined in sec. 3.2. One computes all loop diagrams within the EFT up to the desired order with zero external momentum. Fig. 16.3 shows the relevant diagrams up to two-loop order for $\lambda\Phi^4$-theory. The crucial difference is that the temperature dependence is now fully carried by the effective parameters; no further resummations are required. The computation yields [512]

$$V_{\text{eff}}^{\text{3D}} = \underbrace{\frac{m_3^2}{2}\bar{\phi}^2 + \frac{\lambda_3}{4!}\bar{\phi}^4}_{=V_0^{\text{3D}}} \underbrace{- \frac{1}{12\pi} M_3^3}_{=V_1^{\text{3D}}} + \underbrace{\frac{1}{(4\pi)^2}\left(\frac{\lambda_3}{8}M_3^2 + \frac{(\lambda_3\bar{\phi})^2}{12}\left(\log\left(\frac{M_3}{\bar{\mu}_3}\right) - \frac{1}{2}\right)\right)}_{=V_2^{\text{3D}}}, \tag{16.16}$$

at two-loop order, where $\bar{\phi}$ is the classical 3D background field and

$$M_3^2 = m_3^2 + \frac{\lambda_3}{2}\bar{\phi}^2\,. \tag{16.17}$$

It is straightforward to verify that truncating the two-loop effective mass (16.13) at $\mathcal{O}(\lambda)$ and only taking into account one-loop corrections to $V_{\text{eff}}^{\text{3D}}$ reproduces the one-loop, Daisy resummed result from sec. 3.2. The crucial feature of the two-loop computation, however, is the cancellation of the $\bar{\mu}_3$ dependence of the thermal mass (16.13) by the explicit logarithm in V_0^{3D}. Specifically, this is checked by computing [162, 247, 506, 512]

$$\beta_{m_3^2}\frac{\partial(V_0^{\text{3D}} + V_1^{\text{3D}})}{\partial m_3^2} + \frac{\partial V_2^{\text{3D}}}{\partial \log\bar{\mu}_3} = 0\,, \tag{16.18}$$

where $\beta_{m_3^2} = \lambda m^2/(4\pi)^2$. That is, the remaining RG scale dependence is of higher order than $\mathcal{O}(\lambda^2)$. A variation of both $\bar{\mu}$ and $\bar{\mu}_3$ is hence employed as a measure of theoretical uncertainties due to higher-order effects (see chapter 18.3). Having introduced the basic principles of DR by means of a simple toy model, we are now ready to move on to xSM, i.e., the full SM plus a real gauge singlet scalar field.

17

GAUGE SINGLET EXTENDED STANDARD MODEL

In the following, we first introduce the xSM at zero temperature, including its field content and free parameters. Afterwards, we proceed to study the theory at finite temperature. To this end, we first construct the thermal effective potential in the conventional 4D approach employing Daisy resummation. Here, we use two different renormalization schemes. Then, we compute the dimensionally reduced effective potential up to two-loop order, based on the procedure introduced above.

17.1 FIELD CONTENT

The xSM [171, 320, 478, 493–497] is arguably the simplest SM extension, merely containing one real gauge-singlet scalar field S in addition to the SM particle content. In four dimensions and Euclidean signature, the underlying Lagrangian reads [171]

$$\mathcal{L}_{\text{xSM}} = \mathcal{L}_{\text{YM}} + \mathcal{L}_{\text{f}} + y_t(\bar{q}_t i\sigma_2 \phi^* q_t + \text{h.c.}) + |D_\mu \Phi|^2 + \frac{1}{2}(\partial_\mu S)^2 + V_0(\Phi, S)\,. \tag{17.1}$$

Here, $\mathcal{L}_{\text{YM}}$ denotes the contribution from the SM gauge fields, while $\mathcal{L}_{\text{f}}$ represents the kinetic fermion part. We only include the top quark Yukawa parametrized by y_t, since all other Yukawa couplings are numerically small. The SM Higgs doublet $\Phi = \left(G^+, \frac{1}{\sqrt{2}}(v + h + iG^0)\right)^{\text{T}}$ couples to the $\text{SU}(2)_{\text{L}}$ and $\text{U}(1)_{\text{Y}}$ gauge fields A^a_μ, B_μ, i.e., its covariant derivative is $D_\mu = (\partial_\mu - \frac{1}{2}ig\sigma_a A^a_\mu - \frac{1}{2}ig' B_\mu)\Phi$. Here, g and g' denote the respective gauge couplings, while σ_a with $a \in \{1, 2, 3\}$ are the Pauli matrices. $G^\pm$ and G^0 are the Goldstone modes, which become the longitudinal degrees of freedom of the $Z/W^\pm$ gauge bosons after EWSB. In addition, we split the field into a background field v and a dynamical component h.

We study the theory in the Z_2-symmetric limit, corresponding to a symmetry under $S \to -S$. That is, S only appears in even powers in the scalar potential

$$V_0(\Phi, S) = \mu_h^2 \Phi^\dagger\Phi + \lambda(\Phi^\dagger\Phi)^2 + \frac{1}{2}\mu_s^2 S^2 + \frac{\lambda_s}{4}S^4 + \frac{\lambda_{hs}}{2}S^2\Phi^\dagger\Phi\,. \tag{17.2}$$

We employ the convention where the Higgs mass parameter $\mu_h^2 < 0$, while the singlet mass term $\mu_s^2 > 0$. The portal coupling is denoted by λ_{hs}, while the singlet (Higgs) self-coupling is λ_s (λ). We then decompose the singlet as $S = x + s$, where x is a homogeneous background field while s represents the dynamical field. In terms of the background fields, the tree-level potential reads

$$V_0(v,x) = \frac{1}{2}\mu_h^2 v^2 + \frac{1}{4}\lambda v^4 + \frac{1}{2}\mu_s^2 x^2 + \frac{1}{4}\lambda_s x^4 + \frac{1}{4}\lambda_{hs} v^2 x^2 \,, \tag{17.3}$$

From this expression, we find the physical mass eigenstates by taking the second derivative with respect to the scalar fields,

$$m_h^2 = \mu_h^2 + 3\lambda v^2 + \frac{1}{2}\lambda_{hs} x^2 \,, \tag{17.4}$$

$$m_s^2 = \mu_s^2 + 3\lambda_s x^2 + \frac{1}{2}\lambda_{hs} v^2 \,, \tag{17.5}$$

$$m_G^2 = m_h^2 - 2\lambda v^2 \,. \tag{17.6}$$

Since we employ the Z_2-symmetric limit, no mass mixing emerges between the scalar fields. Further, the weak gauge bosons acquire a mass after EWSB. By diagonalizing the mass matrix, we obtain

$$m_W^2 = \frac{1}{4} g^2 v^2 \,, \tag{17.7}$$

$$m_Z^2 = \frac{1}{4}\left(g^2 + g'^2\right) v^2 \,. \tag{17.8}$$

The top quark mass reads

$$m_t^2 = \frac{y_t}{2} v^2 \,. \tag{17.9}$$

The model hence has three free parameters: the scalar self-coupling λ_s, the portal coupling λ_{hs}, and the physical mass of the singlet m_s. When fixing these input parameters, we have to ensure that the Higgs field obtains its measured mass $m_h \simeq 125.1\,\text{GeV}$ [318]. To this end, we employ two different approaches depending on the resummation scheme we use (see below).

In the Z_2-symmetric xSM, the symmetry breaking pattern is

$$(0,0) \overset{\texttt{step1}}{\longrightarrow} (0,x) \overset{\texttt{step2}}{\longrightarrow} (v_0,0) \,. \tag{17.10}$$

Hence, in the first step the scalar singlet acquires a vev, breaking the Z_2 symmetry. In the second step, the field transitions to the Higgs phase where $v_0 \approx 246\,\text{GeV}$ is the SM Higgs vev, restoring the Z_2 symmetry. In the following we focus on the second step, which, in some parts of the parameter space, is realized as a strong FOPT sourcing GWs.

17.2 EFFECTIVE POTENTIAL IN FOUR DIMENSIONS

To eventually analyze the GW signals in the xSM, we need to construct the effective potential V_{eff} at finite temperature. To this end, we proceed in increasing levels of computational diligence. In this section, we calculate V_{eff} at one-loop order in 4D, using two different renormalization schemes. Afterwards, we build V_{eff} within the 3D EFT up to two-loop order. In the following, we first discuss the 4D $\overline{\text{MS}}$ scheme, employing dimensional regularization to control UV divergencies. Next, we introduce the 4D potential in the on-shell renormalization scheme, treating divergent integrals with a hard momentum cutoff. Note that all approaches use Landau gauge ($\xi = 0$).

$\overline{\text{MS}}$ SCHEME. Let us start with the effective potential computed within the $\overline{\text{MS}}$ scheme. This construction proceeds analogously to the one conducted in sec. 5.2, introduced in sec. 3.2. For completeness, the zero-temperature CW contributions read [477]

$$V_{\text{cw}}^{\overline{\text{MS}}}(v,x) = \sum_i \eta_i n_i \frac{m_i^4(v,x)}{64\pi^2}\left[\log\left(\frac{m_i^2(v,x)}{\bar{\mu}^2}\right) - c_i\right], \tag{17.11}$$

where $\eta_i = +1\,(-1)$ for bosons (fermions), n_i are the degrees of freedom of a species i, and $c_i = 3/2\,(5/6)$ for scalars and fermions (gauge bosons). The sum runs over all particles that receive field-dependent masses $m_i^2(v,x)$.

Here we set the RG scale $\bar{\mu} = v_0$, where all couplings are evaluated.[1] We now introduce the renormalization conditions

$$\partial_v V_0\Big|_{v=v_0} = 0\,, \tag{17.12}$$

$$\partial_v^2 V_0\Big|_{v=v_0} = m_h^2 = (125.10\,\text{GeV})^2\,, \tag{17.13}$$

which ensure that the Higgs field acquires its SM vev and mass at tree-level for a set of input parameters $\{m_s, \lambda_s, \lambda_{hs}\}$. The one-loop corrections (17.11) alter these relations. Therefore, we introduce additional counterterms to preserve the renormalization conditions at the loop-level (see appendix 20.B). To avoid confusion, let us note that in the original $\overline{\text{MS}}$ scheme, counterterms merely remove divergences. Nevertheless, we follow the literature where the presented scheme is usually dubbed $\overline{\text{MS}}$ [165].

1 In the discussion around eq. (5.31), we have already seen that a thermal RG scale is the more reasonable choice when working in the high-T limit. This will shortly be implemented when constructing V_{eff} via DR. Nevertheless, we aim to compare the results from the 3D EFT to earlier findings from more conventional approaches using $\bar{\mu} = v_0$. Therefore we follow this previous literature in our 4D analysis.

Thermal corrections are implemented via

$$V_{\mathrm{T}} = \frac{T^4}{2\pi^2} \sum_i n_i J_{\mathrm{B/F}} \left(\frac{m_i^2}{T^2} \right) , \tag{17.14}$$

where the thermal functions are given in eq. (3.33) and the sum again runs over all fields that couple to the scalars. Since we work at one-loop order, the breakdown of perturbativity in the IR is treated by Daisy resummation (cf. sec. 3.2). To this end, we employ the truncated full dressing approach [167, 169], which amounts to the replacement

$$m_i^2(v,x) \to m_{i,3}^2(v,x,T) = m_i^2(v) + \Pi_i(T) \tag{17.15}$$

in the one-loop part of the effective potential. Here, the subscript "3" indicates masses at finite temperature and $\Pi_i(T)$ denotes the thermal mass of a species i. In the xSM, the thermal masses read [513]

$$\Pi_h(T) = T^2 \left(\frac{3g^2}{16} + \frac{g'^2}{16} + \frac{\lambda}{2} + \frac{y_t^2}{4} + \frac{\lambda_{hs}}{24} \right) , \tag{17.16}$$

$$\Pi_s(T) = T^2 \left(\frac{1}{4}\lambda_s + \frac{1}{6}\lambda_{hs} \right) , \tag{17.17}$$

$$\Pi_{\mathrm{W}} = \Pi_{\mathrm{Z}} = m_{\mathrm{D}}^2(T) = \frac{g^2 T^2}{3} \left(\frac{5}{2} + \frac{N_{\mathrm{c}}+1}{4} N_{\mathrm{f}} \right) , \tag{17.18}$$

where m_{D} denotes the Debye mass of the longitudinal gauge boson modes, with the number of colors and fermion generations $N_{\mathrm{c}} = N_{\mathrm{f}} = 3$. Then, the full effective potential at one-loop order is

$$V_{\mathrm{eff}}(v,x,T) = V_0(v,x) + V_{\mathrm{cw}}^{\overline{\mathrm{MS}}}(v,x,T) + V_{\mathrm{T}}(v,x,T) , \tag{17.19}$$

where the respective terms are given by eqs. (17.3), (17.11), (17.14). The T-dependence in $V_{\mathrm{cw}}^{\overline{\mathrm{MS}}}$ stems from the thermally corrected masses.

ON-SHELL SCHEME As a second 4D approach, we introduce the on-shell scheme [479, 514]. Different from the $\overline{\mathrm{MS}}$ scheme, where dimensional regularization is used, the on-shell scheme regularizes UV-divergent integrals via a hard momentum cutoff Λ,

$$J_{\mathrm{cw}}(m^2,\Lambda) = \frac{1}{2} \int_0^\Lambda \frac{\mathrm{d}^4 P}{(2\pi^4)} \ln\left(P^2 + m^2 \right) . \tag{17.20}$$

Here, P and m denote the four-momentum and mass of the respective fields. Evaluating the integrals yields [159]

$$V_{\mathrm{cw}}^{\mathrm{os}}(v,x) = \frac{1}{32\pi^2} \sum_i \eta_i n_i \left[m_i^2(v,x)\Lambda^2 + \frac{m_i^4(v,x)}{2} \left(\log\left(\frac{m_i^2(v,x)}{\Lambda^2} \right) - \frac{1}{2} \right) \right] . \tag{17.21}$$

By introducing counterterms in the tree-level potential and imposing the same renormalization conditions as above, eqs. (17.12) and (17.13), one finds

$$V_{\text{cw}}^{\text{os}} = \frac{1}{64\pi^2}\sum_i \eta_i n_i \left[m_i^4(v,x)\left(\log\left(\frac{m_i^2(v,x)}{m_i^2(v_0)}\right) - \frac{3}{2}\right) + 2m_i^2(v,x)m_i^2(v_0)\right] . \tag{17.22}$$

For details on the counterterms, we refer to ref. [159]. This expression is structurally different from the one-loop vacuum contribution (17.11) we obtained above. In the $\overline{\text{MS}}$ scheme, the RG scale enters as a parameter which controls the scale at which couplings are evaluated. In the on-shell scheme, the cutoff scale Λ is fixed by the physical mass of the respective field in the electroweak vacuum, $m_i^2(v_0)$. Therefore, this approach does not include the running of the model parameters, which will later be used to analyze theoretical uncertainties form missing higher loop corrections. This is an immediate shortcoming of the on-shell scheme.

Regarding the temperature-dependent corrections, we proceed as outline above. That is, we include the thermal integrals and implement Daisy resummation by thermally correcting the field-dependent masses in the one-loop contributions. Then, the thermal effective potential reads

$$V_{\text{eff}}(v,x,T) = V_0(v,x) + V_{\text{cw}}^{\text{os}}(v,x,T) + V_{\text{T}}(v,x,T)\,. \tag{17.23}$$

17.3 EFFECTIVE POTENTIAL IN THREE DIMENSIONS

Let us now proceed by deriving the thermal effective potential in the EFT approach, largely following ref. [171]. First, we outline how to fix the input parameters of the theory via one-loop corrected vacuum renormalization, before integrating out the hard scale. As an additional simplification, we further integrate out soft fields. Finally, we discuss numerical interpolations that we implement to treat non-analytical terms arising at two-loop order. We again employ Landau gauge ($\xi = 0$), minimizing gauge dependence [171]. As a consequence, ghosts do not couple to scalar and kinetic mixing between scalar and vector degrees of freedom vanishes [515].

INPUT PARAMETERS. Before constructing the thermal EFT, we need to specify the input parameters of the 4D theory. To this end, we will use $\overline{\text{MS}}$ renormalization to regulate UV-divergent integrals. Therefore, we first need to establish a connection between physically measured observables, such as the pole masses of the electroweak fields, to the renormalized $\overline{\text{MS}}$ quantities. In the 4D $\overline{\text{MS}}$ approach outlined above, we have defined the

tree-level Higgs mass as the physically observable one. Then, we have introduced additional counterterms which preserve the Higgs mass and vev at the loop-level for a given set of input parameters $\{m_s, \lambda_s, \lambda_{hs}\}$. This is a simplified matching procedure, since, e.g., the momentum dependence of the pole masses is not included. A more rigorous scheme is used in refs. [171], where physical observables are related to $\overline{\text{MS}}$ quantities via a one-loop corrected vacuum renormalization. This is outlined in the following.

We start from the measured values of the electroweak pole masses [318],[2]

$$(m_t, m_{\text{W}}, m_{\text{Z}}, m_h) = (172.76, 80.379, 91.1876, 125.1)\,\text{GeV}\,. \tag{17.24}$$

The physical singlet mass m_s is a free input parameter and the couplings λ_s and λ_{hs} are directly given in the $\overline{\text{MS}}$ scheme. We minimize the tree-level potential (17.3) along the $x = 0$ direction to find the Higgs vev, which can be expressed as

$$v_0 = \sqrt{\frac{4m_{\text{W}}^2}{g^2}}\,, \tag{17.25}$$

where g is the $\text{SU}(2)_{\text{L}}$ gauge coupling. Via eqs. (17.4) and (17.5), we obtain the tree-level Higgs and singlet mass parameters, μ_h^2 and μ_s^2. The Higgs self-coupling reads

$$\lambda = \frac{m_h^2}{2}\,. \tag{17.26}$$

Regarding the SM couplings, the tree-level relations are [171]

$$g^2 = \frac{8m_{\text{W}}^2 G_\mu}{\sqrt{2}}\,, \quad (g')^2 = \frac{g^2(-m_{\text{W}}^2 + m_{\text{Z}}^2)}{m_{\text{W}}^2}\,, \quad y_t^2 = \frac{g^2 m_t^2}{2m_{\text{W}}^2}\,, \quad g_s^2 = 1.48409\,, \tag{17.27}$$

where $G_\mu = 1.1663787 \times 10^{-5}\,\text{GeV}^{-2}$ is the Fermi constant [318] and g_s is the strong gauge coupling.

We now use the one-loop self-energies, computed within the $\overline{\text{MS}}$ scheme, to relate the physical observables (17.24) to the renormalized masses. Explicitly, bosonic masses, e.g., take the form

$$\mu^2(\bar{\mu}) = m^2 + \text{Re}\,\Pi(m^2)\,, \tag{17.28}$$

with $\Pi(m^2)$ being the self-energy. Likewise, tree-level couplings receive one-loop corrections. These relations are found in ref. [171]. This provides the renormalized model parameters at the electroweak scale $\bar{\mu} = m_{\text{Z}}$. Via the β-functions in appendix 20.A, the model parameters are then evolved to the EFT matching scale $\bar{\mu} = cT$, where c is some constant that we will shortly introduce.

2 Note that ref. [71] has provided updated values of the electroweak observables, however, this effect is negligible in our analysis.

DIMENSIONAL REDUCTION. Having fixed the input parameters, we are now ready to construct the EFT for the xSM, following refs. [171, 497, 511]. The first step is to integrate out the hard scale, as outlined in sec. 16.2. To this end, we impose the power counting

$$\mu_h, \mu_s \sim gT\,, \qquad \lambda, \lambda_s, \lambda_{hs} \sim g^2\,, \qquad y_t, g', g_s \sim g\,. \tag{17.29}$$

The soft 3D action associated to the 4D Lagrangian (17.1) reads [171]

$$\begin{aligned} S_{3D} = \int \mathrm{d}^3x \Big[& \mathcal{L}_{YM}^{3D} + |D_i\Phi|^2 + \frac{1}{2}(\partial_i S)^2 + V_0^{3D}(\Phi, S) + \frac{1}{2}(D_i A_0^a)^2 + \frac{1}{2}m_D^2 A_0^a A_0^a \\ & + \frac{1}{2}(D_i B_0)^2 + \frac{1}{2}(m_D')^2 B_0^2 + \frac{1}{2}(D_i B_0)^2 + \frac{1}{2}m_D'^2 B_0^2 + \frac{1}{2}(D_i C_0^\alpha)^2 \\ & + \frac{1}{2}(m_D'')^2 C_0^a C_0^\alpha + h_3 \Phi^\dagger\Phi A_0^a A_0^a + h_3' \Phi^\dagger\Phi B_0^2 + h_3'' \Phi^\dagger A_0^a \sigma_a \Phi B_0 \\ & + \omega_3 \Phi^\dagger\Phi C_0^\alpha C_0^\alpha + y_3 S^2 A_0^a A_0^a + y_3' S^2 B_0^2 \\ & + (\text{interactions among } A_0, B_0, C_0) \Big]\,. \end{aligned} \tag{17.30}$$

This expression is static and bosonic, as all non-zero Matsubara modes (including fermions) live in the UV. A_0, B_0, and C_0 denote the longitudinal $\mathrm{SU}(2)_\mathrm{L}$, $\mathrm{U}(1)_\mathrm{Y}$, and $\mathrm{SU}(3)_\mathrm{c}$ gauge field components which acquire soft Debye masses m_D (see eq. (17.18)), m_D', and m_D''. Here, m_D is given by eq. (17.18), while m_D' and m_D'' can be found in appendix A of ref. [503]. Interactions between the scalar fields and the longitudinal gauge bosons are parametrized by h_3, h_3', h_3'', ω_3, y_3, and y_3'. Finally, $\mathcal{L}_{YM}^{3D}$ contains the ultrasoft spatial gauge modes. Note that we neglect higher-dimensional operators suppressed by powers of πT.[3] Interactions among A_0, B_0, and C_0 are $\mathcal{O}(g^4)$ [516], therefore start contributing at orders we do not consider. Further note that in the 3D theory, all couplings are dimensionful while fields carry mass dimension 1/2. The 3D fields are then related to their 4D counterparts via[4]

$$\Phi_{4D} = \sqrt{T}\Phi\,, \qquad S_{4D} = \sqrt{T}S\,. \tag{17.31}$$

The scalar potential in eq. (17.30) is

$$V_0^{3D}(v, x) = \mu_{h,3}^2 \Phi^\dagger\Phi + \lambda_3(\Phi^\dagger\Phi)^2 + \frac{1}{2}\mu_{s,3}^2 S^2 + \frac{\lambda_{s,3}}{4}S^4 + \frac{\lambda_{hs,3}}{2}S^2\Phi^\dagger\Phi\,. \tag{17.32}$$

This expression takes the same functional form as in 4D (17.2), with all parameters replaced by their finite-temperature version. In the next step, these effective parameters have to be

3 Recently, ref. [510] has shown that higher-dimensional operators can have a sizable impact on the resulting GW predictions.

4 Note that we do include an explicit subscript "3" to indicate finite-temperature couplings. This subscript is dropped for the fields for simplicity.

determined by matching to the full theory. In practice, the matching relations are obtained via `DRAlgo`. Since, in addition, the soft EFT for the xSM is known [497], we refrain from showing the full computation. However, let us briefly discuss the steps involved.

The scalar fields in eq. (17.32) correspond to the Matsubara zero modes. That is, all hard loops containing non-zero Matsubara modes must be integrated out. To this end, the scalar fields are again decomposed into a constant background and a dynamical part. As long as the background field is smaller than πT, the matching relations are not affected [171], i.e., we choose to expand around the origin. Following the procedure introduced in sec. 16.2, the effective parameters are obtained by matching the 1PI correlation functions between the effective and full theory. This is done at one- and two-loop orders. Referring to refs. [171, 497] and `DRAlgo` [511], the soft matching relations up to $\mathcal{O}(g^4)$, i.e., NLO, read

$$\begin{aligned}\mu_{h,3}^2 = \left(\mu_h^2\right)_{\text{SM}} &+ \frac{\lambda_{hs}T^2}{24} - \frac{L_b}{2(4\pi)^2}\lambda_{hs}\mu_s^2 + \frac{\lambda_{hs}T^2}{(4\pi)^2}\left[\frac{L_b}{24}\left(\frac{3}{4}(3g^2+g'^2)\right.\right.\\ &\left.\left. - 6\lambda - 5\lambda_{hs} - 3\lambda_s\right) - \frac{y_t^2}{8}L_f\right] - \frac{1}{(4\pi)^2}\frac{\lambda_{hs,3}^2}{2}\left(c + \ln\left(\frac{3T}{\bar{\mu}_3}\right)\right)\,,\end{aligned} \tag{17.33}$$

$$\begin{aligned}\mu_{s,3}^2 = \mu_s^2 &+ T^2\left(\frac{\lambda_{hs}}{6} + \frac{\lambda_s}{4}\right) - \frac{L_b}{(4\pi)^2}\left(2\lambda_{hs}\mu_h^2 + 3\lambda_s\mu_s^2\right) + \frac{T^2}{(4\pi)^2}\left[\frac{2+3L_b}{24}\right.\\ &(3g^2+g'^2)\lambda_{hs} - L_b\left(\left(\lambda + \frac{7}{12}\lambda_{hs} + \frac{\lambda_s}{2}\right)\lambda_{hs} + \frac{9}{4}\lambda_s^2\right) - \frac{\lambda_{hs}}{4}y_t^2\\ &\left.(3L_b - L_f)\right] + \frac{1}{(4\pi)^2}\left((3g_3^2 + g_3'^2)\lambda_{hs,3} - 2\lambda_{hs,3}^2 - 6\lambda_{s,3}^2\right)\\ &\left(c + \ln\left(\frac{3T}{\bar{\mu}_3}\right)\right)\,,\end{aligned} \tag{17.34}$$

$$\begin{aligned}\lambda_3 = T\lambda &+ \frac{T}{(4\pi)^2}\left(\frac{2-3L_b}{16}\left(3g^4 + 2g^2g'^2 + g'^4\right)\right) + 3y_t^2L_f\left(y_t^2 - 2\lambda\right)\\ &+ L_b\left(\frac{3}{2}\left(3g^2+g'^2\right)\lambda - 12\lambda^2 - \frac{\lambda_{hs}^2}{4}\right)\,,\end{aligned} \tag{17.35}$$

$$\lambda_{s,3} = T\lambda_s - \frac{T}{(4\pi)^2}L_b\left(\lambda_{hs}^2 + 9\lambda_s^2\right)\,, \tag{17.36}$$

$$\lambda_{hs,3} = T\lambda_{hs} + \frac{T}{(4\pi)^2}\left(L_b\left(\frac{3}{4}\left(3g^2+g'^2\right) - 6\lambda - 2\lambda_{hs} - 3\lambda_s\right)\lambda_{hs} - 3L_fy_t^2\lambda_{hs}\right)\,, \tag{17.37}$$

where $c = -0.348723$ [171]. Here, the SM part of $\mu_{h,3}^2$ is given in ref. [503], while the expressions for g_3 and g_3' are found in ref. [497]. One can easily check that truncating the above expressions reproduces the thermal masses (17.16) and (17.17) obtained via Daisy resummation. Furthermore, we observe that one-loop matching of the scalar couplings induce corrections at NLO, $\mathcal{O}(g^4)$. At LO, the 4D couplings are simply rescaled by the temperature. The RG scale $\bar{\mu}$ is encoded in the EFT parameters via

$$L_b = 2\ln\frac{\bar{\mu}}{T} - 2(\ln 4\pi - \gamma)\,, \tag{17.38}$$

$$L_f = L_b + 4\ln 2\,, \tag{17.39}$$

where γ is the Euler-Mascheroni constant. From this, we see that a natural choice for the RG scale is dictated by the hard Matsubara modes πT, controlling the magnitude of the logarithms.[5] By RG-evolving the parameters in the matching relations, one can show that the dependence on $\bar{\mu}$ vanishes at $\mathcal{O}(g^4)$ (cf. sec. 16.2). This is the great advantage compared to one-loop Daisy resummation, which carries a large theoretical uncertainty from its explicit dependence on the RG scale. The remaining RG scale dependence is governed by the 3D RG scale $\bar{\mu}_3$. This quantity enters by solving the RG evolution within the 3D theory to replace terms $T^2\lambda_{hs}^2 \sim \ln(3T/\bar{\mu})$ with $\sim \lambda_{hs,3}^2 \ln(3T/\bar{\mu}_3)$ [171]. Varying both RG scales $\bar{\mu}$ und $\bar{\mu}_3$ will allow us to systematically study theoretical errors from missing higher-order corrections (see chapter 18).

The matching relations at $\mathcal{O}(g^4)$ for the couplings between the singlet and longitudinal gauge bosons in eq. (17.30) are [171]

$$y_3 = \frac{T}{(4\pi)^2}\frac{1}{2}g^2\lambda_{hs}\,, \tag{17.40}$$

$$y_3' = \frac{T}{(4\pi)^2}\frac{1}{2}g'^2\lambda_{hs}\,. \tag{17.41}$$

This corresponds to one-loop matching. The remaining parameters h_3, h_3', h_3'', and ω_3 are not affected by the BSM physics and can be found in appendix A of ref. [503].

INTEGRATING OUT THE SOFT SCALE. As discussed in sec. 16.1, a transitioning scalar field can become lighter than the soft scale, due to cancellations of the negative vacuum mass and the positive thermal mass. Then, it is possible to simplify the EFT by integrating out the soft scale, i.e., the longitudinal gauge degrees of freedom.[6] The resulting

5 This was already noted in sec. 5.2, where we have shown that logarithms of the vacuum and thermal one-loop contributions combine to $\ln(\bar{\mu}/T)$.

6 The impact of dynamical soft degrees of freedom on our final results turns out to be negligible (cf. sec. 18.3).

softer EFT is structurally identical to an ultrasoft EFT.[7] The perturbative treatment, however, remains viable if the scalar field is heavier than ultrasoft, i.e., if the PT is strong enough. The action at the softer scale is

$$\bar{S}_{\mathrm{3D}} = \int \mathrm{d}^3x \left[\mathcal{L}_{\mathrm{YM}} + |D_i\Phi|^2 + \frac{1}{2}(\partial S)^2 + V_0^{\mathrm{3D}}(\Phi, S)\right] , \tag{17.42}$$

where we follow ref. [171] and supplement softer quantities with a bar. Hence, the remaining dynamical degrees of freedom are the two scalar fields and the spatial gauge fields. Through matching the correlation functions of the ultrasoft and the soft scale, one finds the ultrasoft EFT parameters. These are again obtained by `DRAlgo` [56, 171],

$$\begin{aligned}\bar{\mu}_{h,3}^2 = \mu_{h,3}^2 &- \frac{1}{4\pi}\left(3h_3 m_{\mathrm{D}} + h_3' m_{\mathrm{D}}' + 8\omega_3 m_{\mathrm{D}}''\right) + \frac{1}{(4\pi)^2}\Bigg(3g_3^2 h_3 + 3h_3^2 \\ &- h'^2 - \frac{3}{2}h_3''^2 + \left(-\frac{3}{4}g_3^4 + 12 g_3^2 h_3\right)\ln\frac{\bar{\mu}_3}{2m_{\mathrm{D}}} - 6h_3^2 \ln\frac{\bar{\mu}_3}{2m_{\mathrm{D}}} \\ &- 2h_3'^2 \ln\frac{\bar{\mu}_3}{2m_{\mathrm{D}}} - 3h_3''^2 \ln\frac{\bar{\mu}_3}{m_{\mathrm{D}} + m_{\mathrm{D}}'}\Bigg) ,\end{aligned} \tag{17.43}$$

$$\bar{\mu}_{s,3}^2 = \mu_{s,3}^2 - \frac{1}{2\pi}\left(3m_{\mathrm{D}} y_3 + m_{\mathrm{D}}' y_3'\right) , \tag{17.44}$$

$$\bar{\lambda}_3 = \lambda_3 - \frac{1}{2(4\pi)}\left(\frac{3h_3^2}{m_{\mathrm{D}}} + \frac{h_3'^2}{m_{\mathrm{D}}'} + \frac{h_3''^2}{m_{\mathrm{D}} + m_{\mathrm{D}}'}\right) , \tag{17.45}$$

$$\bar{\lambda}_{s,3} = \ = \lambda_{s,3} - \frac{1}{2\pi}\left(\frac{3y_3^2}{m_{\mathrm{D}}} + \frac{(y_3')^2}{m_{\mathrm{D}}'}\right) , \tag{17.46}$$

$$\bar{\lambda}_{hs,3} = \lambda_{hs,3} - \frac{1}{2\pi}\left(\frac{3y_3 h_3}{m_{\mathrm{D}}} + \frac{y_3' h_3'}{m_{\mathrm{D}}'}\right) , \tag{17.47}$$

$$\bar{g}_3 = g_3^2\left(1 - \frac{g_3^2}{6(4\pi)m_{\mathrm{D}}}\right) \tag{17.48}$$

$$\bar{g}_3' = g_3'^2 . \tag{17.49}$$

With the above relations, we are now ready to compute the effective potential. To this end, the techniques introduced in secs. 3.2 and 16.2 are used. That is, we compute all

7 This is distinct from a supersoft EFT which is usually constructed in the broken phase. Then, transverse gauge bosons become massive and can be integrated out, leaving the transitioning scalar fields as the only dynamical degrees of freedom [164].

EFT matching	One-loop $V_{\text{eff}}^{\text{3D}}$	Two-loop $V_{\text{eff}}^{\text{3D}}$
LO	(3D@LO, V_{eff}@LO)	–
NLO	(3D@NLO, V_{eff}@LO)	(3D@NLO, V_{eff}@NLO)

Table 17.1: Different loop orders in the EFT matching and effective potential that are used in chapter 18.

1PI diagrams at vanishing external momenta within the EFT. Resummation of non-zero Matsubara modes is already accounted for by the hard $\to$ soft matching. The tree-level potential, expressed through the 3D background fields v and x is then simply

$$V_0^{\text{3D}} = \frac{\bar{\mu}_3^2}{2}v^2 + \frac{\bar{\mu}_{s,3}^2}{2}x^2 + \frac{\bar{\lambda}_3}{4}v^4 + \frac{\bar{\lambda}_{s,3}}{4}x^4 + \frac{\bar{\lambda}_{hs,3}}{4}x^2v^2 \,. \tag{17.50}$$

The one-loop potential is given by the well-known thermal integrals

$$V_1^{\text{3D}} = 2(d-1)J_3\left(\bar{m}_W\right) + (d-1)J_3\left(\bar{m}_Z\right) + J_3\left(\bar{m}_h\right) + J_3\left(\bar{m}_s\right) + 3J_3\left(\bar{m}_G\right) \,, \tag{17.51}$$

where $d = 3 - 2\epsilon$, with ϵ begin the expansion parameter used in dimensional regularization, and

$$J_3(m) = \frac{1}{2}\int \frac{\mathrm{d}^3p}{(2\pi)^3} \ln\left(p^2 + m^2\right) = -\frac{m^3}{12\pi} \,. \tag{17.52}$$

Here we have used the high-T expansion. The masses $\bar{m}_W$, $\bar{m}_Z$, $\bar{m}_h$, $\bar{m}_s$, $\bar{m}_G$ are given by eqs. (17.4) – (17.8), where vacuum quantities are replaced by barred ones. The full effective potential then reads

$$V_{\text{eff}}^{\text{3D}} = V_0^{\text{3D}} + V_1^{\text{3D}} + V_2^{\text{3D}} \,, \tag{17.53}$$

where the two-loop contributions V_2^{3D} are again obtained by `DRAlgo`. Since these expressions are extremely lengthy and have been known before, we do not explicitly list them here. Instead, we refer to the appendix of ref. [171] and our Python implementation `DRansitions` [3]. This package contains all matching relations up to NLO. In addition, we include all two-loop topologies contributing to V_{eff} in a general fashion, such that it is straightforward to adapt the code to other models if the matching relations are known. Furthermore, the code can directly be used as an input to `CosmoTransitions` [185], streamlining the computation of the PT parameters.

In the following, we will use the the 3D EFT at different levels of computational diligence; see table 17.1 for an overview. The simplest version, (3D@LO, V_{eff}@LO), employs tree-level

couplings, one-loop thermal masses, and the effective potential up to one-loop order. One can explicitly show that this is equivalent to the effective potential computed in the 4D $\overline{\text{MS}}$ scheme (17.19), up to the different choice of the RG scale $\bar{\mu}$. The second version, (3D@NLO, V_{eff}@LO), utilizes NLO EFT matching in the one-loop effective potential, while (3D@NLO, V_{eff}@NLO) employs NLO matching and V_{eff} at two-loop order.

NUMERICAL APPROACH. To study the phase structure of the xSM, we choose the direct approach outlined in ref. [164], i.e., we directly minimize the effective potential numerically. This induces certain shortcomings. First, V_{eff} is gauge-dependent [517]. Employing Landau gauge, this turns out to be a minor issue compared to RG scale dependence. Second, the effective potential is complex [518]. This is treated by omitting the imaginary part of the effective potential if $\text{Im}\, V_{\text{eff}}^{\text{3D}} < \text{Re}\, V_{\text{eff}}^{\text{3D}}$ at the minima [165], i.e., we replace $V_{\text{eff}}^{\text{3D}} \to \text{Re}\, V_{\text{eff}}^{\text{3D}}$. Then, however, the scalar fields induce divergencies at the two-loop level in the effective potential [56, 164, 501], related to effective squared masses transitioning from negative to positive. This is exemplified by the orange curve in fig. 17.1, where we plot the (3D@NLO, V_{eff}@NLO) case in the x-direction for $\{m_s, \lambda_s, \lambda_{hs}\} = \{110\,\text{GeV}, 1, 0.8\}$ at $T = 120\,\text{GeV}$. Clearly, we observe a non-analytic behavior around $x_{\text{4D}} \sim 40\,\text{GeV}$. To explain this let us consider, e.g., the contribution from the scalar sunset diagram to the two-loop effective potential [171, 505],

$$D_{SSS}(m_1, m_2, m_3) \propto \ln\left(\frac{\bar{\mu}}{m_1 + m_2 + m_3}\right) . \tag{17.54}$$

While the effective scalar masses are negative, $\bar{\mu}_{h,3}, \bar{\mu}_{s,3} < 0$, eq. (17.54) gives purely imaginary contributions. As the scalar masses cross zero, the logarithm diverges, inducing spikes and kinks in the potential such as the ones in fig. 17.1.[8] This is problematic in two ways. First, the numerical minimization algorithm easily gets trapped in the IR spike, impeding the scan of the phase structure. Second, we aim to solve the bounce equation in the next section. This involves derivatives of the effective potential, which are ill-defined as the masses cross zero. Therefore, we implement a practical solution, and set

$$\ln\left(\frac{\bar{\mu}}{m_1 + m_2 + m_3}\right) = 0 \quad \text{for} \quad m_1 + m_2 + m_3 < \bar{\mu}\,. \tag{17.55}$$

Furthermore, we use numerical interpolations to smoothen the resulting potential in order to be able to take derivatives. The result is shown by the blue dash-dotted curve in fig. 17.1.

Let us, however, mention that these pathologies, i.e., gauge dependence and IR divergencies, are cured in a "strict EFT expansion" [164]; see refs. [163, 485] for recent applications.

8 This issue was recently noted in ref. [498], as well.

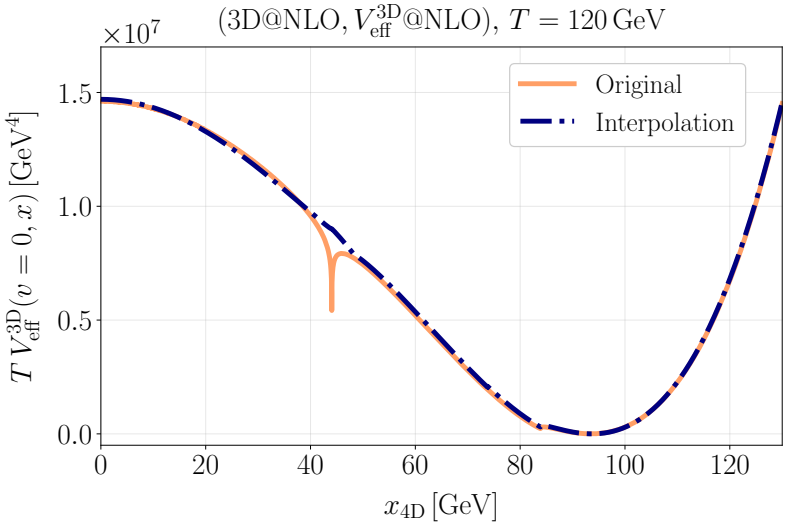

Figure 17.1: Two-loop effective potential for $\{m_s, \lambda_s, \lambda_{hs}\} = \{110\,\text{GeV}, 1, 0.8\}$, $\bar{\mu} = 4\pi e^{-\gamma} T$, and $\bar{\mu}_3 = T$ in the singlet-direction of field space. We have shifted the potential such that the potential energy vanishes in the true minimum. The orange curve shows the original potential, while the blue curve is the interpolated version, smoothening the kinks caused by scalar masses becoming real.

Instead of directly minimizing the NLO effective potential, the theory is consistently expanded order-by-order in $\hbar$ around the true minimum. To this end, additional background field-dependent resummations are required. Since this is not straightforward in multi-field PTs, we stick to the direct approach, relegating a more rigorous analysis to the future.

18

COMPARING RESUMMATION SCHEMES

With the different computations of the effective potential at hand, we are now ready to study their impact on phenomenological predictions. To this end, we start by briefly summarizing our approach to compute the PT dynamics. Subsequently, we study the impact of higher-order resummation on equilibrium thermodynamics, i.e., we investigate the phase structure and crictical temperature. Then, we compute the GW spectra and analyze their robustness under a variation of the RG scale $\bar{\mu}$. Finally, we impose a benchmark spectrum and reconstruct the model parameters for different underlying implementations of V_{eff}.

18.1 PHASE TRANSITION DYNAMICS

To analyze the PT, we follow the steps outlined in sec. 3.2. That is, we solve the bounce equation (3.47) via `CosmoTransitions` [185], where the effective potential from the EFT approach is rescaled via

$$V_{\text{eff}}^{\text{4D}} = T V_{\text{eff}}^{\text{3D}} \,. \tag{18.1}$$

The bounce action S_3 defines the bubble nucleation rate, which we approximate by eq. (3.46). This neglects out-of-equilibrium physics [180], which can be captured in a nucleation EFT [182, 183, 506, 508]. Since we neglect such higher orders for all implementations of the effective potential, we consider this a systematic error in our study.

We proceed by computing the relevant temperature scales (see sec. 3.2) and evaluate the transition strength α and the inverse timescale β/H via eq. (3.54). The bubble wall velocity requires particular care [194–203, 207, 519–523], necessitating out-of-equilibrium calculations. Since this is beyond the scope of this work and we only consider strong transitions with $\alpha \gtrsim 0.1$ which often correspond to detonations, we set $v_{\text{w}} = 1$ in the following. This should, however, be reconsidered in the future to obtain a more precise picture [209].

Due to the polynomial nature of the tree-level potential, PTs in the xSM do not exhibit large amounts of supercooling [186]. Therefore, we do not compute the GW contribution

from bubble collisions [211, 223, 370, 524, 525]. Instead, we focus on GWs generate by sound waves in the thermal bath [217–219, 221, 222, 526]. The parametrization of the GW signal [192, 215, 216] is given by eq. (3.59). Furthermore, we neglect GWs from turbulences [212–214].

18.2 PHASE STRUCTURE AND CRITICAL TEMPERATURE

We commence our study of the xSM by discussing the phase structure predicted by the 3D EFT. Then, we compute the critical temperature and examine its RG scale dependence.

By minimizing the effective potential as a function of temperature, we investigate the evolution of the background scalar fields v and x; see fig. 18.1, where we employ $\{m_s, \lambda_s, \lambda_{hs}\} = \{110\,\text{GeV}, 1, 0.8\}$. Here, we have imposed a matching scale of $\bar{\mu} = 4\pi e^{-\gamma} T$. This is a convenient choice, since it exactly cancels the logarithm in eqs. (17.38) and (17.39). Regarding the 3D RG scale, we set $\bar{\mu}_3 = T$. In addition, we rescale the 3D background fields via eq. (17.31). Different colors denote different levels of computational diligence, while dotted (solid) lines indicate the scalar singlet (Higgs). We observe that at high temperatures the system transitions to the singlet phase $(0,0) \to (0,x)$ in a smooth manner due to the absence of a thermal barrier.[1] At the critical temperature $\mathcal{O}(125-150)$GeV, depending on the loop order, the field jumps to the Higgs phase $(0,x) \to (v,0)$, indicating a FOPT. Further decreasing the temperature, the Higgs vev approaches its zero-T value v_0.

However, this result does not provide any information about the robustness of our computation of $V_{\text{eff}}^{\text{3D}}$. To this end, we repeat the phase scan for different choices

$$\bar{\mu} \in \left(\frac{\pi}{2}T, 4\pi e^{-\gamma} T\right) , \qquad \bar{\mu}_3 \in \left\{\frac{1}{2}T, 2T\right\} , \tag{18.2}$$

and extract T_c. Since the 3D@NLO EFT is independent of $\bar{\mu}$ at $\mathcal{O}(g^4)$, its variation yields information on the impact of higher-order effects. The same is true for the 3D RG scale $\bar{\mu}_3$, which enters the super-renormalizable EFT at the two-loop level. Fig. 18.2 shows the results, where we employ the same input parameters as above. We plot T_c, where the electroweak vacuum becomes the energetically favored one, as a function of $\bar{\mu}$. Color coding indicates the level of computational diligence, while the dotted lines correspond to a variation of the 3D RG scale $\bar{\mu}_3$. Clearly, the (3D@LO, V_{eff}@LO) approach carries the largest dependence on the RG scale. Varying $\bar{\mu}$ by a factor of ~ 4, the critical temperature changes from $T_c = 120\,\text{GeV}$ to $T_c = 140\,\text{GeV}$; this corresponds to an uncertainty of

1 Note that this first step in the symmetry breaking pattern may be realized by a FOPT at the ultrasoft scale, which however requires the lattice. Since ultrasoft PTs are typically extremely weak, we simply assume a second-order transition in the first step, and focus on the second step as the source of GWs.

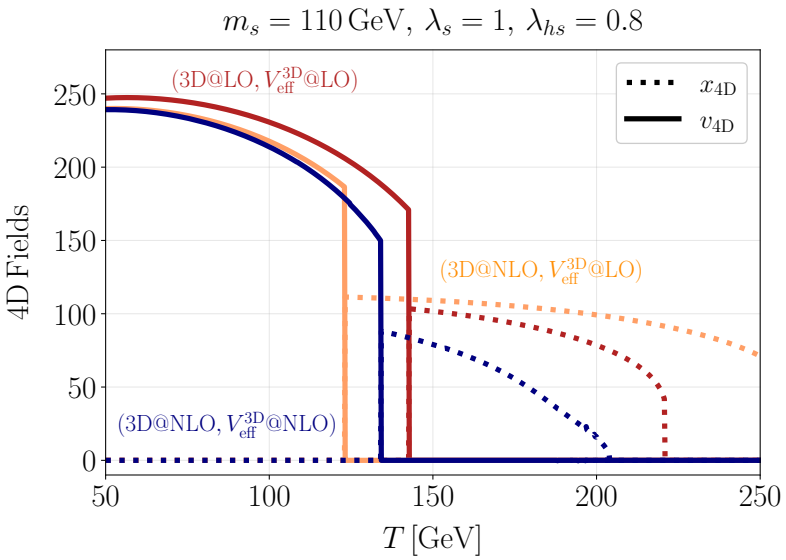

Figure 18.1: Evolution of the 4D scalar background fields as a function of temperature for a set of benchmark parameters. The solid lines correspond to the Higgs field, while the dotted lines indicate the scalar singlet. Different levels of computational diligence are displayed by different colors.

$\mathcal{O}(20\,\%)$. The two approaches employing NLO EFT, on the other hand, show a substantially reduced dependence on $\bar{\mu}$. Here, the same variation of the matching scale induces an error of $\mathcal{O}(3\,\%)$ on T_{c}. However, note that the (3D@NLO, V_{eff}@LO) approach exhibits a residual dependence on $\bar{\mu}_3$ due to missing higher-order corrections in the effective potential. This dependence is alleviated at the two-loop order for the Matsubara zero mode, which is why the (3D@NLO, V_{eff}@NLO) approach yields the most robust results.

These findings demonstrate the shortcomings of LO resummation: a large residual dependence on the matching scale. This is exactly the reason for the large discrepancy of the resulting GW signal that we discussed around fig. 15.1. While the uncertainty on T_{c} may be of $\mathcal{O}(20\,\%)$, this error propagates through the entire computational pipeline. That is, the computation of the percolation temperature, the tunneling rate, and finally the parameters that enter the GW spectrum. This induces order-of-magnitude uncertainties on predictions from single parameter points.

18.3 ROBUSTNESS OF GRAVITATIONAL WAVE PREDICTIONS

We have successfully demonstrated the RG scale dependence of the one-loop effective potential, which induces large uncertainties in the final GW predictions. However, what

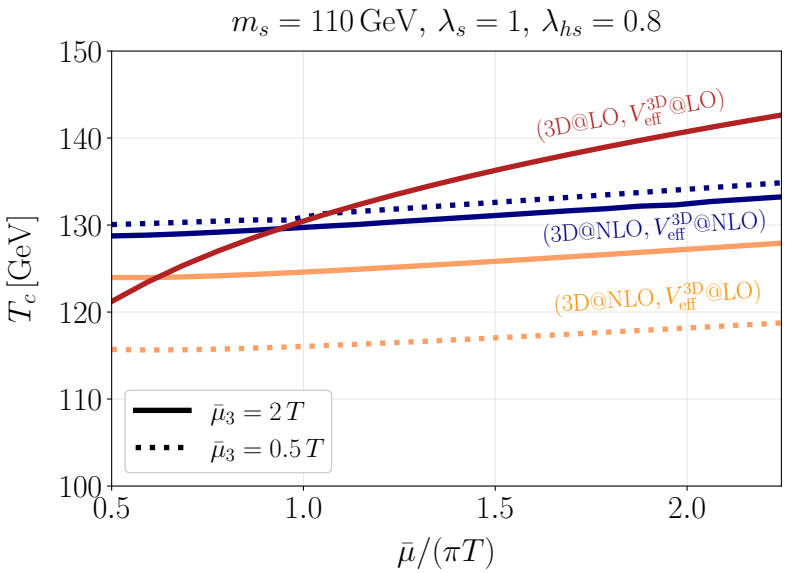

Figure 18.2: Critical temperature as a function of the EFT matching scale $\bar{\mu}$ for different approaches to the effective potential. Dotted lines indicate a variation of the 3D RG scale.

we are ultimately interested in is the effect of such uncertainties on the parameter space of the xSM. In the absence of experimental constraints, it is crucial to have theoretical control over the entire range of parameters. This analysis hence shows whether higher-order corrections simply shift the detectable parameter space or change the global properties of the model.

To this end, we conduct large-scale parameter scans of the xSM, employing five different approaches to the effective potential (see sec. 17). We restrict ourselves to the parameter range $\lambda_{hs} \in [0.1, 1.2]$, $\frac{m_h}{2} < m_s < 130$ GeV,[2] and $\lambda_s \in \{0.1, 1.0\}$. This is based on the reasoning that for large masses $m_s \gg m_h$, the scale hierarchy does not necessarily hold as the scalar singlet is not dynamical in the IR.[3] In addition, we focus on small couplings $\lambda_s, \lambda_{hs} \lesssim 1$ to remain perturbative.

PARAMETER SPACE DEPENDENCE. In fig. 18.3, we show some results of our parameter scan in the $m_s - \lambda_{hs}$ plane, employing $\lambda_s = 1$. Here, the color coding indicates different

2 Note that a substantial fraction of this parameter space is excluded by an overproduction of scalar DM [527]. In addition, the PT could be altered by the emergence of domain walls [528–531]. These constraints can be alleviated by new particles in the dark sector [532, 533], destabilizing the scalar field, while a small Z_2-breaking term annihilates the domain walls [534]. Such modifications would leave our main results unchanged.

3 It has been shown in [493] that a light scalar is required to render the EWPT strongly first-order.

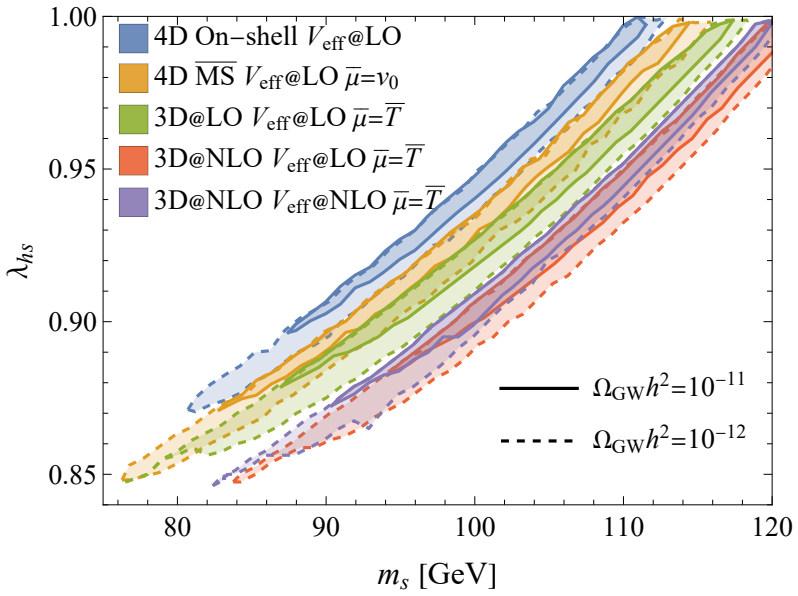

Figure 18.3: Parameter space predicting strong GW signals $\Omega_{\text{GW}}h^2 \geq 10^{-11}$ (solid) and $\Omega_{\text{GW}}h^2 \geq 10^{-12}$ (dashed) from the EWPT in the xSM for different constructions of the effective potential. The input parameters are the physical mass of the scalar singlet m_s, and the portal coupling λ_{hs} at the input scale $\bar{\mu} = m_{\text{Z}}$. The 4D $\overline{\text{MS}}$ scheme employs $\bar{\mu} = v_0$, while we fix $\bar{\mu} = 4\pi e^{-\gamma}T$ in the 3D EFT. Figure created by M. Lewicki.

computational schemes regarding the effective potential, that is, the 4D on-shell (blue) and $\overline{\text{MS}}$ (yellow) schemes, and the 3D EFT in increasing levels of diligence (green, red, purple). We only include strong transitions with $\Omega_{\text{GW}}h^2 \geq 10^{-11}$ (solid) and $\Omega_{\text{GW}}h^2 \geq 10^{-12}$ (dashed). Note that in the regions above the respective curves, percolation is not successful, e.g., this parameter space is excluded. The portal couplings λ_{hs} is shown at the input scale $\bar{\mu} = m_{\text{Z}}$. As explained in chapter 17, the RG scale in the 4D $\overline{\text{MS}}$ scheme is fixed to $\bar{\mu} = v_0$, while we impose $\bar{\mu} = 4\pi e^{-\gamma}T$ for the 3D EFT approaches. Regarding the (3D@NLO, V_{eff}@LO) and (3D@NLO, V_{eff}@NLO) approaches, we fix $\bar{\mu}_3 = T$.

As expected, the most robust results are obtained with the two (3D@NLO) methods, employing matching relations up to two-loop order. This can be seen from the large overlap between the red and purple areas. The parameter space featuring strong GW signals changes little when including two-loop effects into $V_{\text{eff}}^{\text{3D}}$. Next, note that the 4D $\overline{\text{MS}}$ and (3D@LO, V_{eff}@LO) approaches are essentially identical, up to the different RG scale. Therefore, the green and yellow curves largely coincide as expected. The largest deviation from the (3D@NLO, V_{eff}@NLO) result is found with the 4D on-shell scheme, which is arguably the simplest method to compute V_{eff}. Notably, the largest difference in the (m_s, λ_{hs}) model parameter space is of $\mathcal{O}(5\,\%)$, despite the large uncertainties on GW predictions for single parameter points. The overall parameter space that predicts strong GW signals is, however, extremely narrow. Therefore, percent-level shifts of the model parameters do become important, as they can change the nature of the transition in parts of the parameter space.

VARYING λ_s. For our main results in fig. 18.3, we have employed $\lambda_s = 1$. To demonstrate that a variation of the scalar self-coupling does not change our conclusions, we repeat the parameter scan for $\lambda_s = 0.1$. The results are shown in the left panel of fig. 18.4, while the right panel corresponds to $\lambda_s = 1$. Note that for simplicity, we only include the 4D on-shell scheme and the (3D@NLO, V_{eff}@LO) method. Decreasing λ_s shifts the overall parameter space towards smaller portal couplings λ_{hs}. Furthermore, the area predicting stronger signals becomes much narrower. Nonetheless, we find a percent-level deviation between the schemes, which corresponds to a similar uncertainty as for $\lambda_s = 1$. Therefore, we can safely conclude that our main results hold for different values of the scalar quartic couplings λ_s.

RG SCALE DEPENDENCE. Figs. 18.3 and 18.4 do not provide any information about the robustness of the parameter space under a variation of the RG scale, i.e., the potential effects of missing higher-order corrections. To this end, let us stress that the on-shell scheme does not allow for such an analysis in the first place, as the RG scale is implicitly

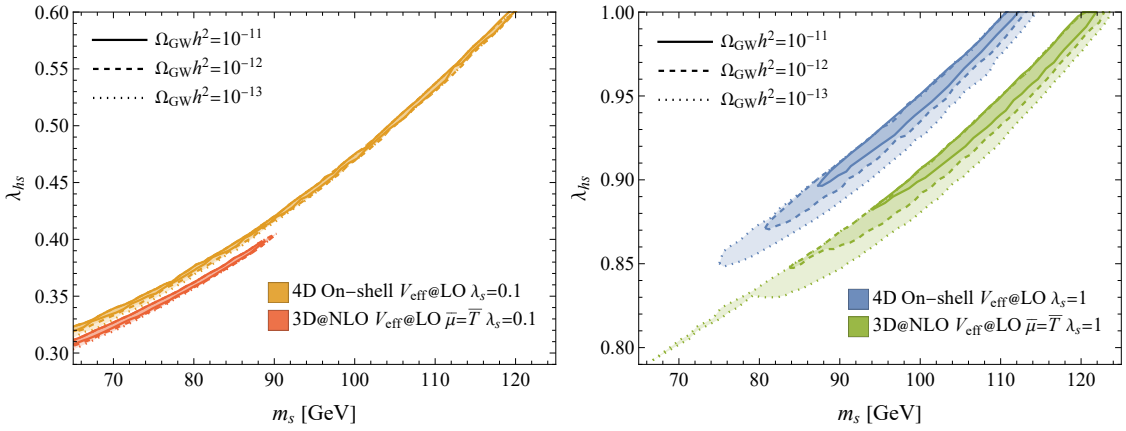

Figure 18.4: Comparison of the parameter space predicting strong GW signals fixing $\lambda_s = 0.1$ (left) and $\lambda_s = 1$ (right). We only focus on the 4D on-shell and (3D@NLO, $V_{\rm eff}$@LO) methods. In the 3D EFT approach, we fix $\bar{\mu} = 4\pi e^{-\gamma} T$. Figure created by M. Lewicki.

fixed at the pole masses of the respective particle species (see chapter 17). Furthermore, the choice of installing $\bar{\mu} = v_0$ in the 4D $\overline{\rm MS}$ scheme effectively fixes the scale as well, since the logarithms that emerge in the CW and thermal part of the effective potential are not treated consistently (see eq. (5.31)). We numerically find that the residual RG scale dependence induces a $\mathcal{O}(0.1\,\%)$ shift of the parameter space when varying $\bar{\mu} \in \{1/2, 2\} \times v_0$. Note, however, that the missing RG scale dependence of the 4D theories does not imply an enhanced theoretical robustness, but merely an incomplete RG improvement.

To assess the RG scale dependence of the parameter space, we therefore focus on the 3D EFT, which effectively contains the 4D $\overline{\rm MS}$, Daisy-resummed version of the effective potential via the (3D@LO, $V_{\rm eff}$@LO) method. We then vary $\bar{\mu} \in \{1/2, 4e^{-\gamma}\} \times \pi T$ and repeat the parameter scan; see fig. 18.5. Here the left panel corresponds to (3D@LO, $V_{\rm eff}$@LO), while the right panel shows the results for (3D@NLO, $V_{\rm eff}$@LO). We only include GW amplitudes $\Omega_{\rm GW}h^2 \geq 10^{-12}$, where the color coding indicates the choice of RG scale. Note that we fix the 3D RG scale $\bar{\mu}_3 = T$, as its variation has a minor effect on the resulting parameter space. In the overlapping areas, we indicate by the heat map the ratio of predicted amplitudes

$$\Delta\Omega_{\rm GW} \equiv \frac{\Omega_{\rm GW}(\bar{\mu} = \frac{1}{2}\pi T)}{\Omega_{\rm GW}(\bar{\mu} = 4e^{-\gamma}\pi T)}\,. \tag{18.3}$$

Let us first note that the RG scale variation induces a shift of the parameter space by $\mathcal{O}(1\%)$. Regarding the ratio of peak amplitudes, we find large deviations up to $\Delta\Omega_{\rm GW} \sim \mathcal{O}(10^3 - 10^4)$. That explains the large uncertainty in the final GW spectrum from single parameter points (see fig. 15.1), but at the same time the small uncertainty of the entire

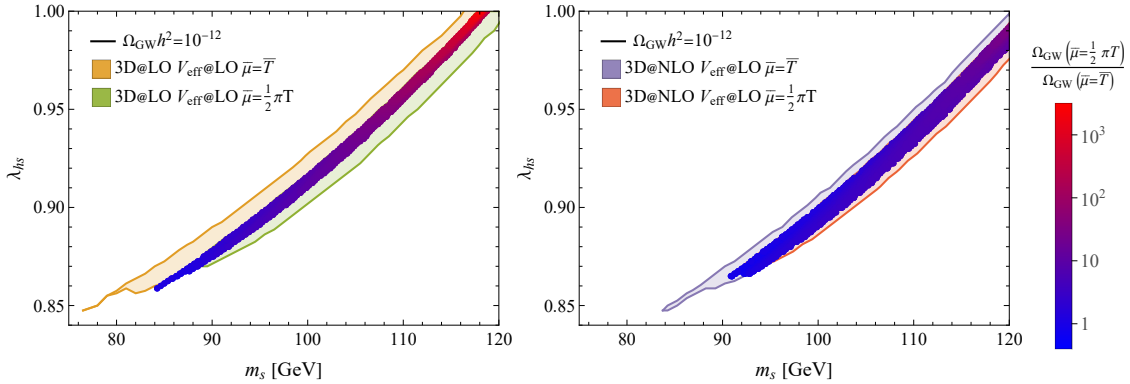

Figure 18.5: RG scale dependence of the xSM parameter space featuring $\Omega_{\rm GW}h^2 \geq 10^{-12}$, employing the LO (left) and NLO (right) EFT matching relations, $V_{\rm eff}$@LO, and $\lambda_s = 1$. We vary the RG scale between $\bar{\mu} \in \{(\pi/2)T, 4\pi e^{-\gamma}T\}$. The color coding in the overlapping area indicates the ratio of peak amplitudes $\Delta\Omega_{\rm GW}$ (cf. eq. (18.3)). Figure created by M. Lewicki.

parameter space. Interestingly, the deviations of the peak amplitudes increases logarithmically with m_s. That is due to the fact that the scalar mass enters the LO effective potential as prefactor of the logarithmic term controlling the running.

We further observe that employing two-loop matching relations yields much more robust results. That can be seen from both the larger overlapping parameter space, and the significantly smaller maximum deviations $\Delta\Omega_{\rm GW} \sim \mathcal{O}(10)$. This is expected, since the $\bar{\mu}$-dependence is of higher order than $\mathcal{O}(g^4)$. Note that this is already true for $V_{\rm eff}^{\rm 3D}$ at one-loop order. Hence, we conclude that while the (3D@LO, $V_{\rm eff}$@LO) approach produces merely small deviations from the (3D@NLO) methods, two-loop DR is required in order to obtain parameter spaces that remain consistent under a RG scale variation.

SOFT-SCALE EFFECTS. As outlined in sec. 17.3, we have constructed the 3D EFT at the softer scale. As a reminder, this EFT is structurally identical to an ultrasoft EFT, that is, longitudinal gauge boson modes are integrated out, while transverse gauge modes are kept dynamical. In the softer EFT, however, the transitioning scalar is always heavier than ultrasoft such that perturbativity is ensured.

To investigate the dependence on the thermal scale, we repeat the (3D@NLO, $V_{\rm eff}$@LO) scan with a soft EFT. That is, we only conduct the first step in the EFT construction of sec. 17.3, such that longitudinal gauge modes $X_0 \in \{A_0, B_0, C_0\}$ do not appear in the matching relations, but remain dynamical. Note, however, that these fields do note acquire

a vev, such that $\langle X_0 \rangle = 0$ holds during the PT [535]. The potential (17.51) then receives additional contributions,

$$V_1^{\mathrm{3D}} \mathrel{+}= 3J_3(\bar{m}_{\mathrm{A}_0}) + J_3(\bar{m}_{\mathrm{B}_0}) + 8J_3(\bar{m}_{\mathrm{C}_0})\,, \tag{18.4}$$

where $\{\bar{m}_{\mathrm{A}_0}, \bar{m}_{\mathrm{B}_0}, \bar{m}_{\mathrm{C}_0}\}$ denote the two-loop masses of the longitudinal gauge modes, which receive thermal and field-dependent contributions. One can check by expanding in $h_3 v^2/m_{\mathrm{D}}$, where h_3 is scalar-temporal gauge field coupling (see sec. 17.3), that that the softer matching relations only contain the first few terms of the additional J_3 contributions [166]. The terms higher-order in $h_3 v^2/m_{\mathrm{D}}$, can however become important for strong transitions involving large field values.

Regarding the parameter space of the xSM, however, we find a minuscule effect of soft corrections, as shown in fig. 18.6. Here, the areas include all parameter points with amplitudes $\Omega_{\mathrm{GW}} h^2 \geq 10^{-13}$, and the color coding indicates the scale of the EFT construction. Clearly, the deviation between the results is far less prominent than the effect of higher-order thermal resummation (cf. fig. 18.3). This, however, is only true in the parameter space where the high-temperature expansion holds. This should be checked explicitly in the future by studying the effect of higher-dimensional operators [510].

18.4 MODEL PARAMETER RECONSTRUCTION

We have analyzed the robustness of the overall parameter space of the xSM featuring strong FOPTs in the last section. Another key aspect of high-precision PT computations concerns the inverse problem [191, 487–492]: reconstructing the underlying microphysics from the detection of a SGWB at a future observatory such as LISA [482, 526, 536–538]. To this end, let us consider the benchmark spectrum shown in fig. 18.7, where we choose a peak frequency and amplitude

$$f_p = 2.4 \times 10^{-3}\,\mathrm{Hz}\,, \qquad h^2 \Omega_{\mathrm{GW}} = 5.2 \times 10^{-13}\,. \tag{18.5}$$

This benchmark is chosen since the corresponding SNR ≈ 10; such a signal is considered to slightly overcome the detection threshold. By analyzing a weak signal, we ensure that our findings are universal, as larger amplitudes would further reduce the experimental uncertainties, increasing the importance of an accurate theoretical treatment.

To investigate the impact of higher-order thermal resummation on the signal reconstruction, we conduct Fisher matrix analyses [500]. The Fisher information matrix can be used to discern errors on model parameters from a given observable, provided the errors are Gaussian and the Likelihood function, i.e., the GW signal and the LISA sensitivity curve,

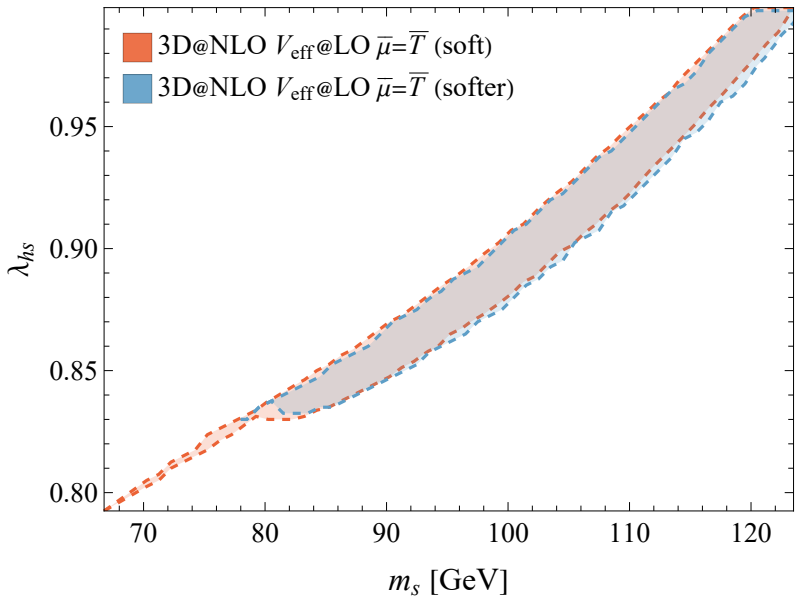

Figure 18.6: Parameter space comparing different scales of the EFT construction. The blue regime corresponds to the softer (3D@NLO, $V_{\rm eff}$@LO) results from fig. 18.3, while the red region is obtained by keeping soft fields dynamical. Only points with $\Omega_{\rm GW}h^2 \geq 10^{-13}$ are included. Both approaches employ $\bar{\mu} = 4\pi e^{-\gamma}T$. Figure created by M. Lewicki.

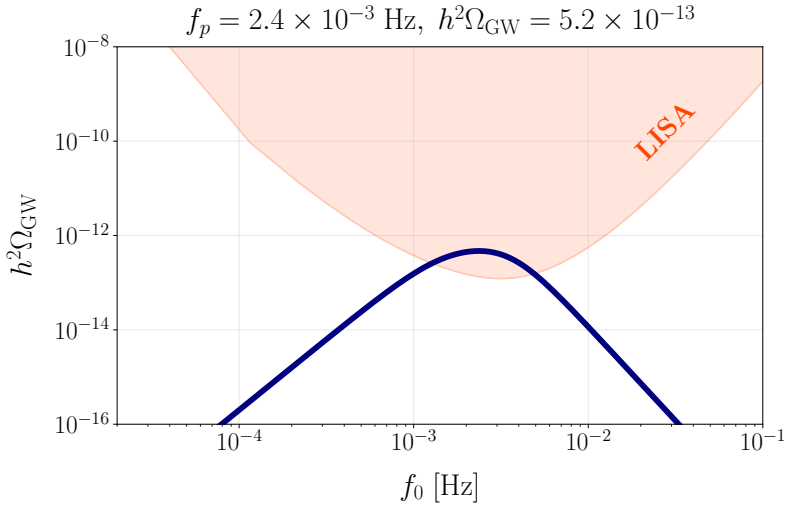

Figure 18.7: Benchmark signal that we impose to study the effect of higher-order thermal resummation on the reconstruction of model parameters. The peak frequency and amplitude are chosen such that the associated SNR = 10, corresponding to a signal just above the detection threshold.

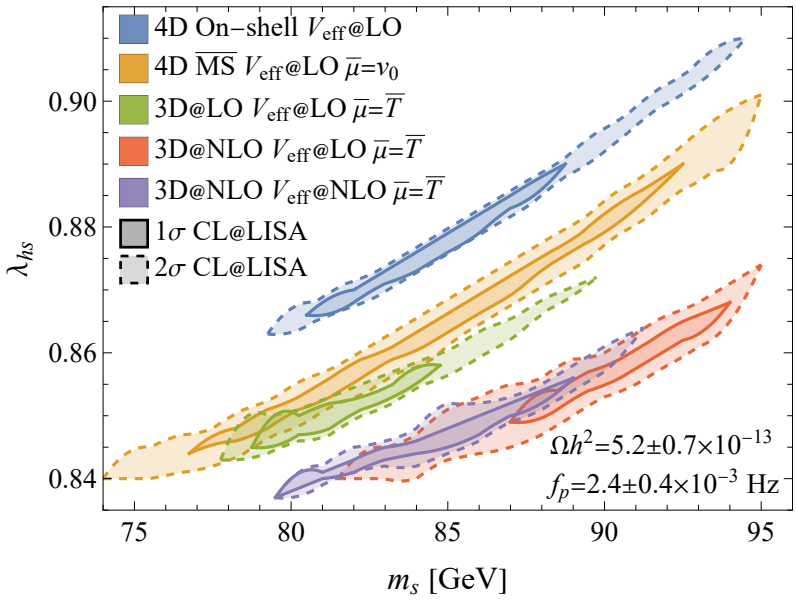

Figure 18.8: Model parameter reconstruction of the benchmark signal shown in fig. 18.7, employing five different implementations of the effective potential as indicated by the color coding. The solid and dashed lines correspond to the 1σ and 2σ confidence levels obtained by the Fisher matrix analyses. While the two-loop (3D@NLO) approaches produce consistent results, the one-loop predictions show no overlap. This indicates that thermal resummation is the dominant error source regarding parameter reconstruction from FOPTs.

is known. In our case, the parameters that characterize the GW spectrum are the peak amplitude and frequency $\theta_i \in \{\Omega_{\rm sw}, f_{\rm sw}\}$, such that the Fisher matrix reads

$$\Gamma_{ij} = \mathcal{T} \int \frac{\mathrm{d}f}{\Omega_{\rm tot}(f)^2} \frac{\partial \Omega_{\rm tot}(f)}{\partial \theta_i} \frac{\partial \Omega_{\rm tot}(f)}{\partial \theta_j} \,. \tag{18.6}$$

The mission operation time $\mathcal{T} = 4\,\mathrm{yrs}$ and the total abundance

$$\Omega_{\rm tot}(f) = \Omega_{\rm GW}(f) + \Omega_{\rm instr}(f) \,, \tag{18.7}$$

is composed of the GW signal (3.59) and the instrumental noise [536]. We thus neglect noise contributions from binary white dwarfs [36, 539] and binary black holes probed by LIGO-Virgo-KAGRA [540]. This is justified since an inclusion of additional noise sources would merely increase the required amplitude to reach SNR = 10. In other words, our results would remain unchanged, we simply would have to impose a stronger benchmark signal that allows for claiming a detection.

The inverse of the Fisher matrix provides an approximation of the covariance matrix [541],

$$(\Gamma_{ij})^{-1} \approx \mathrm{Cov}(\theta_i, \theta_j) = \sigma_{ij}^2 \,. \tag{18.8}$$

Therefore, by inverting the Fisher matrix, we can read off the (co-)variances in the $f - \Omega_{\mathrm{GW}}^{\mathrm{peak}}$ plane. The covariance matrix is then translated into the $m_s - \lambda_{hs}$ parameter space to obtain the associated confidence regions. Let us, however, stress that the Fisher analysis is only an approximation, and a more precise study would require Markov Chain Monte Carlo techniques. Generally, both methods yield similar results if the reconstruction errors are smaller than roughly 10 % [482]. It turns out that this is exactly the regime produced by our benchmark. Hence our approach is valid, however, it would certainly be interesting to see how a Bayesian analysis would affect our results.

The reconstructed model parameters of the benchmark signal are shown in fig. 18.8. We compute the underlying model parameters given the five different implementations of the effective potential. The solid (dashed) lines denote the 1σ (2σ) confidence levels at LISA. First, let us note that the predictions from the (3D@NLO) approaches, i.e., the ones employing NLO matching relations, are consistent. That is, they overlap within their error margins. This changes when considering the LO approaches. While the (3D@LO) result shows a slight overlap with the 4D $\overline{\mathrm{MS}}$ scheme, which is expected as the potentials agree up to the choice of RG scale, they do not share any parameter space with the two-loop results. The same is true for the 4D on-shell scheme, which predicts model parameters inconsistent with the other methods.

Note that while the overall deviation in terms of λ_{hs} is merely at the percent level, the crucial point is that the reconstructed parameter spaces are completely distinct. This indicates that theoretical uncertainties from an incomplete computation of the effective potential exceed experimental errors. Let us again stress that this already holds true for a barely detectable signal. If we imposed a stronger benchmark signal, the associated instrumental uncertainties would decrease, rendering thermodynamic computations the main error source. This further highlights the importance of theoretical state-of-the-art methods to improve the understanding of possible future GW signals.

19

CONCLUSION

In the last main part of this thesis, we have studied the impact of higher-order thermodynamic contributions on the GW phenomenology of BSM theories. To this end, we have conducted large-scale parameter scans of the xSM employing different implementations of the effective potential. This includes the conventional, one-loop thermal effective potential in four dimensions employing both $\overline{\text{MS}}$ and on-shell renormalization. In addition, we have constructed the 3D EFT up to two-loop order using high-temperature DR, facilitating a consistent calculation of the effective potential at $\mathcal{O}(g^4)$. In total, we have thus compared five different thermodynamic approaches. In the parameter regime where the EWPT is rendered strongly first-order, we have computed the relevant PT parameters and estimated the projected GW signals.

Our analysis confirms previous work [56]; we find that employing the one-loop effective potential can induce order-of-magnitude changes of the GW peak amplitude (cf. fig. 15.1). Interestingly, the observable parameter space is more robust. The maximum deviation between the one- and two-loop results is of $\mathcal{O}(5\,\%)$ in, e.g., the portal coupling. However, such small shifts are important as the overall parameter space relevant for GW observations is very narrow. In addition, only the approaches using two-loop thermal masses yield consistent results in the form of a large overlap in parameter space.

Furthermore, we have shown that employing two-loop matching significantly reduces the RG scale dependence of the detectable parameter space. The one-loop approach shows only a small region of parameter space that is consistent under a RG scale variation, with deviations of the GW amplitude up to $\mathcal{O}(10^4)$. Employing two-loop matching, the consistent parameter regime grows, and the largest deviations of the amplitude are $\mathcal{O}(10)$.

Lastly, we have investigated the effect of computational diligence on the GW inverse problem concerning the reconstruction of model parameters from a given GW signal. To this end, we have employed Fisher matrix analyses. We find that uncertainties from missing higher-order corrections translate to deviations in the reconstructed portal coupling at the percent level. Nonetheless, these deviations dominate over experimental uncertainties,

even for signals just above the detection threshold. Again, this analysis shows that only the reconstructed model parameters obtained via NLO matching are consistent within their confidence levels. Therefore, we have shown that equilibrium thermodynamics is one of the dominant sources of uncertainty in FOPT computations.

Let us note that in all approaches we have neglected higher-order corrections to the bubble nucleation rate [179–182]. In the future, it will be interesting to see how the inclusion of such effects modifies our results. In addition, we have neglected higher-dimensional operators, which can have a sizable impact on the PT dynamics [510].

Furthermore, the effective potential in the xSM has a tree-level barrier due to the Z_2 symmetry breaking in the first step of the PT. Hence, our analysis should be extended to models where the thermal barrier is radiatively induced, for instance, CSI models that we have studied in part ii. Such models are typically more sensitive to thermal resummation [183, 247]. As the resulting GW signals are much stronger, the experimental uncertainties are reduced, and computational diligence becomes even more important.

To summarize, our work provides an important step forward regarding the computation of FOPT dynamics and the reconstruction of the resulting GW signal. Nevertheless, further theoretical progress is still required to advance the theoretical framework for robust comparison with future GW observations.

20

APPENDIX

In the appendix of part iv, we list the RGEs of the xSM, which we employ to implement RG improvement into the effective potential. Furthermore we provide more details on the counterterms used in the 4D $\overline{\text{MS}}$ scheme to fix the input parameters.

20.A RENORMALIZATION GROUP EVOLUTION

The β-functions describe the running of the couplings in the xSM and can be obtained via `DRAlgo`, but are also found in [542]. First, we fix the input parameters at the scale $\bar{\mu} = m_Z$. For the thermal EFT, we employ the procedure outlined in sec. 17.3, that is, we relate the physical observables to the $\overline{\text{MS}}$ parameters via one-loop vacuum renormalization. In the 4D $\overline{\text{MS}}$ approach, we choose a simplified procedure described in appendix 20.B. The RGEs are then used to evolve a given parameter from the input scale to the matching scale $\bar{\mu}$. For the 3D approaches, we choose $\bar{\mu} \in \{\frac{\pi}{2}T, 4\pi e^{-\gamma}T\}$, while we fix $\bar{\mu} = v_0$ in the 4D $\overline{\text{MS}}$ approach,. In our conventions and with $t = \log \mu^2$, the β-functions read

$$\partial_t g_1^2 = \frac{g_1^4}{(4\pi)^2}\left(\frac{1}{6} + \frac{20}{9}N_\text{f}\right), \tag{20.1}$$

$$\partial_t g_2^2 = \frac{g_2^4}{(4\pi)^2}\left(-\frac{43}{6} + \frac{4}{3}N_\text{f}\right), \tag{20.2}$$

$$\partial_t g_3^2 = \frac{g_3^4}{(4\pi)^2}\left(-\frac{11N_\text{c}}{3} + \frac{4N_\text{f}}{3}\right), \tag{20.3}$$

$$\partial_t y_t^2 = \frac{y_t^2}{(4\pi)^2}\left(\frac{2N_\text{c}+3}{2}y_t^2 - 8g_3^2 - \frac{9}{4}g_2^2 - \frac{17}{12}g_1^2\right), \tag{20.4}$$

$$\begin{aligned}\partial_t \lambda = \frac{1}{(4\pi)^2}\Bigg(&12\lambda^2 + \frac{\lambda_{hs}^2}{4} - \lambda\frac{3}{2}(3g_2^2 + g_1^2) + \frac{3}{16}g_1^4 + \frac{3}{8}g_2^2 g_1^2 + \frac{9}{16}g_2^4 \\ &- N_\text{c}y_t^4 + 2N_\text{c}y_t^2\lambda\Bigg),\end{aligned} \tag{20.5}$$

$$\partial_t \lambda_{hs} = \frac{\lambda_{hs}}{(4\pi)^2}\left(2\lambda_{hs} + 3\lambda_s - \frac{3}{4}(3g_2^2 + g_1^2) + N_\text{c}y_t^2 + 6\lambda\right), \tag{20.6}$$

$$\partial_t \lambda_s = \frac{1}{(4\pi)^2}\left(\lambda_{hs}^2 + 9\lambda_s^2\right), \tag{20.7}$$

$$\partial_t \mu_h^2 = \frac{1}{(4\pi)^2}\left(\mu_h^2\left(6\lambda + N_c y_t^2 - \frac{9}{4}g_2^2 - \frac{3}{4}g_1^2\right) + \frac{1}{2}\lambda_{hs}\mu_s^2\right), \tag{20.8}$$

$$\partial_t \mu_s^2 = \frac{1}{(4\pi)^2}\left(2\mu_h^2\lambda_{hs} + 3\mu_s^2\lambda_s\right), \tag{20.9}$$

$$\partial_t v = \frac{1}{(4\pi)^2}\frac{1}{2}\left(N_c y_t^2 - \frac{9}{4}g_2^2 - \frac{3}{4}g_1^2\right), \tag{20.10}$$

$$\partial_t x = 0\,. \tag{20.11}$$

Here, g_i with $i = 1, \ldots, 3$ are the $\mathrm{U}(1)_\mathrm{Y}$, $\mathrm{SU}(2)_\mathrm{L}$, $\mathrm{SU}(3)_\mathrm{c}$ gauge couplings, respectively. The top quark Yukawa is denoted by y_t, the Higgs mass parameter is $\mu_h^2 < 0$, and $N_\mathrm{f} = 3$ ($N_\mathrm{c} = 3$) represent the number of fermion families (colors). Furthermore, $\gamma_v = \partial_t v$ and $\gamma_x = \partial_t x$ are the Higgs and singlet anomalous dimensions.

20.B FIXING INPUT PARAMETERS VIA COUNTERTERMS.

As outlined in sec. 17.2, the input parameters in the 4D $\overline{\mathrm{MS}}$ scheme are fixed by imposing the minimization conditions (17.12) and (17.13). One-loop corrections to V_0 alter the location of the true minimum, such that $v = v_0\xi_{v_0}$, where

$$\xi(\bar{\mu}) = \exp\left[\int_{\log(\bar{\mu}^2)}^{\log(m_Z^2)} \mathrm{d}t\, \gamma_v(t)\right], \tag{20.12}$$

corresponds to the solution of the Higgs RGE. This alters the minimization conditions,

$$\left.\frac{\partial V_0}{\partial \phi_i}\right|_{\substack{v\,=\,v_0\xi(v_0)\\ \bar{\mu}\,=\,v_0}} = 0\,, \tag{20.13}$$

$$\left.\frac{\partial^2 V_0}{\partial \phi_i^2}\right|_{\substack{v\,=\,v_0\xi(v_0)\\ \bar{\mu}\,=\,v_0}} = m_i^2\,, \tag{20.14}$$

which translate to

$$\mu_h^2(v_0) = -\frac{1}{2}\frac{m_h^2}{\xi(v_0)^2}\,, \tag{20.15}$$

$$\mu_s^2(v_0) = m_s^2 - \frac{1}{2}\lambda_{hs}(v_0)v_0^2\xi(v_0)^2\,, \tag{20.16}$$

$$\lambda(v_0) = \frac{1}{2}\frac{m_h^2}{v_0^2\xi(v_0)^4}\,. \tag{20.17}$$

To ensure that these relations hold when $V_0 \to V_{\text{eff}}$, we introduce additional counterterms which preserve the vacuum structure [165]. The counterterm potential reads

$$V_{\text{CT}} = \frac{\delta\mu_h^2}{2}v^2 + \frac{\delta\mu_s^2}{2}x^2 + \frac{\delta\lambda}{4}v^4\,, \tag{20.18}$$

with

$$\begin{aligned}
\delta\mu_h^2 &= -\left(\frac{3}{2}\frac{1}{v_0\xi(v_0)}\partial_v - \frac{1}{2}\partial_v^2\right)V_{\text{CW}}\bigg|_{\substack{v\,=\,v_0\xi(v_0)\\ \bar{\mu}\,=\,v_0}}\,,\\
\delta\lambda &= \frac{1}{2v_0^3\xi(v_0)^3}\left(\partial_v - v_0\xi(v_0)\partial_v^2\right)V_{\text{CW}}\bigg|_{\substack{v\,=\,v_0\xi(v_0)\\ \bar{\mu}\,=\,v_0}}\,,\\
\delta\mu_s^2 &= -\partial_x^2 V_{\text{CW}}\bigg|_{\substack{v\,=\,v_0\xi(v_0)\\ \bar{\mu}\,=\,v_0}}\,.
\end{aligned} \tag{20.19}$$

Here, V_{CW} is given by eq. (17.11).

Part V

EPILOGUE

21

SUMMARY AND CONCLUSION

In this thesis, we have explored the early Universe dynamics and phenomenological GW signatures of various SM extensions. In the following, we summarize our main results.

Part ii focused on CSI models, which are characterized by the lack of a mass term in the tree-level potential. Therefore, the SM Higgs mass is replaced by a portal coupling to a new scalar field charged under an additional gauge symmetry. As the Universe cools and the new gauge symmetry is broken via radiative corrections, EWSB is triggered dynamically. Such models can have a significant impact on the thermal history of the Universe, inducing a period of thermal inflation which delays the EWPT to temperatures below the confinement scale of QCD. Then, conformal symmetry breaking through quark condensation can trigger the exit from supercooling. In chapter 6, we have studied QCD-induced conformal symmetry breaking via low-energy effective QCD models. To this end, we have proceeded in a model-agnostic manner, characterizing the CSI SM extension only by the temperature T_i connected to the onset of thermal inflation. Under the assumption that the cosmic QCD transition with six massless flavors is first-order, we have computed the PT dynamics in a supercooled Universe. While the inverse transition timescale is large, i.e., the GW amplitude is suppressed, for T_i below the electroweak scale, the amplitude is significantly enhanced if the new physics scale is large. This implies excellent observational prospects at future observatories such as BBO and ET.

Motivated by recent lattice studies implying a second-order χPT in the chiral limit up to a large number of quark flavors [290], we have developed a novel GW production mechanism in chapter 7. Employing the CSI $\mathrm{U}(1)_{\mathrm{B\text{-}L}}$ extended SM as a benchmark model, we have demonstrated the existence of a large parameter space in which thermal tunneling is inefficient to realize the exit from supercooling. Instead, the CSI scalar field rolls down the effective potential towards the true vacuum as the thermal barrier is canceled by QCD effects. The field crosses a region where its effective mass is imaginary, which triggers a tachyonic instability, leading to an exponential production of horizon-sized scalar fluctuations. Using previous lattice results for tachyonic preheating models, we have estimated the

peak frequency and amplitude of the SGWB associated with the tachyonic instability. This implies detection prospects at LISA, DECIGO, BBO, and ET. Furthermore, we expect the spectral shape to be tightly connected to the dynamics of the tachyonic resonance, hence distinguishable from conventional FOPT-induced signals. To this end, however, lattice simulations are required which accurately capture non-linear effects.

In part iii, we have studied the dynamics of ALPs in the early Universe. Specifically, we have developed an extension of the audible axion mechanism, in which ALPs coupled to dark photons produce chiral GWs through a tachyonic resonance in the dark gauge field. Inspired by our studies in part ii, we have considered the possibility of supercooling the onset of ALP oscillations. This can be achieved via higher-dimensional operators that trap the pseudoscalar initially. The increased efficiency of tachyonic dark photon production enables GW emission for small ALP-dark photon couplings $\alpha \gtrsim 1$, as compared to $\alpha \gtrsim 20$ in the original setup. Furthermore, the supercooling period enhances the relative energy density of the ALP at the onset of oscillations, significantly opening up the parameter space that produces sizable GW signals for small ALP decay constants. This was shown in chapter 11. In chapter 12, we have replaced the dark gauge field with the SM photon. This considerably simplifies the audible axion mechanism since a coupling between the ALP and the SM photon naturally arises in many ALP implementations. At high temperatures, however, the Debye mass m_{D} of the photon impedes efficient tachyonic growth. This is alleviated by the delayed onset of ALP oscillations, supercooling the Universe and suppressing m_{D}. We have identified two distinct, cosmologically consistent regions of parameter space in which the ALP-SM photon system produces sizable GWs, even in the presence of Schwinger pair production of light SM fermions. The resulting signals reach the projected sensitivity regions of μARES and BBO. Furthermore, large ALP masses induce signatures at ultra-high frequencies. Note, however, that parts of the parameter space require a large suppression of the ALP abundance to avoid DM overproduction. In this regard, a lattice simulation of the modified setup may provide crucial insights.

Lastly, we have analyzed the robustness of theoretical predictions of GW signals from FOPTs. Specifically, we have focused on the impact of thermodynamic precision when constructing the thermal effective potential on the overall model parameter space of the xSM, i.e., the SM extended by a gauge-singlet scalar field. To this end, we have computed the effective potential at increasing levels of diligence, including both conventional one-loop techniques using Daisy resummation, and state-of-the-art DR thermal EFT up to two-loop order. We have performed large-scale scans of the parameter space that predicts a strong first-order EWPT. While a variation of the RG scale can induce order-of-magnitude uncertainties in the GW amplitude when using the one-loop effective potential, NLO EFT

matching significantly alleviates these theoretical uncertainties. Conversely, the overall parameter spaces are more robust; missing higher-order effects induce deviations at the percent level. Nonetheless, such small shifts can become important due to the overall small region of parameter space that features a strong FOPT. Furthermore, the parameter space that remains consistent under a variation of the RG scale increases significantly when employing the two-loop computation. Finally, we reconstructed the underlying model parameters from a benchmark GW signal in the LISA frequency band using the different implementations of the effective potential. Intriguingly, although the one-loop methods only predict $\mathcal{O}(1\,\%)$ deviations compared to the two-loop approaches, the reconstructed model parameters are not consistent within their confidence limits. This indicates that missing higher-order corrections introduce errors that exceed the experimental uncertainties.

In conclusion, this thesis highlights the remarkable potential of GW cosmology. Specifically, we have demonstrated that GWs can serve as powerful probes of new physics across a wide range of energy scales and associated GW frequencies. This work contributes to both the development of novel mechanisms for GW production and the refinement of theoretical predictions relevant to cosmological signals. In light of upcoming next-generation observatories such as LISA, our findings underscore the importance of continued theoretical efforts to maximize the discovery potential of GW observations in the coming decades. Entering the era of *precision cosmology*, high-energy physics faces a bright future—one in which groundbreaking discoveries seem not just possible, but imminent.

ACKNOWLEDGEMENTS

All personal references were removed from the electronic version of this dissertation.

First, I would like to express my sincere gratitude to my supervisor for giving me the opportunity to pursue my PhD studies in the DMGW group. Thank you for the remarkable supervision. Your supportive and enthusiastic approach really creates an outstanding working atmosphere. I particularly enjoyed the great freedom in choosing research topics, the opportunity to attend a multitude of schools and conferences, and the many exciting and diverse scientific discussions we had.

In addition, I am thankful to my second supervisor for the co-supervision of my PhD studies. Thank you for your guidance, the collaboration in our common project, and for the numerous discussions during CRC retreats, colloquia, and my visits to Bielefeld University.

A special thanks goes to a former postdoc in the DMGW group. I really enjoyed the close collaboration over the years and I have learned a lot from you. I appreciate the all the discussions we had about thermal field theory and the time you invested trying to explain to me the concept of dimensional reduction.

Furthermore, I would like to thank my master thesis supervisor for the continued guidance and collaboration during my PhD studies. Your encouragement during my time as a master student has strongly influenced my decision to pursue a PhD in the first place.

To all my collaborators, thanks a lot for the exciting research projects and the insightful discussions. I enjoyed working with all of you.

A big thank you to the entire DMGW research group, in particular the people that have accompanied me over a long time, for the amazing and welcoming atmosphere.

I am particularly grateful to all my friends, which have made my undergraduate and PhD studies the best years of my life.

Finally, I would like to express my deepest gratitude to my family, in particular to my parents, for your unconditional support throughout my life. Without you, this thesis would not have been possible.

Lastly, to my partner, thank you for support, encouragement, and for always being there for me.

LIST OF FIGURES

LIST OF TABLES

ACRONYMS

BAU	Baryon asymmetry of the Universe
BBO	Big Bang Observer
BSM	Beyond the Standard Model
CDM	Cold dark matter
CMB	Cosmic microwave background
CP	Charge-parity
χPT	Chiral phase transition
χSB	Chiral symmetry breaking
CSI	Classically scale-invariant
CW	Coleman–Weinberg
DECIGO	DECi-hertz Interferometer Gravitational wave Observatory
DM	Dark matter
DR	Dimensional reduction
EFT	Effective field theory
ET	Einstein Telescope
EWSB	Electroweak symmetry breaking
EWPT	Electroweak phase transition
FLRW	Friedmann–Lemaître–Robertson–Walker
FOPT	First-order phase transition
GW	Gravitational wave
h.c.	Hermitian conjugate

IR	Infrared
MD	Matter domination
MFA	Mean-field approximation
$\overline{\text{MS}}$	Modified minimal subtraction
NJL	Nambu–Jona-Lasinio
LISA	Laser Interferometer Space Antenna
LO	Leading order
NLO	Next-to-leading order
PLI	Power-law integrated
PNJL	Polyakov–Nambu–Jona-Lasinio
QCD	Quantum chromodynamics
QED	Quantum electrodynamics
QFT	Quantum field theory
RD	Radiation domination
RG	Renormalization group
RGE	Renormalization group equation
SGWB	Stochastic gravitational wave background
SKA	Square Kilometre Array
SM	Standard Model
SNR	Signal-to-noise ratio
TT	Transverse-traceless
UV	Ultraviolet
vev	Vacuum expectation value
WFR	Wave function renormalization

xSM	Gauge-singlet extended Standard Model

BIBLIOGRAPHY

[1] Laura Sagunski, Philipp Schicho, and Daniel Schmitt. "Supercool exit: Gravitational waves from QCD-triggered conformal symmetry breaking." In: *Phys. Rev. D* 107.12 (2023), p. 123512. DOI: 10.1103/PhysRevD.107.123512. arXiv: 2303.02450 [hep-ph].

[2] Marek Lewicki, Marco Merchand, Laura Sagunski, Philipp Schicho, and Daniel Schmitt. "Impact of theoretical uncertainties on model parameter reconstruction from GW signals sourced by cosmological phase transitions." In: *Phys. Rev. D* 110.2 (2024), p. 023538. DOI: 10.1103/PhysRevD.110.023538. arXiv: 2403.03769 [hep-ph].

[3] Philipp Schicho and Daniel Schmitt. https://github.com/DMGW-Goethe/DRansitions. 2024.

[4] Daniel Schmitt and Laura Sagunski. "QCD-sourced tachyonic phase transition in a supercooled Universe." In: *JCAP* 02 (2025), p. 075. DOI: 10.1088/1475-7516/2025/02/075. arXiv: 2409.05851 [hep-ph].

[5] Christopher Gerlach, Daniel Schmitt, and Pedro Schwaller. "Supercooled Audible Axions." In: (Apr. 2025). arXiv: 2504.05386 [hep-ph].

[6] Eric Madge, Wolfram Ratzinger, Daniel Schmitt, and Pedro Schwaller. "Audible axions with a booster: Stochastic gravitational waves from rotating ALPs." In: *SciPost Phys.* 12.5 (2022), p. 171. DOI: 10.21468/SciPostPhys.12.5.171. arXiv: 2111.12730 [hep-ph].

[7] Robin Fynn Diedrichs, Daniel Schmitt, and Laura Sagunski. "Binary systems in massive scalar-tensor theories: Next-to-leading order gravitational wave phase from effective field theory." In: *Phys. Rev. D* 110.10 (2024), p. 104073. DOI: 10.1103/PhysRevD.110.104073. arXiv: 2311.04274 [gr-qc].

[8] Maciej Kierkla, Nicklas Ramberg, Philipp Schicho, and Daniel Schmitt. "Theoretical uncertainties for primordial black holes from cosmological phase transitions." In: (June 2025). arXiv: 2506.15496 [hep-ph].

[9] Dietrich Bödeker, Jondalar Kuß, Laura Sagunski, and Daniel Schmitt. "Sterile neutrino dark matter and gravitational waves in a supercooled Universe." *to appear.*

[10] B. P. Abbott et al. "Observation of Gravitational Waves from a Binary Black Hole Merger." In: *Phys. Rev. Lett.* 116.6 (2016), p. 061102. DOI: 10.1103/PhysRevLett.116.061102. arXiv: 1602.03837 [gr-qc].

[11] Albert Einstein. "Approximative Integration of the Field Equations of Gravitation." In: *Sitzungsber. Preuss. Akad. Wiss. Berlin (Math. Phys.)* 1916 (1916), pp. 688–696.

[12] Albert Einstein. "Über Gravitationswellen." In: *Sitzungsber. Preuss. Akad. Wiss. Berlin (Math. Phys.)* 1918 (1918), pp. 154–167.

[13] Michael S. Turner, Erick J. Weinberg, and Lawrence M. Widrow. "Bubble nucleation in first-order inflation and other cosmological phase transitions." In: *Phys. Rev. D* 46 (6 1992), pp. 2384–2403. DOI: 10.1103/PhysRevD.46.2384. URL: https://link.aps.org/doi/10.1103/PhysRevD.46.2384.

[14] N. Aghanim et al. "Planck 2018 results. VI. Cosmological parameters." In: *Astron. Astrophys.* 641 (2020). [Erratum: Astron.Astrophys. 652, C4 (2021)], A6. DOI: 10.1051/0004-6361/201833910. arXiv: 1807.06209 [astro-ph.CO].

[15] Fabio Iocco, Gianpiero Mangano, Gennaro Miele, Ofelia Pisanti, and Pasquale D. Serpico. "Primordial Nucleosynthesis: from precision cosmology to fundamental physics." In: *Phys. Rept.* 472 (2009), pp. 1–76. DOI: 10.1016/j.physrep.2009.02.002. arXiv: 0809.0631 [astro-ph].

[16] J. Ghiglieri and M. Laine. "Gravitational wave background from Standard Model physics: Qualitative features." In: *JCAP* 07 (2015), p. 022. DOI: 10.1088/1475-7516/2015/07/022. arXiv: 1504.02569 [hep-ph].

[17] J. Ghiglieri, G. Jackson, M. Laine, and Y. Zhu. "Gravitational wave background from Standard Model physics: Complete leading order." In: *JHEP* 07 (2020), p. 092. DOI: 10.1007/JHEP07(2020)092. arXiv: 2004.11392 [hep-ph].

[18] Chiara Caprini and Daniel G. Figueroa. "Cosmological Backgrounds of Gravitational Waves." In: *Class. Quant. Grav.* 35.16 (2018), p. 163001. DOI: 10.1088/1361-6382/aac608. arXiv: 1801.04268 [astro-ph.CO].

[19] K. Kajantie, M. Laine, K. Rummukainen, and Mikhail E. Shaposhnikov. "Is there a hot electroweak phase transition at $m_H \gtrsim m_W$?" In: *Phys. Rev. Lett.* 77 (1996), pp. 2887–2890. DOI: 10.1103/PhysRevLett.77.2887. arXiv: hep-ph/9605288.

[20] Y. Aoki, G. Endrodi, Z. Fodor, S. D. Katz, and K. K. Szabo. "The Order of the quantum chromodynamics transition predicted by the standard model of particle physics." In: *Nature* 443 (2006), pp. 675–678. DOI: 10.1038/nature05120. arXiv: hep-lat/0611014.

[21] Y. Fukuda et al. "Evidence for oscillation of atmospheric neutrinos." In: *Phys. Rev. Lett.* 81 (1998), pp. 1562–1567. DOI: 10.1103/PhysRevLett.81.1562. arXiv: hep-ex/9807003.

[22] Marco Cirelli, Alessandro Strumia, and Jure Zupan. "Dark Matter." In: (June 2024). arXiv: 2406.01705 [hep-ph].

[23] A. D. Sakharov. "Violation of CP Invariance, C asymmetry, and baryon asymmetry of the universe." In: *Pisma Zh. Eksp. Teor. Fiz.* 5 (1967), pp. 32–35. DOI: 10.1070/PU1991v034n05ABEH002497.

[24] Zaven Arzoumanian et al. "The NANOGrav 12.5 yr Data Set: Search for an Isotropic Stochastic Gravitational-wave Background." In: *Astrophys. J. Lett.* 905.2 (2020), p. L34. DOI: 10.3847/2041-8213/abd401. arXiv: 2009.04496 [astro-ph.HE].

[25] Zaven Arzoumanian et al. "Searching for Gravitational Waves from Cosmological Phase Transitions with the NANOGrav 12.5-Year Dataset." In: *Phys. Rev. Lett.* 127.25 (2021), p. 251302. DOI: 10.1103/PhysRevLett.127.251302. arXiv: 2104.13930 [astro-ph.CO].

[26] Boris Goncharov et al. "On the Evidence for a Common-spectrum Process in the Search for the Nanohertz Gravitational-wave Background with the Parkes Pulsar Timing Array." In: *Astrophys. J. Lett.* 917.2 (2021), p. L19. DOI: 10.3847/2041-8213/ac17f4. arXiv: 2107.12112 [astro-ph.HE].

[27] S. Chen et al. "Common-red-signal analysis with 24-yr high-precision timing of the European Pulsar Timing Array: inferences in the stochastic gravitational-wave background search." In: *Mon. Not. Roy. Astron. Soc.* 508.4 (2021), pp. 4970–4993. DOI: 10.1093/mnras/stab2833. arXiv: 2110.13184 [astro-ph.HE].

[28] J. Antoniadis et al. "The International Pulsar Timing Array second data release: Search for an isotropic gravitational wave background." In: *Mon. Not. Roy. Astron. Soc.* 510.4 (2022), pp. 4873–4887. DOI: 10.1093/mnras/stab3418. arXiv: 2201.03980 [astro-ph.HE].

[29] Gabriella Agazie et al. "The NANOGrav 15 yr Data Set: Evidence for a Gravitational-wave Background." In: *Astrophys. J. Lett.* 951.1 (2023), p. L8. DOI: 10.3847/2041-8213/acdac6. arXiv: 2306.16213 [astro-ph.HE].

[30] J. Antoniadis et al. "The second data release from the European Pulsar Timing Array - III. Search for gravitational wave signals." In: *Astron. Astrophys.* 678 (2023), A50. DOI: 10.1051/0004-6361/202346844. arXiv: 2306.16214 [astro-ph.HE].

[31] Daniel J. Reardon et al. "Search for an Isotropic Gravitational-wave Background with the Parkes Pulsar Timing Array." In: *Astrophys. J. Lett.* 951.1 (2023), p. L6. DOI: 10.3847/2041-8213/acdd02. arXiv: 2306.16215 [astro-ph.HE].

[32] Heng Xu et al. "Searching for the Nano-Hertz Stochastic Gravitational Wave Background with the Chinese Pulsar Timing Array Data Release I." In: *Res. Astron. Astrophys.* 23.7 (2023), p. 075024. DOI: 10.1088/1674-4527/acdfa5. arXiv: 2306.16216 [astro-ph.HE].

[33] Matthew T. Miles et al. "The MeerKAT Pulsar Timing Array: the first search for gravitational waves with the MeerKAT radio telescope." In: *Mon. Not. Roy. Astron. Soc.* 536.2 (2024), pp. 1489–1500. DOI: 10.1093/mnras/stae2571. arXiv: 2412.01153 [astro-ph.HE].

[34] Adeela Afzal et al. "The NANOGrav 15 yr Data Set: Search for Signals from New Physics." In: *Astrophys. J. Lett.* 951.1 (2023), p. L11. DOI: 10.3847/2041-8213/acdc91. arXiv: 2306.16219 [astro-ph.HE].

[35] LISA collaboration. "Laser Interferometer Space Antenna." In: *arXiv e-prints*, arXiv:1702.00786 (Feb. 2017), arXiv:1702.00786. arXiv: 1702.00786 [astro-ph.IM].

[36] Travis Robson, Neil J. Cornish, and Chang Liu. "The construction and use of LISA sensitivity curves." In: *Class. Quant. Grav.* 36.10 (2019), p. 105011. DOI: 10.1088/1361-6382/ab1101. arXiv: 1803.01944 [astro-ph.HE].

[37] Pierre Auclair et al. "Cosmology with the Laser Interferometer Space Antenna." In: *Living Rev. Rel.* 26.1 (2023), p. 5. DOI: 10.1007/s41114-023-00045-2. arXiv: 2204.05434 [astro-ph.CO].

[38] M. Punturo et al. "The Einstein Telescope: A third-generation gravitational wave observatory." In: *Class. Quant. Grav.* 27 (2010). Ed. by Fulvio Ricci, p. 194002. DOI: 10.1088/0264-9381/27/19/194002.

[39] B. Sathyaprakash et al. "Scientific Objectives of Einstein Telescope." In: *Class. Quant. Grav.* 29 (2012). Ed. by Mark Hannam, Patrick Sutton, Stefan Hild, and Chris van den Broeck. [Erratum: Class.Quant.Grav. 30, 079501 (2013)], p. 124013. DOI: 10.1088/0264-9381/29/12/124013. arXiv: 1206.0331 [gr-qc].

[40] Adrian Abac et al. "The Science of the Einstein Telescope." In: (Mar. 2025). arXiv: 2503.12263 [gr-qc].

[41] Satoshi Iso, Nobuchika Okada, and Yuta Orikasa. "Classically conformal $B-L$ extended Standard Model." In: *Phys. Lett. B* 676 (2009), pp. 81–87. DOI: 10.1016/j.physletb.2009.04.046. arXiv: 0902.4050 [hep-ph].

[42] Peter Minkowski. "$\mu \to e\gamma$ at a Rate of One Out of 10^9 Muon Decays?" In: *Phys. Lett. B* 67 (1977), pp. 421–428. DOI: 10.1016/0370-2693(77)90435-X.

[43] Scott Dodelson and Lawrence M. Widrow. "Sterile-neutrinos as dark matter." In: *Phys. Rev. Lett.* 72 (1994), pp. 17–20. DOI: 10.1103/PhysRevLett.72.17. arXiv: hep-ph/9303287.

[44] Sacha Davidson, Enrico Nardi, and Yosef Nir. "Leptogenesis." In: *Phys. Rept.* 466 (2008), pp. 105–177. DOI: 10.1016/j.physrep.2008.06.002. arXiv: 0802.2962 [hep-ph].

[45] Robert D. Pisarski and Frank Wilczek. "Remarks on the Chiral Phase Transition in Chromodynamics." In: *Phys. Rev. D* 29 (1984), pp. 338–341. DOI: 10.1103/PhysRevD.29.338.

[46] Satoshi Iso, Pasquale D. Serpico, and Kengo Shimada. "QCD-Electroweak First-Order Phase Transition in a Supercooled Universe." In: *Phys. Rev. Lett.* 119.14 (2017), p. 141301. DOI: 10.1103/PhysRevLett.119.141301. arXiv: 1704.04955 [hep-ph].

[47] Gary N. Felder, Juan Garcia-Bellido, Patrick B. Greene, Lev Kofman, Andrei D. Linde, and Igor Tkachev. "Dynamics of symmetry breaking and tachyonic preheating." In: *Phys. Rev. Lett.* 87 (2001), p. 011601. DOI: 10.1103/PhysRevLett.87.011601. arXiv: hep-ph/0012142.

[48] Gary N. Felder, Lev Kofman, and Andrei D. Linde. "Tachyonic instability and dynamics of spontaneous symmetry breaking." In: *Phys. Rev. D* 64 (2001), p. 123517. DOI: 10.1103/PhysRevD.64.123517. arXiv: hep-th/0106179.

[49] R. D. Peccei and Helen R. Quinn. "CP Conservation in the Presence of Instantons." In: *Phys. Rev. Lett.* 38 (1977), pp. 1440–1443. DOI: 10.1103/PhysRevLett.38.1440.

[50] R. D. Peccei and Helen R. Quinn. "Constraints Imposed by CP Conservation in the Presence of Instantons." In: *Phys. Rev. D* 16 (1977), pp. 1791–1797. DOI: 10.1103/PhysRevD.16.1791.

[51] Steven Weinberg. "A New Light Boson?" In: *Phys. Rev. Lett.* 40 (1978), pp. 223–226. DOI: 10.1103/PhysRevLett.40.223.

[52] Frank Wilczek. "Problem of Strong P and T Invariance in the Presence of Instantons." In: *Phys. Rev. Lett.* 40 (1978), pp. 279–282. DOI: 10.1103/PhysRevLett.40.279.

[53] Camila S. Machado, Wolfram Ratzinger, Pedro Schwaller, and Ben A. Stefanek. "Audible Axions." In: *JHEP* 01 (2019), p. 053. DOI: 10.1007/JHEP01(2019)053. arXiv: 1811.01950 [hep-ph].

[54] Luca Di Luzio and Philip Sørensen. "Axion production via trapped misalignment from Peccei-Quinn symmetry breaking." In: *JHEP* 10 (2024), p. 239. DOI: 10.1007/JHEP10(2024)239. arXiv: 2408.04623 [hep-ph].

[55] Andrei D. Linde. "Infrared Problem in Thermodynamics of the Yang-Mills Gas." In: *Phys. Lett. B* 96 (1980), pp. 289–292. DOI: 10.1016/0370-2693(80)90769-8.

[56] Djuna Croon, Oliver Gould, Philipp Schicho, Tuomas V. I. Tenkanen, and Graham White. "Theoretical uncertainties for cosmological first-order phase transitions." In: *JHEP* 04 (2021), p. 055. DOI: 10.1007/JHEP04(2021)055. arXiv: 2009.10080 [hep-ph].

[57] Georges Aad et al. "Observation of a new particle in the search for the Standard Model Higgs boson with the ATLAS detector at the LHC." In: *Phys. Lett. B* 716 (2012), pp. 1–29. DOI: 10.1016/j.physletb.2012.08.020. arXiv: 1207.7214 [hep-ex].

[58] Serguei Chatrchyan et al. "Observation of a New Boson at a Mass of 125 GeV with the CMS Experiment at the LHC." In: *Phys. Lett. B* 716 (2012), pp. 30–61. DOI: 10.1016/j.physletb.2012.08.021. arXiv: 1207.7235 [hep-ex].

[59] F. Englert and R. Brout. "Broken Symmetry and the Mass of Gauge Vector Mesons." In: *Phys. Rev. Lett.* 13 (1964). Ed. by J. C. Taylor, pp. 321–323. DOI: 10.1103/PhysRevLett.13.321.

[60] Peter W. Higgs. "Broken symmetries, massless particles and gauge fields." In: *Phys. Lett.* 12 (1964), pp. 132–133. DOI: 10.1016/0031-9163(64)91136-9.

[61] G. S. Guralnik, C. R. Hagen, and T. W. B. Kibble. "Global Conservation Laws and Massless Particles." In: *Phys. Rev. Lett.* 13 (1964). Ed. by J. C. Taylor, pp. 585–587. DOI: 10.1103/PhysRevLett.13.585.

[62] Peter W. Higgs. "Broken Symmetries and the Masses of Gauge Bosons." In: *Phys. Rev. Lett.* 13 (1964). Ed. by J. C. Taylor, pp. 508–509. DOI: 10.1103/PhysRevLett.13.508.

[63] Peter W. Higgs. "Spontaneous Symmetry Breakdown without Massless Bosons." In: *Phys. Rev.* 145 (1966), pp. 1156–1163. DOI: 10.1103/PhysRev.145.1156.

[64] T. W. B. Kibble. "Symmetry breaking in nonAbelian gauge theories." In: *Phys. Rev.* 155 (1967). Ed. by J. C. Taylor, pp. 1554–1561. DOI: 10.1103/PhysRev.155.1554.

[65] B. P. Abbott et al. "GW170817: Observation of Gravitational Waves from a Binary Neutron Star Inspiral." In: *Phys. Rev. Lett.* 119.16 (2017), p. 161101. DOI: 10.1103/PhysRevLett.119.161101. arXiv: 1710.05832 [gr-qc].

[66] S. L. Glashow. "Partial Symmetries of Weak Interactions." In: *Nucl. Phys.* 22 (1961), pp. 579–588. DOI: 10.1016/0029-5582(61)90469-2.

[67] Steven Weinberg. "A Model of Leptons." In: *Phys. Rev. Lett.* 19 (1967), pp. 1264–1266. DOI: 10.1103/PhysRevLett.19.1264.

[68] Abdus Salam. "Weak and Electromagnetic Interactions." In: *Conf. Proc. C* 680519 (1968), pp. 367–377. DOI: 10.1142/9789812795915_0034.

[69] S. L. Glashow, J. Iliopoulos, and L. Maiani. "Weak Interactions with Lepton-Hadron Symmetry." In: *Phys. Rev. D* 2 (1970), pp. 1285–1292. DOI: 10.1103/PhysRevD.2.1285.

[70] Gerard 't Hooft and M. J. G. Veltman. "Regularization and Renormalization of Gauge Fields." In: *Nucl. Phys. B* 44 (1972), pp. 189–213. DOI: 10.1016/0550-3213(72)90279-9.

[71] S. Navas et al. "Review of particle physics." In: *Phys. Rev. D* 110.3 (2024), p. 030001. DOI: 10.1103/PhysRevD.110.030001.

[72] Chen-Ning Yang and Robert L. Mills. "Conservation of Isotopic Spin and Isotopic Gauge Invariance." In: *Phys. Rev.* 96 (1954). Ed. by Jong-Ping Hsu and D. Fine, pp. 191–195. DOI: 10.1103/PhysRev.96.191.

[73] Murray Gell-Mann. "A Schematic Model of Baryons and Mesons." In: *Phys. Lett.* 8 (1964), pp. 214–215. DOI: 10.1016/S0031-9163(64)92001-3.

[74] H. Fritzsch, Murray Gell-Mann, and H. Leutwyler. "Advantages of the Color Octet Gluon Picture." In: *Phys. Lett. B* 47 (1973), pp. 365–368. DOI: 10.1016/0370-2693(73)90625-4.

[75] H. David Politzer. "Reliable Perturbative Results for Strong Interactions?" In: *Phys. Rev. Lett.* 30 (1973). Ed. by J. C. Taylor, pp. 1346–1349. DOI: 10.1103/PhysRevLett.30.1346.

[76] David J. Gross and Frank Wilczek. "Ultraviolet Behavior of Nonabelian Gauge Theories." In: *Phys. Rev. Lett.* 30 (1973). Ed. by J. C. Taylor, pp. 1343–1346. DOI: 10.1103/PhysRevLett.30.1343.

[77] Julian S. Schwinger. "On Quantum electrodynamics and the magnetic moment of the electron." In: *Phys. Rev.* 73 (1948), pp. 416–417. DOI: 10.1103/PhysRev.73.416.

[78] Julian S. Schwinger. "Quantum electrodynamics. I A covariant formulation." In: *Phys. Rev.* 74 (1948). Ed. by K. A. Milton, p. 1439. DOI: 10.1103/PhysRev.74.1439.

[79] R. P. Feynman. "The Theory of positrons." In: *Phys. Rev.* 76 (1949). Ed. by L. M. Brown, pp. 749–759. DOI: 10.1103/PhysRev.76.749.

[80] R. P. Feynman. "Space - time approach to quantum electrodynamics." In: *Phys. Rev.* 76 (1949). Ed. by L. M. Brown, pp. 769–789. DOI: 10.1103/PhysRev.76.769.

[81] R. P. Feynman. "Mathematical formulation of the quantum theory of electromagnetic interaction." In: *Phys. Rev.* 80 (1950). Ed. by L. M. Brown, pp. 440–457. DOI: 10.1103/PhysRev.80.440.

[82] Michela D'Onofrio and Kari Rummukainen. "Standard model cross-over on the lattice." In: *Phys. Rev. D* 93.2 (2016), p. 025003. DOI: 10.1103/PhysRevD.93.025003. arXiv: 1508.07161 [hep-ph].

[83] Michael E. Peskin and Daniel V. Schroeder. *An Introduction to quantum field theory*. Reading, USA: Addison-Wesley, 1995. ISBN: 978-0-201-50397-5, 978-0-429-50355-9, 978-0-429-49417-8. DOI: 10.1201/9780429503559.

[84] Kenneth G. Wilson. "Confinement of Quarks." In: *Phys. Rev. D* 10 (1974). Ed. by J. C. Taylor, pp. 2445–2459. DOI: 10.1103/PhysRevD.10.2445.

[85] Yoichiro Nambu. "Strings, Monopoles and Gauge Fields." In: *Phys. Rev. D* 10 (1974). Ed. by T. Eguchi, p. 4262. DOI: 10.1103/PhysRevD.10.4262.

[86] Yoichiro Nambu. "Quasiparticles and Gauge Invariance in the Theory of Superconductivity." In: *Phys. Rev.* 117 (1960). Ed. by J. C. Taylor, pp. 648–663. DOI: 10.1103/PhysRev.117.648.

[87] J. Goldstone. "Field Theories with Superconductor Solutions." In: *Nuovo Cim.* 19 (1961), pp. 154–164. DOI: 10.1007/BF02812722.

[88] Tanmoy Bhattacharya et al. "QCD Phase Transition with Chiral Quarks and Physical Quark Masses." In: *Phys. Rev. Lett.* 113.8 (2014), p. 082001. DOI: 10.1103/PhysRevLett.113.082001. arXiv: 1402.5175 [hep-lat].

[89] Edward W. Kolb and Michael S. Turner. *The Early Universe*. Vol. 69. Taylor and Francis, May 2019. ISBN: 978-0-429-49286-0, 978-0-201-62674-2. DOI: 10.1201/9780429492860.

[90] Daniel Baumann. *Cosmology*. Cambridge University Press, July 2022. ISBN: 978-1-108-93709-2, 978-1-108-83807-8. DOI: 10.1017/9781108937092.

[91] Adam G. Riess et al. "A 2.4% Determination of the Local Value of the Hubble Constant." In: *Astrophys. J.* 826.1 (2016), p. 56. DOI: 10.3847/0004-637X/826/1/56. arXiv: 1604.01424 [astro-ph.CO].

[92] Adam G. Riess et al. "A Comprehensive Measurement of the Local Value of the Hubble Constant with 1 km s^{-1} Mpc^{-1} Uncertainty from the Hubble Space Telescope and the SH0ES Team." In: *Astrophys. J. Lett.* 934.1 (2022), p. L7. DOI: 10.3847/2041-8213/ac5c5b. arXiv: 2112.04510 [astro-ph.CO].

[93] Eleonora Di Valentino, Olga Mena, Supriya Pan, Luca Visinelli, Weiqiang Yang, Alessandro Melchiorri, David F. Mota, Adam G. Riess, and Joseph Silk. "In the realm of the Hubble tension—a review of solutions." In: *Class. Quant. Grav.* 38.15 (2021), p. 153001. DOI: 10.1088/1361-6382/ac086d. arXiv: 2103.01183 [astro-ph.CO].

[94] A. G. Adame et al. "DESI 2024 IV: Baryon Acoustic Oscillations from the Lyman alpha forest." In: *JCAP* 01 (2025), p. 124. DOI: 10.1088/1475-7516/2025/01/124. arXiv: 2404.03001 [astro-ph.CO].

[95] A. G. Adame et al. "DESI 2024 VI: cosmological constraints from the measurements of baryon acoustic oscillations." In: *JCAP* 02 (2025), p. 021. DOI: 10.1088/1475-7516/2025/02/021. arXiv: 2404.03002 [astro-ph.CO].

[96] A. G. Adame et al. "DESI 2024 III: baryon acoustic oscillations from galaxies and quasars." In: *JCAP* 04 (2025), p. 012. DOI: 10.1088/1475-7516/2025/04/012. arXiv: 2404.03000 [astro-ph.CO].

[97] M. Abdul Karim et al. "DESI DR2 Results II: Measurements of Baryon Acoustic Oscillations and Cosmological Constraints." In: (Mar. 2025). arXiv: 2503.14738 [astro-ph.CO].

[98] P. J. E. Peebles and Bharat Ratra. "The Cosmological Constant and Dark Energy." In: *Rev. Mod. Phys.* 75 (2003). Ed. by Jong-Ping Hsu and D. Fine, pp. 559–606. DOI: 10.1103/RevModPhys.75.559. arXiv: astro-ph/0207347.

[99] Edmund J. Copeland, M. Sami, and Shinji Tsujikawa. "Dynamics of dark energy." In: *Int. J. Mod. Phys. D* 15 (2006), pp. 1753–1936. DOI: 10.1142/S021827180600942X. arXiv: hep-th/0603057.

[100] Sean Tulin and Hai-Bo Yu. "Dark Matter Self-interactions and Small Scale Structure." In: *Phys. Rept.* 730 (2018), pp. 1–57. DOI: 10.1016/j.physrep.2017.11.004. arXiv: 1705.02358 [hep-ph].

[101] Y. Akrami et al. "Planck 2018 results. X. Constraints on inflation." In: *Astron. Astrophys.* 641 (2020), A10. DOI: 10.1051/0004-6361/201833887. arXiv: 1807.06211 [astro-ph.CO].

[102] Daniel Baumann. "Inflation." In: *Theoretical Advanced Study Institute in Elementary Particle Physics: Physics of the Large and the Small*. 2011, pp. 523–686. DOI: 10.1142/9789814327183_0010. arXiv: 0907.5424 [hep-th].

[103] David H. Lyth and Antonio Riotto. "Particle physics models of inflation and the cosmological density perturbation." In: *Phys. Rept.* 314 (1999), pp. 1–146. DOI: 10.1016/S0370-1573(98)00128-8. arXiv: hep-ph/9807278.

[104] Alan H. Guth. "The Inflationary Universe: A Possible Solution to the Horizon and Flatness Problems." In: *Phys. Rev. D* 23 (1981). Ed. by Li-Zhi Fang and R. Ruffini, pp. 347–356. DOI: 10.1103/PhysRevD.23.347.

[105] Andrei D. Linde. "A New Inflationary Universe Scenario: A Possible Solution of the Horizon, Flatness, Homogeneity, Isotropy and Primordial Monopole Problems." In: *Phys. Lett. B* 108 (1982). Ed. by Li-Zhi Fang and R. Ruffini, pp. 389–393. DOI: 10.1016/0370-2693(82)91219-9.

[106] Richard H. Cyburt, Brian D. Fields, Keith A. Olive, and Tsung-Han Yeh. "Big Bang Nucleosynthesis: 2015." In: *Rev. Mod. Phys.* 88 (2016), p. 015004. DOI: 10.1103/RevModPhys.88.015004. arXiv: 1505.01076 [astro-ph.CO].

[107] Lev Kofman, Andrei D. Linde, and Alexei A. Starobinsky. "Reheating after inflation." In: *Phys. Rev. Lett.* 73 (1994), pp. 3195–3198. DOI: 10.1103/PhysRevLett.73.3195. arXiv: hep-th/9405187.

[108] Y. Shtanov, Jennie H. Traschen, and Robert H. Brandenberger. "Universe reheating after inflation." In: *Phys. Rev. D* 51 (1995), pp. 5438–5455. DOI: 10.1103/PhysRevD.51.5438. arXiv: hep-ph/9407247.

[109] Mikko Laine and Aleksi Vuorinen. *Basics of Thermal Field Theory*. Vol. 925. Springer, 2016. DOI: 10.1007/978-3-319-31933-9. arXiv: 1701.01554 [hep-ph].

[110] Lars Husdal. "On Effective Degrees of Freedom in the Early Universe." In: *Galaxies* 4.4 (2016), p. 78. DOI: 10.3390/galaxies4040078. arXiv: 1609.04979 [astro-ph.CO].

[111] Dietrich Bodeker and Wilfried Buchmuller. "Baryogenesis from the weak scale to the grand unification scale." In: *Rev. Mod. Phys.* 93.3 (2021), p. 035004. DOI: 10.1103/RevModPhys.93.035004. arXiv: 2009.07294 [hep-ph].

[112] Brian D. Fields, Keith A. Olive, Tsung-Han Yeh, and Charles Young. "Big-Bang Nucleosynthesis after Planck." In: *JCAP* 03 (2020). [Erratum: JCAP 11, E02 (2020)], p. 010. DOI: 10.1088/1475-7516/2020/03/010. arXiv: 1912.01132 [astro-ph.CO].

[113] Wayne Hu and Scott Dodelson. "Cosmic Microwave Background Anisotropies." In: *Ann. Rev. Astron. Astrophys.* 40 (2002), pp. 171–216. DOI: 10.1146/annurev.astro.40.060401.093926. arXiv: astro-ph/0110414.

[114] F. Zwicky. "Die Rotverschiebung von extragalaktischen Nebeln." In: *Helv. Phys. Acta* 6 (1933), pp. 110–127. DOI: 10.1007/s10714-008-0707-4.

[115] Vera C. Rubin and W. Kent Ford Jr. "Rotation of the Andromeda Nebula from a Spectroscopic Survey of Emission Regions." In: *Astrophys. J.* 159 (1970), pp. 379–403. DOI: 10.1086/150317.

[116] Maxim Markevitch, A. H. Gonzalez, D. Clowe, A. Vikhlinin, L. David, W. Forman, C. Jones, S. Murray, and W. Tucker. "Direct constraints on the dark matter self-interaction cross-section from the merging galaxy cluster 1E0657-56." In: *Astrophys. J.* 606 (2004), pp. 819–824. DOI: 10.1086/383178. arXiv: astro-ph/0309303.

[117] Douglas Clowe, Marusa Bradac, Anthony H. Gonzalez, Maxim Markevitch, Scott W. Randall, Christine Jones, and Dennis Zaritsky. "A direct empirical proof of the existence of dark matter." In: *Astrophys. J. Lett.* 648 (2006), pp. L109–L113. DOI: 10.1086/508162. arXiv: astro-ph/0608407.

[118] David Harvey, Richard Massey, Thomas Kitching, Andy Taylor, and Eric Tittley. "The non-gravitational interactions of dark matter in colliding galaxy clusters." In: *Science* 347 (2015), pp. 1462–1465. DOI: 10.1126/science.1261381. arXiv: 1503.07675 [astro-ph.CO].

[119] C. S. Frenk and Simon D. M. White. "Dark matter and cosmic structure." In: *Annalen Phys.* 524 (2012), pp. 507–534. DOI: 10.1002/andp.201200212. arXiv: 1210.0544 [astro-ph.CO].

[120] Dragan Huterer. "Growth of cosmic structure." In: *Astron. Astrophys. Rev.* 31.1 (2023), p. 2. DOI: 10.1007/s00159-023-00147-4. arXiv: 2212.05003 [astro-ph.CO].

[121] Frans R. Klinkhamer and N. S. Manton. "A Saddle Point Solution in the Weinberg-Salam Theory." In: *Phys. Rev. D* 30 (1984), p. 2212. DOI: 10.1103/PhysRevD.30.2212.

[122] A. Alavi-Harati et al. "Observation of Direct CP Violation in $K_{S,L} \to \pi\pi$ Decays." In: *Phys. Rev. Lett.* 83 (1999), pp. 22–27. DOI: 10.1103/PhysRevLett.83.22. arXiv: hep-ex/9905060.

[123] David E. Morrissey and Michael J. Ramsey-Musolf. "Electroweak baryogenesis." In: *New J. Phys.* 14 (2012), p. 125003. DOI: 10.1088/1367-2630/14/12/125003. arXiv: 1206.2942 [hep-ph].

[124] C. Abel et al. "Measurement of the Permanent Electric Dipole Moment of the Neutron." In: *Phys. Rev. Lett.* 124.8 (2020), p. 081803. DOI: 10.1103/PhysRevLett.124.081803. arXiv: 2001.11966 [hep-ex].

[125] Cumrun Vafa and Edward Witten. "Parity Conservation in QCD." In: *Phys. Rev. Lett.* 53 (1984), p. 535. DOI: 10.1103/PhysRevLett.53.535.

[126] Giovanni Grilli di Cortona, Edward Hardy, Javier Pardo Vega, and Giovanni Villadoro. "The QCD axion, precisely." In: *JHEP* 01 (2016), p. 034. DOI: 10.1007/JHEP01(2016)034. arXiv: 1511.02867 [hep-ph].

[127] Mark Srednicki. "Axion Couplings to Matter. 1. CP Conserving Parts." In: *Nucl. Phys. B* 260 (1985), pp. 689–700. DOI: 10.1016/0550-3213(85)90054-9.

[128] David J. E. Marsh. "Axion Cosmology." In: *Phys. Rept.* 643 (2016), pp. 1–79. DOI: 10.1016/j.physrep.2016.06.005. arXiv: 1510.07633 [astro-ph.CO].

[129] John Preskill, Mark B. Wise, and Frank Wilczek. "Cosmology of the Invisible Axion." In: *Phys. Lett. B* 120 (1983). Ed. by M. A. Srednicki, pp. 127–132. DOI: 10.1016/0370-2693(83)90637-8.

[130] L. F. Abbott and P. Sikivie. "A Cosmological Bound on the Invisible Axion." In: *Phys. Lett. B* 120 (1983). Ed. by M. A. Srednicki, pp. 133–136. DOI: 10.1016/0370-2693(83)90638-X.

[131] Michael Dine and Willy Fischler. "The Not So Harmless Axion." In: *Phys. Lett. B* 120 (1983). Ed. by M. A. Srednicki, pp. 137–141. DOI: 10.1016/0370-2693(83)90639-1.

[132] B. P. Abbott et al. "GW150914: First results from the search for binary black hole coalescence with Advanced LIGO." In: *Phys. Rev. D* 93.12 (2016), p. 122003. DOI: 10.1103/PhysRevD.93.122003. arXiv: 1602.03839 [gr-qc].

[133] B. P. Abbott et al. "GW150914: Implications for the stochastic gravitational wave background from binary black holes." In: *Phys. Rev. Lett.* 116.13 (2016), p. 131102. DOI: 10.1103/PhysRevLett.116.131102. arXiv: 1602.03847 [gr-qc].

[134] B. P. Abbott et al. "GW151226: Observation of Gravitational Waves from a 22-Solar-Mass Binary Black Hole Coalescence." In: *Phys. Rev. Lett.* 116.24 (2016), p. 241103. DOI: 10.1103/PhysRevLett.116.241103. arXiv: 1606.04855 [gr-qc].

[135] Bruce Allen. "The Stochastic gravity wave background: Sources and detection." In: *Les Houches School of Physics: Astrophysical Sources of Gravitational Radiation*. Apr. 1996, pp. 373–417. arXiv: gr-qc/9604033.

[136] Pierre Binetruy, Alejandro Bohe, Chiara Caprini, and Jean-Francois Dufaux. "Cosmological Backgrounds of Gravitational Waves and eLISA/NGO: Phase Transitions, Cosmic Strings and Other Sources." In: *JCAP* 06 (2012), p. 027. DOI: 10.1088/1475-7516/2012/06/027. arXiv: 1201.0983 [gr-qc].

[137] Chiara Caprini, Ruth Durrer, and Geraldine Servant. "Gravitational wave generation from bubble collisions in first-order phase transitions: An analytic approach." In: *Phys. Rev. D* 77 (2008), p. 124015. DOI: 10.1103/PhysRevD.77.124015. arXiv: 0711.2593 [astro-ph].

[138] John T. Giblin and Eric Thrane. "Estimates of maximum energy density of cosmological gravitational-wave backgrounds." In: *Phys. Rev. D* 90.10 (2014), p. 107502. DOI: 10.1103/PhysRevD.90.107502. arXiv: 1410.4779 [gr-qc].

[139] Juan Garcia-Bellido, Daniel G. Figueroa, and Alfonso Sastre. "A Gravitational Wave Background from Reheating after Hybrid Inflation." In: *Phys. Rev. D* 77 (2008), p. 043517. DOI: 10.1103/PhysRevD.77.043517. arXiv: 0707.0839 [hep-ph].

[140] Jean Francois Dufaux, Amanda Bergman, Gary N. Felder, Lev Kofman, and Jean-Philippe Uzan. "Theory and Numerics of Gravitational Waves from Preheating after Inflation." In: *Phys. Rev. D* 76 (2007), p. 123517. DOI: 10.1103/PhysRevD.76.123517. arXiv: 0707.0875 [astro-ph].

[141] Mustafa A. Amin, Mark P. Hertzberg, David I. Kaiser, and Johanna Karouby. "Nonperturbative Dynamics Of Reheating After Inflation: A Review." In: *Int. J. Mod. Phys. D* 24 (2014), p. 1530003. DOI: 10.1142/S0218271815300037. arXiv: 1410.3808 [hep-ph].

[142] Alexander Vilenkin. "Cosmic Strings and Domain Walls." In: *Phys. Rept.* 121 (1985), pp. 263–315. DOI: 10.1016/0370-1573(85)90033-X.

[143] M. B. Hindmarsh and T. W. B. Kibble. "Cosmic strings." In: *Rept. Prog. Phys.* 58 (1995), pp. 477–562. DOI: 10.1088/0034-4885/58/5/001. arXiv: hep-ph/9411342.

[144] Daniel Baumann, Paul J. Steinhardt, Keitaro Takahashi, and Kiyotomo Ichiki. "Gravitational Wave Spectrum Induced by Primordial Scalar Perturbations." In: *Phys. Rev. D* 76 (2007), p. 084019. DOI: 10.1103/PhysRevD.76.084019. arXiv: hep-th/0703290.

[145] Guillem Domènech. "Scalar Induced Gravitational Waves Review." In: *Universe* 7.11 (2021), p. 398. DOI: 10.3390/universe7110398. arXiv: 2109.01398 [gr-qc].

[146] D. J. Fixsen. "The Temperature of the Cosmic Microwave Background." In: *Astrophys. J.* 707 (2009), pp. 916–920. DOI: 10.1088/0004-637X/707/2/916. arXiv: 0911.1955 [astro-ph.CO].

[147] Marc Kamionkowski, Arthur Kosowsky, and Michael S. Turner. "Gravitational radiation from first order phase transitions." In: *Phys. Rev. D* 49 (1994), pp. 2837–2851. DOI: 10.1103/PhysRevD.49.2837. arXiv: astro-ph/9310044.

[148] Jeff Crowder and Neil J. Cornish. "Beyond LISA: Exploring future gravitational wave missions." In: *Phys. Rev. D* 72 (2005), p. 083005. DOI: 10.1103/PhysRevD.72.083005. arXiv: gr-qc/0506015.

[149] Alberto Sesana et al. "Unveiling the gravitational universe at μ-Hz frequencies." In: *Exper. Astron.* 51.3 (2021), pp. 1333–1383. DOI: 10.1007/s10686-021-09709-9. arXiv: 1908.11391 [astro-ph.IM].

[150] Gemma Janssen et al. "Gravitational wave astronomy with the SKA." In: *PoS* AASKA14 (2015). Ed. by Tyler L. Bourke et al., p. 037. DOI: 10.22323/1.215.0037. arXiv: 1501.00127 [astro-ph.IM].

[151] Nancy Aggarwal et al. "Challenges and Opportunities of Gravitational Wave Searches above 10 kHz." In: (Jan. 2025). arXiv: 2501.11723 [gr-qc].

[152] Moritz Breitbach, Joachim Kopp, Eric Madge, Toby Opferkuch, and Pedro Schwaller. "Dark, Cold, and Noisy: Constraining Secluded Hidden Sectors with Gravitational Waves." In: *JCAP* 07 (2019), p. 007. DOI: 10.1088/1475-7516/2019/07/007. arXiv: 1811.11175 [hep-ph].

[153] Kai Schmitz. "New Sensitivity Curves for Gravitational-Wave Signals from Cosmological Phase Transitions." In: *JHEP* 01 (2021), p. 097. DOI: 10.1007/JHEP01(2021)097. arXiv: 2002.04615 [hep-ph].

[154] Takeo Matsubara. "A New approach to quantum statistical mechanics." In: *Prog. Theor. Phys.* 14 (1955), pp. 351–378. DOI: 10.1143/PTP.14.351.

[155] J. I. Kapusta and Charles Gale. *Finite-temperature field theory: Principles and applications*. Cambridge Monographs on Mathematical Physics. Cambridge University Press, 2011. ISBN: 978-0-521-17322-3, 978-0-521-82082-0, 978-0-511-22280-1. DOI: 10.1017/CBO9780511535130.

[156] Ryogo Kubo. "Statistical mechanical theory of irreversible processes. 1. General theory and simple applications in magnetic and conduction problems." In: *J. Phys. Soc. Jap.* 12 (1957), pp. 570–586. DOI: 10.1143/JPSJ.12.570.

[157] Paul C. Martin and Julian Schwinger. "Theory of Many-Particle Systems. I." In: *Phys. Rev.* 115 (6 1959), pp. 1342–1373. DOI: 10.1103/PhysRev.115.1342. URL: https://link.aps.org/doi/10.1103/PhysRev.115.1342.

[158] L. V. Keldysh. "Diagram technique for nonequilibrium processes." In: *Zh. Eksp. Teor. Fiz.* 47 (1964), pp. 1515–1527. DOI: 10.1142/9789811279461_0007.

[159] Mariano Quiros. "Finite temperature field theory and phase transitions." In: *ICTP Summer School in High-Energy Physics and Cosmology*. Jan. 1999, pp. 187–259. arXiv: hep-ph/9901312.

[160] Steven Weinberg. *The quantum theory of fields. Vol. 2: Modern applications*. Cambridge University Press, Aug. 2013. ISBN: 978-1-139-63247-8, 978-0-521-67054-8, 978-0-521-55002-4. DOI: 10.1017/CBO9781139644174.

[161] Sidney R. Coleman and Erick J. Weinberg. "Radiative Corrections as the Origin of Spontaneous Symmetry Breaking." In: *Phys. Rev. D* 7 (1973), pp. 1888–1910. DOI: 10.1103/PhysRevD.7.1888.

[162] K. Farakos, K. Kajantie, K. Rummukainen, and Mikhail E. Shaposhnikov. "3-d physics and the electroweak phase transition: A Framework for lattice Monte Carlo analysis." In: *Nucl. Phys. B* 442 (1995), pp. 317–363. DOI: 10.1016/0550-3213(95)80129-4. arXiv: hep-lat/9412091.

[163] Andreas Ekstedt, Oliver Gould, and Johan Löfgren. "Radiative first-order phase transitions to next-to-next-to-leading order." In: *Phys. Rev. D* 106.3 (2022), p. 036012. DOI: 10.1103/PhysRevD.106.036012. arXiv: 2205.07241 [hep-ph].

[164] Oliver Gould and Tuomas V. I. Tenkanen. "Perturbative effective field theory expansions for cosmological phase transitions." In: *JHEP* 01 (2024), p. 048. DOI: 10.1007/JHEP01(2024)048. arXiv: 2309.01672 [hep-ph].

[165] Cedric Delaunay, Christophe Grojean, and James D. Wells. "Dynamics of Non-renormalizable Electroweak Symmetry Breaking." In: *JHEP* 04 (2008), p. 029. DOI: 10.1088/1126-6708/2008/04/029. arXiv: 0711.2511 [hep-ph].

[166] K. Kajantie, M. Laine, K. Rummukainen, and Mikhail E. Shaposhnikov. "Generic rules for high temperature dimensional reduction and their application to the standard model." In: *Nucl. Phys. B* 458 (1996), pp. 90–136. DOI: 10.1016/0550-3213(95)00549-8. arXiv: hep-ph/9508379.

[167] Rajesh R. Parwani. "Resummation in a hot scalar field theory." In: *Phys. Rev. D* 45 (1992). [Erratum: Phys.Rev.D 48, 5965 (1993)], p. 4695. DOI: 10.1103/PhysRevD.45.4695. arXiv: hep-ph/9204216.

[168] Peter Brockway Arnold and Olivier Espinosa. "The Effective potential and first order phase transitions: Beyond leading-order." In: *Phys. Rev. D* 47 (1993). [Erratum: Phys.Rev.D 50, 6662 (1994)], p. 3546. DOI: 10.1103/PhysRevD.47.3546. arXiv: hep-ph/9212235.

[169] David Curtin, Patrick Meade, and Harikrishnan Ramani. "Thermal Resummation and Phase Transitions." In: *Eur. Phys. J. C* 78.9 (2018), p. 787. DOI: 10.1140/epjc/s10052-018-6268-0. arXiv: 1612.00466 [hep-ph].

[170] M. E. Carrington. "Effective potential at finite temperature in the standard model." In: *Phys. Rev. D* 45 (8 1992), pp. 2933–2944. DOI: 10.1103/PhysRevD.45.2933. URL: https://link.aps.org/doi/10.1103/PhysRevD.45.2933.

[171] Lauri Niemi, Philipp Schicho, and Tuomas V. I. Tenkanen. "Singlet-assisted electroweak phase transition at two loops." In: *Phys. Rev. D* 103.11 (2021), p. 115035. DOI: 10.1103/PhysRevD.103.115035. arXiv: 2103.07467 [hep-ph].

[172] Fei Gao and Isabel M. Oldengott. "Cosmology Meets Functional QCD: First-Order Cosmic QCD Transition Induced by Large Lepton Asymmetries." In: *Phys. Rev. Lett.* 128.13 (2022), p. 131301. DOI: 10.1103/PhysRevLett.128.131301. arXiv: 2106.11991 [hep-ph].

[173] Fatih Ertas, Felix Kahlhoefer, and Carlo Tasillo. "Turn up the volume: listening to phase transitions in hot dark sectors." In: *JCAP* 02.02 (2022), p. 014. DOI: 10.1088/1475-7516/2022/02/014. arXiv: 2109.06208 [astro-ph.CO].

[174] J. S. Langer. "Statistical theory of the decay of metastable states." In: *Annals Phys.* 54 (1969), pp. 258–275. DOI: 10.1016/0003-4916(69)90153-5.

[175] Sidney Coleman. "Erratum: Fate of the false vacuum: semiclassical theory." In: *Phys. Rev. D* 16 (4 1977), pp. 1248–1248. DOI: 10.1103/PhysRevD.16.1248. URL: https://link.aps.org/doi/10.1103/PhysRevD.16.1248.

[176] Andrei D. Linde. "Fate of the False Vacuum at Finite Temperature: Theory and Applications." In: *Phys. Lett. B* 100 (1981), pp. 37–40. DOI: 10.1016/0370-2693(81)90281-1.

[177] Andrei D. Linde. "Decay of the False Vacuum at Finite Temperature." In: *Nucl. Phys. B* 216 (1983). [Erratum: Nucl.Phys.B 223, 544 (1983)], p. 421. DOI: 10.1016/0550-3213(83)90072-X.

[178] Ian Affleck. "Quantum Statistical Metastability." In: *Phys. Rev. Lett.* 46 (1981), p. 388. DOI: 10.1103/PhysRevLett.46.388.

[179] Andreas Ekstedt. "Bubble nucleation to all orders." In: *JHEP* 08 (2022), p. 115. DOI: 10.1007/JHEP08(2022)115. arXiv: 2201.07331 [hep-ph].

[180] Andreas Ekstedt, Oliver Gould, and Joonas Hirvonen. "BubbleDet: a Python package to compute functional determinants for bubble nucleation." In: *JHEP* 12 (2023), p. 056. DOI: 10.1007/JHEP12(2023)056. arXiv: 2308.15652 [hep-ph].

[181] Andreas Ekstedt. "Higher-order corrections to the bubble-nucleation rate at finite temperature." In: *Eur. Phys. J. C* 82.2 (2022), p. 173. DOI: 10.1140/epjc/s10052-022-10130-5. arXiv: 2104.11804 [hep-ph].

[182] Oliver Gould and Joonas Hirvonen. "Effective field theory approach to thermal bubble nucleation." In: *Phys. Rev. D* 104.9 (2021), p. 096015. DOI: 10.1103/PhysRevD.104.096015. arXiv: 2108.04377 [hep-ph].

[183] Maciej Kierkla, Philipp Schicho, Bogumila Swiezewska, Tuomas V. I. Tenkanen, and Jorinde van de Vis. "Finite-temperature bubble nucleation with shifting scale hierarchies." In: (Mar. 2025). arXiv: 2503.13597 [hep-ph].

[184] Curtis G. Callan Jr. and Sidney R. Coleman. "The Fate of the False Vacuum. 2. First Quantum Corrections." In: *Phys. Rev. D* 16 (1977), pp. 1762–1768. DOI: 10.1103/PhysRevD.16.1762.

[185] Carroll L. Wainwright. "CosmoTransitions: Computing Cosmological Phase Transition Temperatures and Bubble Profiles with Multiple Fields." In: *Comput. Phys. Commun.* 183 (2012), pp. 2006–2013. DOI: 10.1016/j.cpc.2012.04.004. arXiv: 1109.4189 [hep-ph].

[186] John Ellis, Marek Lewicki, and José Miguel No. "On the Maximal Strength of a First-Order Electroweak Phase Transition and its Gravitational Wave Signal." In: *JCAP* 04 (2019), p. 003. DOI: 10.1088/1475-7516/2019/04/003. arXiv: 1809.08242 [hep-ph].

[187] Vinod K. S. Shante and Scott Kirkpatrick. "An introduction to percolation theory†." In: *Advances in Physics* 20.85 (May 1971), pp. 325–357. DOI: 10.1080/00018737100101261.

[188] Alan H. Guth and S. H. H. Tye. "Phase Transitions and Magnetic Monopole Production in the Very Early Universe." In: *Phys. Rev. Lett.* 44 (10 1980), pp. 631–635. DOI: 10.1103/PhysRevLett.44.631. URL: https://link.aps.org/doi/10.1103/PhysRevLett.44.631.

[189] Alan H. Guth and Erick J. Weinberg. "Cosmological consequences of a first-order phase transition in the SU_5 grand unified model." In: *Phys. Rev. D* 23 (4 1981), pp. 876–885. DOI: 10.1103/PhysRevD.23.876. URL: https://link.aps.org/doi/10.1103/PhysRevD.23.876.

[190] Jose R. Espinosa, Thomas Konstandin, Jose M. No, and Geraldine Servant. "Energy Budget of Cosmological First-order Phase Transitions." In: *JCAP* 06 (2010), p. 028. DOI: 10.1088/1475-7516/2010/06/028. arXiv: 1004.4187 [hep-ph].

[191] Chiara Caprini et al. "Detecting gravitational waves from cosmological phase transitions with LISA: an update." In: *JCAP* 03 (2020), p. 024. DOI: 10.1088/1475-7516/2020/03/024. arXiv: 1910.13125 [astro-ph.CO].

[192] Mark Hindmarsh, Stephan J. Huber, Kari Rummukainen, and David J. Weir. "Shape of the acoustic gravitational wave power spectrum from a first order phase transition." In: *Phys. Rev. D* 96.10 (2017). [Erratum: Phys.Rev.D 101, 089902 (2020)], p. 103520. DOI: 10.1103/PhysRevD.96.103520. arXiv: 1704.05871 [astro-ph.CO].

[193] Luca Marzola, Antonio Racioppi, and Ville Vaskonen. "Phase transition and gravitational wave phenomenology of scalar conformal extensions of the Standard Model." In: *Eur. Phys. J. C* 77.7 (2017), p. 484. DOI: 10.1140/epjc/s10052-017-4996-1. arXiv: 1704.01034 [hep-ph].

[194] Bao-Hua Liu, Larry D. McLerran, and Neil Turok. "Bubble nucleation and growth at a baryon number producing electroweak phase transition." In: *Phys. Rev. D* 46 (1992), pp. 2668–2688. DOI: 10.1103/PhysRevD.46.2668.

[195] Michael Dine, Robert G. Leigh, Patrick Y. Huet, Andrei D. Linde, and Dmitri A. Linde. "Towards the theory of the electroweak phase transition." In: *Phys. Rev. D* 46 (1992), pp. 550–571. DOI: 10.1103/PhysRevD.46.550. arXiv: hep-ph/9203203.

[196] Guy D. Moore and Tomislav Prokopec. "How fast can the wall move? A Study of the electroweak phase transition dynamics." In: *Phys. Rev. D* 52 (1995), pp. 7182–7204. DOI: 10.1103/PhysRevD.52.7182. arXiv: hep-ph/9506475.

[197] Guy D. Moore and Tomislav Prokopec. "Bubble wall velocity in a first order electroweak phase transition." In: *Phys. Rev. Lett.* 75 (1995), pp. 777–780. DOI: 10.1103/PhysRevLett.75.777. arXiv: hep-ph/9503296.

[198] Thomas Konstandin, Germano Nardini, and Ingo Rues. "From Boltzmann equations to steady wall velocities." In: *JCAP* 09 (2014), p. 028. DOI: 10.1088/1475-7516/2014/09/028. arXiv: 1407.3132 [hep-ph].

[199] Jonathan Kozaczuk. "Bubble Expansion and the Viability of Singlet-Driven Electroweak Baryogenesis." In: *JHEP* 10 (2015), p. 135. DOI: 10.1007/JHEP10(2015)135. arXiv: 1506.04741 [hep-ph].

[200] Stefania De Curtis, Luigi Delle Rose, Andrea Guiggiani, Ángel Gil Muyor, and Giuliano Panico. "Bubble wall dynamics at the electroweak phase transition." In: *JHEP* 03 (2022), p. 163. DOI: 10.1007/JHEP03(2022)163. arXiv: 2201.08220 [hep-ph].

[201] Benoit Laurent and James M. Cline. "Fluid equations for fast-moving electroweak bubble walls." In: *Phys. Rev. D* 102.6 (2020), p. 063516. DOI: 10.1103/PhysRevD.102.063516. arXiv: 2007.10935 [hep-ph].

[202] Glauber C. Dorsch, Stephan J. Huber, and Thomas Konstandin. "A sonic boom in bubble wall friction." In: *JCAP* 04.04 (2022), p. 010. DOI: 10.1088/1475-7516/2022/04/010. arXiv: 2112.12548 [hep-ph].

[203] Benoit Laurent and James M. Cline. "First principles determination of bubble wall velocity." In: *Phys. Rev. D* 106.2 (2022), p. 023501. DOI: 10.1103/PhysRevD.106.023501. arXiv: 2204.13120 [hep-ph].

[204] Shyam Balaji, Michael Spannowsky, and Carlos Tamarit. "Cosmological bubble friction in local equilibrium." In: *JCAP* 03 (2021), p. 051. DOI: 10.1088/1475-7516/2021/03/051. arXiv: 2010.08013 [hep-ph].

[205] Wen-Yuan Ai, Bjorn Garbrecht, and Carlos Tamarit. "Bubble wall velocities in local equilibrium." In: (Sept. 2021). arXiv: 2109.13710 [hep-ph].

[206] Siyu Jiang, Fa Peng Huang, and Xiao Wang. "Bubble wall velocity during electroweak phase transition in the inert doublet model." In: *Phys. Rev. D* 107.9 (2023), p. 095005. DOI: 10.1103/PhysRevD.107.095005. arXiv: 2211.13142 [hep-ph].

[207] Wen-Yuan Ai, Benoit Laurent, and Jorinde van de Vis. "Model-independent bubble wall velocities in local thermal equilibrium." In: *JCAP* 07 (2023), p. 002. DOI: 10.1088/1475-7516/2023/07/002. arXiv: 2303.10171 [astro-ph.CO].

[208] Mikel Sanchez-Garitaonandia and Jorinde van de Vis. "Prediction of the bubble wall velocity for a large jump in degrees of freedom." In: *Phys. Rev. D* 110.2 (2024), p. 023509. DOI: 10.1103/PhysRevD.110.023509. arXiv: 2312.09964 [hep-ph].

[209] Andreas Ekstedt, Oliver Gould, Joonas Hirvonen, Benoit Laurent, Lauri Niemi, Philipp Schicho, and Jorinde van de Vis. "How fast does the WallGo? A package for computing wall velocities in first-order phase transitions." In: (Nov. 2024). arXiv: 2411.04970 [hep-ph].

[210] K. Enqvist, J. Ignatius, K. Kajantie, and K. Rummukainen. "Nucleation and bubble growth in a first-order cosmological electroweak phase transition." In: *Phys. Rev. D* 45 (10 1992), pp. 3415–3428. DOI: 10.1103/PhysRevD.45.3415. URL: https://link.aps.org/doi/10.1103/PhysRevD.45.3415.

[211] Marek Lewicki and Ville Vaskonen. "Gravitational waves from bubble collisions and fluid motion in strongly supercooled phase transitions." In: *Eur. Phys. J. C* 83.2 (2023), p. 109. DOI: 10.1140/epjc/s10052-023-11241-3. arXiv: 2208.11697 [astro-ph.CO].

[212] Alberto Roper Pol, Sayan Mandal, Axel Brandenburg, Tina Kahniashvili, and Arthur Kosowsky. "Numerical simulations of gravitational waves from early-universe turbulence." In: *Phys. Rev. D* 102.8 (2020), p. 083512. DOI: 10.1103/PhysRevD.102.083512. arXiv: 1903.08585 [astro-ph.CO].

[213] Tina Kahniashvili, Axel Brandenburg, Grigol Gogoberidze, Sayan Mandal, and Alberto Roper Pol. "Circular polarization of gravitational waves from early-Universe helical turbulence." In: *Phys. Rev. Res.* 3.1 (2021), p. 013193. DOI: 10.1103/PhysRevResearch.3.013193. arXiv: 2011.05556 [astro-ph.CO].

[214] Alberto Roper Pol, Sayan Mandal, Axel Brandenburg, and Tina Kahniashvili. "Polarization of gravitational waves from helical MHD turbulent sources." In: *JCAP* 04.04 (2022), p. 019. DOI: 10.1088/1475-7516/2022/04/019. arXiv: 2107.05356 [gr-qc].

[215] Mark Hindmarsh, Stephan J. Huber, Kari Rummukainen, and David J. Weir. "Gravitational waves from the sound of a first order phase transition." In: *Phys. Rev. Lett.* 112 (2014), p. 041301. DOI: 10.1103/PhysRevLett.112.041301. arXiv: 1304.2433 [hep-ph].

[216] Mark Hindmarsh, Stephan J. Huber, Kari Rummukainen, and David J. Weir. "Numerical simulations of acoustically generated gravitational waves at a first order phase transition." In: *Phys. Rev. D* 92.12 (2015), p. 123009. DOI: 10.1103/PhysRevD.92.123009. arXiv: 1504.03291 [astro-ph.CO].

[217] Mark Hindmarsh. "Sound shell model for acoustic gravitational wave production at a first-order phase transition in the early Universe." In: *Phys. Rev. Lett.* 120.7 (2018), p. 071301. DOI: 10.1103/PhysRevLett.120.071301. arXiv: 1608.04735 [astro-ph.CO].

[218] Mark Hindmarsh and Mulham Hijazi. "Gravitational waves from first order cosmological phase transitions in the Sound Shell Model." In: *JCAP* 12 (2019), p. 062. DOI: 10.1088/1475-7516/2019/12/062. arXiv: 1909.10040 [astro-ph.CO].

[219] Ryusuke Jinno, Thomas Konstandin, and Henrique Rubira. "A hybrid simulation of gravitational wave production in first-order phase transitions." In: *JCAP* 04 (2021), p. 014. DOI: 10.1088/1475-7516/2021/04/014. arXiv: 2010.00971 [astro-ph.CO].

[220] Ryusuke Jinno, Thomas Konstandin, Henrique Rubira, and Isak Stomberg. "Higgsless simulations of cosmological phase transitions and gravitational waves." In: *JCAP* 02 (2023), p. 011. DOI: 10.1088/1475-7516/2023/02/011. arXiv: 2209.04369 [astro-ph.CO].

[221] Alberto Roper Pol, Simona Procacci, and Chiara Caprini. "Characterization of the gravitational wave spectrum from sound waves within the sound shell model." In:

Phys. Rev. D 109.6 (2024), p. 063531. DOI: 10.1103/PhysRevD.109.063531. arXiv: 2308.12943 [gr-qc].

[222] Ramkishor Sharma, Jani Dahl, Axel Brandenburg, and Mark Hindmarsh. "Shallow relic gravitational wave spectrum with acoustic peak." In: *JCAP* 12 (2023), p. 042. DOI: 10.1088/1475-7516/2023/12/042. arXiv: 2308.12916 [gr-qc].

[223] John Ellis, Marek Lewicki, José Miguel No, and Ville Vaskonen. "Gravitational wave energy budget in strongly supercooled phase transitions." In: *JCAP* 06 (2019), p. 024. DOI: 10.1088/1475-7516/2019/06/024. arXiv: 1903.09642 [hep-ph].

[224] John Ellis, Marek Lewicki, and José Miguel No. "Gravitational waves from first-order cosmological phase transitions: lifetime of the sound wave source." In: *JCAP* 07 (2020), p. 050. DOI: 10.1088/1475-7516/2020/07/050. arXiv: 2003.07360 [hep-ph].

[225] Huai-Ke Guo, Kuver Sinha, Daniel Vagie, and Graham White. "Phase Transitions in an Expanding Universe: Stochastic Gravitational Waves in Standard and Non-Standard Histories." In: *JCAP* 01 (2021), p. 001. DOI: 10.1088/1475-7516/2021/01/001. arXiv: 2007.08537 [hep-ph].

[226] Krzysztof A. Meissner and Hermann Nicolai. "Conformal Symmetry and the Standard Model." In: *Phys. Lett. B* 648 (2007), pp. 312–317. DOI: 10.1016/j.physletb.2007.03.023. arXiv: hep-th/0612165.

[227] Robert Foot, Archil Kobakhidze, Kristian L. McDonald, and Raymond R. Volkas. "A Solution to the hierarchy problem from an almost decoupled hidden sector within a classically scale invariant theory." In: *Phys. Rev. D* 77 (2008), p. 035006. DOI: 10.1103/PhysRevD.77.035006. arXiv: 0709.2750 [hep-ph].

[228] J. R. Espinosa, T. Konstandin, J. M. No, and M. Quiros. "Some Cosmological Implications of Hidden Sectors." In: *Phys. Rev. D* 78 (2008), p. 123528. DOI: 10.1103/PhysRevD.78.123528. arXiv: 0809.3215 [hep-ph].

[229] Satoshi Iso, Nobuchika Okada, and Yuta Orikasa. "The minimal B-L model naturally realized at TeV scale." In: *Phys. Rev. D* 80 (2009), p. 115007. DOI: 10.1103/PhysRevD.80.115007. arXiv: 0909.0128 [hep-ph].

[230] Satoshi Iso and Yuta Orikasa. "TeV Scale B-L model with a flat Higgs potential at the Planck scale: In view of the hierarchy problem." In: *PTEP* 2013 (2013), 023B08. DOI: 10.1093/ptep/pts099. arXiv: 1210.2848 [hep-ph].

[231] Arsham Farzinnia, Hong-Jian He, and Jing Ren. "Natural Electroweak Symmetry Breaking from Scale Invariant Higgs Mechanism." In: *Phys. Lett. B* 727 (2013), pp. 141–150. DOI: 10.1016/j.physletb.2013.09.060. arXiv: 1308.0295 [hep-ph].

[232] Christoph Englert, Joerg Jaeckel, V. V. Khoze, and Michael Spannowsky. "Emergence of the Electroweak Scale through the Higgs Portal." In: *JHEP* 04 (2013), p. 060. DOI: 10.1007/JHEP04(2013)060. arXiv: 1301.4224 [hep-ph].

[233] Michio Hashimoto, Satoshi Iso, and Yuta Orikasa. "Radiative symmetry breaking at the Fermi scale and flat potential at the Planck scale." In: *Phys. Rev. D* 89.1 (2014), p. 016019. DOI: 10.1103/PhysRevD.89.016019. arXiv: 1310.4304 [hep-ph].

[234] Valentin V. Khoze, Christopher McCabe, and Gunnar Ro. "Higgs vacuum stability from the dark matter portal." In: *JHEP* 08 (2014), p. 026. DOI: 10.1007/JHEP08(2014)026. arXiv: 1403.4953 [hep-ph].

[235] Taeil Hur and P. Ko. "Scale invariant extension of the standard model with strongly interacting hidden sector." In: *Phys. Rev. Lett.* 106 (2011), p. 141802. DOI: 10.1103/PhysRevLett.106.141802. arXiv: 1103.2571 [hep-ph].

[236] Matti Heikinheimo, Antonio Racioppi, Martti Raidal, Christian Spethmann, and Kimmo Tuominen. "Physical Naturalness and Dynamical Breaking of Classical Scale Invariance." In: *Mod. Phys. Lett. A* 29 (2014), p. 1450077. DOI: 10.1142/S0217732314500771. arXiv: 1304.7006 [hep-ph].

[237] Martin Holthausen, Jisuke Kubo, Kher Sham Lim, and Manfred Lindner. "Electroweak and Conformal Symmetry Breaking by a Strongly Coupled Hidden Sector." In: *JHEP* 12 (2013), p. 076. DOI: 10.1007/JHEP12(2013)076. arXiv: 1310.4423 [hep-ph].

[238] Jisuke Kubo, Kher Sham Lim, and Manfred Lindner. "Electroweak Symmetry Breaking via QCD." In: *Phys. Rev. Lett.* 113 (2014), p. 091604. DOI: 10.1103/PhysRevLett.113.091604. arXiv: 1403.4262 [hep-ph].

[239] Yoshitaka Ametani, Mayumi Aoki, Hiromitsu Goto, and Jisuke Kubo. "Nambu-Goldstone Dark Matter in a Scale Invariant Bright Hidden Sector." In: *Phys. Rev. D* 91.11 (2015), p. 115007. DOI: 10.1103/PhysRevD.91.115007. arXiv: 1505.00128 [hep-ph].

[240] Jisuke Kubo and Masatoshi Yamada. "Scale and electroweak first-order phase transitions." In: *PTEP* 2015.9 (2015), 093B01. DOI: 10.1093/ptep/ptv114. arXiv: 1506.06460 [hep-ph].

[241] Hisaki Hatanaka, Dong-Won Jung, and Pyungwon Ko. "AdS/QCD approach to the scale-invariant extension of the standard model with a strongly interacting hidden sector." In: *JHEP* 08 (2016), p. 094. DOI: 10.1007/JHEP08(2016)094. arXiv: 1606.02969 [hep-ph].

[242] Pietro Baratella, Alex Pomarol, and Fabrizio Rompineve. "The Supercooled Universe." In: *JHEP* 03 (2019), p. 100. DOI: 10.1007/JHEP03(2019)100. arXiv: 1812.06996 [hep-ph].

[243] Carlo Marzo, Luca Marzola, and Ville Vaskonen. "Phase transition and vacuum stability in the classically conformal B–L model." In: *Eur. Phys. J. C* 79.7 (2019), p. 601. DOI: 10.1140/epjc/s10052-019-7076-x. arXiv: 1811.11169 [hep-ph].

[244] John Ellis, Marek Lewicki, and Ville Vaskonen. "Updated predictions for gravitational waves produced in a strongly supercooled phase transition." In: *JCAP* 11 (2020), p. 020. DOI: 10.1088/1475-7516/2020/11/020. arXiv: 2007.15586 [astro-ph.CO].

[245] Thede de Boer, Manfred Lindner, and Andreas Trautner. "Electroweak hierarchy from conformal and custodial symmetry." In: (July 2024). arXiv: 2407.15920 [hep-ph].

[246] Maciej Kierkla, Alexandros Karam, and Bogumila Swiezewska. "Conformal model for gravitational waves and dark matter: A status update." In: *JHEP* 03 (Oct. 2023), p. 007. DOI: 10.1007/JHEP03(2023)007. arXiv: 2210.07075 [astro-ph.CO].

[247] Maciej Kierkla, Bogumila Swiezewska, Tuomas V. I. Tenkanen, and Jorinde van de Vis. "Gravitational waves from supercooled phase transitions: dimensional transmutation meets dimensional reduction." In: *JHEP* 02 (2024), p. 234. DOI: 10.1007/JHEP02(2024)234. arXiv: 2312.12413 [hep-ph].

[248] João Gonçalves, Danny Marfatia, António P. Morais, and Roman Pasechnik. "Gravitational waves from supercooled phase transitions in conformal Majoron models of neutrino mass." In: *JHEP* 02 (2025), p. 110. DOI: 10.1007/JHEP02(2025)110. arXiv: 2412.02645 [hep-ph].

[249] João Gonçalves, Danny Marfatia, António P. Morais, and Roman Pasechnik. "Supercooled phase transitions in conformal dark sectors explain NANOGrav data." In: (Jan. 2025). arXiv: 2501.11619 [hep-ph].

[250] Sowmiya Balan, Torsten Bringmann, Felix Kahlhoefer, Jonas Matuszak, and Carlo Tasillo. "Sub-GeV dark matter and nano-Hertz gravitational waves from a classically conformal dark sector." In: (Feb. 2025). arXiv: 2502.19478 [hep-ph].

[251] William A Bardeen. *On naturalness in the standard model*. Tech. rep. Batavia, IL: FERMILAB, 1995. URL: https://cds.cern.ch/record/295811.

[252] Thomas Konstandin and Geraldine Servant. "Cosmological Consequences of Nearly Conformal Dynamics at the TeV scale." In: *JCAP* 12 (2011), p. 009. DOI: 10.1088/1475-7516/2011/12/009. arXiv: 1104.4791 [hep-ph].

[253] Thomas Konstandin and Geraldine Servant. "Natural Cold Baryogenesis from Strongly Interacting Electroweak Symmetry Breaking." In: *JCAP* 07 (2011), p. 024. DOI: 10.1088/1475-7516/2011/07/024. arXiv: 1104.4793 [hep-ph].

[254] Geraldine Servant. "Baryogenesis from Strong CP Violation and the QCD Axion." In: *Phys. Rev. Lett.* 113.17 (2014), p. 171803. DOI: 10.1103/PhysRevLett.113.171803. arXiv: 1407.0030 [hep-ph].

[255] Valentin V. Khoze and Gunnar Ro. "Leptogenesis and Neutrino Oscillations in the Classically Conformal Standard Model with the Higgs Portal." In: *JHEP* 10 (2013), p. 075. DOI: 10.1007/JHEP10(2013)075. arXiv: 1307.3764 [hep-ph].

[256] Djuna Croon, Jessica N. Howard, Seyda Ipek, and Timothy M. P. Tait. "QCD baryogenesis." In: *Phys. Rev. D* 101.5 (2020), p. 055042. DOI: 10.1103/PhysRevD.101.055042. arXiv: 1911.01432 [hep-ph].

[257] Aleksandr Azatov, Miguel Vanvlasselaer, and Wen Yin. "Baryogenesis via relativistic bubble walls." In: *JHEP* 10 (2021), p. 043. DOI: 10.1007/JHEP10(2021)043. arXiv: 2106.14913 [hep-ph].

[258] Iason Baldes, Simone Blasi, Alberto Mariotti, Alexander Sevrin, and Kevin Turbang. "Baryogenesis via relativistic bubble expansion." In: *Phys. Rev. D* 104.11 (2021), p. 115029. DOI: 10.1103/PhysRevD.104.115029. arXiv: 2106.15602 [hep-ph].

[259] Peisi Huang and Ke-Pan Xie. "Leptogenesis triggered by a first-order phase transition." In: *JHEP* 09 (2022), p. 052. DOI: 10.1007/JHEP09(2022)052. arXiv: 2206.04691 [hep-ph].

[260] Arnab Dasgupta, P. S. Bhupal Dev, Anish Ghoshal, and Anupam Mazumdar. "Gravitational wave pathway to testable leptogenesis." In: *Phys. Rev. D* 106.7 (2022), p. 075027. DOI: 10.1103/PhysRevD.106.075027. arXiv: 2206.07032 [hep-ph].

[261] Eung Jin Chun, Tomasz P. Dutka, Tae Hyun Jung, Xander Nagels, and Miguel Vanvlasselaer. "Bubble-assisted leptogenesis." In: *JHEP* 09 (2023), p. 164. DOI: 10.1007/JHEP09(2023)164. arXiv: 2305.10759 [hep-ph].

[262] Thomas Hambye and Alessandro Strumia. "Dynamical generation of the weak and Dark Matter scale." In: *Phys. Rev. D* 88 (2013), p. 055022. DOI: 10.1103/PhysRevD.88.055022. arXiv: 1306.2329 [hep-ph].

[263] Christopher D. Carone and Raymundo Ramos. "Classical scale-invariance, the electroweak scale and vector dark matter." In: *Phys. Rev. D* 88 (2013), p. 055020. DOI: 10.1103/PhysRevD.88.055020. arXiv: 1307.8428 [hep-ph].

[264] Valentin V. Khoze. "Inflation and Dark Matter in the Higgs Portal of Classically Scale Invariant Standard Model." In: *JHEP* 11 (2013), p. 215. DOI: 10.1007/JHEP11(2013)215. arXiv: 1308.6338 [hep-ph].

[265] T. G. Steele, Zhi-Wei Wang, D. Contreras, and R. B. Mann. "Viable dark matter via radiative symmetry breaking in a scalar singlet Higgs portal extension of the standard model." In: *Phys. Rev. Lett.* 112.17 (2014), p. 171602. DOI: 10.1103/PhysRevLett.112.171602. arXiv: 1310.1960 [hep-ph].

[266] Sanjin Benic and Branimir Radovcic. "Majorana dark matter in a classically scale invariant model." In: *JHEP* 01 (2015), p. 143. DOI: 10.1007/JHEP01(2015)143. arXiv: 1409.5776 [hep-ph].

[267] Jun Guo, Zhaofeng Kang, P. Ko, and Yuta Orikasa. "Accidental dark matter: Case in the scale invariant local B-L model." In: *Phys. Rev. D* 91.11 (2015), p. 115017. DOI: 10.1103/PhysRevD.91.115017. arXiv: 1502.00508 [hep-ph].

[268] Satsuki Oda, Nobuchika Okada, and Dai-suke Takahashi. "Right-handed neutrino dark matter in the classically conformal U(1)' extended standard model." In: *Phys. Rev. D* 96.9 (2017), p. 095032. DOI: 10.1103/PhysRevD.96.095032. arXiv: 1704.05023 [hep-ph].

[269] Thomas Hambye, Alessandro Strumia, and Daniele Teresi. "Super-cool Dark Matter." In: *JHEP* 08 (2018), p. 188. DOI: 10.1007/JHEP08(2018)188. arXiv: 1805.01473 [hep-ph].

[270] Aleksandr Azatov, Miguel Vanvlasselaer, and Wen Yin. "Dark Matter production from relativistic bubble walls." In: *JHEP* 03 (2021), p. 288. DOI: 10.1007/JHEP03(2021)288. arXiv: 2101.05721 [hep-ph].

[271] Iason Baldes, Yann Gouttenoire, Filippo Sala, and Géraldine Servant. "Supercool composite Dark Matter beyond 100 TeV." In: *JHEP* 07 (2022), p. 084. DOI: 10.1007/JHEP07(2022)084. arXiv: 2110.13926 [hep-ph].

[272] Kiyoharu Kawana. "Cosmology of a supercooled universe." In: *Phys. Rev. D* 105.10 (2022), p. 103515. DOI: 10.1103/PhysRevD.105.103515. arXiv: 2201.00560 [hep-ph].

[273] Valentin V. Khoze and Daniel L. Milne. "Gravitational waves and dark matter from classical scale invariance." In: *Phys. Rev. D* 107.9 (2023), p. 095012. DOI: 10.1103/PhysRevD.107.095012. arXiv: 2212.04784 [hep-ph].

[274] Mads T. Frandsen, Mattias E. Thing, Matti Heikinheimo, Kimmo Tuominen, and Martin Rosenlyst. *Vector dark matter in supercooled Higgs portal models*. Dec. 2022. arXiv: 2301.00041 [hep-ph].

[275] Aleksandr Azatov, Xander Nagels, Miguel Vanvlasselaer, and Wen Yin. "Populating secluded dark sector with ultra-relativistic bubbles." In: (June 2024). arXiv: 2406.12554 [hep-ph].

[276] Ryusuke Jinno and Masahiro Takimoto. "Probing a classically conformal B-L model with gravitational waves." In: *Phys. Rev. D* 95.1 (2017), p. 015020. DOI: 10.1103/PhysRevD.95.015020. arXiv: 1604.05035 [hep-ph].

[277] Jisuke Kubo and Masatoshi Yamada. "Scale genesis and gravitational wave in a classically scale invariant extension of the standard model." In: *JCAP* 12 (2016), p. 001. DOI: 10.1088/1475-7516/2016/12/001. arXiv: 1610.02241 [hep-ph].

[278] Mayumi Aoki and Jisuke Kubo. "Gravitational waves from chiral phase transition in a conformally extended standard model." In: *JCAP* 04 (2020), p. 001. DOI: 10.1088/1475-7516/2020/04/001. arXiv: 1910.05025 [hep-ph].

[279] Tomislav Prokopec, Jonas Rezacek, and Bogumiła Świeżewska. "Gravitational waves from conformal symmetry breaking." In: *JCAP* 02 (2019), p. 009. DOI: 10.1088/1475-7516/2019/02/009. arXiv: 1809.11129 [hep-ph].

[280] Xiao Wang, Fa Peng Huang, and Xinmin Zhang. "Phase transition dynamics and gravitational wave spectra of strong first-order phase transition in supercooled universe." In: *JCAP* 05 (2020), p. 045. DOI: 10.1088/1475-7516/2020/05/045. arXiv: 2003.08892 [hep-ph].

[281] Edward Witten. "Cosmological Consequences of a Light Higgs Boson." In: *Nucl. Phys. B* 177 (1981), pp. 477–488. DOI: 10.1016/0550-3213(81)90182-6.

[282] Benedict von Harling and Geraldine Servant. "QCD-induced Electroweak Phase Transition." In: *JHEP* 01 (2018), p. 159. DOI: 10.1007/JHEP01(2018)159. arXiv: 1711.11554 [hep-ph].

[283] Dietrich Bödeker. "Remarks on the QCD-electroweak phase transition in a supercooled universe." In: *Phys. Rev. D* 104.11 (2021), p. L111501. DOI: 10.1103/PhysRevD.104.L111501. arXiv: 2108.11966 [hep-ph].

[284] Suntharan Arunasalam, Archil Kobakhidze, Cyril Lagger, Shelley Liang, and Albert Zhou. "Low temperature electroweak phase transition in the Standard Model with hidden scale invariance." In: *Phys. Lett. B* 776 (2018), pp. 48–53. DOI: 10.1016/j.physletb.2017.11.017. arXiv: 1709.10322 [hep-ph].

[285] Seyda Ipek and Tim M. P. Tait. "Early Cosmological Period of QCD Confinement." In: *Phys. Rev. Lett.* 122.11 (2019), p. 112001. DOI: 10.1103/PhysRevLett.122.112001. arXiv: 1811.00559 [hep-ph].

[286] Yuepeng Guan and Shinya Matsuzaki. "Ladder top-quark condensation imprints in supercooled electroweak phase transition." In: (May 2024). arXiv: 2405.03265 [hep-ph].

[287] Wei Liu and Ke-Pan Xie. "Probing radiative electroweak symmetry breaking with colliders and gravitational waves." In: (Aug. 2024). arXiv: 2408.03649 [hep-ph].

[288] Jens Braun and Holger Gies. "Chiral phase boundary of QCD at finite temperature." In: *JHEP* 06 (2006), p. 024. DOI: 10.1088/1126-6708/2006/06/024. arXiv: hep-ph/0602226.

[289] Frank R. Brown, Frank P. Butler, Hong Chen, Norman H. Christ, Zhi-hua Dong, Wendy Schaffer, Leo I. Unger, and Alessandro Vaccarino. "On the existence of a phase transition for QCD with three light quarks." In: *Phys. Rev. Lett.* 65 (1990), pp. 2491–2494. DOI: 10.1103/PhysRevLett.65.2491.

[290] Francesca Cuteri, Owe Philipsen, and Alessandro Sciarra. "On the order of the QCD chiral phase transition for different numbers of quark flavours." In: *JHEP* 11 (2021), p. 141. DOI: 10.1007/JHEP11(2021)141. arXiv: 2107.12739 [hep-lat].

[291] Jean-Francois Dufaux, Gary Felder, Lev Kofman, and Olga Navros. "Gravity Waves from Tachyonic Preheating after Hybrid Inflation." In: *JCAP* 03 (2009), p. 001. DOI: 10.1088/1475-7516/2009/03/001. arXiv: 0812.2917 [astro-ph].

[292] Daniel G. Figueroa and Francisco Torrenti. "Gravitational wave production from preheating: parameter dependence." In: *JCAP* 10 (2017), p. 057. DOI: 10.1088/1475-7516/2017/10/057. arXiv: 1707.04533 [astro-ph.CO].

[293] Jessica L. Cook and Lorenzo Sorbo. "Particle production during inflation and gravitational waves detectable by ground-based interferometers." In: *Phys. Rev. D* 85 (2012). [Erratum: Phys.Rev.D 86, 069901 (2012)], p. 023534. DOI: 10.1103/PhysRevD.85.023534. arXiv: 1109.0022 [astro-ph.CO].

[294] Wilfried Buchmüller, Valerie Domcke, Kohei Kamada, and Kai Schmitz. "The Gravitational Wave Spectrum from Cosmological $B-L$ Breaking." In: *JCAP* 10 (2013), p. 003. DOI: 10.1088/1475-7516/2013/10/003. arXiv: 1305.3392 [hep-ph].

[295] Camila S. Machado, Wolfram Ratzinger, Pedro Schwaller, and Ben A. Stefanek. "Gravitational wave probes of axionlike particles." In: *Phys. Rev. D* 102.7 (2020), p. 075033. DOI: 10.1103/PhysRevD.102.075033. arXiv: 1912.01007 [hep-ph].

[296] Daniel G. Figueroa, Adrien Florio, Francisco Torrenti, and Wessel Valkenburg. "The art of simulating the early Universe – Part I." In: *JCAP* 04 (2021), p. 035. DOI: 10.1088/1475-7516/2021/04/035. arXiv: 2006.15122 [astro-ph.CO].

[297] Yago Bea, Jorge Casalderrey-Solana, Thanasis Giannakopoulos, Aron Jansen, Sven Krippendorf, David Mateos, Mikel Sanchez-Garitaonandia, and Miguel Zilhão. "Spinodal Gravitational Waves." In: (Dec. 2021). arXiv: 2112.15478 [hep-th].

[298] Juan Garcia-Bellido and Ester Ruiz Morales. "Particle production from symmetry breaking after inflation." In: *Phys. Lett. B* 536 (2002), pp. 193–202. DOI: 10.1016/S0370-2693(02)01820-8. arXiv: hep-ph/0109230.

[299] Edmund J. Copeland, S. Pascoli, and A. Rajantie. "Dynamics of tachyonic preheating after hybrid inflation." In: *Phys. Rev. D* 65 (2002), p. 103517. DOI: 10.1103/PhysRevD.65.103517. arXiv: hep-ph/0202031.

[300] Anders Tranberg and Jan Smit. "Baryon asymmetry from electroweak tachyonic preheating." In: *JHEP* 11 (2003), p. 016. DOI: 10.1088/1126-6708/2003/11/016. arXiv: hep-ph/0310342.

[301] Mariel Desroche, Gary N. Felder, Jan M. Kratochvil, and Andrei D. Linde. "Preheating in new inflation." In: *Phys. Rev. D* 71 (2005), p. 103516. DOI: 10.1103/PhysRevD.71.103516. arXiv: hep-th/0501080.

[302] Teruaki Suyama, Takahiro Tanaka, Bruce Bassett, and Hideaki Kudoh. "Black hole production in tachyonic preheating." In: *JCAP* 04 (2006), p. 001. DOI: 10.1088/1475-7516/2006/04/001. arXiv: hep-ph/0601108.

[303] Wilfried Buchmuller, Valerie Domcke, and Kai Schmitz. "Spontaneous B-L Breaking as the Origin of the Hot Early Universe." In: *Nucl. Phys. B* 862 (2012), pp. 587–632. DOI: 10.1016/j.nuclphysb.2012.05.001. arXiv: 1202.6679 [hep-ph].

[304] W. Buchmuller, V. Domcke, K. Kamada, and K. Schmitz. "A Minimal Supersymmetric Model of Particle Physics and the Early Universe." In: (2013). Ed. by Luis Álvarez-Gaumé, Goran S. Djordjevic, and Dejan Stojkovic, pp. 47–77. arXiv: 1309.7788 [hep-ph].

[305] Anders Tranberg, Sara Tähtinen, and David J. Weir. "Gravitational waves from non-Abelian gauge fields at a tachyonic transition." In: *JCAP* 04 (2018), p. 012. DOI: 10.1088/1475-7516/2018/04/012. arXiv: 1706.02365 [hep-ph].

[306] Javier Rubio and Eemeli S. Tomberg. "Preheating in Palatini Higgs inflation." In: *JCAP* 04 (2019), p. 021. DOI: 10.1088/1475-7516/2019/04/021. arXiv: 1902.10148 [hep-ph].

[307] Minxi He, Ryusuke Jinno, Kohei Kamada, Alexei A. Starobinsky, and Jun'ichi Yokoyama. "Occurrence of tachyonic preheating in the mixed Higgs-R^2 model." In: *JCAP* 01 (2021), p. 066. DOI: 10.1088/1475-7516/2021/01/066. arXiv: 2007.10369 [hep-ph].

[308] Alexandros Karam, Eemeli Tomberg, and Hardi Veermäe. "Tachyonic preheating in Palatini R 2 inflation." In: *JCAP* 06 (2021), p. 023. DOI: 10.1088/1475-7516/2021/06/023. arXiv: 2102.02712 [astro-ph.CO].

[309] Eemeli Tomberg and Hardi Veermäe. "Tachyonic preheating in plateau inflation." In: *JCAP* 12.12 (2021), p. 035. DOI: 10.1088/1475-7516/2021/12/035. arXiv: 2108.10767 [astro-ph.CO].

[310] Niko Koivunen, Eemeli Tomberg, and Hardi Veermäe. "The linear regime of tachyonic preheating." In: *JCAP* 07.07 (2022), p. 028. DOI: 10.1088/1475-7516/2022/07/028. arXiv: 2201.04145 [astro-ph.CO].

[311] Frédéric Dux, Adrien Florio, Juraj Klarić, Andrey Shkerin, and Inar Timiryasov. "Preheating in Palatini Higgs inflation on the lattice." In: *JCAP* 09 (2022), p. 015. DOI: 10.1088/1475-7516/2022/09/015. arXiv: 2203.13286 [hep-ph].

[312] Bibhushan Shakya. "The Tachyonic Higgs and the Inflationary Universe." In: (Jan. 2023). arXiv: 2301.08754 [hep-ph].

[313] Felix Brümmer, Giacomo Ferrante, and Michele Frigerio. "Hybrid inflation and gravitational waves from accidentally light scalars." In: (June 2024). arXiv: 2406.02531 [astro-ph.CO].

[314] K. N. Abazajian et al. "Light Sterile Neutrinos: A White Paper." In: (Apr. 2012). arXiv: 1204.5379 [hep-ph].

[315] M. Drewes et al. "A White Paper on keV Sterile Neutrino Dark Matter." In: *JCAP* 01 (2017), p. 025. DOI: 10.1088/1475-7516/2017/01/025. arXiv: 1602.04816 [hep-ph].

[316] Morad Aaboud et al. "Search for new high-mass phenomena in the dilepton final state using 36 fb^{-1} of proton-proton collision data at $\sqrt{s} = 13$ TeV with the ATLAS detector." In: *JHEP* 10 (2017), p. 182. DOI: 10.1007/JHEP10(2017)182. arXiv: 1707.02424 [hep-ex].

[317] Miguel Escudero, Samuel J. Witte, and Nuria Rius. "The dispirited case of gauged $\mathrm{U}(1)_{B-L}$ dark matter." In: *JHEP* 08 (2018), p. 190. DOI: 10.1007/JHEP08(2018)190. arXiv: 1806.02823 [hep-ph].

[318] P. A. Zyla et al. "Review of Particle Physics." In: *PTEP* 2020.8 (2020), p. 083C01. DOI: 10.1093/ptep/ptaa104.

[319] R. L. Workman et al. "Review of Particle Physics." In: *PTEP* 2022 (2022), p. 083C01. DOI: 10.1093/ptep/ptac097.

[320] Oliver Gould and Tuomas V. I. Tenkanen. "On the perturbative expansion at high temperature and implications for cosmological phase transitions." In: *JHEP* 06 (2021), p. 069. DOI: 10.1007/JHEP06(2021)069. arXiv: 2104.04399 [hep-ph].

[321] Cristina Benso, Felix Kahlhoefer, and Henda Mansour. "Dark matter phase-in: producing feebly-interacting particles after a first-order phase transition." In: (Apr. 2025). arXiv: 2504.10593 [hep-ph].

[322] Shinsuke Kawai and Nobuchika Okada. "Reheating consistency condition on the classically conformal U(1)B–L Higgs inflation model." In: *Phys. Rev. D* 108.1 (2023), p. 015013. DOI: 10.1103/PhysRevD.108.015013. arXiv: 2303.00342 [hep-ph].

[323] Iason Baldes and María Olalla Olea-Romacho. "Primordial black holes as dark matter: interferometric tests of phase transition origin." In: *JHEP* 01 (2024), p. 133. DOI: 10.1007/JHEP01(2024)133. arXiv: 2307.11639 [hep-ph].

[324] G. Fejos and T. Hatsuda. "Order of the SU(Nf)×SU(Nf) chiral transition via the functional renormalization group." In: *Phys. Rev. D* 110.1 (2024), p. 016021. DOI: 10.1103/PhysRevD.110.016021. arXiv: 2404.00554 [hep-ph].

[325] F. Karsch. "Lattice QCD at high temperature and density." In: *Lect. Notes Phys.* 583 (2002). Ed. by Willibald Plessas and L. Mathelitsch, pp. 209–249. DOI: 10.1007/3-540-45792-5_6. arXiv: hep-lat/0106019.

[326] Kenji Fukushima and Vladimir Skokov. "Polyakov loop modeling for hot QCD." In: *Prog. Part. Nucl. Phys.* 96 (2017), pp. 154–199. DOI: 10.1016/j.ppnp.2017.05.002. arXiv: 1705.00718 [hep-ph].

[327] Y. Nambu and G. Jona-Lasinio. "Dynamical Model of Elementary Particles Based on an Analogy with Superconductivity. II." In: *Phys. Rev.* 124 (1 1961), pp. 246–254. DOI: 10.1103/PhysRev.124.246. URL: https://link.aps.org/doi/10.1103/PhysRev.124.246.

[328] Alexander M. Polyakov. "Compact Gauge Fields and the Infrared Catastrophe." In: *Phys. Lett. B* 59 (1975). Ed. by J. C. Taylor, pp. 82–84. DOI: 10.1016/0370-2693(75)90162-8.

[329] Alexander J. Helmboldt, Jisuke Kubo, and Susan van der Woude. "Observational prospects for gravitational waves from hidden or dark chiral phase transitions." In: *Phys. Rev. D* 100.5 (2019), p. 055025. DOI: 10.1103/PhysRevD.100.055025. arXiv: 1904.07891 [hep-ph].

[330] Manuel Reichert, Francesco Sannino, Zhi-Wei Wang, and Chen Zhang. "Dark confinement and chiral phase transitions: gravitational waves vs matter representations." In: *JHEP* 01 (2022), p. 003. DOI: 10.1007/JHEP01(2022)003. arXiv: 2109.11552 [hep-ph].

[331] M. Baldo, M. Buballa, F. Burgio, F. Neumann, M. Oertel, and H. J. Schulze. "Neutron stars and the transition to color superconducting quark matter." In: *Phys. Lett. B* 562 (2003), pp. 153–160. DOI: 10.1016/S0370-2693(03)00556-2. arXiv: nucl-th/0212096.

[332] Toru Kojo, Philip D. Powell, Yifan Song, and Gordon Baym. "Phenomenological QCD equation of state for massive neutron stars." In: *Phys. Rev. D* 91.4 (2015), p. 045003. DOI: 10.1103/PhysRevD.91.045003. arXiv: 1412.1108 [hep-ph].

[333] Hosein Gholami, Ishfaq Ahmad Rather, Marco Hofmann, Michael Buballa, and Jürgen Schaffner-Bielich. "Astrophysical constraints on color-superconducting phases in compact stars within the RG-consistent NJL model." In: *Phys. Rev. D* 111.10 (2025), p. 103034. DOI: 10.1103/PhysRevD.111.103034. arXiv: 2411.04064 [hep-ph].

[334] Jan-Erik Christian, Ishfaq Ahmad Rather, Hosein Gholami, and Marco Hofmann. "Comprehensive Analysis of Constructing Hybrid Stars with an RG-consistent NJL Model." In: (Mar. 2025). arXiv: 2503.13626 [astro-ph.HE].

[335] S. P. Klevansky. "The Nambu-Jona-Lasinio model of quantum chromodynamics." In: *Rev. Mod. Phys.* 64 (1992), pp. 649–708. DOI: 10.1103/RevModPhys.64.649.

[336] Michael Buballa. "NJL model analysis of quark matter at large density." In: *Phys. Rept.* 407 (2005), pp. 205–376. DOI: 10.1016/j.physrep.2004.11.004. arXiv: hep-ph/0402234.

[337] T. Kunihiro. "Effects of the $U_A(1)$ anomaly on the Quark Condensates and Meson Properties at Finite Temperature." In: *Phys. Lett. B* 219 (1989). [Erratum: Phys.Lett.B 245, 687 (1990)], pp. 363–368. DOI: 10.1016/0370-2693(89)90405-X.

[338] P. Rehberg, S. P. Klevansky, and J. Hufner. "Hadronization in the SU(3) Nambu-Jona-Lasinio model." In: *Phys. Rev. C* 53 (1996), pp. 410–429. DOI: 10.1103/PhysRevC.53.410. arXiv: hep-ph/9506436.

[339] G. 't Hooft. "Symmetry Breaking through Bell-Jackiw Anomalies." In: *Phys. Rev. Lett.* 37 (1 1976), pp. 8–11. DOI: 10.1103/PhysRevLett.37.8. URL: https://link.aps.org/doi/10.1103/PhysRevLett.37.8.

[340] M. Kobayashi and T. Maskawa. "Chiral symmetry and $\eta - X$ mixing." In: *Prog. Theor. Phys.* 44 (1970), pp. 1422–1424. DOI: 10.1143/PTP.44.1422.

[341] M. Kobayashi, H. Kondo, and T. Maskawa. "Symmetry breaking of the chiral U(3)×U(3) and the quark model." In: *Prog. Theor. Phys.* 45 (1971), pp. 1955–1959. DOI: 10.1143/PTP.45.1955.

[342] Teiji Kunihiro and Tetsuo Hatsuda. "A Selfconsistent Mean Field Approach to the Dynamical Symmetry Breaking: The Effective Potential of the Nambu-Jona-Lasinio Model." In: *Prog. Theor. Phys.* 71 (1984), p. 1332. DOI: 10.1143/PTP.71.1332.

[343] Tetsuo Hatsuda and Teiji Kunihiro. "QCD phenomenology based on a chiral effective Lagrangian." In: *Phys. Rept.* 247 (1994), pp. 221–367. DOI: 10.1016/0370-1573(94)90022-1. arXiv: hep-ph/9401310.

[344] T. Hatsuda and T. Kunihiro. "Fluctuation effects in hot quark matter: Precursors of chiral transition at finite temperature." In: *Phys. Rev. Lett.* 55 (2 1985), pp. 158–161. DOI: 10.1103/PhysRevLett.55.158. URL: https://link.aps.org/doi/10.1103/PhysRevLett.55.158.

[345] Kenji Fukushima. "Phase diagrams in the three-flavor Nambu-Jona-Lasinio model with the Polyakov loop." In: *Phys. Rev. D* 77 (2008). [Erratum: Phys.Rev.D 78, 039902 (2008)], p. 114028. DOI: 10.1103/PhysRevD.77.114028. arXiv: 0803.3318 [hep-ph].

[346] H. Kohyama, D. Kimura, and T. Inagaki. "Regularization dependence on phase diagram in Nambu–Jona-Lasinio model." In: *Nucl. Phys. B* 896 (2015), pp. 682–715. DOI: 10.1016/j.nuclphysb.2015.05.015. arXiv: 1501.00449 [hep-ph].

[347] H. Hansen, W. M. Alberico, A. Beraudo, A. Molinari, M. Nardi, and C. Ratti. "Mesonic correlation functions at finite temperature and density in the Nambu-Jona-Lasinio model with a Polyakov loop." In: *Phys. Rev. D* 75 (2007), p. 065004. DOI: 10.1103/PhysRevD.75.065004. arXiv: hep-ph/0609116.

[348] Kenji Fukushima and Chihiro Sasaki. "The phase diagram of nuclear and quark matter at high baryon density." In: *Prog. Part. Nucl. Phys.* 72 (2013), pp. 99–154. DOI: 10.1016/j.ppnp.2013.05.003. arXiv: 1301.6377 [hep-ph].

[349] Alexander M. Polyakov. "Thermal Properties of Gauge Fields and Quark Liberation." In: *Phys. Lett. B* 72 (1978), pp. 477–480. DOI: 10.1016/0370-2693(78)90737-2.

[350] Benjamin Svetitsky and Laurence G. Yaffe. "Critical Behavior at Finite Temperature Confinement Transitions." In: *Nucl. Phys. B* 210 (1982), pp. 423–447. DOI: 10.1016/0550-3213(82)90172-9.

[351] Benjamin Svetitsky. "Symmetry Aspects of Finite Temperature Confinement Transitions." In: *Phys. Rept.* 132 (1986), pp. 1–53. DOI: 10.1016/0370-1573(86)90014-1.

[352] Kenji Fukushima and Tetsuo Hatsuda. "The phase diagram of dense QCD." In: *Rept. Prog. Phys.* 74 (2011), p. 014001. DOI: 10.1088/0034-4885/74/1/014001. arXiv: 1005.4814 [hep-ph].

[353] Larry D. McLerran and Benjamin Svetitsky. "Quark Liberation at High Temperature: A Monte Carlo Study of SU(2) Gauge Theory." In: *Phys. Rev. D* 24 (1981), p. 450. DOI: 10.1103/PhysRevD.24.450.

[354] Sudhir Nadkarni. "Nonabelian Debye Screening. 1. The Color Averaged Potential." In: *Phys. Rev. D* 33 (1986), p. 3738. DOI: 10.1103/PhysRevD.33.3738.

[355] Sudhir Nadkarni. "Nonabelian Debye Screening. 2. The Singlet Potential." In: *Phys. Rev. D* 34 (1986), p. 3904. DOI: 10.1103/PhysRevD.34.3904.

[356] Peter N. Meisinger and Michael C. Ogilvie. "Chiral symmetry restoration and Z(N) symmetry." In: *Phys. Lett. B* 379 (1996), pp. 163–168. DOI: 10.1016/0370-2693(96)00447-9. arXiv: hep-lat/9512011.

[357] Kenji Fukushima. "Chiral effective model with the Polyakov loop." In: *Phys. Lett. B* 591 (2004), pp. 277–284. DOI: 10.1016/j.physletb.2004.04.027. arXiv: hep-ph/0310121.

[358] Claudia Ratti, Michael A. Thaler, and Wolfram Weise. "Phases of QCD: Lattice thermodynamics and a field theoretical model." In: *Phys. Rev. D* 73 (2006), p. 014019. DOI: 10.1103/PhysRevD.73.014019. arXiv: hep-ph/0506234.

[359] Robert D. Pisarski. "Quark gluon plasma as a condensate of SU(3) Wilson lines." In: *Phys. Rev. D* 62 (2000), p. 111501. DOI: 10.1103/PhysRevD.62.111501. arXiv: hep-ph/0006205.

[360] Robert D. Pisarski. "Tests of the Polyakov loops model." In: *Nucl. Phys. A* 702 (2002). Ed. by F. Karsch and H. Satz, pp. 151–158. DOI: 10.1016/S0375-9474(02)00699-1. arXiv: hep-ph/0112037.

[361] Simon Roessner, Claudia Ratti, and W. Weise. "Polyakov loop, diquarks and the two-flavour phase diagram." In: *Phys. Rev. D* 75 (2007), p. 034007. DOI: 10.1103/PhysRevD.75.034007. arXiv: hep-ph/0609281.

[362] Wei-Chih Huang, Manuel Reichert, Francesco Sannino, and Zhi-Wei Wang. "Testing the dark SU(N) Yang-Mills theory confined landscape: From the lattice to gravitational waves." In: *Phys. Rev. D* 104.3 (2021), p. 035005. DOI: 10.1103/PhysRevD.104.035005. arXiv: 2012.11614 [hep-ph].

[363] Bernd-Jochen Schaefer, Jan M. Pawlowski, and Jochen Wambach. "The Phase Structure of the Polyakov–Quark-Meson Model." In: *Phys. Rev. D* 76 (2007), p. 074023. DOI: 10.1103/PhysRevD.76.074023. arXiv: 0704.3234 [hep-ph].

[364] T. Kahara, M. Ruggieri, and K. Tuominen. "Deconfinement vs. chiral symmetry and higher representation matter." In: *Phys. Rev. D* 85 (2012), p. 094020. DOI: 10.1103/PhysRevD.85.094020. arXiv: 1202.1769 [hep-ph].

[365] Lisa M. Haas, Rainer Stiele, Jens Braun, Jan M. Pawlowski, and Jürgen Schaffner-Bielich. "Improved Polyakov-loop potential for effective models from functional calculations." In: *Phys. Rev. D* 87.7 (2013), p. 076004. DOI: 10.1103/PhysRevD.87.076004. arXiv: 1302.1993 [hep-ph].

[366] Leonard Fister and Jan M. Pawlowski. "Confinement from Correlation Functions." In: *Phys. Rev. D* 88 (2013), p. 045010. DOI: 10.1103/PhysRevD.88.045010. arXiv: 1301.4163 [hep-ph].

[367] Enrico Morgante, Nicklas Ramberg, and Pedro Schwaller. "Gravitational waves from dark SU(3) Yang-Mills theory." In: *Phys. Rev. D* 107.3 (2023), p. 036010. DOI: 10.1103/PhysRevD.107.036010. arXiv: 2210.11821 [hep-ph].

[368] Francesco Bigazzi, Alessio Caddeo, Aldo L. Cotrone, and Angel Paredes. "Dark Holograms and Gravitational Waves." In: *JHEP* 04 (2021), p. 094. DOI: 10.1007/JHEP04(2021)094. arXiv: 2011.08757 [hep-ph].

[369] Marek Lewicki, Oriol Pujolàs, and Ville Vaskonen. "Escape from supercooling with or without bubbles: gravitational wave signatures." In: *Eur. Phys. J. C* 81.9 (2021), p. 857. DOI: 10.1140/epjc/s10052-021-09669-6. arXiv: 2106.09706 [astro-ph.CO].

[370] Marek Lewicki and Ville Vaskonen. "Gravitational wave spectra from strongly supercooled phase transitions." In: *Eur. Phys. J. C* 80.11 (2020), p. 1003. DOI: 10.1140/epjc/s10052-020-08589-1. arXiv: 2007.04967 [astro-ph.CO].

[371] John T. Giblin and James B. Mertens. "Gravitional radiation from first-order phase transitions in the presence of a fluid." In: *Phys. Rev. D* 90.2 (2014), p. 023532. DOI: 10.1103/PhysRevD.90.023532. arXiv: 1405.4005 [astro-ph.CO].

[372] Dietrich Bodeker and Guy D. Moore. "Can electroweak bubble walls run away?" In: *JCAP* 05 (2009), p. 009. DOI: 10.1088/1475-7516/2009/05/009. arXiv: 0903.4099 [hep-ph].

[373] Yann Gouttenoire, Ryusuke Jinno, and Filippo Sala. "Friction pressure on relativistic bubble walls." In: *JHEP* 05 (2022), p. 004. DOI: 10.1007/JHEP05(2022)004. arXiv: 2112.07686 [hep-ph].

[374] Wei-Chih Huang, Francesco Sannino, and Zhi-Wei Wang. "Gravitational Waves from Pati-Salam Dynamics." In: *Phys. Rev. D* 102.9 (2020), p. 095025. DOI: 10.1103/PhysRevD.102.095025. arXiv: 2004.02332 [hep-ph].

[375] Joseph I. Kapusta. "Quantum Chromodynamics at High Temperature." In: *Nucl. Phys. B* 148 (1979), pp. 461–498. DOI: 10.1016/0550-3213(79)90146-9.

[376] Robert D. Pisarski. "Computing Finite Temperature Loops with Ease." In: *Nucl. Phys. B* 309 (1988), pp. 476–492. DOI: 10.1016/0550-3213(88)90454-3.

[377] Tomasz P. Dutka, Tae Hyun Jung, and Chang Sub Shin. "What happens when supercooling is terminated by curvature flipping of the effective potential?" In: (Dec. 2024). arXiv: 2412.15864 [hep-ph].

[378] A. D. Dolgov and D. P. Kirilova. "ON PARTICLE CREATION BY A TIME DEPENDENT SCALAR FIELD." In: *Sov. J. Nucl. Phys.* 51 (1990), pp. 172–177.

[379] Jennie H. Traschen and Robert H. Brandenberger. "Particle Production During Out-of-equilibrium Phase Transitions." In: *Phys. Rev. D* 42 (1990), pp. 2491–2504. DOI: 10.1103/PhysRevD.42.2491.

[380] Lev Kofman, Andrei D. Linde, and Alexei A. Starobinsky. "Towards the theory of reheating after inflation." In: *Phys. Rev. D* 56 (1997), pp. 3258–3295. DOI: 10.1103/PhysRevD.56.3258. arXiv: hep-ph/9704452.

[381] T. S. Bunch and P. C. W. Davies. "Quantum Field Theory in de Sitter Space: Renormalization by Point Splitting." In: *Proc. Roy. Soc. Lond. A* 360 (1978), pp. 117–134. DOI: 10.1098/rspa.1978.0060.

[382] Alexander Vilenkin. "Quantum fluctuations in the new inflationary universe." In: *Nuclear Physics B* 226.2 (1983), pp. 527–546. ISSN: 0550-3213. DOI: https://doi.org/10.1016/0550-3213(83)90208-0. URL: https://www.sciencedirect.com/science/article/pii/0550321383902080.

[383] Konstantinos Dimopoulos, Tommi Markkanen, Antonio Racioppi, and Ville Vaskonen. "Primordial Black Holes from Thermal Inflation." In: *JCAP* 07 (2019), p. 046. DOI: 10.1088/1475-7516/2019/07/046. arXiv: 1903.09598 [astro-ph.CO].

[384] Anson Hook, John Kearney, Bibhushan Shakya, and Kathryn M. Zurek. "Probable or Improbable Universe? Correlating Electroweak Vacuum Instability with the Scale of Inflation." In: *JHEP* 01 (2015), p. 061. DOI: 10.1007/JHEP01(2015)061. arXiv: 1404.5953 [hep-ph].

[385] N. D. Birrell and P. C. W. Davies. *Quantum Fields in Curved Space*. Cambridge Monographs on Mathematical Physics. Cambridge, UK: Cambridge Univ. Press, Feb. 1984. ISBN: 978-0-521-27858-4, 978-0-521-27858-4. DOI: 10.1017/CBO9780511622632.

[386] Daniel G. Figueroa, Adrien Florio, Francisco Torrenti, and Wessel Valkenburg. "CosmoLattice: A modern code for lattice simulations of scalar and gauge field dynamics in an expanding universe." In: *Comput. Phys. Commun.* 283 (2023), p. 108586. DOI: 10.1016/j.cpc.2022.108586. arXiv: 2102.01031 [astro-ph.CO].

[387] Naoki Seto, Seiji Kawamura, and Takashi Nakamura. "Possibility of direct measurement of the acceleration of the universe using 0.1-Hz band laser interferometer gravitational wave antenna in space." In: *Phys. Rev. Lett.* 87 (2001), p. 221103. DOI: 10.1103/PhysRevLett.87.221103. arXiv: astro-ph/0108011.

[388] Shuichi Sato et al. "The status of DECIGO." In: *J. Phys. Conf. Ser.* 840.1 (2017). Ed. by Domencio Giardini and Philippe Jetzer, p. 012010. DOI: 10.1088/1742-6596/840/1/012010.

[389] Seiji Kawamura et al. "Current status of space gravitational wave antenna DECIGO and B-DECIGO." In: *PTEP* 2021.5 (2021), 05A105. DOI: 10.1093/ptep/ptab019. arXiv: 2006.13545 [gr-qc].

[390] Katherine Freese, Joshua A. Frieman, and Angela V. Olinto. "Natural inflation with pseudo - Nambu-Goldstone bosons." In: *Phys. Rev. Lett.* 65 (1990), pp. 3233–3236. DOI: 10.1103/PhysRevLett.65.3233.

[391] Enrico Pajer and Marco Peloso. "A review of Axion Inflation in the era of Planck." In: *Class. Quant. Grav.* 30 (2013), p. 214002. DOI: 10.1088/0264-9381/30/21/214002. arXiv: 1305.3557 [hep-th].

[392] Peter Adshead, John T. Giblin, Timothy R. Scully, and Evangelos I. Sfakianakis. "Gauge-preheating and the end of axion inflation." In: *JCAP* 12 (2015), p. 034. DOI: 10.1088/1475-7516/2015/12/034. arXiv: 1502.06506 [astro-ph.CO].

[393] Ryuji Daido, Fuminobu Takahashi, and Wen Yin. "The ALP miracle: unified inflaton and dark matter." In: *JCAP* 05 (2017), p. 044. DOI: 10.1088/1475-7516/2017/05/044. arXiv: 1702.03284 [hep-ph].

[394] Fuminobu Takahashi and Wen Yin. "Challenges for heavy QCD axion inflation." In: *JCAP* 10 (2021), p. 057. DOI: 10.1088/1475-7516/2021/10/057. arXiv: 2105.10493 [hep-ph].

[395] Valerie Domcke, Yohei Ema, and Kyohei Mukaida. "Chiral Anomaly, Schwinger Effect, Euler-Heisenberg Lagrangian, and application to axion inflation." In: *JHEP* 02 (2020), p. 055. DOI: 10.1007/JHEP02(2020)055. arXiv: 1910.01205 [hep-ph].

[396] Naoya Kitajima, Shota Nakagawa, and Fuminobu Takahashi. "Nonthermally trapped inflation by tachyonic dark photon production." In: *Phys. Rev. D* 105.10 (2022), p. 103011. DOI: 10.1103/PhysRevD.105.103011. arXiv: 2111.06696 [hep-ph].

[397] Edward Witten. "Some Properties of O(32) Superstrings." In: *Phys. Lett. B* 149 (1984), pp. 351–356. DOI: 10.1016/0370-2693(84)90422-2.

[398] Peter Svrcek and Edward Witten. "Axions In String Theory." In: *JHEP* 06 (2006), p. 051. DOI: 10.1088/1126-6708/2006/06/051. arXiv: hep-th/0605206.

[399] Asimina Arvanitaki, Savas Dimopoulos, Sergei Dubovsky, Nemanja Kaloper, and John March-Russell. "String Axiverse." In: *Phys. Rev. D* 81 (2010), p. 123530. DOI: 10.1103/PhysRevD.81.123530. arXiv: 0905.4720 [hep-th].

[400] Ciaran O'Hare. *cajohare/AxionLimits: AxionLimits*. https://cajohare.github.io/AxionLimits/. Version v1.0. July 2020. DOI: 10.5281/zenodo.3932430.

[401] Mohamed M. Anber and Lorenzo Sorbo. "Naturally inflating on steep potentials through electromagnetic dissipation." In: *Phys. Rev. D* 81 (2010), p. 043534. DOI: 10.1103/PhysRevD.81.043534. arXiv: 0908.4089 [hep-th].

[402] Mohamed M. Anber and Lorenzo Sorbo. "Non-Gaussianities and chiral gravitational waves in natural steep inflation." In: *Phys. Rev. D* 85 (2012), p. 123537. DOI: 10.1103/PhysRevD.85.123537. arXiv: 1203.5849 [astro-ph.CO].

[403] Neil Barnaby, Jordan Moxon, Ryo Namba, Marco Peloso, Gary Shiu, and Peng Zhou. "Gravity waves and non-Gaussian features from particle production in a sector gravitationally coupled to the inflaton." In: *Phys. Rev. D* 86 (2012), p. 103508. DOI: 10.1103/PhysRevD.86.103508. arXiv: 1206.6117 [astro-ph.CO].

[404] Valerie Domcke, Mauro Pieroni, and Pierre Binétruy. "Primordial gravitational waves for universality classes of pseudoscalar inflation." In: *JCAP* 06 (2016), p. 031. DOI: 10.1088/1475-7516/2016/06/031. arXiv: 1603.01287 [astro-ph.CO].

[405] Patrick B. Greene, Lev Kofman, Andrei D. Linde, and Alexei A. Starobinsky. "Structure of resonance in preheating after inflation." In: *Phys. Rev. D* 56 (1997), pp. 6175–6192. DOI: 10.1103/PhysRevD.56.6175. arXiv: hep-ph/9705347.

[406] Azadeh Maleknejad. "Axion Inflation with an SU(2) Gauge Field: Detectable Chiral Gravity Waves." In: *JHEP* 07 (2016), p. 104. DOI: 10.1007/JHEP07(2016)104. arXiv: 1604.03327 [hep-ph].

[407] Daniel G. Figueroa and Francisco Torrenti. "Parametric resonance in the early Universe—a fitting analysis." In: *JCAP* 02 (2017), p. 001. DOI: 10.1088/1475-7516/2017/02/001. arXiv: 1609.05197 [astro-ph.CO].

[408] Peter Adshead, John T. Giblin, and Zachary J. Weiner. "Gravitational waves from gauge preheating." In: *Phys. Rev. D* 98.4 (2018), p. 043525. DOI: 10.1103/PhysRevD.98.043525. arXiv: 1805.04550 [astro-ph.CO].

[409] Jose Roberto Canivete Cuissa and Daniel G. Figueroa. "Lattice formulation of axion inflation. Application to preheating." In: *JCAP* 06 (2019), p. 002. DOI: 10.1088/1475-7516/2019/06/002. arXiv: 1812.03132 [astro-ph.CO].

[410] David Cyncynates and Zachary J. Weiner. "Detectable, defect-free dark photon dark matter." In: (Oct. 2023). arXiv: 2310.18397 [hep-ph].

[411] David Cyncynates and Zachary J. Weiner. "Experimental targets for dark photon dark matter." In: (Oct. 2024). arXiv: 2410.14774 [hep-ph].

[412] Aleksandr Chatrchyan and Joerg Jaeckel. "Gravitational waves from the fragmentation of axion-like particle dark matter." In: *JCAP* 02 (2021), p. 003. DOI: 10.1088/1475-7516/2021/02/003. arXiv: 2004.07844 [hep-ph].

[413] Borna Salehian, Mohammad Ali Gorji, Shinji Mukohyama, and Hassan Firouzjahi. "Analytic study of dark photon and gravitational wave production from axion." In: *JHEP* 05 (2021), p. 043. DOI: 10.1007/JHEP05(2021)043. arXiv: 2007.08148 [hep-ph].

[414] Ryo Namba and Motoo Suzuki. "Implications of Gravitational-wave Production from Dark Photon Resonance to Pulsar-timing Observations and Effective Number of Relativistic Species." In: *Phys. Rev. D* 102 (2020), p. 123527. DOI: 10.1103/PhysRevD.102.123527. arXiv: 2009.13909 [astro-ph.CO].

[415] Thomas Kite, Andrea Ravenni, Subodh P. Patil, and Jens Chluba. "Bridging the gap: spectral distortions meet gravitational waves." In: *Mon. Not. Roy. Astron. Soc.* 505.3 (2021), pp. 4396–4405. DOI: 10.1093/mnras/stab1558. arXiv: 2010.00040 [astro-ph.CO].

[416] Naoya Kitajima, Jiro Soda, and Yuko Urakawa. "Nano-Hz Gravitational-Wave Signature from Axion Dark Matter." In: *Phys. Rev. Lett.* 126.12 (2021), p. 121301. DOI: 10.1103/PhysRevLett.126.121301. arXiv: 2010.10990 [astro-ph.CO].

[417] Wolfram Ratzinger, Pedro Schwaller, and Ben A. Stefanek. "Gravitational Waves from an Axion-Dark Photon System: A Lattice Study." In: *SciPost Phys.* 11 (2021), p. 001. DOI: 10.21468/SciPostPhys.11.1.001. arXiv: 2012.11584 [astro-ph.CO].

[418] Abhishek Banerjee, Eric Madge, Gilad Perez, Wolfram Ratzinger, and Pedro Schwaller. "Gravitational wave echo of relaxion trapping." In: *Phys. Rev. D* 104.5 (2021), p. 055026. DOI: 10.1103/PhysRevD.104.055026. arXiv: 2105.12135 [hep-ph].

[419] Cem Eröncel, Ryosuke Sato, Geraldine Servant, and Philip Sørensen. "ALP dark matter from kinetic fragmentation: opening up the parameter window." In: *JCAP* 10 (2022), p. 053. DOI: 10.1088/1475-7516/2022/10/053. arXiv: 2206.14259 [hep-ph].

[420] Eric Madge, Enrico Morgante, Cristina Puchades-Ibáñez, Nicklas Ramberg, Wolfram Ratzinger, Sebastian Schenk, and Pedro Schwaller. "Primordial gravitational waves in the nano-Hertz regime and PTA data — towards solving the GW inverse problem." In: *JHEP* 10 (2023), p. 171. DOI: 10.1007/JHEP10(2023)171. arXiv: 2306.14856 [hep-ph].

[421] Hong Su, Baoyu Xu, Ju Chen, Chang Liu, and Yun-Long Zhang. "Detectability of the chiral gravitational wave background from audible axions with the LISA-Taiji network." In: (Mar. 2025). arXiv: 2503.20778 [astro-ph.CO].

[422] Anson Hook and Gustavo Marques-Tavares. "Relaxation from particle production." In: *JHEP* 12 (2016), p. 101. DOI: 10.1007/JHEP12(2016)101. arXiv: 1607.01786 [hep-ph].

[423] Prateek Agrawal, Gustavo Marques-Tavares, and Wei Xue. "Opening up the QCD axion window." In: *JHEP* 03 (2018), p. 049. DOI: 10.1007/JHEP03(2018)049. arXiv: 1708.05008 [hep-ph].

[424] Raymond T. Co, Lawrence J. Hall, and Keisuke Harigaya. "Axion Kinetic Misalignment Mechanism." In: *Phys. Rev. Lett.* 124.25 (2020), p. 251802. DOI: 10.1103/PhysRevLett.124.251802. arXiv: 1910.14152 [hep-ph].

[425] Chia-Feng Chang and Yanou Cui. "New Perspectives on Axion Misalignment Mechanism." In: *Phys. Rev. D* 102.1 (2020), p. 015003. DOI: 10.1103/PhysRevD.102.015003. arXiv: 1911.11885 [hep-ph].

[426] Raymond T. Co, Keisuke Harigaya, and Aaron Pierce. "Gravitational waves and dark photon dark matter from axion rotations." In: *JHEP* 12 (2021), p. 099. DOI: 10.1007/JHEP12(2021)099. arXiv: 2104.02077 [hep-ph].

[427] Baoyu Xu, Keyi Ding, Hong Su, Ju Chen, and Yun-Long Zhang. "Chiral Gravitational Wave Background from Audible Axion via Nieh-Yan Term." In: (Nov. 2024). arXiv: 2411.08691 [hep-ph].

[428] Nicklas Ramberg, Wolfram Ratzinger, and Pedro Schwaller. "One μ to rule them all: CMB spectral distortions can probe domain walls, cosmic strings and low scale phase transitions." In: *JCAP* 02 (2023), p. 039. DOI: 10.1088/1475-7516/2023/02/039. arXiv: 2209.14313 [hep-ph].

[429] Yanou Cui, Pankaj Saha, and Evangelos I. Sfakianakis. "Gravitational Wave Symphony from Oscillating Spectator Scalar Fields." In: *Phys. Rev. Lett.* 133.2 (2024), p. 021004. DOI: 10.1103/PhysRevLett.133.021004. arXiv: 2310.13060 [hep-ph].

[430] Tetsutaro Higaki, Kwang Sik Jeong, Naoya Kitajima, and Fuminobu Takahashi. "Quality of the Peccei-Quinn symmetry in the Aligned QCD Axion and Cosmological Implications." In: *JHEP* 06 (2016), p. 150. DOI: 10.1007/JHEP06(2016)150. arXiv: 1603.02090 [hep-ph].

[431] Masahiro Kawasaki, Fuminobu Takahashi, and Masaki Yamada. "Adiabatic suppression of the axion abundance and isocurvature due to coupling to hidden monopoles." In: *JHEP* 01 (2018), p. 053. DOI: 10.1007/JHEP01(2018)053. arXiv: 1708.06047 [hep-ph].

[432] Shota Nakagawa, Fuminobu Takahashi, and Masaki Yamada. "Trapping Effect for QCD Axion Dark Matter." In: *JCAP* 05 (2021), p. 062. DOI: 10.1088/1475-7516/2021/05/062. arXiv: 2012.13592 [hep-ph].

[433] Luca Di Luzio, Belen Gavela, Pablo Quilez, and Andreas Ringwald. "An even lighter QCD axion." In: *JHEP* 05 (2021), p. 184. DOI: 10.1007/JHEP05(2021)184. arXiv: 2102.00012 [hep-ph].

[434] Luca Di Luzio, Belen Gavela, Pablo Quilez, and Andreas Ringwald. "Dark matter from an even lighter QCD axion: trapped misalignment." In: *JCAP* 10 (2021), p. 001. DOI: 10.1088/1475-7516/2021/10/001. arXiv: 2102.01082 [hep-ph].

[435] Naoya Kitajima and Fuminobu Takahashi. "Resonant production of dark photons from axions without a large coupling." In: *Phys. Rev. D* 107.12 (2023), p. 123518. DOI: 10.1103/PhysRevD.107.123518. arXiv: 2303.05492 [hep-ph].

[436] Curtis G. Callan Jr., Roger F. Dashen, and David J. Gross. "Toward a Theory of the Strong Interactions." In: *Phys. Rev. D* 17 (1978). Ed. by Mikhail A. Shifman, p. 2717. DOI: 10.1103/PhysRevD.17.2717.

[437] David J. Gross, Robert D. Pisarski, and Laurence G. Yaffe. "QCD and Instantons at Finite Temperature." In: *Rev. Mod. Phys.* 53 (1981), p. 43. DOI: 10.1103/RevModPhys.53.43.

[438] Gian Francesco Giudice. "Naturally Speaking: The Naturalness Criterion and Physics at the LHC." In: (Jan. 2008). Ed. by Gordon Kane and Aaron Pierce, pp. 155–178. DOI: 10.1142/9789812779762_0010. arXiv: 0801.2562 [hep-ph].

[439] Jihn E. Kim. "Weak Interaction Singlet and Strong CP Invariance." In: *Phys. Rev. Lett.* 43 (1979), p. 103. DOI: 10.1103/PhysRevLett.43.103.

[440] Mikhail A. Shifman, A. I. Vainshtein, and Valentin I. Zakharov. "Can Confinement Ensure Natural CP Invariance of Strong Interactions?" In: *Nucl. Phys. B* 166 (1980), pp. 493–506. DOI: 10.1016/0550-3213(80)90209-6.

[441] Jihn E. Kim, Hans Peter Nilles, and Marco Peloso. "Completing natural inflation." In: *JCAP* 01 (2005), p. 005. DOI: 10.1088/1475-7516/2005/01/005. arXiv: hep-ph/0409138.

[442] Prateek Agrawal, Jiji Fan, and Matthew Reece. "Clockwork Axions in Cosmology: Is Chromonatural Inflation Chrononatural?" In: *JHEP* 10 (2018), p. 193. DOI: 10.1007/JHEP10(2018)193. arXiv: 1806.09621 [hep-th].

[443] Richard Holman, Stephen D. H. Hsu, Thomas W. Kephart, Edward W. Kolb, Richard Watkins, and Lawrence M. Widrow. "Solutions to the strong CP problem in a world with gravity." In: *Phys. Lett. B* 282 (1992), pp. 132–136. DOI: 10.1016/0370-2693(92)90491-L. arXiv: hep-ph/9203206.

[444] Masha Baryakhtar, Marios Galanis, Robert Lasenby, and Olivier Simon. "Black hole superradiance of self-interacting scalar fields." In: *Phys. Rev. D* 103.9 (2021), p. 095019. DOI: 10.1103/PhysRevD.103.095019. arXiv: 2011.11646 [hep-ph].

[445] Matthew J. Stott. "Ultralight Bosonic Field Mass Bounds from Astrophysical Black Hole Spin." In: (Sept. 2020). arXiv: 2009.07206 [hep-ph].

[446] Sebastian Hoof, David J. E. Marsh, Júlia Sisk-Reynés, James H. Matthews, and Christopher Reynolds. "Getting More Out of Black Hole Superradiance: a Statistically Rigorous Approach to Ultralight Boson Constraints." In: (June 2024). arXiv: 2406.10337 [hep-ph].

[447] Caner Ünal, Fabio Pacucci, and Abraham Loeb. "Properties of ultralight bosons from heavy quasar spins via superradiance." In: *JCAP* 05 (2021), p. 007. DOI: 10.1088/1475-7516/2021/05/007. arXiv: 2012.12790 [hep-ph].

[448] Samuel J. Witte and Andrew Mummery. "Stepping Up Superradiance Constraints on Axions." In: (Dec. 2024). arXiv: 2412.03655 [hep-ph].

[449] Vitor Cardoso, Óscar J. C. Dias, Gavin S. Hartnett, Matthew Middleton, Paolo Pani, and Jorge E. Santos. "Constraining the mass of dark photons and axion-like particles through black-hole superradiance." In: *JCAP* 03 (2018), p. 043. DOI: 10.1088/1475-7516/2018/03/043. arXiv: 1801.01420 [gr-qc].

[450] Patrick J. Fox, Neal Weiner, and Huangyu Xiao. "Recurrent axion stars collapse with dark radiation emission and their cosmological constraints." In: *Phys. Rev. D* 108.9 (2023), p. 095043. DOI: 10.1103/PhysRevD.108.095043. arXiv: 2302.00685 [hep-ph].

[451] Liam McAllister, Eva Silverstein, and Alexander Westphal. "Gravity Waves and Linear Inflation from Axion Monodromy." In: *Phys. Rev. D* 82 (2010), p. 046003. DOI: 10.1103/PhysRevD.82.046003. arXiv: 0808.0706 [hep-th].

[452] Eva Silverstein and Alexander Westphal. "Monodromy in the CMB: Gravity Waves and String Inflation." In: *Phys. Rev. D* 78 (2008), p. 106003. DOI: 10.1103/PhysRevD.78.106003. arXiv: 0803.3085 [hep-th].

[453] Arthur Hebecker, Sebastian C. Kraus, and Lukas T. Witkowski. "D7-Brane Chaotic Inflation." In: *Phys. Lett. B* 737 (2014), pp. 16–22. DOI: 10.1016/j.physletb.2014.08.028. arXiv: 1404.3711 [hep-th].

[454] Liam McAllister, Eva Silverstein, Alexander Westphal, and Timm Wrase. "The Powers of Monodromy." In: *JHEP* 09 (2014), p. 123. DOI: 10.1007/JHEP09(2014)123. arXiv: 1405.3652 [hep-th].

[455] Ralph Blumenhagen and Erik Plauschinn. "Towards Universal Axion Inflation and Reheating in String Theory." In: *Phys. Lett. B* 736 (2014), pp. 482–487. DOI: 10.1016/j.physletb.2014.08.007. arXiv: 1404.3542 [hep-th].

[456] Fernando Marchesano, Gary Shiu, and Angel M. Uranga. "F-term Axion Monodromy Inflation." In: *JHEP* 09 (2014), p. 184. DOI: 10.1007/JHEP09(2014)184. arXiv: 1404.3040 [hep-th].

[457] Julian S. Schwinger. "On gauge invariance and vacuum polarization." In: *Phys. Rev.* 82 (1951). Ed. by K. A. Milton, pp. 664–679. DOI: 10.1103/PhysRev.82.664.

[458] Valerie Domcke and Kyohei Mukaida. "Gauge Field and Fermion Production during Axion Inflation." In: *JCAP* 11 (2018), p. 020. DOI: 10.1088/1475-7516/2018/11/020. arXiv: 1806.08769 [hep-ph].

[459] Valerie Domcke, Kai Schmitz, and Tevong You. "Cosmological relaxation through the dark axion portal." In: *JHEP* 07 (2022), p. 126. DOI: 10.1007/JHEP07(2022)126. arXiv: 2108.11295 [hep-ph].

[460] U. Kraemmer, A. K. Rebhan, and H. Schulz. "Resummations in hot scalar electrodynamics." In: *Annals Phys.* 238 (1995), pp. 286–331. DOI: 10.1006/aphy.1995.1023. arXiv: hep-ph/9403301.

[461] Michel Le Bellac. *Thermal Field Theory*. Cambridge Monographs on Mathematical Physics. Cambridge University Press, Mar. 2011. ISBN: 978-0-511-88506-8, 978-0-521-65477-7. DOI: 10.1017/CBO9780511721700.

[462] W. Heisenberg and H. Euler. "Consequences of Dirac's theory of positrons." In: *Z. Phys.* 98.11-12 (1936), pp. 714–732. DOI: 10.1007/BF01343663. arXiv: physics/0605038.

[463] Takeshi Kobayashi and Niayesh Afshordi. "Schwinger Effect in 4D de Sitter Space and Constraints on Magnetogenesis in the Early Universe." In: *JHEP* 10 (2014), p. 166. DOI: 10.1007/JHEP10(2014)166. arXiv: 1408.4141 [hep-th].

[464] Takahiro Hayashinaka, Tomohiro Fujita, and Jun'ichi Yokoyama. "Fermionic Schwinger effect and induced current in de Sitter space." In: *JCAP* 07 (2016), p. 010. DOI: 10.1088/1475-7516/2016/07/010. arXiv: 1603.04165 [hep-th].

[465] Shin'ichiro Ando and Alexander Kusenko. "Evidence for Gamma-Ray Halos Around Active Galactic Nuclei and the First Measurement of Intergalactic Magnetic Fields." In: *Astrophys. J. Lett.* 722 (2010), p. L39. DOI: 10.1088/2041-8205/722/1/L39. arXiv: 1005.1924 [astro-ph.HE].

[466] F. Tavecchio, G. Ghisellini, L. Foschini, G. Bonnoli, G. Ghirlanda, and P. Coppi. "The intergalactic magnetic field constrained by Fermi/LAT observations of the TeV blazar 1ES 0229+200." In: *Mon. Not. Roy. Astron. Soc.* 406 (2010), pp. L70–L74. DOI: 10.1111/j.1745-3933.2010.00884.x. arXiv: 1004.1329 [astro-ph.CO].

[467] Andrii Neronov and Ievgen Vovk. "Evidence for Strong Extragalactic Magnetic Fields from Fermi Observations of TeV Blazars." In: *Science* 328.5974 (2010), pp. 73–75. DOI: 10.1126/science.1184192. eprint: https://www.science.org/doi/pdf/10.1126/science.1184192. URL: https://www.science.org/doi/abs/10.1126/science.1184192.

[468] Warren Essey, Shin'ichiro Ando, and Alexander Kusenko. "Determination of intergalactic magnetic fields from gamma ray data." In: *Astropart. Phys.* 35 (2011), pp. 135–139. DOI: 10.1016/j.astropartphys.2011.06.010. arXiv: 1012.5313 [astro-ph.HE].

[469] Wenlei Chen, James H. Buckley, and Francesc Ferrer. "Search for GeV γ -Ray Pair Halos Around Low Redshift Blazars." In: *Phys. Rev. Lett.* 115 (2015), p. 211103. DOI: 10.1103/PhysRevLett.115.211103. arXiv: 1410.7717 [astro-ph.HE].

[470] M. Ackermann et al. "The Search for Spatial Extension in High-latitude Sources Detected by the *Fermi* Large Area Telescope." In: *Astrophys. J. Suppl.* 237.2 (2018), p. 32. DOI: 10.3847/1538-4365/aacdf7. arXiv: 1804.08035 [astro-ph.HE].

[471] K. Kajantie, M. Laine, K. Rummukainen, and Mikhail E. Shaposhnikov. "The Electroweak phase transition: A Nonperturbative analysis." In: *Nucl. Phys. B* 466 (1996), pp. 189–258. DOI: 10.1016/0550-3213(96)00052-1. arXiv: hep-lat/9510020.

[472] Guy D. Moore and Kari Rummukainen. "Electroweak bubble nucleation, nonperturbatively." In: *Phys. Rev.* D63 (2001), p. 045002. DOI: 10.1103/PhysRevD.63.045002. arXiv: hep-ph/0009132 [hep-ph].

[473] Oliver Gould, Sinan Güyer, and Kari Rummukainen. "First-order electroweak phase transitions: A nonperturbative update." In: *Phys. Rev. D* 106.11 (2022), p. 114507. DOI: 10.1103/PhysRevD.106.114507. arXiv: 2205.07238 [hep-lat].

[474] Lauri Niemi, Michael J. Ramsey-Musolf, and Guotao Xia. "Nonperturbative study of the electroweak phase transition in the real scalar singlet extended standard model." In: *Phys. Rev. D* 110.11 (2024), p. 115016. DOI: 10.1103/PhysRevD.110.115016. arXiv: 2405.01191 [hep-ph].

[475] Jose Ramon Espinosa and Mariano Quiros. "Novel Effects in Electroweak Breaking from a Hidden Sector." In: *Phys. Rev. D* 76 (2007), p. 076004. DOI: 10.1103/PhysRevD.76.076004. arXiv: hep-ph/0701145.

[476] Stefano Profumo, Michael J. Ramsey-Musolf, and Gabe Shaughnessy. "Singlet Higgs phenomenology and the electroweak phase transition." In: *JHEP* 08 (2007), p. 010. DOI: 10.1088/1126-6708/2007/08/010. arXiv: 0705.2425 [hep-ph].

[477] Hiren H. Patel and Michael J. Ramsey-Musolf. "Baryon Washout, Electroweak Phase Transition, and Perturbation Theory." In: *JHEP* 07 (2011), p. 029. DOI: 10.1007/JHEP07(2011)029. arXiv: 1101.4665 [hep-ph].

[478] Jose R. Espinosa, Thomas Konstandin, and Francesco Riva. "Strong Electroweak Phase Transitions in the Standard Model with a Singlet." In: *Nucl. Phys. B* 854 (2012), pp. 592–630. DOI: 10.1016/j.nuclphysb.2011.09.010. arXiv: 1107.5441 [hep-ph].

[479] David Curtin, Patrick Meade, and Chiu-Tien Yu. "Testing Electroweak Baryogenesis with Future Colliders." In: *JHEP* 11 (2014), p. 127. DOI: 10.1007/JHEP11(2014)127. arXiv: 1409.0005 [hep-ph].

[480] Mikael Chala, Claudius Krause, and Germano Nardini. "Signals of the electroweak phase transition at colliders and gravitational wave observatories." In: *JHEP* 07 (2018), p. 062. DOI: 10.1007/JHEP07(2018)062. arXiv: 1802.02168 [hep-ph].

[481] Peter Athron, Csaba Balázs, Andrew Fowlie, Lachlan Morris, and Lei Wu. "Cosmological phase transitions: From perturbative particle physics to gravitational waves." In: *Prog. Part. Nucl. Phys.* 135 (2024), p. 104094. DOI: 10.1016/j.ppnp.2023.104094. arXiv: 2305.02357 [hep-ph].

[482] Chiara Caprini, Ryusuke Jinno, Marek Lewicki, Eric Madge, Marco Merchand, Germano Nardini, Mauro Pieroni, Alberto Roper Pol, and Ville Vaskonen. "Gravitational waves from first-order phase transitions in LISA: reconstruction pipeline and physics interpretation." In: *JCAP* 10 (2024), p. 020. DOI: 10.1088/1475-7516/2024/10/020. arXiv: 2403.03723 [astro-ph.CO].

[483] Paul H. Ginsparg. "First Order and Second Order Phase Transitions in Gauge Theories at Finite Temperature." In: *Nucl. Phys.* B170 (1980), pp. 388–408. DOI: 10.1016/0550-3213(80)90418-6.

[484] Thomas Appelquist and Robert D. Pisarski. "High-Temperature Yang-Mills Theories and Three-Dimensional Quantum Chromodynamics." In: *Phys. Rev.* D23 (1981), p. 2305. DOI: 10.1103/PhysRevD.23.2305.

[485] Andreas Ekstedt, Philipp Schicho, and Tuomas V. I. Tenkanen. "Cosmological phase transitions at three loops: the final verdict on perturbation theory." In: (May 2024). arXiv: 2405.18349 [hep-ph].

[486] Oliver Gould and Cheng Xie. "Higher orders for cosmological phase transitions: a global study in a Yukawa model." In: *JHEP* 12 (2023), p. 049. DOI: 10.1007/JHEP12(2023)049. arXiv: 2310.02308 [hep-ph].

[487] Leon S. Friedrich, Michael J. Ramsey-Musolf, Tuomas V. I. Tenkanen, and Van Que Tran. "Addressing the Gravitational Wave - Collider Inverse Problem." In: (Mar. 2022). arXiv: 2203.05889 [hep-ph].

[488] Christophe Grojean and Geraldine Servant. "Gravitational Waves from Phase Transitions at the Electroweak Scale and Beyond." In: *Phys. Rev. D* 75 (2007), p. 043507. DOI: 10.1103/PhysRevD.75.043507. arXiv: hep-ph/0607107.

[489] Chiara Caprini et al. "Science with the space-based interferometer eLISA. II: Gravitational waves from cosmological phase transitions." In: *JCAP* 04 (2016), p. 001. DOI: 10.1088/1475-7516/2016/04/001. arXiv: 1512.06239 [astro-ph.CO].

[490] Zhaofeng Kang, P. Ko, and Toshinori Matsui. "Strong first order EWPT & strong gravitational waves in Z_3-symmetric singlet scalar extension." In: *JHEP* 02 (2018), p. 115. DOI: 10.1007/JHEP02(2018)115. arXiv: 1706.09721 [hep-ph].

[491] Katsuya Hashino, Mitsuru Kakizaki, Shinya Kanemura, Pyungwon Ko, and Toshinori Matsui. "Gravitational waves and Higgs boson couplings for exploring first order phase transition in the model with a singlet scalar field." In: *Phys. Lett. B* 766 (2017), pp. 49–54. DOI: 10.1016/j.physletb.2016.12.052. arXiv: 1609.00297 [hep-ph].

[492] Ligong Bian, Huai-Ke Guo, Yongcheng Wu, and Ruiyu Zhou. "Gravitational wave and collider searches for electroweak symmetry breaking patterns." In: *Phys. Rev. D* 101.3 (2020), p. 035011. DOI: 10.1103/PhysRevD.101.035011. arXiv: 1906.11664 [hep-ph].

[493] Oliver Gould, Jonathan Kozaczuk, Lauri Niemi, Michael J. Ramsey-Musolf, Tuomas V. I. Tenkanen, and David J. Weir. "Nonperturbative analysis of the gravitational waves from a first-order electroweak phase transition." In: *Phys. Rev. D* 100.11 (2019), p. 115024. DOI: 10.1103/PhysRevD.100.115024. arXiv: 1903.11604 [hep-ph].

[494] A. Ashoorioon and T. Konstandin. "Strong electroweak phase transitions without collider traces." In: *JHEP* 07 (2009), p. 086. DOI: 10.1088/1126-6708/2009/07/086. arXiv: 0904.0353 [hep-ph].

[495] Stefano Profumo, Michael J. Ramsey-Musolf, Carroll L. Wainwright, and Peter Winslow. "Singlet-catalyzed electroweak phase transitions and precision Higgs boson studies." In: *Phys. Rev. D* 91.3 (2015), p. 035018. DOI: 10.1103/PhysRevD.91.035018. arXiv: 1407.5342 [hep-ph].

[496] Tomáš Brauner, Tuomas V. I. Tenkanen, Anders Tranberg, Aleksi Vuorinen, and David J. Weir. "Dimensional reduction of the Standard Model coupled to a new singlet scalar field." In: *JHEP* 03 (2017), p. 007. DOI: 10.1007/JHEP03(2017)007. arXiv: 1609.06230 [hep-ph].

[497] Philipp M. Schicho, Tuomas V. I. Tenkanen, and Juuso Österman. "Robust approach to thermal resummation: Standard Model meets a singlet." In: *JHEP* 06 (2021), p. 130. DOI: 10.1007/JHEP06(2021)130. arXiv: 2102.11145 [hep-ph].

[498] Lauri Niemi and Tuomas V. I. Tenkanen. "Investigating two-loop effects for first-order electroweak phase transitions." In: (Aug. 2024). arXiv: 2408.15912 [hep-ph].

[499] Oliver Gould and Paul Saffin. "Perturbative gravitational wave predictions for the real-scalar extended Standard Model." In: (Nov. 2024). arXiv: 2411.08951 [hep-ph].

[500] R. A. Fisher. "On the Mathematical Foundations of Theoretical Statistics." In: *Phil. Trans. Roy. Soc. Lond. A* 222 (1922), pp. 309–368. DOI: 10.1098/rsta.1922.0009.

[501] M. Laine. "Gauge dependence of the high temperature two loop effective potential for the Higgs field." In: *Phys. Rev. D* 51 (1995), pp. 4525–4532. DOI: 10.1103/PhysRevD.51.4525. arXiv: hep-ph/9411252.

[502] Eric Braaten and Agustin Nieto. "Effective field theory approach to high temperature thermodynamics." In: *Phys. Rev. D* 51 (1995), pp. 6990–7006. DOI: 10.1103/PhysRevD.51.6990. arXiv: hep-ph/9501375.

[503] Lauri Niemi, Hiren H. Patel, Michael J. Ramsey-Musolf, Tuomas V. I. Tenkanen, and David J. Weir. "Electroweak phase transition in the real triplet extension of the SM: Dimensional reduction." In: *Phys. Rev. D* 100.3 (2019), p. 035002. DOI: 10.1103/PhysRevD.100.035002. arXiv: 1802.10500 [hep-ph].

[504] Kimmo Kainulainen, Venus Keus, Lauri Niemi, Kari Rummukainen, Tuomas V. I. Tenkanen, and Ville Vaskonen. "On the validity of perturbative studies of the electroweak phase transition in the Two Higgs Doublet model." In: *JHEP* 06 (2019), p. 075. DOI: 10.1007/JHEP06(2019)075. arXiv: 1904.01329 [hep-ph].

[505] Lauri Niemi, Michael J. Ramsey-Musolf, Tuomas V. I. Tenkanen, and David J. Weir. "Thermodynamics of a Two-Step Electroweak Phase Transition." In: *Phys. Rev. Lett.* 126.17 (2021), p. 171802. DOI: 10.1103/PhysRevLett.126.171802. arXiv: 2005.11332 [hep-ph].

[506] Joonas Hirvonen, Johan Löfgren, Michael J. Ramsey-Musolf, Philipp Schicho, and Tuomas V. I. Tenkanen. "Computing the gauge-invariant bubble nucleation rate in finite temperature effective field theory." In: *JHEP* 07 (2022), p. 135. DOI: 10.1007/JHEP07(2022)135. arXiv: 2112.08912 [hep-ph].

[507] Tuomas V. I. Tenkanen and Jorinde van de Vis. "Speed of sound in cosmological phase transitions and effect on gravitational waves." In: *JHEP* 08 (2022), p. 302. DOI: 10.1007/JHEP08(2022)302. arXiv: 2206.01130 [hep-ph].

[508] Johan Löfgren, Michael J. Ramsey-Musolf, Philipp Schicho, and Tuomas V. I. Tenkanen. "Nucleation at Finite Temperature: A Gauge-Invariant Perturbative Framework." In: *Phys. Rev. Lett.* 130.25 (2023), p. 251801. DOI: 10.1103/PhysRevLett.130.251801. arXiv: 2112.05472 [hep-ph].

[509] Mårten Bertenstam, Marco Finetti, António P. Morais, Roman Pasechnik, and Johan Rathsman. "Gravitational waves from color restoration in a leptoquark model of radiative neutrino masses." In: (Jan. 2025). arXiv: 2501.01286 [hep-ph].

[510] Fabio Bernardo, Philipp Klose, Philipp Schicho, and Tuomas V. I. Tenkanen. "Higher-dimensional operators at finite-temperature affect gravitational-wave predictions." In: (Mar. 2025). arXiv: 2503.18904 [hep-ph].

[511] Andreas Ekstedt, Philipp Schicho, and Tuomas V. I. Tenkanen. "DRalgo: A package for effective field theory approach for thermal phase transitions." In: *Comput. Phys. Commun.* 288 (2023), p. 108725. DOI: 10.1016/j.cpc.2023.108725. arXiv: 2205.08815 [hep-ph].

[512] Oliver Gould. "Real scalar phase transitions: a nonperturbative analysis." In: *JHEP* 04 (2021), p. 057. DOI: 10.1007/JHEP04(2021)057. arXiv: 2101.05528 [hep-ph].

[513] John Ellis, Marek Lewicki, Marco Merchand, José Miguel No, and Mateusz Zych. "The scalar singlet extension of the Standard Model: gravitational waves versus baryogenesis." In: *JHEP* 01 (2023), p. 093. DOI: 10.1007/JHEP01(2023)093. arXiv: 2210.16305 [hep-ph].

[514] Greg W. Anderson and Lawrence J. Hall. "The Electroweak phase transition and baryogenesis." In: *Phys. Rev. D* 45 (1992), pp. 2685–2698. DOI: 10.1103/PhysRevD.45.2685.

[515] Stephen P. Martin and Hiren H. Patel. "Two-loop effective potential for generalized gauge fixing." In: *Phys. Rev. D* 98.7 (2018), p. 076008. DOI: 10.1103/PhysRevD.98.076008. arXiv: 1808.07615 [hep-ph].

[516] Tyler Gorda, Andreas Helset, Lauri Niemi, Tuomas V. I. Tenkanen, and David J. Weir. "Three-dimensional effective theories for the two Higgs doublet model at high temperature." In: *JHEP* 02 (2019), p. 081. DOI: 10.1007/JHEP02(2019)081. arXiv: 1802.05056 [hep-ph].

[517] Carroll L. Wainwright, Stefano Profumo, and Michael J. Ramsey-Musolf. "Phase Transitions and Gauge Artifacts in an Abelian Higgs Plus Singlet Model." In: *Phys. Rev. D* 86 (2012), p. 083537. DOI: 10.1103/PhysRevD.86.083537. arXiv: 1204.5464 [hep-ph].

[518] Erick J. Weinberg and Ai-qun Wu. "UNDERSTANDING COMPLEX PERTURBATIVE EFFECTIVE POTENTIALS." In: *Phys. Rev. D* 36 (1987), p. 2474. DOI: 10.1103/PhysRevD.36.2474.

[519] Avi Friedlander, Ian Banta, James M. Cline, and David Tucker-Smith. "Wall speed and shape in singlet-assisted strong electroweak phase transitions." In: *Phys. Rev. D* 103.5 (2021), p. 055020. DOI: 10.1103/PhysRevD.103.055020. arXiv: 2009.14295 [hep-ph].

[520] Dietrich Bodeker and Guy D. Moore. "Electroweak Bubble Wall Speed Limit." In: *JCAP* 05 (2017), p. 025. DOI: 10.1088/1475-7516/2017/05/025. arXiv: 1703.08215 [hep-ph].

[521] James M. Cline, Avi Friedlander, Dong-Ming He, Kimmo Kainulainen, Benoit Laurent, and David Tucker-Smith. "Baryogenesis and gravity waves from a UV-completed electroweak phase transition." In: *Phys. Rev. D* 103.12 (2021), p. 123529. DOI: 10.1103/PhysRevD.103.123529. arXiv: 2102.12490 [hep-ph].

[522] Marek Lewicki, Marco Merchand, and Mateusz Zych. "Electroweak bubble wall expansion: gravitational waves and baryogenesis in Standard Model-like thermal plasma." In: *JHEP* 02 (2022), p. 017. DOI: 10.1007/JHEP02(2022)017. arXiv: 2111.02393 [astro-ph.CO].

[523] Tomasz Krajewski, Marek Lewicki, and Mateusz Zych. "Bubble-wall velocity in local thermal equilibrium: hydrodynamical simulations vs analytical treatment." In: *JHEP* 05 (2024), p. 011. DOI: 10.1007/JHEP05(2024)011. arXiv: 2402.15408 [astro-ph.CO].

[524] Marek Lewicki and Ville Vaskonen. "On bubble collisions in strongly supercooled phase transitions." In: *Phys. Dark Univ.* 30 (2020), p. 100672. DOI: 10.1016/j.dark.2020.100672. arXiv: 1912.00997 [astro-ph.CO].

[525] Marek Lewicki and Ville Vaskonen. "Gravitational waves from colliding vacuum bubbles in gauge theories." In: *Eur. Phys. J. C* 81.5 (2021), p. 437. DOI: 10.1140/epjc/s10052-021-09232-3. arXiv: 2012.07826 [astro-ph.CO].

[526] Chloe Gowling and Mark Hindmarsh. "Observational prospects for phase transitions at LISA: Fisher matrix analysis." In: *JCAP* 10 (2021), p. 039. DOI: 10.1088/1475-7516/2021/10/039. arXiv: 2106.05984 [astro-ph.CO].

[527] Ankit Beniwal, Marek Lewicki, James D. Wells, Martin White, and Anthony G. Williams. "Gravitational wave, collider and dark matter signals from a scalar singlet electroweak baryogenesis." In: *JHEP* 08 (2017), p. 108. DOI: 10.1007/JHEP08(2017)108. arXiv: 1702.06124 [hep-ph].

[528] Simone Blasi and Alberto Mariotti. "Domain Walls Seeding the Electroweak Phase Transition." In: *Phys. Rev. Lett.* 129.26 (2022), p. 261303. DOI: 10.1103/PhysRevLett.129.261303. arXiv: 2203.16450 [hep-ph].

[529] Simone Blasi, Ryusuke Jinno, Thomas Konstandin, Henrique Rubira, and Isak Stomberg. "Gravitational waves from defect-driven phase transitions: domain walls." In: *JCAP* 10 (2023), p. 051. DOI: 10.1088/1475-7516/2023/10/051. arXiv: 2302.06952 [astro-ph.CO].

[530] Prateek Agrawal, Simone Blasi, Alberto Mariotti, and Michael Nee. "Electroweak Phase Transition with a Double Well Done Doubly Well." In: (Dec. 2023). arXiv: 2312.06749 [hep-ph].

[531] Yang Li, Ligong Bian, and Yongtao Jia. "Solving the domain wall problem with first-order phase transition." In: (Apr. 2023). arXiv: 2304.05220 [hep-ph].

[532] Ankit Beniwal, Marek Lewicki, Martin White, and Anthony G. Williams. "Gravitational waves and electroweak baryogenesis in a global study of the extended scalar singlet model." In: *JHEP* 02 (2019), p. 183. DOI: 10.1007/JHEP02(2019)183. arXiv: 1810.02380 [hep-ph].

[533] Ligong Bian and Yi-Lei Tang. "Thermally modified sterile neutrino portal dark matter and gravitational waves from phase transition: The Freeze-in case." In: *JHEP* 12 (2018), p. 006. DOI: 10.1007/JHEP12(2018)006. arXiv: 1810.03172 [hep-ph].

[534] Aleksandr Azatov, Giulio Barni, Sabyasachi Chakraborty, Miguel Vanvlasselaer, and Wen Yin. "Ultra-relativistic bubbles from the simplest Higgs portal and their cosmological consequences." In: *JHEP* 10 (2022), p. 017. DOI: 10.1007/JHEP10(2022)017. arXiv: 2207.02230 [hep-ph].

[535] K. Kajantie, M. Laine, A. Rajantie, K. Rummukainen, and M. Tsypin. "The Phase diagram of three-dimensional SU(3) + adjoint Higgs theory." In: *JHEP* 11 (1998), p. 011. DOI: 10.1088/1126-6708/1998/11/011. arXiv: hep-lat/9811004.

[536] Tristan L. Smith, Tristan L. Smith, Robert R. Caldwell, and Robert Caldwell. "LISA for Cosmologists: Calculating the Signal-to-Noise Ratio for Stochastic and Deterministic Sources." In: *Phys. Rev. D* 100.10 (2019). [Erratum: Phys.Rev.D 105, 029902 (2022)], p. 104055. DOI: 10.1103/PhysRevD.100.104055. arXiv: 1908.00546 [astro-ph.CO].

[537] Mauro Pieroni and Enrico Barausse. "Foreground cleaning and template-free stochastic background extraction for LISA." In: *JCAP* 07 (2020). [Erratum: JCAP 09, E01 (2020)], p. 021. DOI: 10.1088/1475-7516/2020/07/021. arXiv: 2004.01135 [astro-ph.CO].

[538] Raphael Flauger, Nikolaos Karnesis, Germano Nardini, Mauro Pieroni, Angelo Ricciardone, and Jesús Torrado. "Improved reconstruction of a stochastic gravitational wave background with LISA." In: *JCAP* 01 (2021), p. 059. DOI: 10.1088/1475-7516/2021/01/059. arXiv: 2009.11845 [astro-ph.CO].

[539] Neil Cornish and Travis Robson. "Galactic binary science with the new LISA design." In: *J. Phys. Conf. Ser.* 840.1 (2017). Ed. by Domencio Giardini and Philippe Jetzer, p. 012024. DOI: 10.1088/1742-6596/840/1/012024. arXiv: 1703.09858 [astro-ph.IM].

[540] Marek Lewicki and Ville Vaskonen. "Impact of LIGO-Virgo black hole binaries on gravitational wave background searches." In: *Eur. Phys. J. C* 83.2 (2023), p. 168. DOI: 10.1140/epjc/s10052-023-11323-2. arXiv: 2111.05847 [astro-ph.CO].

[541] Max Tegmark, Andy Taylor, and Alan Heavens. "Karhunen-Loeve eigenvalue problems in cosmology: How should we tackle large data sets?" In: *Astrophys. J.* 480 (1997), p. 22. DOI: 10.1086/303939. arXiv: astro-ph/9603021.

[542] Matthew Gonderinger, Yingchuan Li, Hiren Patel, and Michael J. Ramsey-Musolf. "Vacuum Stability, Perturbativity, and Scalar Singlet Dark Matter." In: *JHEP* 01 (2010), p. 053. DOI: 10.1007/JHEP01(2010)053. arXiv: 0910.3167 [hep-ph].